

INTERIM
IN-20-CR

PENNSYLVANIA STATE UNIVERSITY



PROPULSION ENGINEERING RESEARCH CENTER

1993 ANNUAL REPORT
VOLUME II
NOVEMBER, 1993

A UNIVERSITY SPACE ENGINEERING
RESEARCH CENTER

FIFTH ANNUAL SYMPOSIUM
SEPTEMBER 8-9, 1993

106 RESEARCH BUILDING EAST
UNIVERSITY PARK, PENNSYLVANIA 16801

N94-23028
--THRU--
N94-23071
Unclas

G3/20 0198261

(NASA-CR-194719-Vol-2) NASA
PROPULSION ENGINEERING RESEARCH
CENTER, VOLUME 2 Annual Report
(Pennsylvania State Univ.) 223 p

**NASA PROPULSION ENGINEERING RESEARCH CENTER
ANNUAL REPORT 1993
VOLUME II**

FIFTH ANNUAL SYMPOSIUM

**SEPTEMBER 8-9, 1993
THE PENNSYLVANIA STATE UNIVERSITY
UNIVERSITY PARK, PA**

**THE PENNSYLVANIA STATE UNIVERSITY
UNIVERSITY PARK, PA**

TABLE OF CONTENTS

Summary.....	i
Technical Program.....	ii
<u>Steady State Combustion and Performance</u>	
Measurement of Intact-Core Length of Atomizing Liquid Jets by Image Deconvolution.....	1 ✓
Small Rocket Flowfield Diagnostic Chambers.....	5 ✓
A Theoretical Evaluation of Aluminum Gel Propellant Two-Phase Flow Losses on Vehicle Performance.....	12 ✓
Laser Diagnostics for Small Rockets.....	17 ✓
CFD Analyses of Combustor and Nozzle Flowfields.....	23 ✓
LOX Droplet Vaporization in a Supercritical Forced Convective Environment.....	28 ✓
Evaporation and Combustion of LOX Under Supercritical and Subcritical Conditions.....	33 ✓
Droplet Turbulence Interactions Under Subcritical and Supercritical Conditions.....	39 ✓
SSME Fuel Preburner Injector Characterization.....	46 ✓
Small Rocket Research and Technology.....	50 ✓
Fundamental Rocket Injector/Spray Programs at the Phillips Laboratory.....	54 ✓
An Experimental Study of Characteristic Combustion-Driven Flows for CFD Validation.....	58 ✓
<u>Combustion Stability</u>	
Numerical Parametric Studies of Spray Combustion Instabilities.....	64 ✓
Spray Formation Processes of Impinging Jet Injectors.....	69 ✓
Inherent Stability of Central Element Coaxial Liquid-Liquid Injectors.....	75 ✓
Axisymmetric Single Shear Element Combustion Instability Experiment.....	77 ✓
Development of a Droplet Breakup Model Considering Aerodynamic and Droplet Collision Effects.....	82 ✓
Development of a Computational Testbed for Numerical Simulation of Combustion Instability.....	88 ✓
Shear Coaxial Injector Instability Mechanisms.....	93 ✓

**TABLE OF CONTENTS
(continued)**

<u>Heat Transfer and Fluid Mechanics</u>	
Numerical Investigation of Two- and Three-Dimensional Heat Transfer in Expander Cycle Engines.....	97 ✓
Flow Visualization Study in High Aspect Ratio Cooling Channels for Rocket Engines.....	101 ✓
CFD Analyses of Coolant Channel Flowfields.....	106 ✓
Heat Transfer in Rocket Combustion Chambers.....	111 ✓
Advanced Materials for Radiation-Cooled Rockets.....	115 ✓
Molecular Gas Dynamics Applied to Low-Thrust Propulsion.....	119 ✓
CFD Applications in Rocket Propulsion Analysis and Design.....	125 ✓
Efficiency and Reliability Enhancements in Propulsion Flowfield Modeling.....	130 ✓
Computation of Propulsion-Related Flowfields Using Unstructured Adaptive Meshes.....	135 ✓
Dual-Bell Altitude Compensating Nozzles.....	140 ✓
<u>Turbomachinery Aero- and Hydro-Dynamics</u>	
Foil Bearing Research at Penn State.....	148 ✓
Two Stage Turbine for Rockets.....	152 ✓
Computational Fluid Dynamic Modelling of Cavitation.....	159 ✓
A Technique to Measure Rotordynamic Coefficients in Hydrostatic Bearings.....	164 ✓
Computation of Flows in a Turn-Around Duct and a Turbine Cascade Using Advanced Turbulence Models.....	170 ✓
Brush Seals for Cryogenic Applications.....	176 ✓
Reliability Enhancement of Navier-Stokes Codes Through Convergence Enhancement.....	181 ✓
<u>Advanced Space Propulsion Concepts</u>	
Optimization of Energy Transfer in Microwave Electrothermal Thrusters.....	187 ✓
CFD Modeling of Microwave Electrothermal Thrusters.....	191 ✓
Advanced Space Propulsion Concepts.....	195 ✓
Advanced Nuclear Thermal Propulsion Concepts.....	199 ✓
An Anti-Proton Driver for ICF Propulsion.....	203 ✓
Performance Assessment of Low Pressure Nuclear Thermal Propulsion.....	207 ✓
Nuclear Propulsion Control and Health Monitoring.....	212 ✓

SUMMARY

On September 8-9, 1993, the Propulsion Engineering Research Center at The Pennsylvania State University held its Fifth Annual Symposium at the Penn State campus in University Park, PA. The Propulsion Engineering Research Center was initiated in 1988 by a grant from the NASA Office of Aeronautics and Space Technology as a part of the University Space Engineering Research Center (USERC) program; the purpose of the USERC program is to replenish and enhance the capabilities of our Nation's engineering community to meet its future space technology needs. These Centers are designed to advance the state-of-the-art in key space-related engineering disciplines and to promote and support engineering education for the next generation of engineers for the national space program and related commercial space endeavors. A broadly-based research program in propulsion has been established at the Center, with over 100 students, faculty and staff working on research related to the areas of liquid, solid, and hybrid chemical propulsion, nuclear propulsion, electrical propulsion, and advanced propulsion concepts. An important means of interaction with the propulsion community is our Annual Symposium. At this year's Symposium, 43 papers on propulsion science were presented by representatives from industry, government laboratories, and academia. Twenty-two of the 43 papers were presented by students and faculty of the Propulsion Engineering Research Center. This volume contains abstracts of the work presented at the Symposium.

Propulsion Engineering Research Center
Fifth Annual Symposium
The Pennsylvania State University
University Park, Pennsylvania
September 8-9, 1993

Wednesday Morning, September 8

5th Floor Keller Conference Center

7:45 - 8:30 Registration

Room 506 Keller Conference Center

- 8:30 - 8:45 Welcome and Introductory Remarks - *C.L. Merkle, Director, Propulsion Engineering Research Center*
Steady State Combustion and Performance 1 Chaired by *D. Talley, Phillips Laboratory*
- 8:45 - 9:10 Measurement of Intact-Core Length of Atomizing Liquid Jets by Image Deconvolution -
R. Woodward, R. Burch, F.-B. Cheung, and K. Kuo, PSU
- 9:10 - 9:35 Small Rocket Flowfield Diagnostic Chambers - *B. Reed and S. Morren, Lewis Research Center*
- 9:35 - 10:00 A Theoretical Evaluation of Aluminum Gel Propellant Two-Phase Flow Losses on Vehicle Performance -
D. Mueller and S. Turns, PSU
- 10:00 - 10:25 Dual-Bell Altitude Compensating Nozzles - *S. Fisher and M. Horn, Rocketdyne*
- 10:25 - 10:45 Break
- 10:45 - 11:10 Laser Diagnostics for Small Rockets - *F. Zupanc and W. deGroot, Lewis Research Center*
- 11:10 - 11:35 CFD Analyses of Combustor and Nozzle Flowfields - *H.-H. Tsuei and C. Merkle, PSU*
- 11:35 - 12:00 Computation of Propulsion-Related Flowfields Using Unstructured Adaptive Meshes -
J. Weiss and J. Murphy, Fluent, Inc.

Room 507 Keller Conference Center

Advanced Space Propulsion Concepts Chaired by *M. Micci, PSU*

- 8:45 - 9:10 Optimization of Energy Transfer in Microwave Electrothermal Thrusters - *D. Sullivan and M. Micci, PSU*
- 9:10 - 9:35 CFD Modeling of Microwave Electrothermal Thrusters - *D. Schwer, S. Venkateswaran, and C. Merkle, PSU*
- 10:00 - 10:25 Advanced Nuclear Thermal Propulsion Concepts - *S. Howe, Los Alamos National Laboratory*
- 10:25 - 10:45 Break
- 10:45 - 11:10 An Anti-Proton Driver for ICF Propulsion - *G. Smith, P.-R. Chiang, R. Lewis, C. Gazze, K. Higman,
R. Newton, M. Chiaverini, J. Dailey, M. Surratt, W. Werthman, P. Cracraft, and S. Chakrabarti, PSU*
- 11:10 - 11:35 Performance Assessment of Low Pressure Nuclear Thermal Propulsion -
H. Gerrish and G. Doughty, Marshall Space Flight Center
- 11:35 - 12:00 Nuclear Propulsion Control and Health Monitoring - *P. Walter and R. Edwards, PSU*

Wednesday Afternoon, September 8

Multi-Purpose Room, Ground Floor, Keller Conference Center

- 12:15 - 1:00 Lunch
1:00 - 1:45 Invited Speech: "Access to Space" - *R. Ryan, Marshall Space Flight Center*

Room 506 Keller Conference Center

Steady State Combustion and Performance 2 *Chaired by S. Schneider, Lewis Research Center*

- 1:50 - 2:15 LOX Droplet Vaporization in a Supercritical Forced Convective Environment -
C.C. Hsiao and V. Yang, PSU
- 2:15 - 2:40 Evaporation and Combustion of LOX Under Supercritical and Subcritical Conditions -
A. Yang, K. Kuo, and W.-H. Hsieh, PSU
- 2:40 - 3:30 Droplet Turbulence Interactions Under Subcritical and Supercritical Conditions -
E. Coy, S. Greenfield, M. Ondas, Y.-H. Song, T. Spegar, and D. Santavicca, PSU
- 3:30 - 3:50 Break
- 3:50 - 4:15 SSME Fuel Preburner Injector Characterization - *J. Hutt, Marshall Space Flight Center*
- 4:15 - 4:40 Small Rocket Research and Technology - *S. Schneider and J. Biaglow, Lewis Research Center*
- 4:40 - 5:05 Fundamental Rocket Injector/Spray Programs at the Phillips Laboratory - *D. Talley, Phillips Laboratory*
- 5:05 - 5:30 An Experimental Study of Characteristic Combustion-Driven Flows for CFD Validation -
S. Pal, M. Moser, J. Merenich, and R. Santoro, PSU

Room 507 Keller Conference Center

Turbomachinery Aero- and Hydro-Dynamics *Chaired by B. Lakshminarayana, PSU*

- 1:50 - 2:15 Foil Bearing Research at Penn State - *M. Carpino, PSU*
- 2:15 - 2:40 Two Stage Turbine for Rockets - *J. Veres, Lewis Research Center*
- 2:40 - 3:05 Computational Fluid Dynamic Modeling of Cavitation - *M. Deshpande, J. Feng, and C. Merkle, PSU*
- 3:05 - 3:30 A Technique to Measure Rotordynamic Coefficients in Hydrostatic Bearings -
R. Capaldi, Lewis Research Center
- 3:30 - 3:50 Break
- 3:50 - 4:15 Computation of Flows in a Turn-Around Duct and a Turbine Cascade Using Advanced Turbulence Models -
B. Lakshminarayana and J. Luo, PSU
- 4:15 - 4:40 Brush Seals for Cryogenic Applications - *M. Proctor, Lewis Research Center*
- 4:40 - 5:05 Reliability Enhancement of Navier-Stokes Codes Through Convergence Enhancement -
K.-Y. Choi and G. Dulikravich, PSU

Wednesday Evening, September 8

Propulsion Engineering Research Center

- 6:00 - 7:30 Reception and Open House

Thursday Morning, September 9

Room 506 Keller Conference Center

Combustion Stability *Chaired by K. Breisacher, Lewis Research Center*

- 8:15 - 8:40 Numerical Parametric Studies of Spray Combustion Instabilities - *M. Pindera, CFD Research*
- 8:40 - 9:05 Spray Formation Processes of Impinging Jet Injectors -
H. Ryan, W. Anderson, S. Pal, and R. Santoro, PSU
- 9:05 - 9:30 Inherent Stability of Central Element Coaxial Liquid-Liquid Injectors - *F. Stoddard, TRW*
- 9:30 - 9:55 Axisymmetric Single Shear Element Combustion Instability Experiment -
K. Breisacher, Lewis Research Center
- 9:55 - 10:15 Break
- 10:15 - 10:40 Development of a Droplet Breakup Model Considering Aerodynamic and Droplet Collision Effects -
K. Wert and H.R. Jacobs, PSU
- 10:40 - 11:05 Development of a Computational Testbed for Numerical Simulation of Combustion Instability -
J. Grenda, S. Venkateswaran, and C. Merkle, PSU
- 11:05 - 11:30 Shear Coaxial Injector Instability Mechanisms - *T. Kaltz, M. Glogowski, and M. Micci, PSU*

Room 507 Keller Conference Center

Heat Transfer and Fluid Mechanics *Chaired by P. McConnaughey, Marshall Space Flight Center*

- 8:15 - 8:40 Numerical Investigation of Two- and Three-Dimensional Heat Transfer in Expander Cycle Engines -
R. Burch and F.-B. Cheung, PSU
- 8:40 - 9:05 Flow Visualization Study in High Aspect Ratio Cooling Channels for Rocket Engines -
M. Meyer and J. Giuliani, Lewis Research Center
- 9:05 - 9:30 CFD Analyses of Coolant Channel Flowfields - *J. Yagley, J. Feng, and C. Merkle, PSU*
- 9:30 - 9:55 Heat Transfer in Rocket Combustion Chambers - *P. Anderson, G. Cheng, and R. Farmer, SECA*
- 9:55 - 10:15 Break
- 10:15 - 10:40 Advanced Materials for Radiation-Cooled Rockets -
B. Reed, J. Biaglow, and S. Schneider, Lewis Research Center
- 10:40 - 11:05 Molecular Gas Dynamics Applied to Low-Thrust Propulsion -
D. Zelesnik and P. Penko, Lewis Research Center, and I. Boyd, Cornell University
- 11:05 - 11:30 CFD Applications in Rocket Propulsion Analysis and Design -
P. McConnaughey, R. Garcia, L. Griffin, and J. Ruf, Marshall Space Flight Center
- 11:30 - 11:55 Efficiency and Reliability Enhancements in Propulsion Flowfield Modeling -
P. Buelow, S. Venkateswaran, and C. Merkle, PSU

Room 507 Keller Conference Center

- 11:55 - 12:00 Closing Remarks - *C. Merkle, PSU*

MEASUREMENT OF INTACT-CORE LENGTH
OF ATOMIZING LIQUID JETS BY IMAGE DECONVOLUTION

Roger Woodward, Robert Burch, Kenneth Kuo, and Fan-Bill Cheung
Propulsion Engineering Research Center

and
Department of Mechanical Engineering
The Pennsylvania State University
University Park, PA 16802

SUMMARY:

The investigation of liquid jet breakup and spray development is critical to the understanding of combustion phenomena in liquid-propellant rocket engines. Much work has been done to characterize low-speed liquid jet breakup and dilute sprays, but atomizing jets and dense sprays have yielded few quantitative measurements due to their high liquid load fractions and hence their optical opacity. This work focuses on a characteristic of the primary breakup process of round liquid jets, namely the length of the intact-liquid core. The specific application considered is that of shear-coaxial-type rocket engine injectors in which liquid oxygen is injected through the center post while high-velocity gaseous hydrogen is injected through a concentric annulus, providing a shear force to the liquid jet surface. Real-time x-ray radiography, capable of imaging through the dense two-phase region surrounding the liquid core, is used to make the measurements. The intact-liquid-core length data have been obtained and interpreted using two conceptually different methods to illustrate the effects of chamber pressure, gas-to-liquid momentum ratio, and cavitation.

TECHNICAL DISCUSSION:

The focus of this study is the measurement of the intact-core length of coaxial jets using X-ray radiography. Two injector sizes are used, having liquid exit diameters and annular-gas-flow exit areas of 1) 4.8 mm (3/16 in) and 45 mm² (0.069 in²) and 2) 2.4 mm (3/32 in) and 11 mm² (0.017 in²). The propellant simulants consist of a solution of potassium iodide (KI) in water for the LOX and gaseous nitrogen or helium for the annular-flowing hydrogen. Iodide is a X-ray absorber, thus allowing of line-of-sight imaging of the spray. A detailed description of the test and image processing equipment, setup, and calibration has been given previously (1-3). Following Beer's law, the measured radiance levels of the resulting image are a function of liquid thickness. Through the use of calibration cells, the integrated liquid thickness at each point in the jet can be obtained.

In the course of this study, two different methods of data analysis have been used to determine the intact core length from the X-ray images: a threshold criterion technique based on the integrated liquid thickness, and a threshold criterion based on mean liquid volume fraction using a deconvolution technique. In previous studies by this research group [1-3], the intact-core length was obtained from the processed images using a threshold value based on an integrated liquid thickness corresponding to the end of the intact core. The threshold criterion was selected to be the mean radiance of the 1.6 mm calibration cell for the larger injector and for the smaller injector, a radiance level corresponding to one-fourth that thickness. The core length was measured directly from the image for each of ten

images corresponding to that one flow condition. These measurements were then averaged for one mean value at each condition. Figure 1 presents dimensionless intact-core length (L_b/D) results obtained using this image threshold technique versus dimensionless chamber pressure for a range of gas velocities and two sets of liquid velocities ($v_l = 15$ and 27 m/s). Figure 2 presents similar results for the smaller injector over a range of gas velocities and two sets of liquid velocities ($v_l = 30$ and 60 m/s). These results are discussed in detail by Woodward [3].

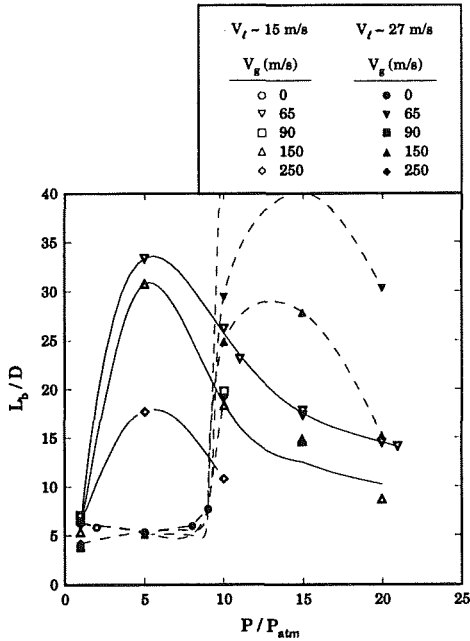


Figure 1. Effect of chamber pressure (gas density) on intact-core length for larger injector using liquid thickness threshold criterion length.

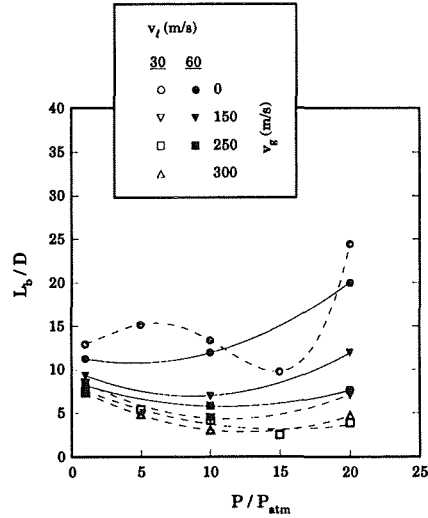


Figure 2. Effect of chamber pressure on intact-core length for injector B (smaller injector).

The selection of the aforementioned threshold criterion is somewhat arbitrary since it is based on an integrated liquid thickness over the entire jet cross section and not an actual core diameter (although such a technique is largely dependent on the core diameter). The alternate technique, based on image deconvolution, considers the combined x-ray path length through the gas as well as the liquid, accounting for the two-phase regions of the coaxial spray. This technique requires the following assumptions to determine radial distributions of the mean liquid volume fraction: axial symmetry of the jet and statistically steady flow. The 33 ms exposures used are of a sufficient length of time for the jet to adequately meet these assumptions. The time-averaged intact-liquid-core and the radial boundary is demarcated by the departure from unity of the liquid volume fraction.

As recommended by Dasch [4], to accomplish the jet image deconvolutions, the three-point Abel inversion has been applied to the present problem since it is relatively easy to calculate and was shown to be more robust and less noisy in controlled tests cases than other common methods. All deconvolution techniques are very sensitive to noise present in the original line-of-sight projection data. To improve the smoothness of the x-ray absorption profiles across the liquid jet in the normalized injection images, the entire series of ten images per test case is averaged together to create one clean normalized image at that injection condition; and lastly, a spatial smoothing is applied to this averaged image.

To determine mean liquid volume fractions, which by definition vary from zero to unity, the deconvolution results are normalized by centerline results very near the injector exit where the liquid volume fraction is at least approximately unity. The intact-liquid-core length is determined for each image by thresholding the resultant deconvoluted-jet image at a mean liquid volume fraction value of 0.9. The core length is then measured in terms of pixels directly from this image.

Figure 3 presents the intact-core length results obtained from jet image deconvolutions for tests conducted with the larger injector. Dimensionless core length is plotted versus dimensionless chamber pressure. As in Fig. 1, two sets of liquid jet velocity data ($v_\ell=15$ and 27 m/s) are represented. It is apparent from Fig. 3 that the core-length curves representing constant gas and liquid velocity have a shape and trend very similar to their threshold technique counterparts in Fig. 1. However, since these figures being compared are plotted at the same scale, it is obvious that the results obtained from the jet image deconvolutions are considerably shorter than those obtained using the threshold technique. The reduction in intact-core length compared to the previous results is not of a constant factor. On average for the results reported in Fig. 3, the intact-core lengths from the deconvoluted jet images are 40% shorter than those obtained using the threshold technique with the 1.59 mm (1/16 in.) threshold criterion. This reduction factor varies over a range of 20% to nearly 70% for one extreme case. Although the intact-core measurements resulting from the determination of liquid volume fraction distributions are much shorter than the corresponding results from the threshold method, the single jet tests in the non-cavitating regime (at $P_c = 4$ atm and above for $v_\ell \approx 15$ m/s and at $P_c = 10$ atm and above for $v_\ell \approx 27$ m/s) still indicate off-scale (> 30 liquid exit diameters) core lengths. On the other hand, the $v_\ell = 30$ m/s, $v_g = 65$ m/s core length result at an ambient pressure condition of 15 atm that was previously off-scale now shows a measurable intact length of 19.8 injector diameters.

Although the deconvolution results presented in Fig. 3 match in general the breakup length trends exhibited by the corresponding threshold method results, there is one data point that shows a major discrepancy. The point at 15 atm on the $v_\ell \approx 27$ m/s, $v_g \approx 150$ m/s curve is below its neighboring points at 10 and 20 atm. Based on the other $v_\ell \approx 27$ m/s curve of Fig. 3 and the corresponding results of Fig. 1, the 15 atm point in question should be near the peak of the curve. Also, the $v_\ell \approx 15$ m/s, $v_g \approx 65$ m/s data point lies above the higher liquid velocity point as shown so that another disagreement occurs with the reasoning that the larger liquid jet momentum associated with the higher jet velocity should result in a longer intact core length. It is suspected that this stray data point is an anomaly and that previous findings should not be refuted by this.

Analogous to Fig. 3, Fig. 4 is a plot of the intact-core-length-via-deconvolution results obtained this time using the smaller injector. While Fig. 3 appeared as a squashed but similar version of the corresponding threshold results, Fig. 4 bears little resemblance to the corresponding threshold technique results in Fig. 2. Some of the indicated core lengths are shorter and some are longer than their counterparts determined by the previous method. No consistent trend is exhibited by these deconvolution results for the smaller injector. It is likely that the measurement of intact-core length by the deconvolution method is more unreliable for the smaller injector. This is quite conceivable considering the lower x-ray attenuation levels associated with the smaller diameter jet and the fact that there are only a few pixels across the liquid jet. The spatial resolution as well as the gray level resolution may be

insufficient to produce a decent deconvolution of the smaller jet, especially considering that the injection images of the smaller injector are subject to the same noise levels seen in the larger injector images.

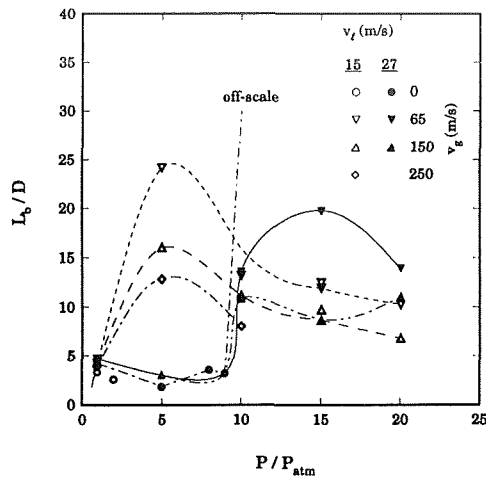


Figure 3. Intact-core length results obtained using the image deconvolution method for injector A tests.

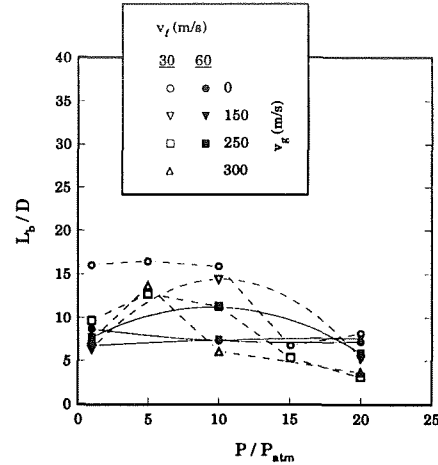


Figure 4. Intact-core length results obtained using the image deconvolution method for injector B tests.

Two conceptually different methods have been used to determine intact-liquid-core lengths for coaxial injection at realistic flow rate conditions: 1) thresholding of jet images to reveal the core region corresponding to a specified liquid integrated thickness and 2) deconvolution of time-averaged jet images to get mean liquid volume fraction distributions. Intact-core results between these two methods agree in form but not in magnitude. Theoretically, the deconvolution method is the more correct one to use; however, it is difficult to obtain an accurate deconvolution due to sensitivity to noise in the line-of-sight image data. Hence, the intact-core lengths obtained using this method are of uncertain accuracy and even questionable for the smaller injector. The threshold technique was applied to the larger injector by using a 1.59 mm (1/16 in.) integrated liquid thickness as the criterion to determine the extent of the core. The consistently shorter deconvolution results indicate that this criterion thickness may be too thin. A major problem with the threshold technique is that different thickness criteria are needed for different size injectors.

REFERENCES:

- 1 Woodward, R. D., Burch R. L., Kline M. C., Kuo, K. K., and Cheung, F.-B., "Measurement of Intact-Liquid-Core Length of Rocket Engine Coaxial Injectors," Fourth Annual PERC Symposium, NASA-MSFC, Huntsville, AL, September 1992.
- 2 Woodward, R. D., Burch R. L., Kuo, K. K., and Cheung, F.-B., "Real-Time X-Ray Radiography Study of Liquid Jet Breakup from Rocket Engine Coaxial Injectors," The Third International Symposium of Special Topics in Chemical Propulsion: Non-Intrusive Combustion Diagnostics, Scheveningen, The Netherlands, May 1993.
- 3 Woodward, R. D., Primary Atomization of Liquid Jets Issuing from Rocket Engine Coaxial Injectors, Ph.D. Thesis, The Pennsylvania State University, Aug. 1993.
- 4 Dasch, C. J., "One-Dimensional Tomography: A Comparison of Abel, Onion-Peeling, and Filtered Backprojection Methods," *Applied Optics*, Vol. 31, No. 8, March 1992, pp. 1146-1152.

SMALL ROCKET FLOWFIELD DIAGNOSTIC CHAMBERS

Sybil Morren and Brian Reed
NASA Lewis Research Center

SUMMARY

Instrumented and optically-accessible rocket chambers are being developed to be used for diagnostics of small rocket (< 440 N thrust level) flowfields. These chambers are being tested to gather local fluid dynamic and thermodynamic flowfield data over a range of test conditions. This flowfield database is being used to better understand mixing and heat transfer phenomena in small rockets, influence the numerical modeling of small rocket flowfields, and characterize small rocket components. The diagnostic chamber designs include: 1) a chamber design for gathering wall temperature profiles to be used as boundary conditions in a finite element heat flux model; 2) a chamber design for gathering inner wall temperature and static pressure profiles; and 3) optically-accessible chamber designs, to be used with a suite of laser-based diagnostics for gathering local species concentration, temperature, density, and velocity profiles. These chambers were run with gaseous hydrogen/gaseous oxygen (GH₂/GO₂) propellants, while subsequent versions will be run on liquid oxygen/hydrocarbon (LOX/HC) propellants. This presentation summarizes the purpose, design, and initial test results of these small rocket flowfield diagnostic chambers.

HEAT FLUX DIAGNOSTIC CHAMBER

A chamber was designed and fabricated to determine steady-state heat flux to the inner wall to be used as a diagnostic of the flowfield behavior.¹ The heat flux chamber design is an instrumented, water-cooled chamber used to gather steady-state wall temperature profiles from measured and interpolated thermocouple data. These temperature profiles are used as boundary conditions in a finite element analysis program, MSC/NASTRAN, to calculate the local radial and axial heat fluxes in the chamber. Normal heat flux down the length of the chamber is then calculated as the dot product of the total heat flux and normal vectors. It is important to emphasize that heat flux is used here as a flowfield diagnostic - the objective is not to find absolute heat flux values (which would change for differing wall conditions), but rather to use heat flux as an indicator of fundamental characteristics of the flowfield over a range of conditions.

A schematic of a heat flux chamber used with a GH₂/GO₂ injector is shown in figure 1. The chamber was fabricated from Oxygen-Free, High-Conductivity (OFHC) copper, with a 1.27 cm thick wall. An OFHC copper housing was welded onto the chamber to provide an annulus for water cooling along the outer wall. Chromel-alumel, grounded-junction thermocouples were embedded in the inner wall, nominally 0.159 cm from the inner wall and attached to the outer wall and exit face. It was found that boundary condition definition was critical to the accuracy and resolution of the heat flux profiles generated by the finite element program. Details of the chamber fabrication and the heat flux methodology are given in reference 1.

This heat flux chamber was used to gather temperature data over a range of mixture ratios at 61 percent fuel film cooling (FFC) and 414 kPa chamber pressure. The normal heat flux profiles (as a function of axial position) generated from the temperature data is shown in figure 2. The heat flux profiles showed a significant increase in

shear layer mixing in the barrel section of the chamber for mixture ratios above five, indicated by the sharp heat flux peaks there. This increase was felt not to be a result of the flow transitioning to turbulent, since Reynolds numbers were well within the laminar regime, but rather due to increased chemical reactions in the shear layer between the hydrogen film cooling and oxidizer-rich core flows. It was uncertain what the trigger mechanism was for this increased shear layer mixing at higher mixture ratios. This heat flux methodology will be used further for investigation of flowfield behavior and characterization of LOX/HC small rocket injector configurations.

TEMPERATURE/PRESSURE DIAGNOSTIC CHAMBER

A chamber was designed to investigate small rocket flowfields via inner wall temperature and static pressure measurements,² as shown in figure 3. The chamber liner was fabricated from OFHC copper, with milled channels on the back side to provide water cooling. An OFHC copper outer housing was split into two parts axially along its length and slid over the chamber liner in a clam-shell fashion. The housing was joined to the liner at the inlet and outlet water manifolds, and sealed along the two axial housing seams. The chamber contained 4 axial rows of thermocouple ports which spanned from the combustion chamber to the nozzle section. The chromel-alumel thermocouples were located 0.076 cm from the hot gas side wall. The chamber also contained one row of static pressure ports. Because the backside of the chamber was not sealed to the outer housing, instrumentation seals were developed to accommodate the chamber cooling system.

The diagnostic chamber was hot fired using two platelet stack injectors of two, slightly different designs, designated SN 02 and SN 03. The chamber was operated at 262 kPa, 379 kPa, and 517 kPa chamber pressures and 60% and 75% FFC, for mixture ratios between 4.0 and 8.0. At 75% FFC, both chambers exhibited the same performance and thermal trends. However, at 60% FFC the data trends differed between the two injectors. Figure 4 show the axial inner wall temperature profiles for both injectors at 60% FFC. The inner wall temperatures for the SN02 injector displayed a greater sensitivity to mixture ratio than for the SN03 injector. Furthermore, the inner wall temperature generally increased with increasing mixture ratio for the SN02 injector, while the opposite trend was observed for the SN03 injector. The results of this testing indicated that small rocket flowfield behavior may be very sensitive to minor changes in operating conditions and injector design. Further discussion of tests results and the details of the chamber design and fabrication are found in Reference 2.

This diagnostic chamber design will be used further for investigation of flowfield behavior (in particular, an unsteady flowfield phenomenon suspected to be associated with the GH2/GO2 injectors used previously), characterization of LOX/HC small rocket injector configurations, and investigation of low Reynolds number nozzle design issues. Furthermore, the pressure ports of this chamber could be utilize for gas sampling and for the insertion of fiber optics for laser-based diagnostics.

OPTICALLY-ACCESSIBLE CHAMBERS FOR LASER-BASED DIAGNOSTICS

Optical access to the combustion chamber allows the use of non-intrusive, laser based diagnostics to gather local fluid dynamic and thermodynamic data. These diagnostics include Raman spectroscopy to measure species concentrations, gas temperatures, and flow velocity profiles near the injector and Laser-Induced Fluorescence (LIF) used to visualize the shear layer mixing process and to measure minor species concentrations.³ Schlieren and

shadowgraph techniques could also be used with optically accessible chambers to visualize the flowfield. A square rocket chamber was designed, fabricated, and hot fired to provide optical access to the combustion chamber from the sides. The square (2D), optically-accessible chamber was seen as an intermediate step toward an axisymmetric (3D), optically-accessible chamber and was therefore designed to be robust.

The 2D chamber is shown in figure 5. The chamber was machined out of OFHC copper with water cooling channels drilled in the wall above and below the combustion chamber and nozzle. On the left and right side of the chamber there were slots for the placement of 13.3 cm by 6.35 cm by 1.27 cm windows. High optical quality, fused silica was selected as the window material. Fused silica has a maximum operating temperature of only 980 °C, but has a relatively low coefficient of thermal expansion compared to sapphire. Furthermore fused silica can be machined with better surface qualities compared to sapphire, reducing the amount of diffuse scattering of laser light within the chamber. Gaseous nitrogen was injected against the windows for cooling.

The 2D chamber provides optical access down the entire length of the rocket. Because the windows are cooled independently, the interaction of fuel film cooling flow with the oxidizer-rich core flow in the shear layer (a critical phenomenon in small rocket flows) can be studied without the threat of a film cooling layer breakdown melting the windows. The main drawback, however, is that the measurements - and any conclusions drawn from them - are restricted to a two-dimensional flowfield. It will be important to distinguish between effects that are representative of the flowfield behavior and effects that result from the two dimensionality of the chamber. Also the nitrogen flow, though directed against the windows, will slowly penetrate into the hydrogen/oxygen flow.

The 2D chamber was checked out using copper slabs instrumented with thermocouples in place of the windows. The nitrogen flow was sufficient to keep the inner wall temperature below 93 °C, with no more than a 27 °C temperature variation across the slab. The chamber was then run with the windows in a series of 15-second duration tests at a chamber pressure of 296 kPa and a total mass flowrate of 0.033 kg/s. At an overall mixture ratio 6 and 55% FFC, the core mixture ratio was 13.3. After a total of 232 tests with the same set of windows, there was no evidence of cracking or degradation of the windows. Laser Raman spectroscopy was used to measure the gas temperature and oxygen concentration at the exit of the chamber sleeve insert used with the injector. The measured temperature and oxygen concentration profiles were found to be significantly different from the profiles that are usually assumed in numerical calculations. Detailed discussion of the Raman measurements with this chamber can be found in reference 4.

The next step from the 2D chamber will be an axisymmetric, optically-accessible rocket chamber. The preliminary design of a 3D chamber to be used with GH₂/GO₂ propellants is shown in figure 6. A modular design is envisioned with a flush-mounted injector, a cylindrical, fused silica window for the barrel section, and a water-cooled converging/diverging nozzle, all clamped together. A concern with this design are the thermal stresses that could be induced by temperature differences between the window mating surfaces. Fuel film cooling from the injector and water cooling of the nozzle section should keep the mating surfaces at a fairly uniform temperature. Water cooling of the nozzle section should also minimize thermal soakback into the window, although a low thermal conductivity interface could be used between the window and nozzle if water cooling is not sufficient.

As with the 2D chamber, the 3D chamber will allow the use of Raman spectroscopy, LIF, Schlieren, and shadowgraph diagnostics, but optical access will only be provided in the head end, relatively low temperature region

of the barrel section. It is thought that much of the shear layer reactions probably occurs in this region, however. Cooling of the window will be by the hydrogen film cooling layer only, so care must be taken that the window section does not extend too far into the chamber or that the chamber is not run at conditions where the film layer will breakdown quickly. Results from the 2D chamber should provide guidance in this design issue. Later versions of the 3D chamber could include a fused silica nozzle extension to study low Reynolds number flow in the nozzle and window slots in the throat region.

REFERENCES

1. Reed, B.D., "Small Hydrogen/Oxygen Rocket Flowfield Behavior From Heat Flux Measurements", AIAA Paper 93-2162, NASA TM-106233, June 1993.
2. Morren, S., et. al., "A Laboratory Model of a Hydrogen/Oxygen Engine for Combustion and Nozzle Studies", AIAA Paper 93-1825, NASA TM-106281, June 1993.
3. Schneider, S.J., "Low Thrust Chemical Rocket Technology", IAF Paper 92-0669, NASA TM-105927, August 1992.
4. DeGroot, W.A., "Gaseous Hydrogen/Oxygen Injector Performance Characterization", AIAA Paper 94-0220, to be presented at 1994 AIAA Aerospace Sciences Meeting.

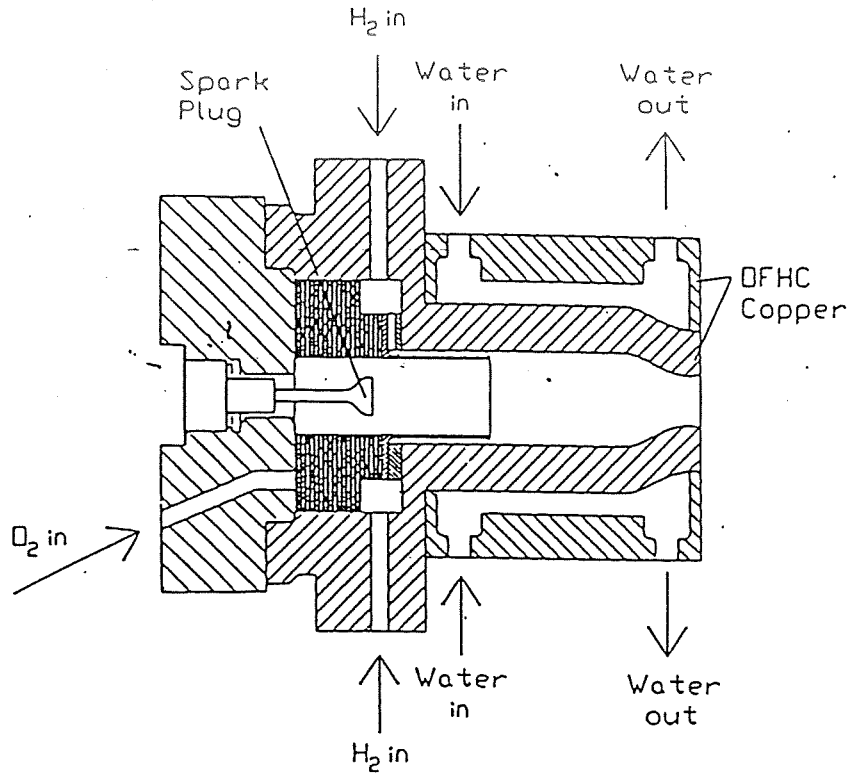


Figure 1: Schematic of Heat Flux Chamber

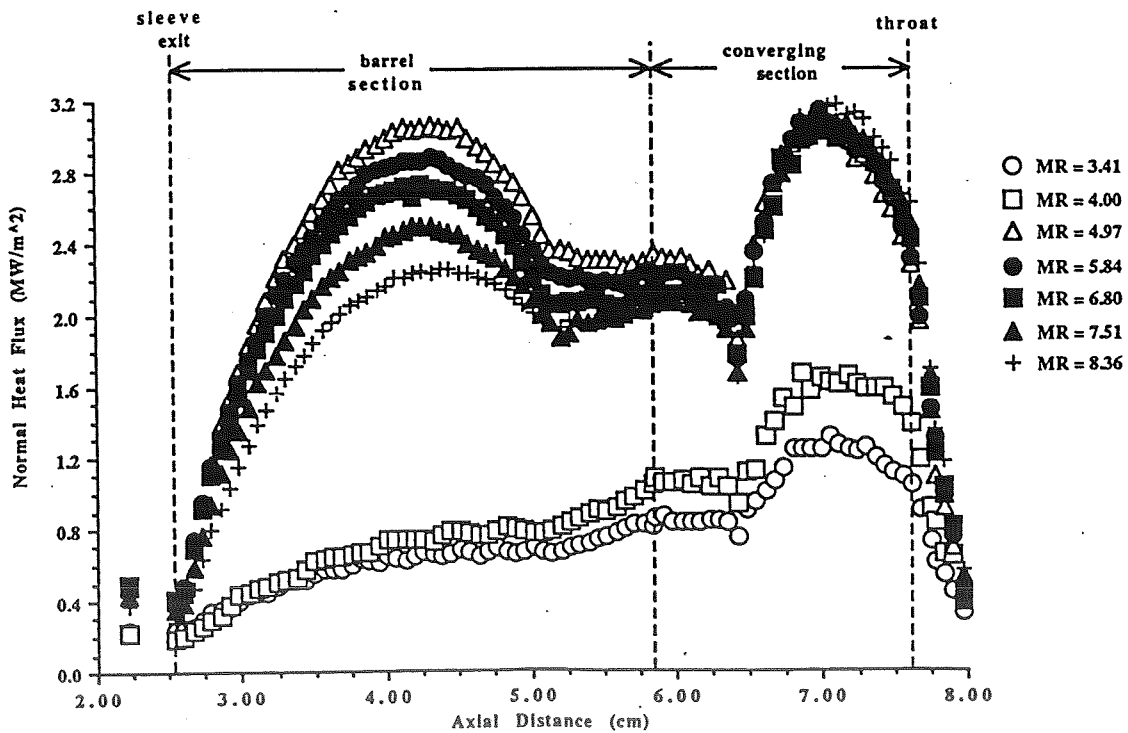


Figure 2: Inner Wall, Normal Heat Flux vs. Axial Distance

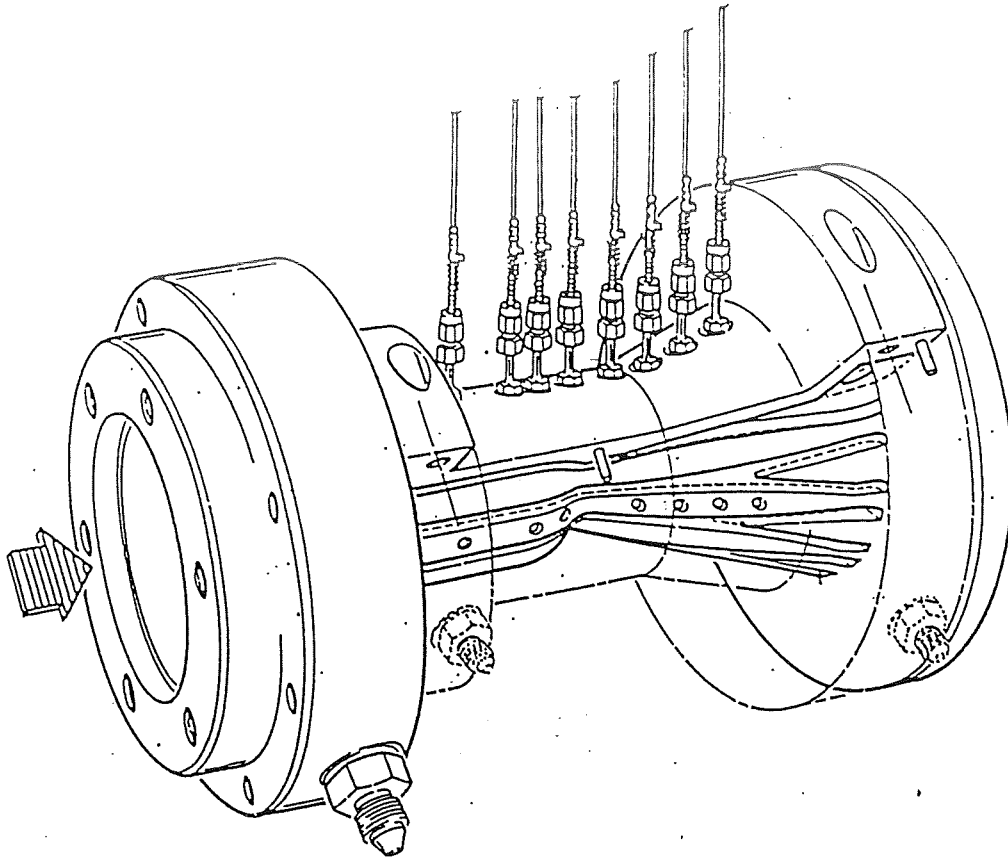


Figure 3: Temperature/Pressure Diagnostic Chamber

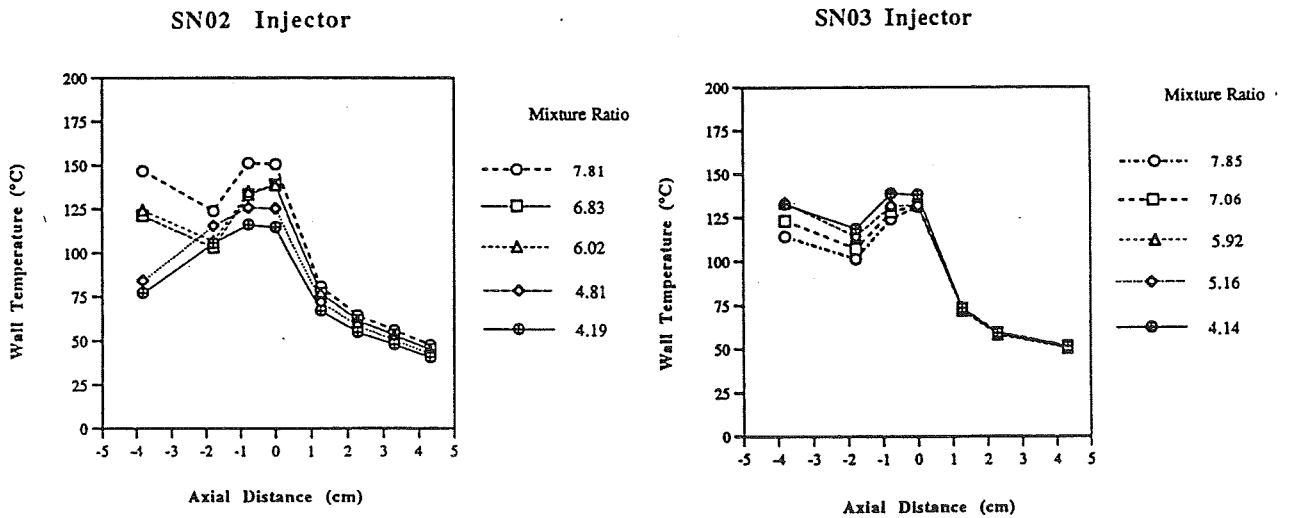


Figure 4: Axial Inner Wall Temperature Profiles
60% FFC, Chamber Pressure = 490 to 516 kPa

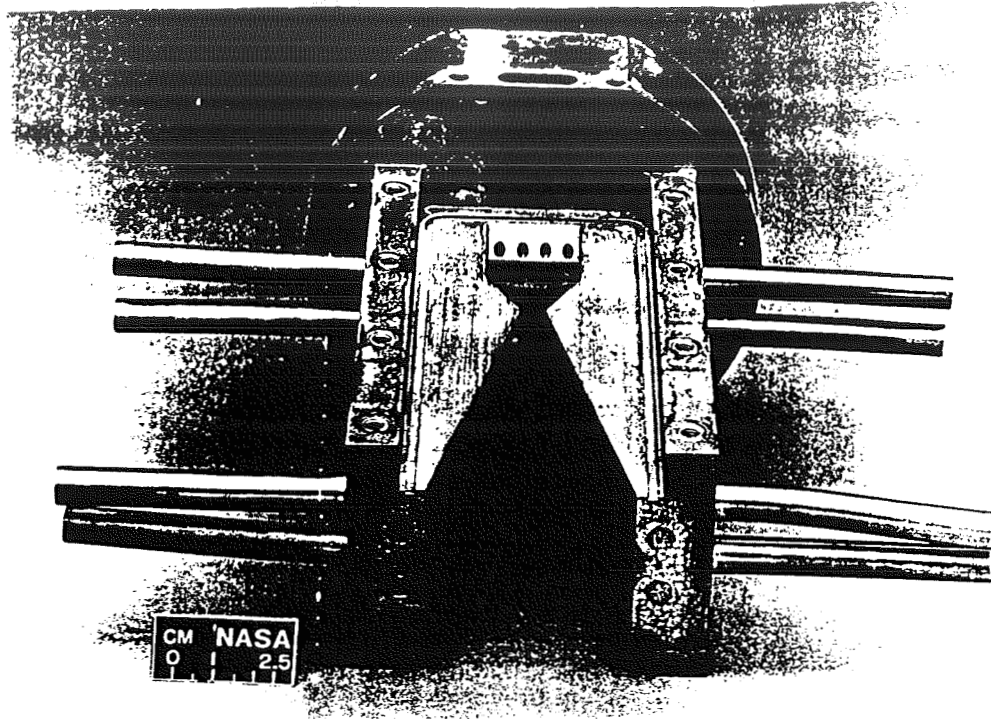


Figure 5: 2D, Optically-Accessible Chamber

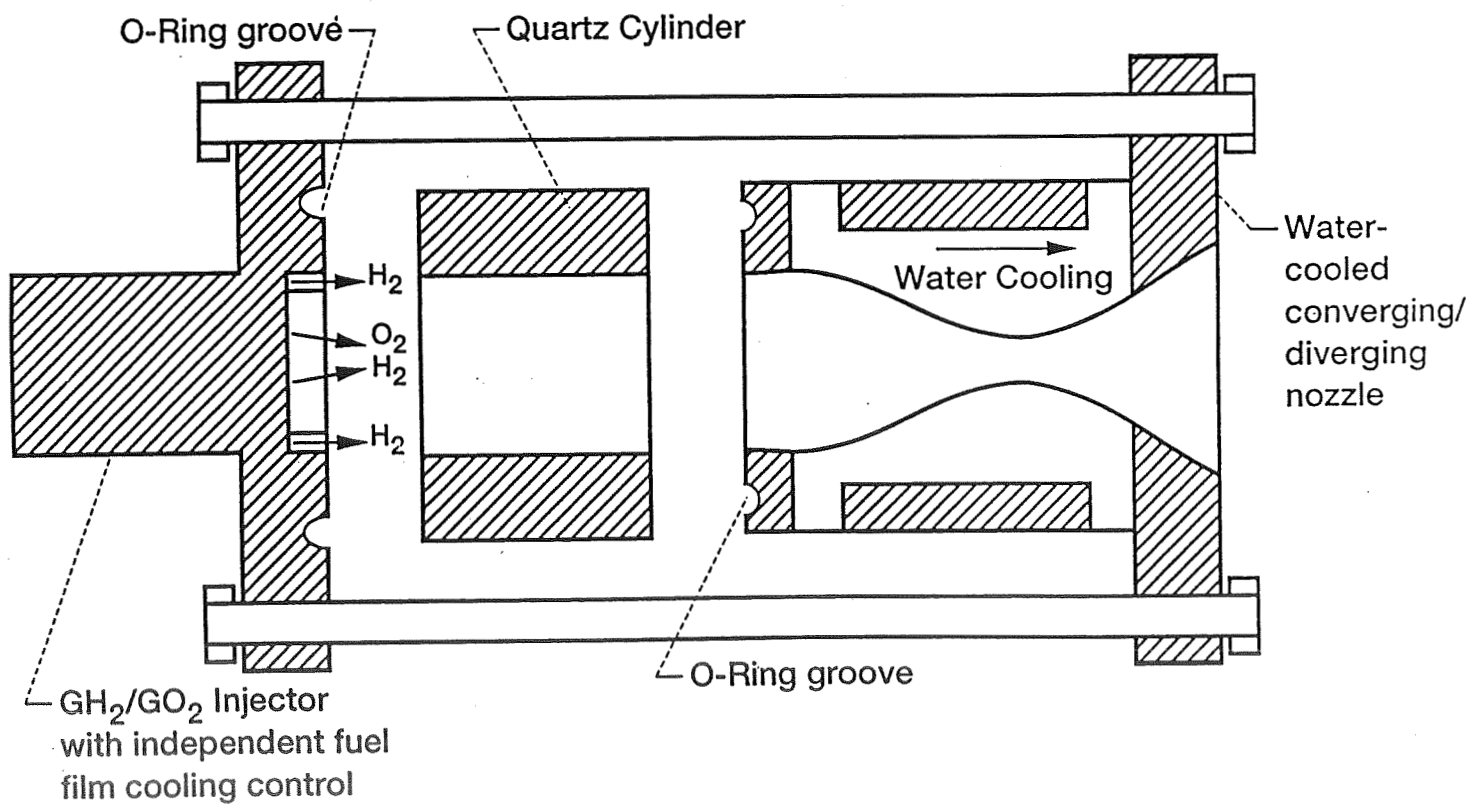


Figure 6: Schematic of 3D, Optically-Accessible Chamber

A THEORETICAL EVALUATION OF ALUMINUM GEL PROPELLANT TWO-PHASE
FLOW LOSSES ON VEHICLE PERFORMANCE

Donn C. Mueller and Stephen R. Turns
Propulsion Engineering Research Center
and
Department of Mechanical Engineering
The Pennsylvania State University
University Park, PA 16802

SUMMARY:

A one-dimensional model of a hydrocarbon/ Al/O_2 (gaseous) fueled rocket combustion chamber has been developed to study secondary atomization effects on propellant combustion. This chamber model has been coupled with a two-dimensional, two-phase flow nozzle code to estimate the two-phase flow losses associated with solid combustion products. Results indicate that moderate secondary atomization significantly reduces propellant burnout distance and Al_2O_3 particle size; however, secondary atomization provides only moderate decreases in two-phase flow induced I_{sp} losses. Despite these two-phase flow losses, a simple mission study indicates that aluminum gel propellants may permit a greater maximum payload than the hydrocarbon/ O_2 bi-propellant combination for a vehicle of fixed propellant volume. Secondary atomization was also found to reduce radiation losses from the solid combustion products to the chamber walls, primarily through reductions in propellant burnout distance.

TECHNICAL DISCUSSION:

Gel propellants, in which a solid constituent, composed of very fine particles (~1-5 μm in diameter), is suspended in a gelled liquid carrier, offer potential performance and/or safety advantages over conventional liquid and solid propellants in rocket applications. Theoretical performance evaluations show that gel propellants may provide increases in specific impulse and/or propellant density over conventional liquid propellants, thereby increasing mission ΔV or payload.¹⁻⁵ It should be noted, however, that these theoretical studies on gelled propellants do not include performance losses associated with gel combustion such as increased propellant combustion times, radiation heat transfer from condensed combustion products to the chamber walls, and nozzle two-phase flow losses. Since gel-induced I_{sp} efficiency losses of 1.5-4% are sufficient to eliminate the benefits of gel propellants in a volume and mass constrained vehicle,⁴ the above losses must be determined before the performance of gel propellants can be accurately evaluated.

Since propellant combustion times and solid combustion product size, and therefore two-phase flow losses, are proportional to initial droplet size, small droplets are desirable. Although fine spray atomization of gelled propellants is difficult to achieve, research has indicated that small droplets may be produced through secondary atomization of large droplets, a process in which a droplet shatters into a number of smaller droplets due to rigid particle shell formation and internal vaporization of the liquid carrier fluid.^{6,7} Little work has been done, however, to evaluate gel performance losses and secondary atomization effects on these losses.

A one-dimensional model of a JP-10/Al/O₂(gaseous) fueled rocket combustion chamber has been developed to evaluate secondary atomization effects on propellant combustion.⁸ In brief, a radially uniform spray, consisting of four droplet size classes, enters the combustion chamber and burns in a process incorporating liquid carrier burnout, droplet secondary atomization, aluminum agglomerate heat up and combustion, two-phase particle flow, and radiation from solid combustion products to the chamber walls. A schematic of this combustion process for a single droplet, with and without secondary atomization, is presented in Fig. 1. Because the post-secondary atomization droplet size distributions are currently unknown, droplets are assumed to fragment into a given number of equal-sized droplets where the number of secondary droplets produced per initial droplet is defined as the fragmentation ratio, β , which is treated as a model parameter. This combustor code is used in conjunction with a two-dimensional two-phase nozzle performance code (SPP)⁹ to determine two-phase flow losses in the engine nozzle and propellant mass flowrate through the engine.

RESULTS:

To simulate an upper-stage booster, the one-dimensional combustor and SPP codes were exercised using the chamber diameter, pressure, flow rates, aluminum mass loading, and nozzle geometry presented in Table 1. Because of comparable total propellant aluminum mass loadings, a solid motor nozzle profile (Extended Delta)⁹ was used for the nozzle geometry. Moderate secondary atomization ($\beta=5$) was found to significantly reduce propellant burnout distance (40%) and final Al₂O₃ residual diameter (60%). Results also indicate that radiation losses to the chamber walls are a function of secondary atomization, primarily through changes in propellant burnout distance. These radiation losses range from 0.4-5% of the sensible enthalpy entering the combustion chamber and should be even less in larger engines where the flow optical thickness is greater than the case considered here.

It should be noted, however, that Al₂O₃ residual size predicted by the combustor code may not be correct for nozzle performance calculations. Since the Al₂O₃ particles are molten throughout most of the nozzle, and because small particles accelerate more quickly than large particles, particle size may increase through coagulation. Similarly, additional Al₂O₃ may be produced through the recombination of gas-phase radicals as the exhaust gases cool during expansion, resulting in the nucleation of additional particles and/or growth of previously formed particles. Particle size may also decrease due to shear breakup of droplets, particularly in the throat region of the nozzle. Because of these uncertainties in Al₂O₃ particle size, two methods of estimating particle size, which should bound the true particle size, are used in the evaluation of nozzle performance. In the first method, we use an Al₂O₃ particle size in the nozzle that is determined by the one-dimensional combustor code, making secondary atomization the primary mechanism governing particle size. In the second method, secondary atomization is assumed to have no effect on mean particle size; rather, coagulation, particle surface growth, and shear induced droplet breakup are assumed to be the dominant mechanisms affecting particle size. Based on predictions of Al₂O₃ particle size in solid rockets,^{9,10} a particle mass mean diameter, D_{43} , of 5.6 μm was determined for this second case.

A comparison of two-phase flow losses for the above methods of determining Al_2O_3 particle size are presented in Fig. 2 for a 60 wt% aluminum gel. As can be seen, secondary atomization may reduce two-phase flow losses but does not affect two-phase flow losses as significantly as propellant burnout distance. Using the second, more conservative, method of estimating Al_2O_3 particle size, engine I_{sp} was calculated for a range of aluminum mass loadings and propellant mixture ratios and compared with I_{sp} calculations for a JP-10/ O_2 bi-propellant. Figure 3 show that I_{sp} decreases with increasing aluminum loading and that the maximum I_{sp} mixture ratio becomes richer, as has been predicted by other studies.⁵

Because I_{sp} alone does not indicate mission performance, a simple mission study of a vehicle of fixed propellant volume and dry mass was conducted, incorporating two-phase flow losses. Maximum payload was calculated for different propellant mixture ratios and aluminum mass loadings using the mission/vehicle parameters, which approximate an upper-stage LEO-GEO orbital transfer, and payload mass equation presented in Table 2.⁵ From this analysis, shown in Fig. 4, it was found that maximum payload increases with aluminum mass loading up to an aluminum mass loading of 60% and then decreases as additional aluminum is added. The maximum payload for the aluminum gels was found to be 7% greater than that of the JP-10/ O_2 bi-propellant combination.

CONCLUSIONS:

The above results indicate that only moderate secondary atomization is required to effectively reduce overall propellant burnout distance and final Al_2O_3 residual size. Preliminary results indicate that secondary atomization provides only moderate decreases in two-phase flow induced I_{sp} losses. A simple mission study indicates that hydrocarbon/Al gels may offer payload increases over a hydrocarbon/ O_2 bi-propellant for a vehicle of fixed propellant volume and dry mass. It should be noted that vehicle mass limitations and propellant density effects on propellant tank size, and therefore vehicle dry mass, could alter the above performance results.⁴

REFERENCES:

1. Palaszewski, B., "Metallized Propellants for the Human Exploration of Mars," NASA Technical Paper 3062, Nov. 1990.
2. Palaszewski, B., "Advanced Launch Vehicle Upper Stages Using Liquid Propulsion and Metallized Propellants," NASA Technical Memorandum 103622, Oct. 1990.
3. Palaszewski, B., and Powell, R., "Launch Vehicle Performance Using Metallized Propellants," AIAA Paper 91-2050, presented at 27th AIAA/ASME/SAE/ASEE Joint Propulsion Conference, Sacramento CA, June 1990.
4. Palaszewski, B, and Rapp, D., "Design Issues for Propulsion Systems Using Metallized Propellants", AIAA Paper 91-3424, presented at AIAA/NASA/OAI Conference on Advanced SEI Technologies, Cleveland, OH, Sept 4-6, 1991.
5. Zurawski, R. L., and Green, J. M., "An Evaluation of Metallized Propellants Based on Vehicle Performance," AIAA Paper 87-1773, June-July 1987.
6. Cho, S. Y., Takahashi, F., and Dryer, F. L., "Some Theoretical Considerations on the Combustion and Disruption of Free Slurry Droplets," *Combustion Science and Technology*, Vol. 67, 1989, pp. 37-57.
7. Mueller, D. C., and Turns, S. R., "Some Aspects of Secondary Atomization of Aluminum/Hydrocarbon Slurry Propellants," *Journal of Propulsion and Power*, Vol. 9, May-June 1993, pp. 345-352.
8. Turns, S. R., and Mueller, D. C., "Ignition and Combustion Characteristics of Metallized Propellants." NAG 3-1044, Final Report to NASA Lewis Research Center, Jan 1993.

9. Nickerson, G.R., et. al., "The Solid Propellant Rocket Motor Performance Prediction Computer Program (SPP), Version 6.0," AFAL/TSTR, Edwards AFB, CA, Dec 1987.
10. Bartlett, R. W., and Delaney, L. J., "Effect of Liquid Surface Tension on Maximum Particle Size in Two-Phase Nozzle Flow," *Pyrodynamics*, Vol. 4, 1964, pp. 337-341.
11. Miller, W., Solid Rocket Motor Performance and Analysis, NASA SP-8039, National Technical Information Service, May, 1971.

Table 1. Engine Geometry and Operating Conditions

Chamber Diameter	0.19 m
Chamber Pressure	3867 kPa
Throat Diameter	0.109 m
Expansion Ratio	30.8
Gel Flow Rate	10.78 kg/s
Al Mass Loading	60%
Oxidizer Flow Rate	11.75 kg/s

Table 2. Mission/Vehicle Parameters and Payload Mass Equation

Mission ΔV	4267.2 m/s
Vehicle Propellant Volume	56.63 m ³
Vehicle Dry Mass	2761.6 kg

$$M_{PL} = \frac{\rho_{prop} \cdot Vol_{prop} - M_{dry} [\exp(\Delta V/l_{sp}g) - 1]}{[\exp(\Delta V/l_{sp}g) - 1]}$$

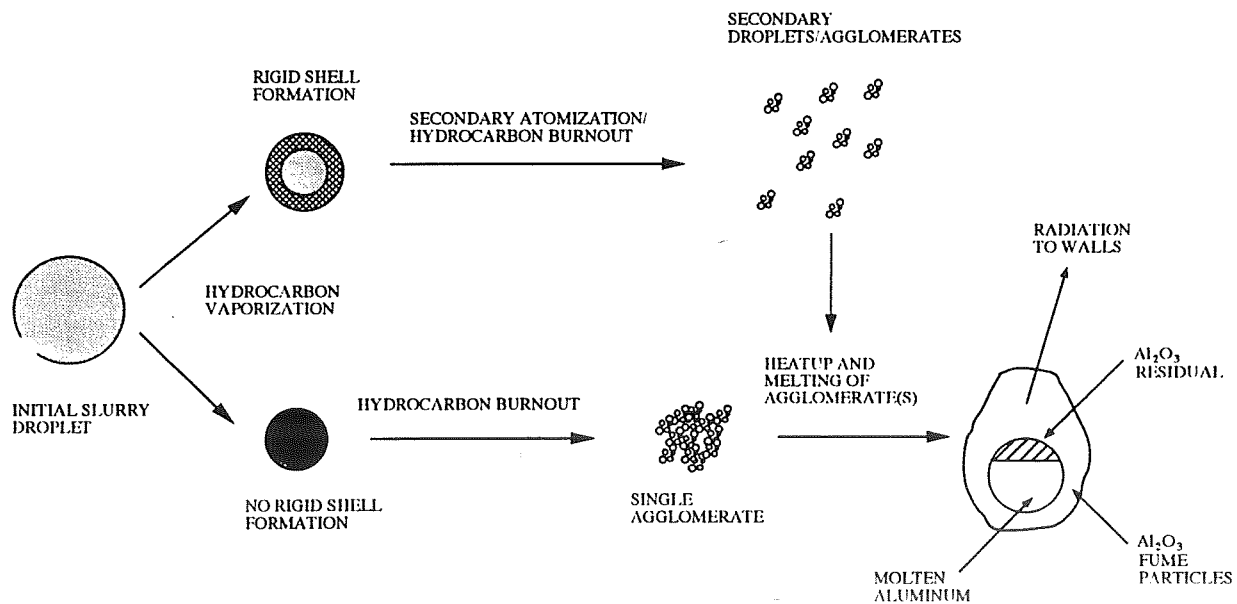


Figure 1. Schematic of the gel combustion process in a rocket combustion chamber, with and without secondary atomization.

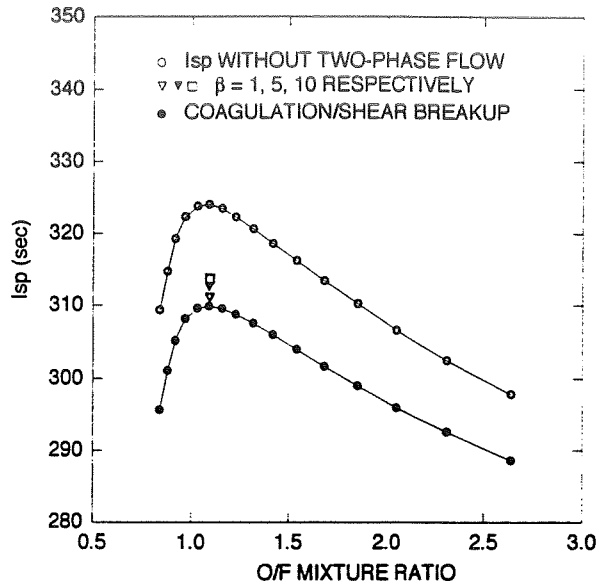


Figure 2. Effects of two-phase flow on engine I_{sp} for a 60 wt% Al gel. Data are for two methods of determining Al_2O_3 particle size; size predicted by one-dimensional model and size based on Al_2O_3 particle coagulation and shear-induced particle breakup.

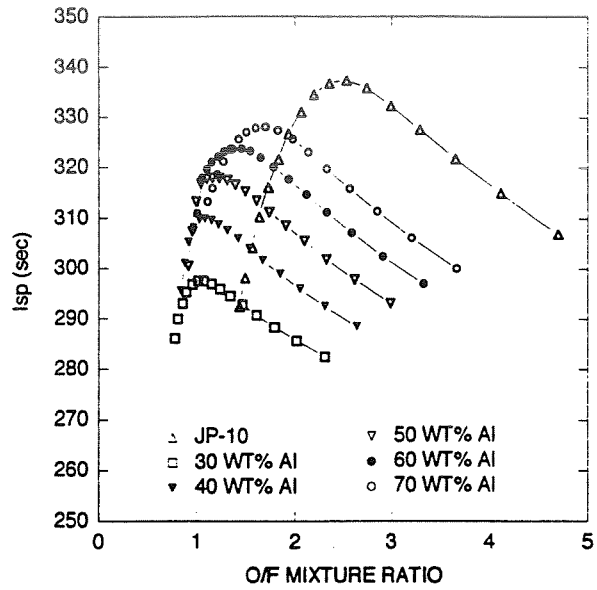


Figure 3. Engine I_{sp} as a function of propellant mixture ratio and gel aluminum weight percentage.

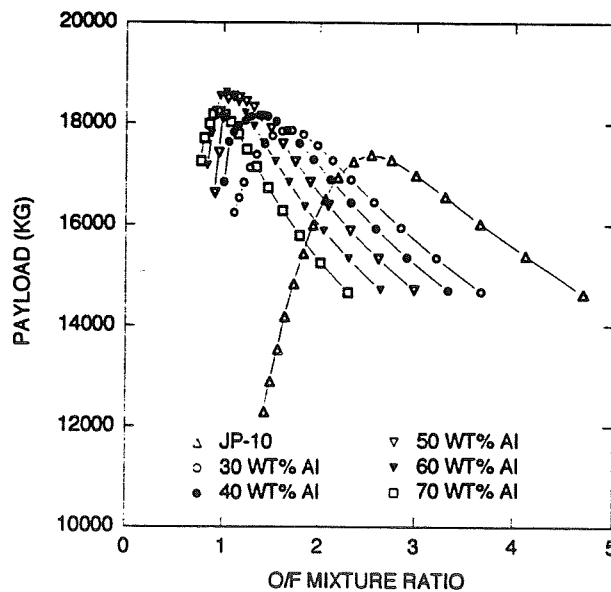


Figure 4. Maximum payload for a vehicle of fixed propellant volume and dry mass as a function of mixture ratio and gel aluminum weight percentage.

LASER DIAGNOSTICS FOR SMALL ROCKETS

Frank J. Zupanc
National Aeronautics and Space Administration
Lewis Research Center
Cleveland, OH

Wilhelmus A. de Groot
Sverdrup Technology, Inc.
Lewis Research Center Group
Brook Park, OH

SUMMARY

Two nonintrusive flowfield diagnostics based on spectrally-resolved elastic (Rayleigh) and inelastic (Raman) laser light scattering have been developed for obtaining local flowfield measurements in low-thrust gaseous H_2/O_2 rocket engines. The objective is to provide an improved understanding of phenomena occurring in small chemical rockets in order to facilitate the development and validation of advanced computational fluid dynamics (CFD) models for analyzing engine performance. The laser Raman scattering diagnostic has been developed to measure major polyatomic species number densities and rotational temperatures in the high-density flowfield region extending from the injector through the chamber throat. Initial application of the Raman scattering diagnostic has provided O_2 number density and rotational temperature measurements in the exit plane of a low area-ratio nozzle and in the combustion chamber of a two-dimensional, optically-accessible rocket engine. In the low-density nozzle exit plane region where the Raman signal is too weak, a Doppler-resolved laser Rayleigh scattering diagnostic has been developed to obtain axial and radial mean gas velocities, and in certain cases, H_2O translational temperature and number density. The results from these measurements have been compared with theoretical predictions from the RPLUS CFD code for analyzing rocket engine performance. Initial conclusions indicate that a detailed and rigorous modeling of the injector is required in order to make direct comparisons between laser diagnostic measurements and CFD predictions at the local level.

TECHNICAL DISCUSSION

Small, low thrust chemical rockets are currently used in almost all spacecraft auxiliary propulsion systems (APS). Since spacecraft payload and operating lifetime are limited by the amount of propellant carried on-board, optimizing the performance of the APS thrusters is of critical importance. Standardized performance analysis methodologies, while effective for large thrust classes, are generally inadequate for modeling the thick reacting shear and boundary layers present in small, fuel-film cooled rockets. Advanced computational fluid dynamic (CFD) models, such as the RPLUS code¹⁻³, provide the potential for enhanced rocket engine performance analysis through a more rigorous modeling of the combustor and nozzle flowfields. Localized flowfield data are necessary, however, for both assessing the accuracy of the model, as well as providing an improved phenomenological understanding of the processes occurring inside low thrust chemical rockets. To meet this objective, two

diagnostics have been developed based on spectrally-resolved laser Rayleigh and Raman scattering. The Raman scattering diagnostic has been directed toward the measurement of major polyatomic species number densities and rotational temperatures in the higher density regions of the thrust chamber, specifically from the injector and combustor regions through the throat. Due to the relatively weak Raman scattering cross-sections, however, the signal strength in the low density nozzle exit and plume region is generally too low to obtain a sufficient signal-to-noise ratio (SNR). In this region, Doppler-resolved laser Rayleigh scattering has been developed to obtain measurements of axial and radial mean gas velocity and, in certain situations, H₂O translational temperature and number density. Each technique is discussed in more detail in the following sections along with initial results and a comparison with CFD predictions from the RPLUS model.

The Rayleigh and Raman scattering diagnostics were implemented in a low thrust rocket test facility at the NASA Lewis Research Center. The facility was developed to support performance and life testing of gaseous hydrogen/oxygen rocket engines with thrust levels of 22-220 N. Testing was conducted in a low pressure test chamber capable of simulating an altitude of 35 km. The altitude chamber measured 1.82 m in length by 0.91 m in diameter. Three optical access ports were located at 90° relative to the thruster axis with a fourth additional port canted at 60°. A supersonic diffuser with an inlet diameter of 102 mm was used to capture the rocket exhaust and transport it outside of the altitude chamber. A complete description of the test facility is given in Reference 4.

Laser Rayleigh Scattering

The laser Rayleigh scattering diagnostic is described in detail in References 5-8. In rarefied gases, such as those found in the rocket exhausts used in these tests, the Rayleigh scattered spectrum is simply the sum contribution of the scattering from all molecules in the probe volume. Under sufficiently high spectral resolution, the mean gas velocity can be obtained from the net Doppler shift in the profile, the translational temperature from the Doppler width, and the number density from the total scattered power. The measurement of the temperature and number density using Rayleigh scattering is subject to the requirement that the species composition be known, which is generally not the case. For fuel-rich mixtures, however, the scattering is largely dominated by water molecules, thus temperature and density measurements can be obtained with minimal error due to uncertainty in the actual composition. For flowfields with oxidizer-rich regions, temperature and density measurements are subject to greater uncertainty. In these situations, the Rayleigh technique is used primarily as a flowfield velocimeter. The requirement of a known composition does not affect the measurement of the mean gas velocity and thus this represents the most robust aspect of the technique.

Initially, the Rayleigh diagnostic utilized a continuous wave argon ion laser and photon counting signal detection electronics. Due to the weak signal from the low density plumes, the Rayleigh spectrum was readily swamped by combustion generated luminosity emanating from the combustion chamber. This prevented measurements from being obtained at the nozzle exit. In order to reduce the sensitivity of the technique to luminous interferences, the cw argon ion laser and photon counter were replaced with a pulsed, injection-seeded Nd:YAG laser (150 MHz spectral bandwidth) and time-gated signal detection electronics. This allowed

measurements to be obtained at the nozzle exit plane, thereby providing a more direct comparison with exit plane predictions from rocket performance models. As the Rayleigh scattered signal was at essentially the same wavelength as the laser, extensive use of apertures, baffles, and light traps was required in order to eliminate interferences from stray scattered laser light within the chamber. A schematic of the pulsed Rayleigh scattering diagnostic is shown in Figure 1.

For each test run, the Fabry-Perot interferometer was used to obtain a reference scan of the unshifted laser line and a scan of the Rayleigh scattered light from the rocket exhaust. A maximum likelihood curve fit procedure was then applied to the reference scan in order to obtain the instrument response function. The same curve fitting procedure was then applied to the hot fire data by convolving the Rayleigh scattering model function with the instrument response function to estimate the net Doppler shift, Doppler width, and total scattered power. Representative examples of the reference and Rayleigh scans, along with their associated curve fits, are shown in Figure 2. By traversing the collection probe along the beam path across the exit plane, a radial profile was obtained. Axial and radial velocity profiles obtained on a Space Station prototype thruster with a 30:1 nozzle exit area ratio are shown in Figure 3, along with the predictions from the RPLUS model. Discrepancies between the measured and predicted profiles are attributed to flow stratification between the hydrogen and oxygen in the core region of the thruster which was not addressed in the model.

Laser Raman Scattering

A complete description of the Raman diagnostics facility is given in References 8-10. The layout of the facility is shown in Figure 4. A flashlamp pumped dye laser, lasing at a nominal wavelength of 595 nm, was delivered via a fiberoptic cable into the altitude chamber and then focused into the plume of a low area ratio rocket nozzle. The Raman scattered signal was then coupled into a second fiberoptic cable and transported out of the altitude chamber for spectral processing. The collected light was focused into a spectrometer containing either a 300 or 1200 groove grating, dependent on the application. For simultaneous multispecies detection, the 300 groove grating provided a spectral resolution which allowed simultaneous detection of oxygen, nitrogen, and water with a single linear array detector. For temperature measurements where high resolution of the line shapes was required, a 1200 groove grating was used instead. A Raman notch filter with 10^6 rejection at the laser wavelength was used to eliminate interferences from spuriously scattered laser light.

An gated-intensified linear diode array was used to measure the Raman scattered signal. With the use of background subtraction, this pulsed system could extract very weak signals from the noise. The measured temperature could be extracted from the measured line shapes using a model function based on Raman theory and the instrument function of the detection equipment. Calibration factors were obtained from a reference gas at known temperature and number density. A maximum likelihood parameter estimation procedure completed the data reduction. The instrument function was measured using a helium neon laser line and a mercury lamp. Oxygen and nitrogen spectra obtained in atmospheric air were used as calibration spectra. Typical nitrogen spectra, both measured and calculated, for two different temperatures are shown in Figure 5. The Raman diagnostic was then

applied near the exit of a low area ratio (1.4:1) nozzle where the density was still high enough to generate a measurable signal. The injector and chamber geometry were the same as in the Rayleigh scattering measurements shown in Figure 3, except for the cutoff nozzle. The oxygen number density and rotational temperature profiles from these measurements are shown in Figure 6. As with the Rayleigh results, it is believed that the discrepancies between the measurements and predictions are the result of incomplete mixing and flow stratification in the core flow region between the hydrogen and oxygen. Current efforts are directed toward obtaining Raman measurements inside the combustion chamber through the use of a two-dimensional, optically-accessible rocket engine. Results from these efforts will be presented in Reference 11.

REFERENCES

1. Weiss, J.M. and Merkle, C.L., "Numerical Investigation of Reacting Flowfields in Low-Thrust Rocket Engine Combustors," AIAA-91-2080, 1991.
2. Weiss, J.M., Daines, R.L., and Merkle, C.L., "Computation of Reacting Flowfields in Low-Thrust Rocket Engines," AIAA-91-3557, 1991.
3. Weiss, J.M. and Merkle, C.L., "Prediction of Engine and Near-Field Plume Reacting Flowfields in Low-Thrust Rocket Engines," AIAA-93-0237, 1993.
4. Arrington, L.A. and Schneider, S.J., "Low Thrust Rocket Test Facility," AIAA-90-2503, 1990.
5. Seasholtz, R.G., Zupanc, F.J., and Schneider, S.J., "Spectrally Resolved Rayleigh Scattering Diagnostic for Hydrogen-Oxygen Rocket Plume Studies," *Journal of Propulsion and Power*, **8**, 935-942, 1992.
6. Zupanc, F.J. and Weiss, J.M., "Rocket Plume Flowfield Characterization Using Laser Rayleigh Scattering," AIAA-92-3351, 1992.
7. Zupanc, F.J., "Pulsed Laser Rayleigh Scattering Diagnostic for Hydrogen/Oxygen Rocket Exit Plane Flowfield Velocimetry," AIAA-93-0805, 1993.
8. de Groot, W.A. and Zupanc, F.J., "Laser Rayleigh and Raman Diagnostics for Small Hydrogen/Oxygen Rockets," NASA TM-105999, Prepared for the SPIE International Symposium on Lasers, Sensors, and Applications, Los Angeles, CA, January 16-23, 1993.
9. de Groot, W.A., "The Development of a Fiber Optic Raman Temperature Measurement System for Rocket Flows," AIAA-91-2316, 1991.
10. de Groot, W.A. and Weiss, J.M., "Species and Temperature Measurement in H₂/O₂ Rocket Flow Fields by Means of Raman Scattering Diagnostics," AIAA-92-3353, 1992.
11. de Groot, W.A., "Gaseous Hydrogen/Oxygen Injector Performance Characterization," AIAA-94-0220, *to be presented at the 32nd Aerospace Sciences Meeting, Reno, NV, 1994.*

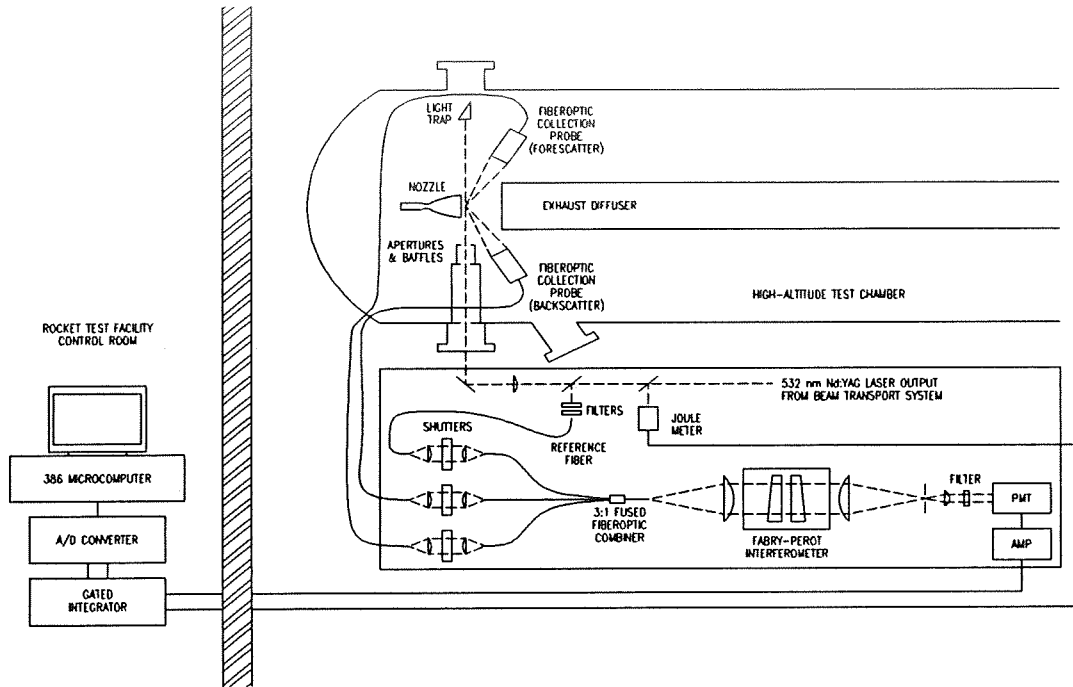


Figure 1. Schematic diagram of overall optical arrangement of pulsed laser Rayleigh scattering diagnostic.

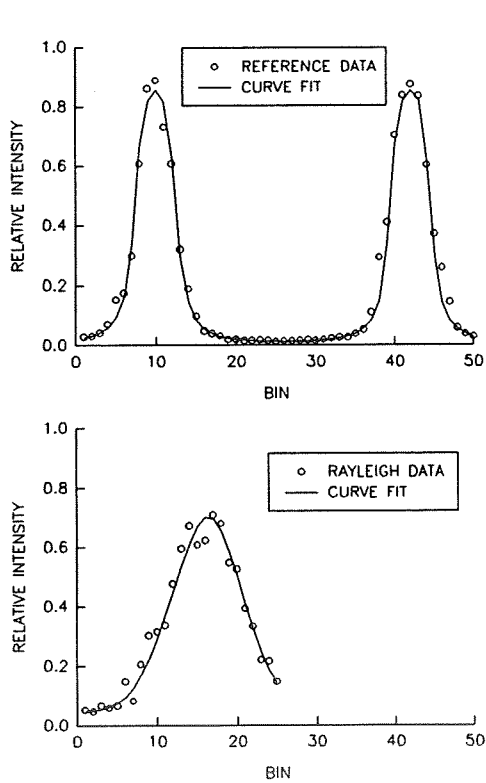


Figure 2. Fabry-Perot scan measurements of unshifted reference laser line (top) and Rayleigh scattering profile in rocket exhaust (bottom).

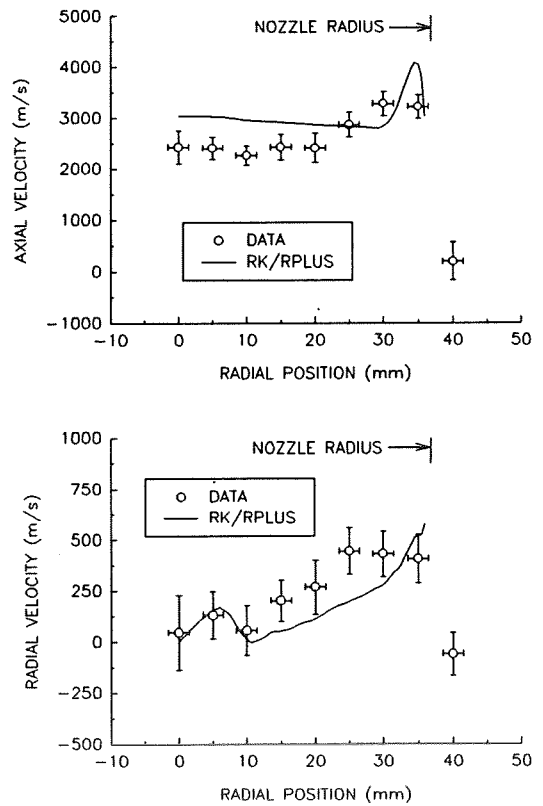


Figure 3. Comparison of measured axial (top) and radial (bottom) velocity profiles with RPLUS predictions.

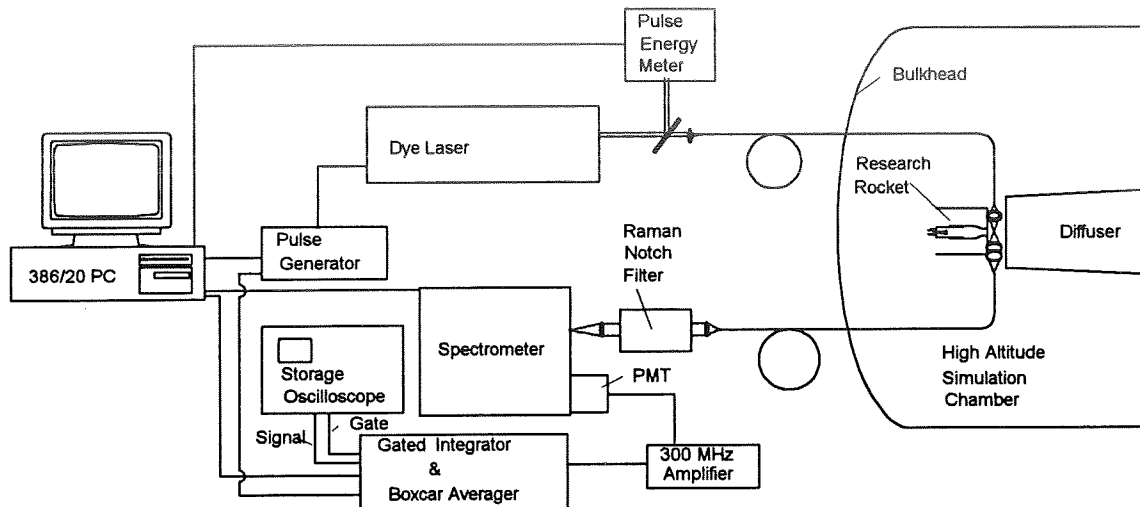


Figure 4. Schematic of Raman scattering diagnostics data acquisition system.

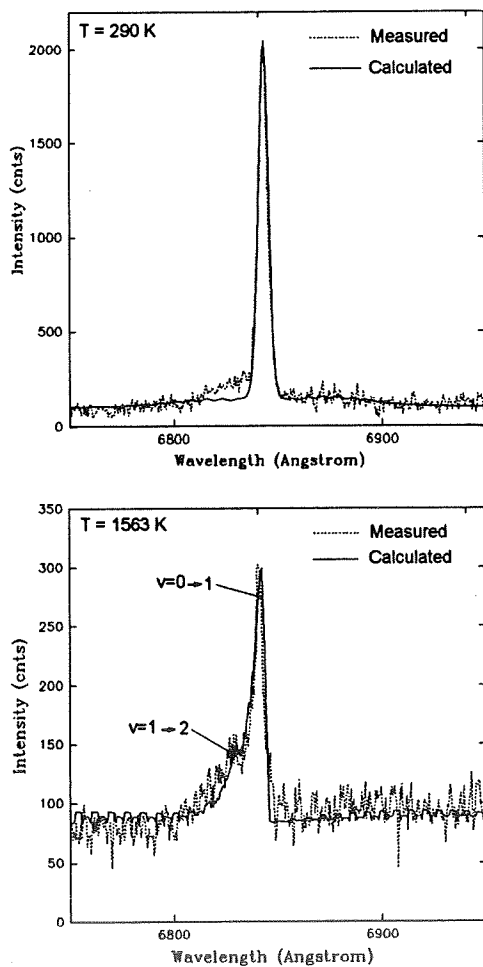


Figure 5. Measured and calculated Raman Q-branch spectra of nitrogen at T=290 K (top) and T=1563 K (bottom).

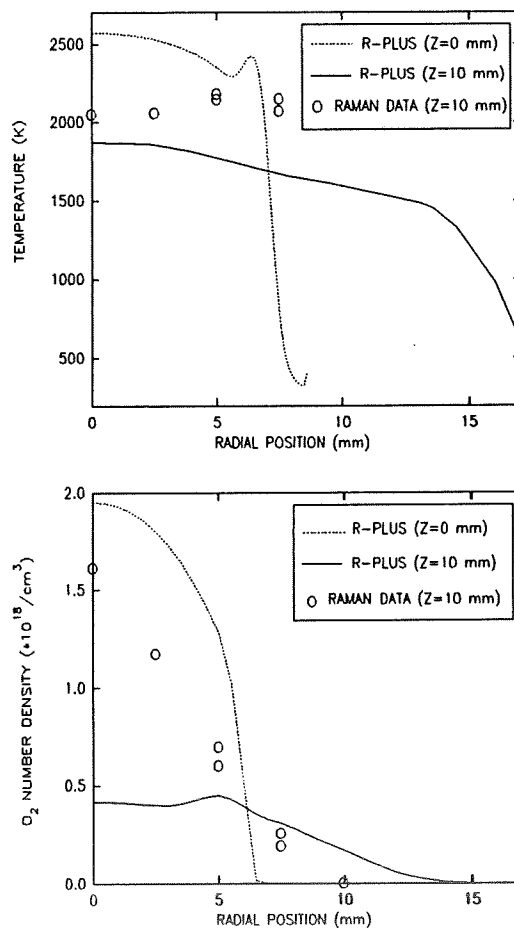


Figure 6. Raman temperature (top) and O_2 number density (bottom) measurements in the exit plane of a low area ratio nozzle.

CFD ANALYSES OF COMBUSTOR AND NOZZLE FLOWFIELDS

Hsin-Hua Tsuei[†] and Charles L. Merkle[§]
 Propulsion Engineering Research Center
 and
 Department of Mechanical Engineering
 The Pennsylvania State University
 University Park, PA 16802

SUMMARY:

The objectives of the present research are to improve design capabilities for low thrust rocket engines through understanding of the detailed mixing and combustion processes. A Computational Fluid Dynamic (CFD) technique is employed to model the flowfields within the combustor, nozzle and near plume field. The computational modeling of the rocket engine flowfields requires the application of the complete Navier-Stokes equations, coupled with species diffusion equations. Of particular interest is a small gaseous hydrogen-oxygen thruster which is considered as a coordinated part of a on-going experimental program at NASA LeRC. The numerical procedure is performed on both time-marching and time-accurate algorithms, using an LU approximate factorization in time, flux split upwinding differencing in space. The integrity of fuel film cooling along the wall, its effectiveness in the mixing with the core flow including unsteady large scale effects, the resultant impact on performance and the assessment of the near plume flow expansion to finite pressure altitude chamber is addressed.

TECHNICAL DISCUSSION:

Propulsion related flowfields are characterized by a wide variety of physical phenomena. In the rocket engine combustion chamber, mixing and combustion processes between the fuel and oxidizer result in regions of strong heat release and species generation. The present paper addresses a small gaseous H_2/O_2 engine in which about 60% of the fuel is used for film cooling. The velocity and molecular weight differences in these two streams suggest the likelihood that large scale vortices are present in the resulting shear layer. Downstream of the combustor, the flow accelerates from low subsonic to supersonic speed through a convergent-divergent nozzle. The Mach number increases rapidly because of the increasing flow speed, while the chemical reaction processes slow down and the heat release is small. In the supersonic portion of the nozzle, the flow is essentially frozen. A computational model that is capable of calculating reacting flows at both subsonic and supersonic speed is of immediate interest.

Although the application of reactive Navier-Stokes equations to rocket engines is appropriate for all engine sizes, the primary near-term usage is for low thrust, auxiliary propulsion engines [1-7]. Accurate numerical predictions of global performance and local flowfields in these small motors require detailed consideration of the mixing, viscous diffusion, species generation and heat release associated with the combustion processes. Small engines are characterized by low Reynolds numbers and therefore the wall boundary layer occupies a significant portion of the combustor. The specific engine we consider in the current research is a gaseous hydrogen-oxygen engine designed for NASA LeRC to provide auxiliary propulsion and attitude control for the Space Station freedom [1]. This small engine provides about 110 N (25 lbf) of thrust.

[†] Graduate Research Assistant

[§] Distinguished Alumni Professor

Previous research has been done both experimentally [2-4] and numerically [5-7] for these types of engines. Comparisons have shown qualitative agreement [5-7] but some important physics must be included in the computational model in order to provide more accurate engine performance prediction and local flowfield characteristics. Engine global performance parameters such as thrust and specific impulse have been consistently underpredicted [5,6] by 4 %, despite the fact that ideal combustion was assumed in the numerical modeling of the core flow. Further, comparisons with detailed local flowfield point data measurement in the near plume region have been made by postulating that the plume is expanded into a vacuum, ignoring the fact that the altitude chamber always runs at finite back pressure [7].

The primary objective of this paper is to apply both steady state and transient numerical modeling to the chemically reacting flowfield to address the issue to improve engine performance prediction. Current analyses focus on the effects of unsteady, large-scale mixing in the reacting shear layer along the chamber wall in order to understand the physics of underpredictions for thrust and specific impulse. Simultaneous emphasis on the impact of finite altitude chamber pressure on the near plume flowfield is also discussed.

The numerical algorithm is based on extending earlier supersonic reacting flow calculations [8-10] to subsonic combustion problems [11,12]. The analysis uses a three-dimensional, finite volume Navier Stokes procedure that includes chemical non-equilibrium effects. The equations can be written in a generalized coordinate system as :

$$\frac{\partial(VQ)}{\partial t} + \frac{\partial(E - E_v)}{\partial \xi} + \frac{\partial(F - F_v)}{\partial \eta} + \frac{\partial(G - G_v)}{\partial \zeta} = VH \quad (1)$$

where $Q = (\rho, \rho u, \rho v, \rho w, e, \rho Y_i)^T$ is the vector of primary dependent variables, and $E, F,$ and G are the inviscid flux vectors, and $E_v, F_v,$ and G_v the viscous flux vectors in the ξ, η and ζ directions, respectively. The vector H represents the source terms associated with chemical reactions and V is the cell volume.

Numerical computation for steady flow is achieved by an implicit time-marching algorithm using an LU approximate factorization in time and flux split upwinding differencing in space. The time-accurate calculation for unsteady flow is conducted by a dual time stepping procedure [13]. The finite rate chemical reaction model used in the present work for gaseous hydrogen-oxygen combustion [9], involves nine chemical species and eighteen elementary reactions. Both two-dimensional and three-dimensional formulations are available.

RESULTS:

Detailed flowfield analyses of the combustion chamber, nozzle and near plume region for Aerojet auxiliary thruster [1-4] are presented. For the purpose of experimental measurements, the thruster has both a full nozzle (expansion ratio about 30 to 1) and a shortened nozzle (expansion ratio about 1.5 to 1). The engine throat diameter is 1.27 cm (0.5 in). Hydrogen fuel is used for both regenerative and wall film cooling (specified as percent fuel-film cooling, or % FFC). The fuel which is not used for wall cooling mixes with the oxidizer and is then ignited by a spark plug. The present computational domain starts downstream of the spark plug insert, assuming complete combustion for the core flow. The designed baseline operating conditions for the Aerojet auxiliary thruster are given by an overall oxidizer to fuel ratio of 7.71, 60.9 FFC while hydrogen film is injected at about 670 K into the combustion chamber. The total propellant mass flow rate of the baseline operating condition is 0.03435 kg/s, with oxidizer and fuel mass flow rates 0.0304 kg/s and 0.00395 kg/s, respectively. The measured chamber pressure is 524 KPa.

Mach number contours for the Aerojet cutoff nozzle are given in Figure 1. This nozzle is cutoff at an area ratio of about 1.5 to 1 to provide a sufficient number density of the major chemical species for the measurement by means of a Raman scattering technique. The upper portion of the figure demonstrates the plume profile for the altitude chamber at 1 KPa pressure while the lower portion shows plume expansion into a vacuum to compare with previous research [7]. During the experiment, a build-up finite test chamber pressure ranging from 1 to 5 KPa is detected. finite altitude chamber pressure pushes the shear layer inwards, but the computational results in the supersonic core region for expansion to vacuum and finite back pressure calculations are identical. The experimental traverse line for data taking does however extend across the plume boundary for the finite back pressure, so including back pressure effect is necessary. The cutoff nozzle plume under 1 KPa back pressure is still underexpanded.

Results of the combustor-nozzle-plume calculation of the Aerojet full nozzle thruster are given in Figure 2. The upper part shows the predicted Mach number contours while lower part shows the pressure contours, both plots are for expansion to 1 KPa altitude chamber pressure. Each Mach number contour line represents a 0.5 increment. Pressure contours are plotted on a logarithmic scale, with the pressure on each contour line being essentially 10 % lower than the previous one. Inside the combustor the pressure is nearly constant, but decreases rapidly as the flow accelerates through the nozzle. An oblique shock wave can be observed from both pressure and Mach number contours, which is a result of the flow experiencing continuous compression through the bell-shaped nozzle. The exhausted plume is nearly perfectly expanded and a shear layer is formed at the plume boundary under 1 KPa test chamber pressure.

Representative solutions of the unsteady, reactive mixing shear layer inside the combustor are given in Figure 3 and Figure 4. Figure 3 shows the spatial variation of OH radical concentration and temperature contours in the combustor. Time-accurate, unsteady calculations indicate that unsteady flow exists in the mixing layer between the heavier hot core gas and lighter hydrogen cooling film. Because of the presence of the injector base region which divides the core gas and hydrogen cooling film, large-scale vortices are shed from the base region and causes unsteady mixing in the reacting shear layer. Vortex roll-up is, however, minimized by the proximity of the combustor wall. The core flow enters the combustor at 2950 K while the hydrogen film flows along the wall at 670 K. The core gas temperature remains almost constant in the combustor. A large temperature gradient is also observed in the reacting shear layer. The temperature first increases to a peak of 3450 K because of the presence of a diffusion flame between the core gas and the cooling layer, then decreases to the coolant film temperature. The OH radical concentration is here used as an indicator of the location of the diffusion flame. It has very high concentration in the flame zone and diminishes quickly outside the flame zone. In Figure 3, the OH concentration is about 6 % in the preburned hot core gas, then rises to 16 % in the shear layer which confirms the location of the diffusion flame and finally decreases to zero in the wall cooling layer.

Figure 4 shows the temporal fluctuations of the OH concentration at several points lying across the mixing layer. Symbols in Figure 3 denote where the OH radical concentration samples are taken in the unsteady mixing layer. At the lower edge of the shear layer (symbol a), the OH concentration is constant. In the shear layer, the OH radical concentrations are plotted at three traverse stations (symbols b,c,d). It is observed that OH starts to fluctuate on different levels with respect to time at all three locations. Near the wall, in the hydrogen coolant film (symbol e), OH concentration remains nearly zero at all times.

Efforts centering on the time-averaged mixing and its impact on improving engine performance are currently underway. The predicted unsteadiness of the coolant layer and the three-dimensional nature of the

mixing layer on enhanced mixing, combustion processes, and wall cooling will also be assessed. Additional comparisons with counterpart experiments will be made.

REFERENCES:

- [1] Reed,B.D., Penko,P.F., Schneider,S.J. and Kim,S.C., "Experimental and Analytical Comparison of Flowfields in a 110 N (25 lbf) H_2/O_2 Rocket", AIAA Paper 91-2283, 1991, Sacramento, CA.
- [2] de Groot,W. and Weiss,J.M., "Species and Temperature Measurement in H_2/O_2 Rocket Flow Fields by Means of Raman Scattering Diagnostics", AIAA Paper 92-3353, 1992, Nashville, TN.
- [3] Zupanc,F.J. and Weiss,J.M., "Rocket Plume Flowfield Characterization Using Laser Rayleigh Scattering", AIAA Paper 92-3351, 1992, Nashville, TN.
- [4] Arrington,L.A. and Reed,B.D., "Performance Comparison of Axisymmetric and Three-Dimensional Hydrogen Film Coolant Injection in a 110 N Hydrogen/Oxygen Rocket", AIAA Paper 92-3390, 1992, Nashville, TN.
- [5] Weiss,J.M. and Merkle,C.L., "Numerical Investigation of Reacting Flowfields in Low-Thrust Rocket Engine Combustor", AIAA Paper 91-2080, 1991, Sacramento, CA.
- [6] Weiss,J.M.,Daines,R.L. and Merkle,C.L., "Computation of Reacting Flowfields in Low-Thrust Rocket Engines", AIAA Paper 91-3557, 1991, Cleveland, OH.
- [7] Weiss,J.M. and Merkle,C.L., "Prediction of Engine and Near-Field Plume Reacting Flows in Low-Thrust Chemical Rockets", AIAA Paper 93-0237, 1993, Reno, NV.
- [8] Shuen,J.S. and Yoon,S., "Numerical Study of Chemically Reacting Flows Using a Lower-Upper Symmetric Successive Overrelaxation Scheme", AIAA Journal, Vol. 27, No. 12, pp.1752-1760, 1989.
- [9] Yu,S.T.,Tsai,Y-L.P. and Shuen,J.S., "Three-Dimensional Calculations of Supersonic Reacting Flows Using a LU Scheme", AIAA Paper 89-0391, 1989, Reno, NV.
- [10] Molvik,G.A. and Merkle,C.L., "A Set of Strongly Coupled Upwind Algorithms for Computing Flows in Chemical Non-Equilibrium", AIAA Paper 89-0199, 1989, Reno, NV
- [11] Venkateswaran,S.,Weiss,J.M.,Merkle,C.L. and Choi,Y.-H., "Propulsion-Related Flowfields Using the Preconditioned Navier-Stokes Equations", AIAA Paper 92-3437, 1992, Nashville, TN.
- [12] Tsuei,H.-H. and Merkle,C.L., "Heat Release and Molecular Weight Effects in Shear Layer", AIAA Paper 94-0553, to be presented at AIAA Aerospace Sciences Meeting, Reno, 1994.
- [13] Shuen,J.-S., Chen,K.-H. and Choi,Y., "A Time-Accurate Algorithm for Chemical Non-Equilibrium Viscous Flows at All Speeds", AIAA Paper 92-3639, 1992, Nashville, TN.

Figure 1. Mach Number Contours for Aerojet Cutoff Nozzle.

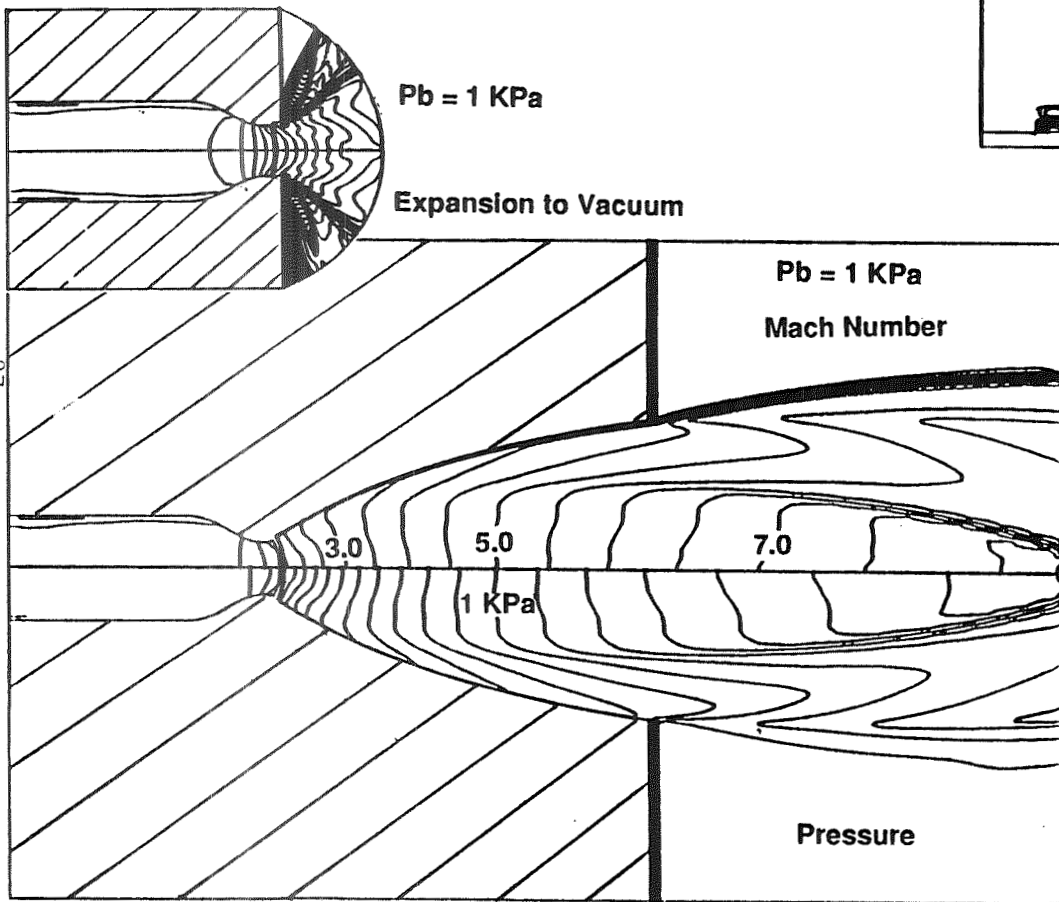


Figure 2. Mach Number and Pressure Contours for Aerojet Full Nozzle.

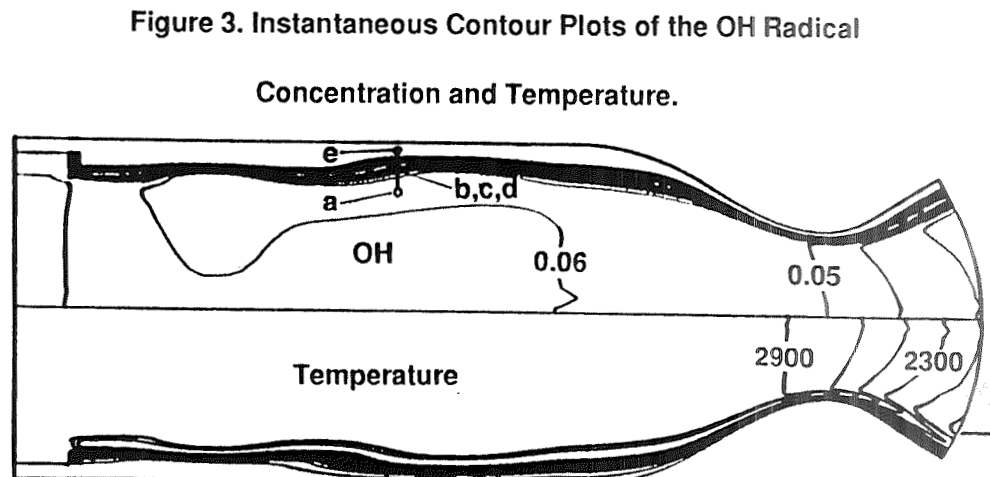


Figure 3. Instantaneous Contour Plots of the OH Radical Concentration and Temperature.

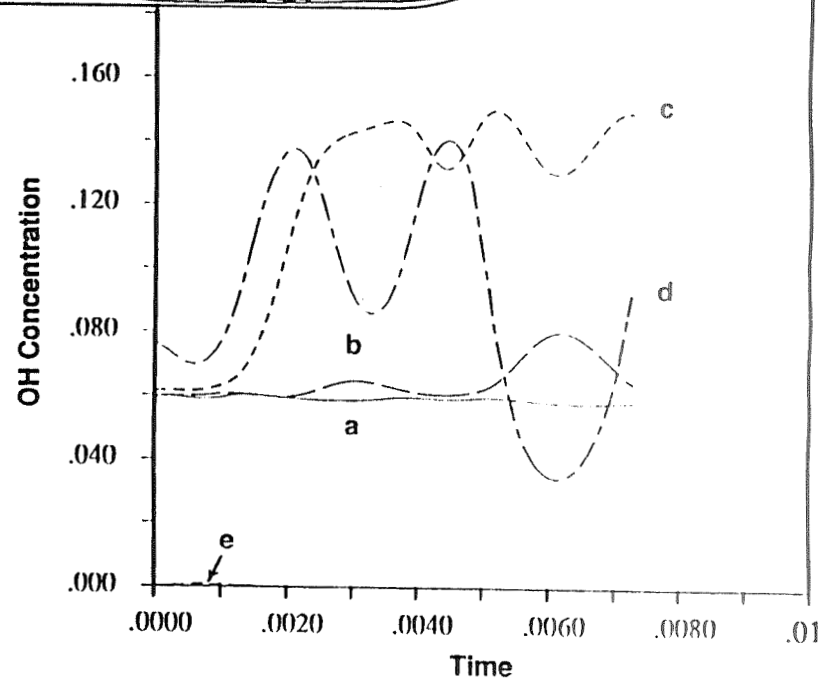
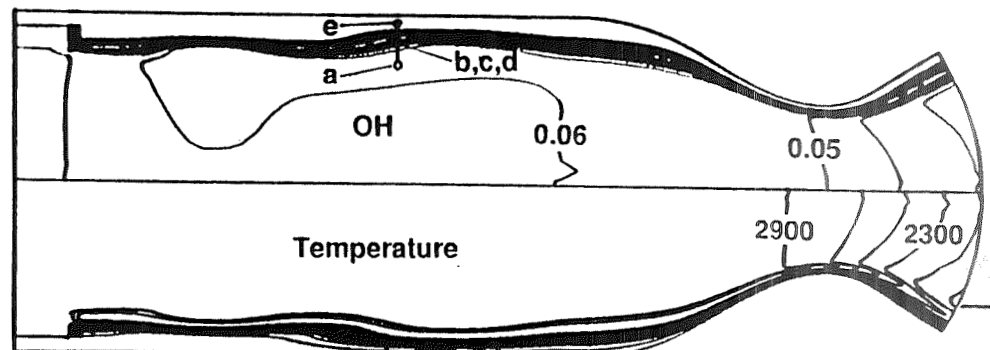


Figure 4. Temporal Variations of the OH Radical Concentration across the Mixing Layer.

LOX DROPLET VAPORIZATION IN A SUPERCRITICAL
FORCED CONVECTIVE ENVIRONMENT

Chia-chun Hsiao and Vigor Yang
Propulsion Engineering Research Center
Department of Mechanical Engineering
The Pennsylvania State University
University Park, PA 16802

SUMMARY:

Modern liquid rocket engines often use liquid oxygen (LOX) and liquid hydrogen (LH_2) as propellants to achieve high performance, with the engine operational conditions in the supercritical regimes of the propellants. Once the propellant exceeds its critical state, it essentially becomes a puff of dense fluid. The entire field becomes a continuous medium, and no distinct interfacial boundary between the liquid and gas exists. Although several studies have been undertaken to investigate the supercritical droplet behavior at quiescent conditions, very little effort has been made to address the fundamental mechanisms associated with LOX droplet vaporization in a supercritical, forced convective environment. The purpose of this work is to establish a theoretical framework within which supercritical droplet dynamics and vaporization can be studied systematically by means of an efficient and robust numerical algorithm.

TECHNICAL DISCUSSION:

Several analyses based on the model of a spherical droplet in a quiescent environment were recently developed to address the characteristics of supercritical droplet vaporization([1][2][3][4]). The model is adequate only for small droplets which become equilibrium with the ambient flow. Contrarily, convective effect is clearly observed for large droplets as a result of high momentum inertia of the liquid phase. Figure 1 depicts the situation examined here, showing an isolated vaporizing LOX droplet in a convective hydrogen environment. The initial temperature of the droplet is subcritical, but the ambient temperature and pressure are in the supercritical regime of oxygen. As a result of heat transfer from the surrounding gases, the droplet surface temperature increases rapidly and reaches its critical mixing point. Under this condition, the sharp distinction between gas and liquid phases disappears. The droplet regression can be best characterized by tracing the location of the critical temperature.

Governing Equation

The analytical model is based on the complete time-dependent conservation equations of mass, momentum, energy and species concentration for a multicomponent system with variable properties. If body forces, viscous dissipation, radiation, and chemical reaction are ignored, these equation can be written in the following vector form.

Mass:

$$\frac{\partial}{\partial t} \iiint \rho dV + \iint \rho u_j dA_j = 0. \quad (1)$$

Momentum:

$$\frac{\partial}{\partial t} \iiint \rho u_i dV + \iint \rho u_i u_j dA_j = \iint \tau_{ij} dA_j. \quad (2)$$

Energy:

$$\frac{\partial}{\partial t} \iiint \rho e dV + \iint \rho e u_j dA_j = \iint \tau_{ij} u_i dA_j - \iint (q_T)_j dA_j. \quad (3)$$

Species Concentration:

$$\frac{\partial}{\partial t} \iiint \rho Y_l dV + \iint \rho Y_l u_j dA_j = - \iint (q_{M,l})_j dA_j. \quad (4)$$

where

$$\tau_{ij} = -p\delta_{ij} + 2\mu e_{ij} - \frac{2}{3}\mu(\nabla \cdot u)\delta_{ij}.$$

Standard notations in fluid mechanics and thermodynamics are used in (1)-(4). The specific total energy e is defined as

$$e = \sum_{i=1}^l Y_i \int_{T_{ref}}^T C_{p,i} dT - \frac{p}{\rho} + \frac{u_i u_i}{2},$$

where the index l represents the number of species considered, Y_l the mass fraction of species l , and T_{ref} the reference temperature for energy. Fick's and Fourier's laws are used to approximate the species and thermal diffusion in (3) and (4), respectively.

Property Evaluation

Thermophysical properties, including both thermodynamic and transport properties, play a decisive role in determining droplet vaporization behavior. It is generally accepted that thermal conductivities and heat capacities of pure fluids and fluid mixtures can be divided into three contributions, and correlated in terms of density and temperature. For example, the thermal conductivity of fluid oxygen can be expressed as [5]

$$\lambda(\rho, T) = \lambda_o(T) + \Delta\lambda_{exc}(\rho, T) + \Delta\lambda_{crit}(\rho, T). \quad (5)$$

The first term on the right-hand side represents the value in the dilute-gas or zero-density limit, which is independent of density and can be accurately predicted by kinetic-theory equations and an m-6-8 model potential. The second is the excess thermal conductivity which, with the exclusion of unusual variations near the critical point, characterizes the deviation from λ_o for a dense fluid. The sum of λ_o and $\Delta\lambda_{exc}$ is sometimes called the "background" thermal conductivity. The third term refers to the critical enhancement which accounts for the anomalous increase above the background thermal conductivity as the critical point is approached. There are two separate regions where the critical enhancement of thermal properties is important. The first region is located in the close vicinity of the critical point, and is the region where a scaled equation of state must be used, as defined by Sengers et al[6]. For oxygen with $T_c = 154.581$ K and $\rho_c = 0.436$ g/cm³, this region is bounded approximately by $150 \leq T \leq 160$ K and $0.32 \leq \rho \leq 0.544$ g/cm³. The second region, designated as the extended critical region, covers the ρ - T domain in which critical enhancement is significant, but the fluid behavior can be described by an analytical equation of state such as a modified Benedict-Webb-Rubin (BWR) type. This region can extend to quite high temperatures, up to approximately $2T_c$. The critical enhancement along various isotherms can be centered on a density, ρ_{center} , which deviates slightly from the critical density and decreases with increasing temperature. More detail description can be found in [4].

Numerical Algorithm

The model considered here is characterized by strong couplings among heat transfer, transient diffusion, and phase transition, etc.. Because various time and length scales are involved in the entire process, the numerical scheme for solving this serious stiffness problem becomes a challenge. Moreover, the singular behavior of momentum balance in the limit of diffusion-dominant process adds further complications. In view of these difficulties, a numerical algorithm capable of treating time-accurate low Mach-number compressible

flow has been developed. The scheme is constructed in two steps. First, a rescaled pressure term is used in the momentum equation to circumvent the pressure singularity at very low Mach number.

$$p(x, y, t) = p_0 + \bar{p}(x, y, t)$$

The second step is based on the establishment of a dual time-stepping integration procedure. With the addition of a set of well-conditioned artificial time derivatives to the conservation laws, a new system of governing equations is obtained whose converged solution in pseudo-time corresponds to a time-accurate solution in the physical-time domain.

$$\Gamma \frac{\partial Z}{\partial \tau} + \frac{\partial Q}{\partial t} + \frac{\partial(E - E_v)}{\partial x} + \frac{\partial(F - F_v)}{\partial y} = S$$

where τ presents pseudo time, and $Z = (p', u, v, h, Y_i)$.

RESULTS:

As a first study of supercritical droplet behavior, A spherical droplet with an introductory temperature of 300 K is first placed in a supercritical, forced convective environment ($T_\infty = 1000K$). The droplet Reynolds number based on the relative velocity is 60. The droplet is 100 μm in diameter and contains 100% oxygen initially. As a result of large temperature gradient between gas and liquid phases, surface temperature raises and reaches critical condition shortly. Due to the diminishment of surface tension, droplet deformation and shattering can be clearly observed. Figure 2 shows the density contours, streamlines, and velocity vectors at $t = 0.02ms$ in a supercritical environment with H_2 as the ambient gas. Figure 3 shows the oxygen concentration contours. Results indicate that the ambient gas mass diffusivity plays an important role in determining the droplet behavior. A high mass diffusivity causes rapid penetration of the ambient gas into the droplet, and consequently modifies the droplet dynamics (e.g., deformation, shattering, etc.) caused by the density difference between the droplet and the gas.

REFERENCE:

- [1] Litchford, R. J. and Jeng, S. M., "LOX Vaporization in High-Pressure, Hydrogen-Rich Gas.", AIAA Paper 90-2191, 1990.
- [2] Delpanque, J. P. and Sirignano, W. A., "Transient Vaporization and Burning for an Oxygen Droplet at Sub- and Near-Critical Conditions.", AIAA Paper 91-0075, 1991.
- [3] Delpanque, J. P. and Sirignano, W. A., "Oscillatory and Transcritical Vaporization of an Oxygen Droplet.", AIAA Paper 92-0104, 1992.
- [4] Yang, V., Lin, N. C., and Shuen, J. S., "Vaporization of Liquid Oxygen (LOX) Droplets at Supercritical Conditions", AIAA Paper 92-0103, presented at the AIAA 20th Aerospace Sciences Meeting, January 1992.
- [5] Roder, H. M., "The Thermal Conductivity of Oxygen", Journal of Research, National Bureau of Standards, 87(4), 279.
- [6] Sengers, J. V., Basu, R. S., and Levelt Sengers, "Representative Equations for the Thermodynamic and Transport Properties of Fluids Near the Gas-Liquid Critical Point.", NASA Contractor Report 3424.

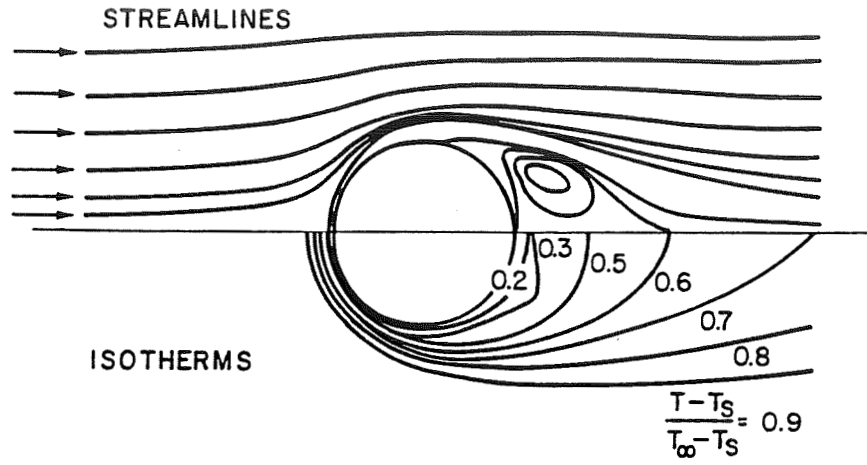


Figure 1: Schematic of a vaporizing LOX droplet in hydrogen stream.

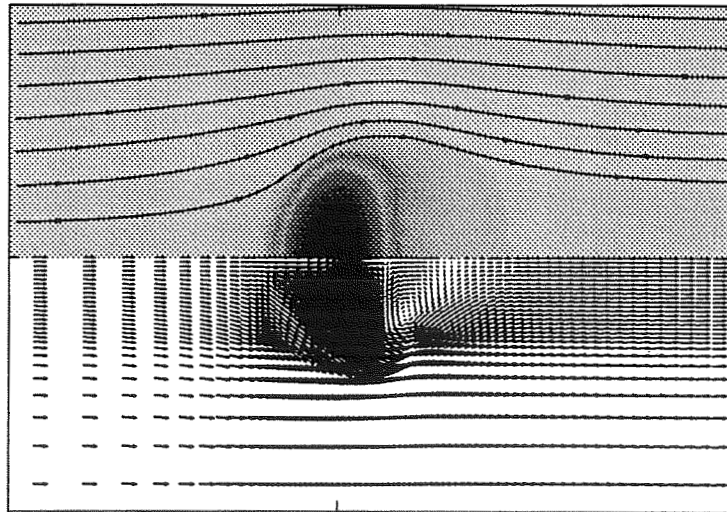


Figure 2: Density contours, streamlines and velocity vectors of LOX droplet vaporizing in a hydrogen environment. $Re = 60, t = 0.02ms$.

Mass Diffusion Exerts Strong Influence on Droplet Behavior in a Supercritical, Forced-Convective Environment

• High Mass Diffusivity

• Low Mass Diffusivity

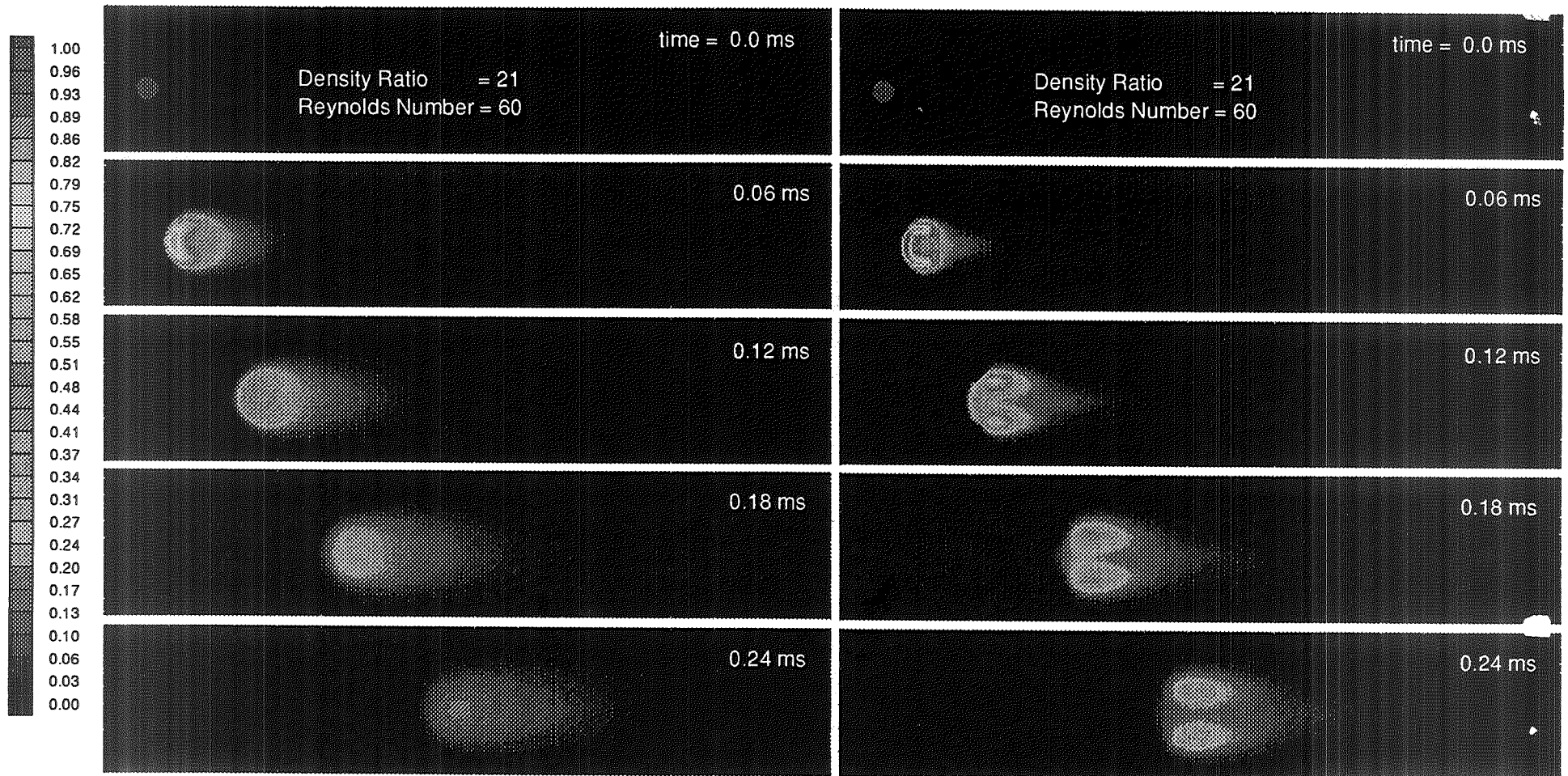


Figure 3: Time history of mass fraction of a vaporizing droplet at supercritical condition.

**EVAPORATION AND COMBUSTION OF LOX UNDER
SUPERCRITICAL AND SUBCRITICAL CONDITIONS***

A. S. Yang,‡ W. H. Hsieh,† and K. K. Kuo§

Propulsion Engineering Research Center
andDepartment of Mechanical Engineering
The Pennsylvania State University
University Park, PA 16802**SUMMARY:**

The objective of this investigation is to study the evaporation and combustion of LOX under supercritical and subcritical conditions both experimentally and theoretically. In the evaporation studies, evaporation rate and surface temperature were measured when LOX vaporizing in helium environments at pressures ranging from 5 to 68 atm. A Varian 3700 gas chromatograph was employed to measure the oxygen concentration above the LOX surface. For the combustion tests, high-magnification video photography was used to record direct images of the flame shape of a LOX/H₂/He laminar diffusion flame. The gas composition in the post-flame region is also being measured with the gas sampling and chromatography analysis. These data are being used to validate the theoretical model. A comprehensive theoretical model with the consideration of the solubility of ambient gases as well as variable thermophysical properties was formulated and solved numerically to study the gasification and burning of LOX at elevated pressures. The calculated flame shape agreed reasonably well with the edge of the observed luminous flame surface. The effect of gravity on the flame structure of laminar diffusion flames was found to be significant. In addition, the predicted results using the flame-sheet model were compared with those based upon full equilibrium calculations (which considered the formation of intermediate species) at supercritical pressures. Except at the flame front where temperature exceeded 2,800 K, the flame-sheet and equilibrium solutions in terms of temperature distributions were in very close agreement. The temperature deviation in the neighborhood of the flame front is caused by the effect of high-temperature dissociation.

TECHNICAL DISCUSSION:

Liquid oxygen (LOX) and hydrogen have been used in various types of liquid rocket engines because of their high specific impulse and low exhaust pollution.[1] Inside a liquid rocket engine, the oxygen and hydrogen are injected into a combustion chamber. Through the large shear force between the fuel and oxidizer streams, the primary atomization of oxygen is accomplished to form a spray of droplets. The vaporizing behavior of a single LOX droplet in high-pressure

* This paper represents a part of the research work sponsored by NASA/MSFC and PSU/PERC. The encouragement and support of Mr. Klaus Gross of MSFC are highly appreciated.

‡ Ph.D. Candidate

† Assistant Professor

§ Distinguished Professor and Director of the High Pressure Combustion Lab

hydrogen-rich environments has been studied extensively by Litchford and Jeng[2], Delplanque and Sirignano[3], and Yang et al.[4] However, no comparison of their predictions with experimental data was established for these evaporation studies due to the unavailability of testing results.

One of the major obstacles involved in the evaporation and combustion studies of a single droplet is that the size of a typical LOX droplet is usually too small to allow detailed measurements of flow properties in its neighborhood. In order to overcome this problem, a liquid strand test setup has been employed to maintain the surface of the liquid oxygen at a fixed location. In the LOX feeding system, gaseous oxygen was delivered into a cylinder immersed in a liquid nitrogen bath. Cooled by liquid N_2 , the oxygen was liquefied and eventually filled in the interior space of a cylinder serving as a reservoir for LOX. By adjusting the opening of a micro-metering valve, the LOX mass consumption rate can be satisfactorily controlled to maintain a stable surface at the exit of the LOX feeding tube under prespecified steady-state operating conditions. In combustion tests, ignition of LOX with the surrounding hydrogen was achieved using a spiral nichrome-wire ignitor. The chamber pressure was maintained at a prespecified level by a computer feedback-controlled gas purging system. The surface temperature at the exit of the LOX feeding tube was measured using a $75\ \mu\text{m}$ Fe/Cu-Ni (J-type) fine-wire thermocouple. Direct images of the flame shape of a LOX/hydrogen laminar diffusion flame were also recorded using high-magnification video photography. For species concentration measurements, a quartz micro-probe with an orifice diameter of $25\ \mu\text{m}$ is used to sample the gas mixture in the post-flame region. The gas mixture composition is measured using a Varian 3700 gas chromatograph (GC) with a thermal conductivity detector. Detailed description of the experimental setup can be found in Ref. 5.

Theoretically, a comprehensive model was formulated to simulate the evaporation and combustion processes of liquid oxygen with the hydrogen/helium mixture at elevated pressures. The model was based on the conservation equations of mass, momentum, energy, and species concentrations for a multi-component system. With allowance for the axial diffusion, the model described by a set of coupled elliptic partial differential equations was solved numerically. The gravitational body force was considered to account for the influence of natural convection. In the treatment of the real-gas behavior, pressure and temperature effects were included for evaluating thermodynamic and transport properties.[5] The flame-sheet approximation with consideration different mass diffusivities for individual species was used to model the combustion process of oxygen and hydrogen under supercritical conditions. To characterize the high-pressure solubility of the ambient gas into the liquid, a fugacity-based multicomponent thermodynamic analysis with quantum-gas mixing rules was also carried out. Calculations were performed by solving the governing equations with an iterative SIMPLE (Semi-Implicit Method for Pressure-Linked Equations) algorithm.

Results obtained in the evaporation study are given in Ref. 6. Results from the combustion study are presented and discussed as follows. In the combustion tests, a stable onion-shaped LOX/ H_2 /He diffusion flame was achieved at a pressure of 30 atm. (The laminar diffusion flame studied had a oxygen supply rate of 0.018 gm/s, hydrogen of 0.052 gm/s, and helium of 0.12 gm/s.) However, the LOX surface was below the exit of the feeding tube by about 1.5 mm. To raise the

LOX surface to the port of the feeding tube, the oxygen supply rate was gradually increased to 0.024 gm/s. When the LOX surface approached to the tube exit, the region near the tube rim was cooled down significantly by the LOX. This decrease in temperature caused the increase of heat loss from the flame as well as reducing radical concentrations in chemical reactions. Thus, the flame tended to detach from the tube rim and became unstable. This quenching effect sometimes even caused extinguishment of the flame.

To verify the present axisymmetric steady-state combustion code, a numerical simulation was conducted by considering the LOX surface fixed at the position of 1.5 mm below the exit of the feeding tube. From surface temperature measurements, the LOX surface was 136.2 K at $P = 30$ atm. The temperature of the surrounding hydrogen/helium mixture was 295 K. Based on measured mass flow rates of oxygen, hydrogen, and helium, the gas velocities of the H₂/He mixture flow and vaporized LOX were 1.5 and 0.523 cm/s, respectively. The oxygen mass fraction at the LOX surface was also determined to be 0.981 from the phase equilibrium analysis. Figure 1 presents the comparison between predicted and experimentally-observed steady flame shape for the coflowing LOX/H₂/He laminar diffusion flame at a pressure of 30 atm. In general, the calculated flame shape was in reasonable agreement with the observed luminous flame surface. In the prediction of the flame height, the calculated flame front was found to be very close to the edge of observed flame surface (as shown in Fig. 2). More measurements of the species concentration in the post-flame region are being conducted with a gas sampling system coupled with a GC for further code validation.

To study the influence of the LOX surface position on the flame shape, another simulation was conducted for the case in which the LOX surface was maintained at the exit of the feeding tube. Same boundary conditions (as used in the former case study) were employed except that the oxygen supply rate was increased from 0.018 to 0.024 gm/s. Corresponding to this flow rate, the gas velocity above the LOX surface was 0.7 cm/s. Figure 3 presents the predicted and observed flame shape at a pressure of 30 atm. In a global view, the size of the calculated flame zone becomes larger when the LOX surface moves to the exit plane of the port. Compared to the former case, the flame height (defined by the axial distance between the locations of the LOX surface and the peak temperature) increased from 7.1 to 12.0 mm.

The theoretical model was also used to predict the structure of a LOX/H₂/He laminar diffusion flame with a H₂/He mass ratio of 30/70 at a pressure of 68 atmospheres. The inflow velocity of vaporized oxygen was 0.218 cm/s above the LOX surface and the flow velocity of the surrounding hydrogen/helium mixture was 1.5 cm/s. The temperatures of the LOX surface and the surrounding flow were 153.3 and 295 K, respectively. The phase equilibrium analysis was applied to determine boundary conditions of species concentration at the LOX surface. The oxygen mass fraction at the LOX surface was 0.988 in this case.

Figure 4 shows temperature contours with respect to both axial and radial coordinates. In general, the high temperature area spanned from the interface region of the oxidizer and fuel inlets near the tube rim to the center line. The peak temperature along the center line was about 3310

K. The flame height was found to be 1.66 cm above the tube exit. The steep axial temperature gradients were noted in the vicinity of the LOX surface, which indicated a strong heat feedback from the flame to the LOX surface, to provide the energy required in the phase change of oxygen from a compressed liquid to a superheated vapor. To examine the effect of gravity on the flame structure, another calculation (using same boundary conditions) was performed with zero gravity. Figure 5 exhibits temperature contours without considering the body-force effect. Compared with Fig. 4, significant difference in the temperature plot is noted as the gravity term is removed from the axial momentum equation. In the case with gravity effect, the buoyancy force accelerates the flow in the reaction zone and thereby increases the entrainment of the surrounding H_2/He mixture. This suction-like effect induces an inward radial flow motion near the port exit plane to enhance combustion and drive the flame closer to the center line. In contrast to the above case, the flame tends to expand in the radial direction and its flame height is taller at the zero-gravity condition. This result demonstrates that the buoyancy effect can be very important in influencing the shape of diffusion flame. These results can be utilized to interpret flame structures under microgravity conditions.

To examine the reaction zone broadening due to dissociation, the predicted temperature distribution along the centerline from the flame-sheet model is compared with that of equilibrium calculations, which considered the formation of intermediate species such as hydrogen atom, oxygen atom and hydroxyl radical in the flame. Figure 6 presents the comparison of these two solutions. Below 2,800 K, the difference was found to be within 2.5%. However, the flame-sheet model with no dissociation overpredicted the peak temperature by 8.5% at the axial location of the flame front ($x = 1.66$ cm). This discrepancy is obviously attributed to the fact that intermediate species produced in the dissociation process are considered in the equilibrium solution.

REFERENCES:

1. Sutton, G. P., *Rocket Propulsion Elements*, John Wiley & Sons, New York, 1986.
2. Litchford, R. J. and Jeng, S. M., "LOX Vaporization in High-Pressure, Hydrogen-Rich Gas," AIAA Paper No. 90-2191, 1990.
3. Delplanque, J. P. and Sirignano, W. A., "Transient Vaporization and Burning for an Oxygen Droplet at Sub- and Near-Critical Conditions," AIAA Paper No. 91-75, 1991.
4. Yang, V., Lin, N. N., and Shuen, J. S., "Vaporization of Liquid Oxygen (LOX) Droplets at Supercritical Conditions," AIAA Paper No. 92-103, 1992.
5. Kuo, K. K., Hsieh, W. H., Yang, A. S., and Brown, J. J., "Combustion of LOX with $H_{2(g)}$ under Subcritical, Critical, and Supercritical Conditions," Annual Report to NASA/MSFC, February, 1992.
6. Yang, A. S., Hsieh, W. H., Kuo, K. K., and Brown, J. J., "Evaporation of LOX under Supercritical and Subcritical Conditions," AIAA Paper No. 93-2188, 1993.

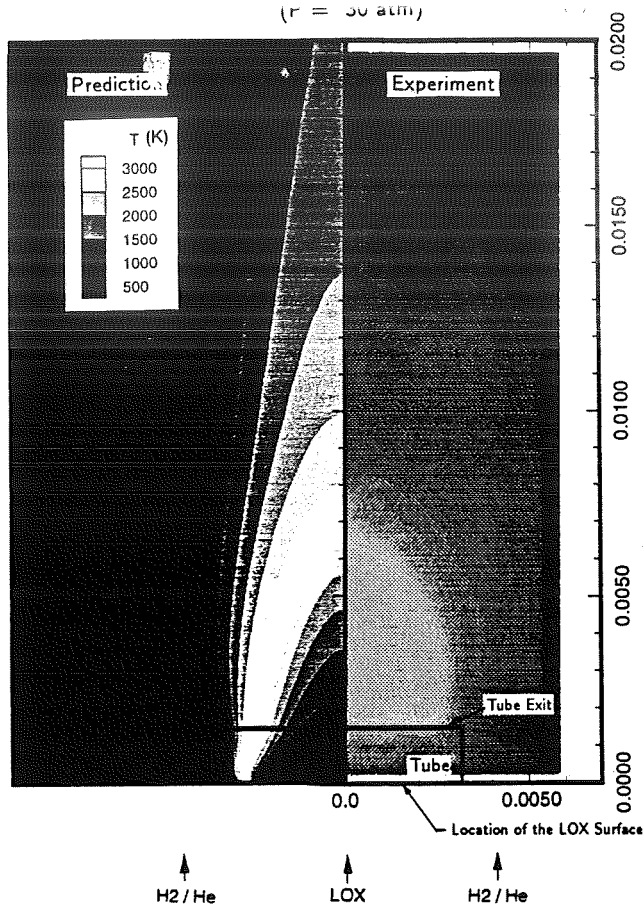


Figure 1 Predicted and Experimentally-observed Flame Shape with an Oxygen Supply Rate of 0.018 gm/sec at a Pressure of 30 atm

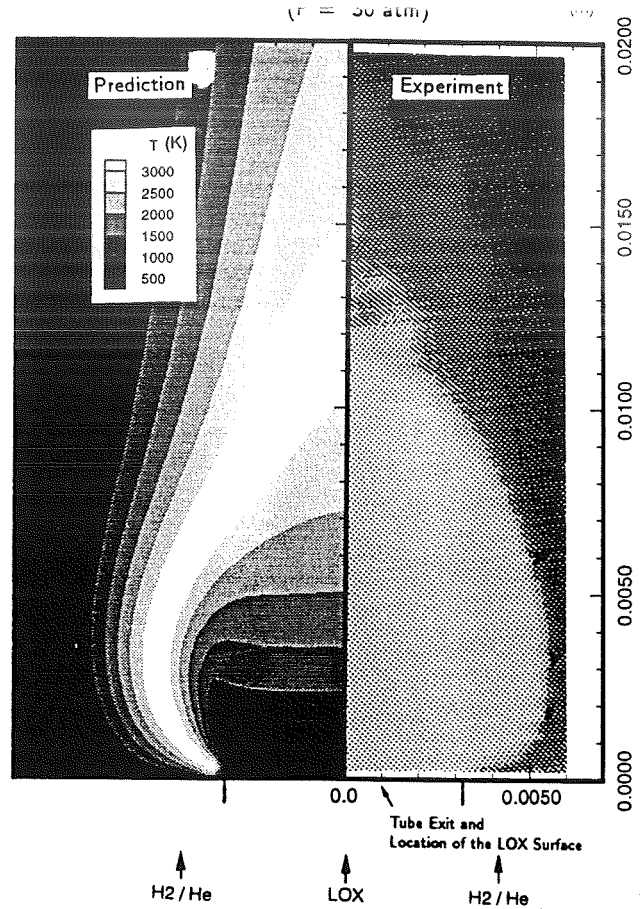


Figure 3 Predicted and Experimentally-observed Flame Shape with an Oxygen Supply Rate of 0.024 gm/sec at a Pressure of 30 atm

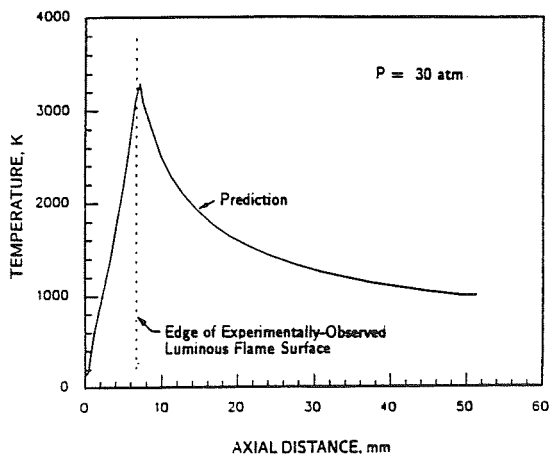


Figure 2 Predicted Center-line Temperature Profile and Location of Luminous Flame Surface at a Pressure of 30 atm

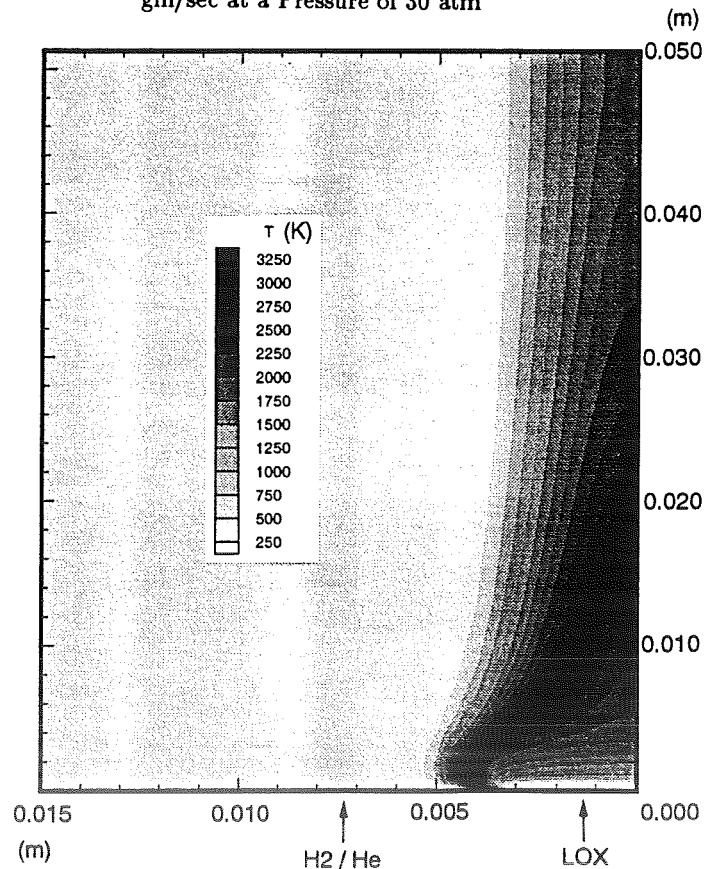


Figure 4 Temperature Contour for the Coflowing LOX/Hydrogen/Helium Laminar Diffusion Flame at a Pressure of 68 atm

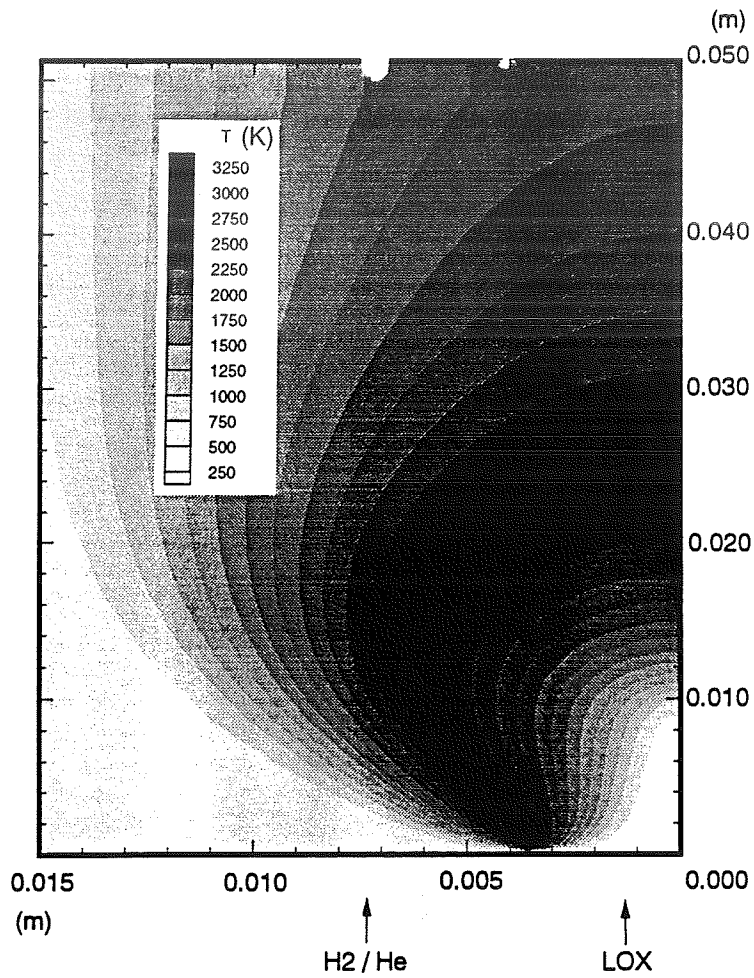


Figure 5 Temperature Contour for the Coflowing LOX/
Hydrogen/Helium Laminar Diffusion Flame with-
out the Effect of Gravity (P = 68 atm)

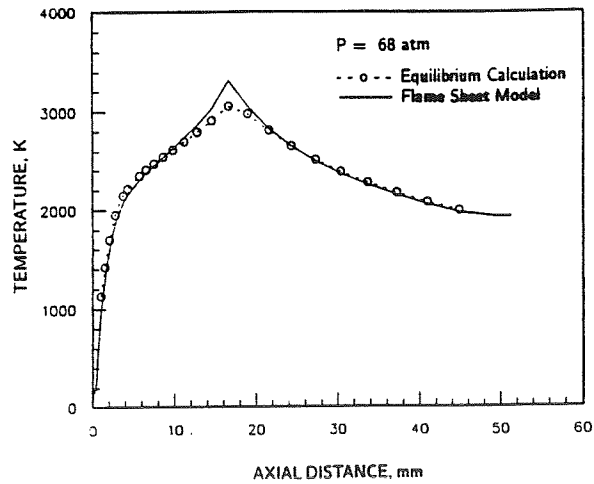


Figure 6 Comparison between Equilibrium Calculations
and the Predicted Center-line Temperature Pro-
file (P = 68 atm)

DROPLET TURBULENCE INTERACTIONS
UNDER SUBCRITICAL AND SUPERCRITICAL CONDITIONS

E. B. Coy, S. C. Greenfield, M. S. Ondas,
Y. -H. Song, T. D. Spegar, and D. A. Santavicca
Penn State University

The goal of this research is to experimentally characterize the behavior of droplets in vaporizing liquid sprays under conditions typical of those encountered in high pressure combustion systems such as liquid fueled rocket engines. Of particular interest are measurements of droplet drag, droplet heating, droplet vaporization, droplet distortion, and secondary droplet breakup, under both subcritical and supercritical conditions. The following is a brief description of the specific accomplishments which have been made over this past year.

Measurements of the Dynamics of Droplet-Turbulence Interactions (E.B. Coy)

Preliminary experiments have been performed on the motion of droplets in the self-generated turbulence of a spray. The following results demonstrate the capability of the measurement technique for determining the size-velocity correlation.

Experimental Apparatus: A schematic drawing of the apparatus is shown in Figure 1. It is basically an adaptation of the Particle Image Velocimetry technique.¹ The laser beams are focused into sheets which coincide with the image plane of the 35mm camera. The camera shutter is opened and the lasers are fired in rapid succession forming two distinct images of each droplet. The components of droplet velocity in the object plane are determined from the displacement of the images and the time interval between pulses. Matching the droplet images is facilitated if the order of laser pulses can be distinguished by color. This is accomplished by doping the liquid with two fluorescent dyes (e.g., Rhodamine 610 and Stilbene 420). Rhodamine 610 absorbs at the second harmonic (532 nm) and emits at 610 nm while Stilbene 420 absorbs at the third harmonic (355 nm) and emits at 420 nm. These characteristics permit the intense elastic scattering of the excitation wavelengths to be eliminated with a narrow band mirror and edge filter thus permitting only the fluorescent emission from the droplets to be captured on 35 mm color slide film. The images are recorded at 2:1 magnification which gives a field of view of 18 mm by 12 mm. The film used is ASA 200 color reversal film (e.g., Kodak Ektachrome 200).

The slides are automatically analyzed using a microcomputer based image processing system. The slides are placed in a translation stage system which positions the slide relative to an RS-170, CCD camera and allows the slide to be analyzed in 225 fields, 2.4 mm wide by 1.6 mm high. For each field an image of the blue droplets is obtained by interposing a bandpass filter between the quartz-halogen lamp and the slide. The digitized image is scanned and the droplets are located and sized. The process is repeated for the red droplets.

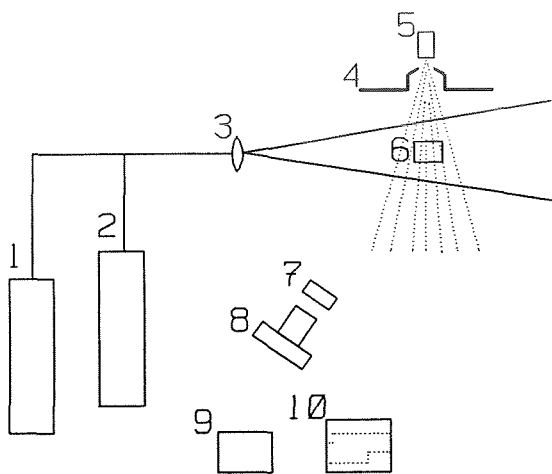


Figure 1. Experimental Apparatus: 1-355nm beam, 2-532nm beam, 3-light sheet optics, 4-skimmer, 5-nozzle, 6-sample volume, 7-532nm mirror, 8-35mm camera, 9-timing circuit, 10-oscilloscope

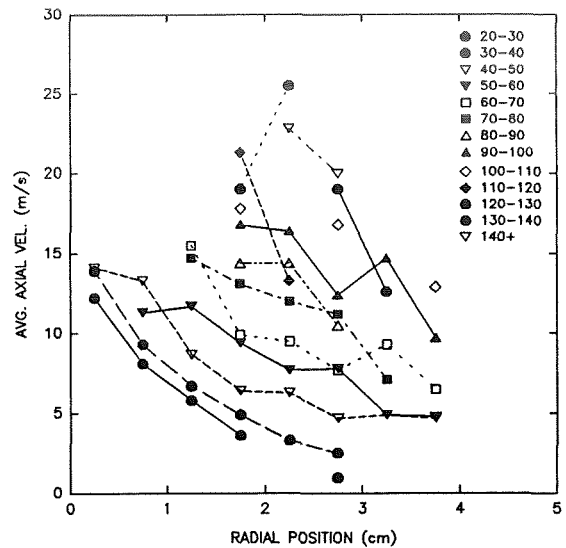


Figure 2. Average velocity as function of radial position for several size ranges of droplets for WDB 4.0 atomizer

The drop size and position is stored for post processing for velocity. The time required to analyze a single slide containing about 1000 droplet images is about 25 minutes.

Size-Velocity Data: Droplet image velocimetry measurements were made along a radius 5 cm below the nozzle exit for three nozzles. Average axial velocity as a function of radial position for several drop sizes is shown in Figure 2. It appears that larger samples will be required to achieve smooth velocity profiles; however, the trends with respect to drop size and radial position are evident and the velocities of the largest droplets agree favorably with the initial axial velocity based on thrust and mass flow. The large droplets are clustered about the 2 cm radial position indicating that the initial direction acquired at the breakup of the cone has not been significantly modified by the gas flow. The large droplets also are traveling at velocities approaching the outlet velocity. Small droplet velocities have already assumed the characteristic Gaussian profile of a turbulent jet.

An Experimental Study of Droplet Motion in Laminar and Highly Turbulent Flows (Y.-H. Song)

Overview: The objective of this study is to experimentally study the motion of droplets undergoing unsteady curvilinear motion in laminar and turbulent flows. Droplet or particle motion has been studied for a long time, and some aspects of droplet motion are well understood. For example, for a non-vaporizing solid sphere undergoing steady rectilinear motion in a laminar flow, the standard drag curve and the steady equation of motion can be used to accurately predict the sphere's velocity and trajectory. However, for the case of droplet motion in actual spray combustion systems, where vaporization, unsteady curvilinear motion and free-stream turbulence must also be accounted for, such information is not available. In order to study these effects on droplet motion, small (90-300 μm) single droplets were transversely injected into an air flow, producing

unsteady curvilinear trajectories. The present experiments were conducted using the experimental apparatus shown schematically in Figure 3, which has the capability of generating laminar or highly turbulent flows (up to 40% relative turbulence intensity) with variable temperature (up to 700 K) and pressure (up to 70 atm) conditions. The droplet Reynolds numbers investigated in this study range from 10 to 500, which covers typical droplet Reynolds numbers in spray combustion systems.

Results: Presented below are results on the effect of vaporization on droplet drag in a laminar flow and the increased droplet drag forces in a turbulent flow. The experimentally obtained drag coefficients in a laminar flow, without and with correcting for vaporization, are compared with the standard drag correlation in Figures 4-a and 4-b, respectively. In Figure 4-a, the droplet Reynolds numbers are calculated using the free stream air density and viscosity. In Figure 4-b, the droplet Reynolds numbers are estimated using the 1/3 rule, and the measured drag coefficients are multiplied by $(1+B)^{0.32}$ to correct for vaporization. Figure 4-a shows that the drag coefficients of evaporating droplets are significantly reduced as the air temperature increases. As shown in Figure 4-b, if the effect of vaporization on drag is included, the measured drag coefficients agree well with the standard drag curve.

Measured droplet acceleration in a turbulent flow is compared with the estimated droplet acceleration using the standard drag curve in Figure 5. These results show that the time averaged drag force ($m \cdot a$) in a turbulent flow is larger than that in a laminar flow at the same droplet Reynolds number, which indicates that free-stream turbulence increases the momentum transfer rate (drag force).

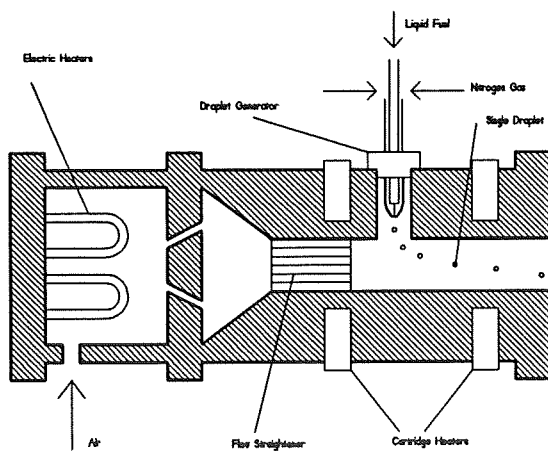


Figure 3. Schematic of Experimental Apparatus

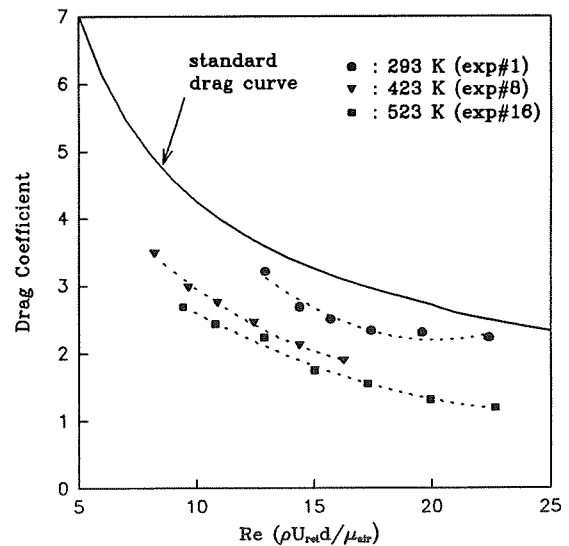


Figure 4-a. Measured drag coefficients at different temperatures

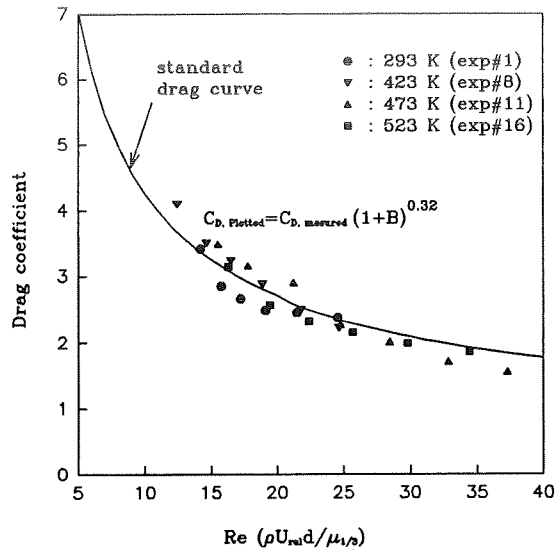


Figure 4-b. Corrected drag coefficients at different temperatures

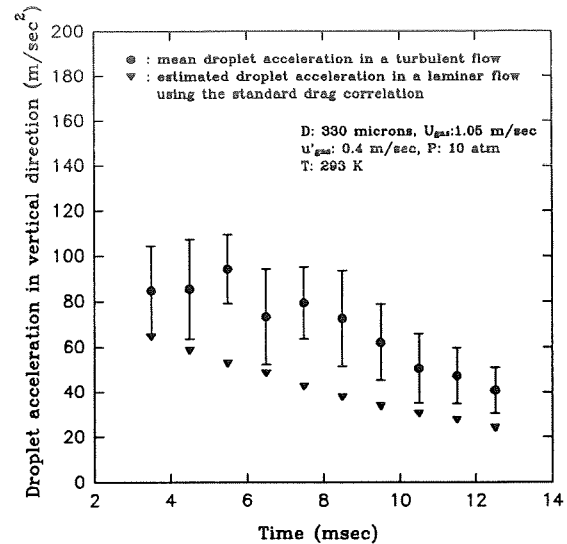


Figure 5. Measured and estimated droplet acceleration in a turbulent flow

Exciplex Thermometry (S.C. Greenfield)

Measurement of droplet temperature is important because of its influence on droplet vaporization, e.g., droplet models require droplet temperatures to accurately predict vaporization rates. Most prior experiments involved the suspension of a droplet on a thermocouple, however, this disrupts both the internal and external flowfields of the droplet. Exciplex thermometry has the advantage of being a non-intrusive fluorescence technique, thus preserving the natural flowfields surrounding and within the droplet.

The exciplex system chosen for this experiment was 2.5% (by weight) tetramethyl-1,4-phenylenediamine (TMPD) and 1.0% 1-methylnaphthalene (1MN) in tetradecane (TD). Upon UV-laser excitation (Nd:YAG, 355 nm), two distinct fluorescence signals are produced, centered at 400 nm and 500 nm. The ratio of intensities at these two wavelengths is temperature-dependent and upon calibration, can be used as a thermometer. These chemicals were chosen for both their exciplex-forming capabilities and because their boiling points are similar (TMPD-260°C, 1MN-242°C, TD-252°C). This is important because the intensity ratio versus temperature curve is concentration-dependent; differential component vaporization would bias the measurements, especially at elevated temperatures.

Many attempts were made to produce a calibration curve using droplets of known temperature. Unfortunately, wide variability existed in the intensity ratio measurements of droplets presumably at the same temperature. Three of the most probable causes of this variability can be identified. First, even though the droplets were preheated for isothermal injection into the surrounding environment, vaporization would still cool the droplets; thus, the exact temperature was uncertain. Second, the purchased TMPD showed a fairly high degree of oxidation, the affect of which is not yet fully known. Finally, there appears to be a viewing angle affect resulting from the use of a split-image filter (which produces two images of one object) to simultaneously

image the exciplex (500 nm) and monomer (400 nm) fluorescence. Because a droplet is three-dimensional and not planar, the two images appear to emanate from different parts of the droplet, the left image biased towards the front of the droplet and the right towards the back. Thus, as the droplet location changes from left to right, the region that is imaged changes as well. Since the fluorescence is more intense on the front face (i.e., in the optically thick case, where the laser first contacts the droplet), the intensity ratio will be biased by the droplet location within the field of view.

To circumvent these problems, a new experiment was designed. Instead of droplets, an Amersil TO8 quartz tube (1 mm ID, 2 mm OD) containing a thermocouple was used for calibration purposes. A 120 micron pinhole was placed in front of the tubing to prevent image overlap (caused by the split-image filter) during acquisition. Additionally, a sublimation unit was purchased to purify the TMPD. An initial set of calibration data was acquired with a Princeton Instruments intensified CCD camera and is shown in Figure 6.

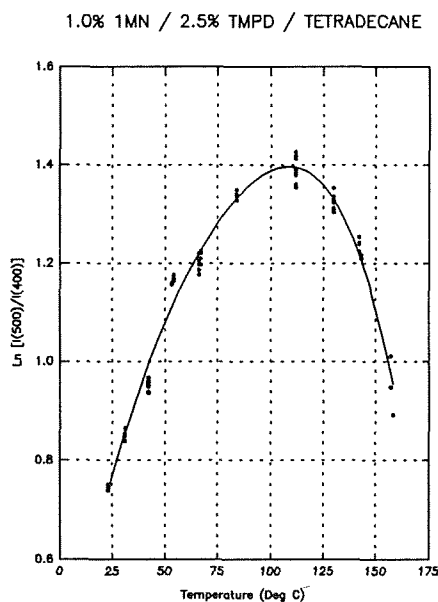


Figure 6. Exciplex Calibration Curve

Droplet Vaporization in an Acoustic Field (M.S. Ondas)

In recent years, there has been much discussion about what mechanisms may be responsible for high frequency combustion instabilities. Some reasons for this discussion are the destructive nature of high frequency instabilities and the current lack of fundamental knowledge about their causes and sustaining mechanisms. During the JANNAF sponsored workshop on Liquid Rocket Engine Combustion Driven Instability Mechanisms,² five categories of basic combustion physics were identified: fluid mechanics, injection,

atomization, vaporization, and mixing. These mechanisms were discussed and then ranked according to how important each is likely to be to the instability process. Vaporization was considered to be a priority issue in both the subcritical and supercritical regimes. Fundamental data on the vaporization process is critical for basic physical understanding as well as for providing a database for analytical and computational models. In order to obtain information on vaporization rates and vapor concentration wake structure around the droplet, a single vaporizing droplet is used. This is done to eliminate any possible coupling effects with other mechanisms, such as atomization. A droplet is either suspended from the end of a syringe or transversely injected into a 1.9 cm square duct with a length of 259 cm. The mean velocity of the flow is up to 10 m/s with an average pressure of up to 10.0 atm and temperature capabilities of up to 260°C. A six-orifice rotating disk is used to periodically open and close the end of the duct. With this technique, standing longitudinal waves from 100 to 500 Hz can be generated with peak to peak amplitudes of up to $\pm 10\%$ of the mean chamber pressure.

The most recent work was done using two different visualization techniques. The first technique was an exciplex vapor/liquid visualization system. Tetradecane was doped with the exciplex additives and the vaporizing droplets were suspended by a syringe tip and illuminated using either the 355 nm or the 266 nm beam from an Nd:YAG laser. The flow conditions were 1.3 m/s at 220°C and a pressure of 7.8 atm. The filtered image showing the vapor wake signal was recorded using a Princeton Instruments intensified CCD array camera. This technique provided some images of the vapor wake, but the signal to noise ratio was low. In order to increase the amount of fuel vapor in the wake, a more volatile fuel was used. The second technique used acetone as the fuel. Acetone is very volatile and it also fluoresces when excited by an ultraviolet laser source. The flow conditions were from 1.2-1.5 m/s at 50-85°C and 6.4 atm. The 266 nm beam from an Nd:YAG laser was used as the excitation source. The images were once again obtained using the intensified array camera. Due to the increased volatility of the acetone, the image quality was better than those obtained with the tetradecane exciplex mixture.

One problem that remains is the effect the syringe has on the droplet. The droplet tends to adhere to the syringe and form a teardrop shape. This is undesirable since the droplets are no longer spherical and because of the disruption in the flow field around the droplet. Also, the syringe causes some scattering of the incident laser sheet. The upcoming experiments will use an acetone droplet that is in free fall to alleviate the interference from the syringe. The droplet and its vapor wake will be illuminated by a laser sheet cutting the vertical plane of motion. The CCD array camera will be focused on this plane to record the image. Once the data acquisition system is more fully developed and images are of sufficient quality, an acoustic field will be induced on the mean gas flow and droplet vaporization in the presence of an acoustic wave can be studied.

Raman Imaging of Supercritical Droplets and Jets (T. D. Spegar)

In liquid propellant rocket engines, the behavior of the injected liquid highly influences the subsequent combustion process. Often, the combustion chamber pressure and temperature exceed the critical temperature

and pressure of the injected fuel and/or oxidizer. Transport processes in the spray dictate how the temperature of the droplets will change. Since the temperature of the combustion chamber generally surpasses the liquid temperature at injection, one might expect the liquid temperature to increase and approach the surrounding temperature. However, conditions may exist where the vaporization rate is so high that the droplet temperature decreases or total vaporization is achieved before the droplet reaches its critical temperature. But, if the droplet temperature approaches or exceeds its critical temperature, the corresponding decrease in surface tension will play an important role in droplet behavior. Specifically, droplet distortion, breakup, vaporization rate and drag, as well as enhanced permeation of the surrounding gas, can be significantly affected by a decrease or absence of surface tension. The objective of this work is to experimentally investigate the above phenomena in the helium-nitrogen system. Helium and nitrogen have highly dissimilar critical temperatures and pressures, much as the hydrogen-oxygen system.

Liquid nitrogen is injected into a helium environment at pressures up to 100 atmospheres. The injection was previously collinear with a downward helium flow but the problem of helium cooling from the droplet generator was encountered. Being cooler, the helium disturbed the field of view below the injection point due to the presence of density fluctuations. The test chamber has since been mounted on its side, with nitrogen injection downward into a crossflow of helium which can be adjusted to continuously flush the field of view. The helium velocity may also be increased to observe the effect of a strong crossflow on jet and droplet behavior. Pressurized liquid nitrogen is obtained by condensing high-pressure gaseous nitrogen upstream of the jet within the liquid nitrogen-cooled droplet generator. Jet velocity can now be measured indirectly by use of a small pressurized rotameter in the nitrogen supply line. The jet diameter is 0.004" which produces droplets of about 100 microns in diameter.

Single droplets and jets of liquid nitrogen have been injected into the helium environment at selected pressures and were viewed using a CCD video camera. Various jet structures have been observed to occur at different experimental conditions. In particular, pressure appears to play an important role in jet behavior. Using a flashlamp-pumped dye laser and an intensified CCD camera, Raman scattering measurements have been initiated to determine relative nitrogen concentrations in the jet and droplet wakes and possibly within the jet and droplets themselves. The latter technique is much more difficult due to the intense elastic scattering off the liquid surface, but may be accomplished if the liquid reaches its supercritical temperature causing the surface to no longer be well defined.

References

1. Adrian, R.J., Multi-point Optical Measurements of Simultaneous Vectors in Unsteady Flow - A Review, *Int. J. Heat and Fluid Flow*, 1986.
2. Jensen, R.J., "A Summary of the JANNAF Workshop on Liquid Rocket Engine Combustion Driven Instability Mechanisms", presented at the 26th JANNAF Combustion Meeting, Pasadena, CA, October, 1989.

SSME FUEL PREBURNER INJECTOR CHARACTERIZATION

John J. Hutt

Propulsion Laboratory
Marshall Space Flight Center
Huntsville, AL 35812**SUMMARY**

A project has been initiated at the Marshall Space Flight Center to determine if preburner inter- or intraclement mixture ratio maldistributions are the cause of temperature variations in The Space Shuttle Main Engine (SSME) High Pressure Fuel Turbopump (HPFTP) turbine inlet region. Temperature nonuniformity may contribute to the many problems experienced in this region. The project will involve high pressure cold-flow testing and Computational Fluid Dynamics (CFD) modeling.

INTRODUCTION

Since the beginning of the Space Shuttle program, the Space Shuttle Main Engine (SSME) has experienced a variety of problems in the high pressure fuel turbopump (HPFTP) turbine inlets. These problems include turbine blade cracks, blade erosion, and sheet metal cracks. The problems may be caused from the severe environment that is generated during start-up and shut-down or to temperature striations that exist during nominal operation. Recent studies have also suggested that the sheet metal cracking may be the result from mechanical vibrations during steady-state operation. In order to properly analyze these problems the thermal environment must be known. It has been shown that temperature striations due to distributions of mixture ratio during steady-state operations persist into the turbine. In a series of recent tests at the Marshall Space Flight Center (MSFC) temperature measurements were taken at various locations along the turbine inlet. Figure 1 shows the locations of the temperature measurements and the measured temperatures of a representative test. A measurement of the temperature of the suction side of a nozzle blade measured above 2300 degrees Rankine, several hundred degrees higher than expected. In general, it is expected that the upstream nozzle temperatures would be higher at the midspan and lower on the edges due to film cooling and Augmented Spark Igniter (ASI) flow. The data showed that the temperatures along the inner diameter were higher than those at the midspan. Thermocouples directly downstream of the baffles did not show temperatures that were notably cooler than those at other circumferential locations. The measurements made on the outer diameter edge of the nozzle blade tended to read lower, showing the effects of the film coolant, but the readings were inconsistent with circumferential variations of over 200 degrees. The thermocouples were placed in some degree of contact with cooled metal surfaces and the amount of cooling at each point is not well known. If it is assumed that the thermocouple does not lose significant heat to the hardware and that the thermocouples are accurate and properly calibrated, the temperatures measured represent the adiabatic wall temperature, which is close to the freestream stagnation

temperature. Variations in the freestream stagnation temperature are caused from variations in the upstream mixture ratio. Variations in upstream mixture ratio are caused from the ASI flow, the coolant flow, and the baffles, but these variations follow particular patterns that do not explain the seemingly random variations in the data. Another source of mixture ratio variation are inter and intraelement mass flow variations. Interelement variations result from manifold pressures and variations in flow resistance in the element due to geometric variations within design tolerances. Intraelement is the variation in mixture ratio across an element streamtube due to incomplete mixing. A study is being conducted to determine if either of these effects is the cause of the temperature nonuniformity. If intraelement effects are found to be important, possible design modifications will be examined.

APPROACH

The SSME uses liquid oxygen (LOX) and gaseous hydrogen (GH₂) as its propellants. These propellants enter the preburner through shear coaxial injector elements (Figure 2). The LOX flows through a central tube that exits into a cup region where it is shrouded by a coaxial flow of high velocity GH₂. An alternative design that is sometimes employed with LOX/GH₂ is the swirl coaxial element in which the central LOX flow enters the element with angular momentum giving the flow a radial component at the element exit to enhance mixing. The objective of this study is to assess the mixture ratio variation that should be expected from the current preburner element and to assess the possible benefits that a swirl element would offer.

In order to isolate the injector effects and to simplify the experiment, it is common practice to characterize injector performance with cold-flow tests using simulants for the fuel and oxidizer. However, most of these tests have been conducted with the elements flowing to open air. It is not possible to simulate realistic conditions unless a high back pressure is imposed at the element exit. Because of this, the ambient back pressure testing may be misleading. Specifically the SSME preburner element has been compared to a swirl element [Ref 1]. Under these test conditions the swirl element produced a superior liquid mass distribution. It is not possible to scale this data to the expected hot-fire conditions because unrealistically high mach numbers are required to produce mass flows that are comparable to the hot-fire conditions. In order to obtain a truly realistic comparison, the experiments need to be repeated at a back pressure of at least 560 psig.

Currently, two high pressure cold-flow chambers are available for use at MSFC. These chambers were designed for another test program and will require some modification. A new manifold system has already been developed in-house to accommodate the SSME preburner element and a comparable swirl element. When tested at ambient back pressure the swirl element generates a far superior liquid mass distribution to that of the shear element. However, at high pressure conditions, it is not known how the elements will compare. Based on the characteristics of their operation, it is expected that the shear element performance will improve and swirl element performance will degrade at high pressure. The shear element

relies on the momentum of the gas to break-up and disperse the liquid stream. At high pressure, the density of the gas increases, allowing high momentum to be achieved at a low mach number. The swirl element uses radial momentum to disperse the liquid. At high pressure, the increase in gas momentum retards the effect of the radial liquid momentum. However, the gas momentum will enhance the liquid break-up. Basically, the difference in mixing efficiency of the two element types will not be as drastic at high pressure. However, it is expected that the difference still be quite significant. A temperature striation of 200 degrees Rankine only requires a mixture ratio variation of approximately 0.13 from a nominal 0.893 value.

Typically, at ambient back pressure the mixing of the liquid propellant is measured directly using a mechanical patternator, which is simply an array of capture tubes positioned downstream of the injector element exit to measure the mass flux distribution. High back pressure tests require a closed pressure chamber. Mechanical patterning is very difficult to integrate into a pressure chamber. Recently, optical methods of measuring mass distribution have been applied with good success [ref. 2].

The technique involves doping the liquid simulant with a small amount of fluorescing dye which is then excited using a laser sheet and mapping the fluorescence. This method will be used and work is ongoing to address the gas phase mixing with nonintrusive measurements

The variation in the element resistance can be measured by simple water flow tests. However, because it is impossible to insure that the LOX post is positioned exactly in the center of the fuel annulus, circumferential variation in mixture ratios occur. Mixing measurements will be made in the high pressure chamber with the LOX post canted to measure the resulting mixture ratio nonuniformity as well as the variation in the overall flow resistance of the element.

An attempt will be made to use the data generated on this program along with the hot-fire data generated at The Pennsylvania State University to anchor CFD models which will allow an overall prediction to be made of the downstream intraelement mixing effect.

References

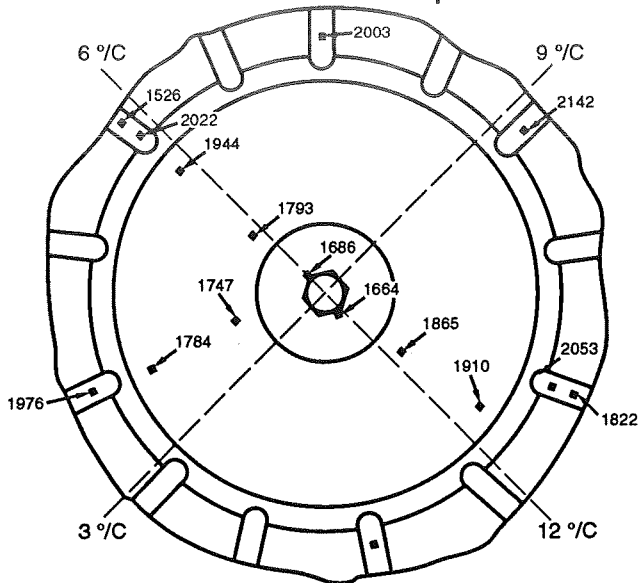
[1] Cox, G.B., "Rocket Engine Injection Element Characterization" , AIAA/SAE/ASME/ASEE 24th Joint Propulsion Conference, Boston , July 1988.

[2] Hartfield, R. J. and Eskridge, R., "Experimental Investigation of a Simulated LOX Injector Flow Field," AIAA/SAE/ASME/ASEE, 29th Joint Propulsion Conference, Monterey, June 1993.

[3] Pal, S., Moser, M.D., Ryan, H.M., Foust, M.J., and Santoro, R.J., "Flowfield Characteristics In a Liquid Propellant Rocket", AIAA/SAE/ASME/ASEE, 29th Joint Propulsion Conference, Monterey, June 1993.

Figure 1

HPFTP Turbine Inlet Dome and Strut Temperature Measurements



HPFTP First Stage Nozzle Temperature Measurements

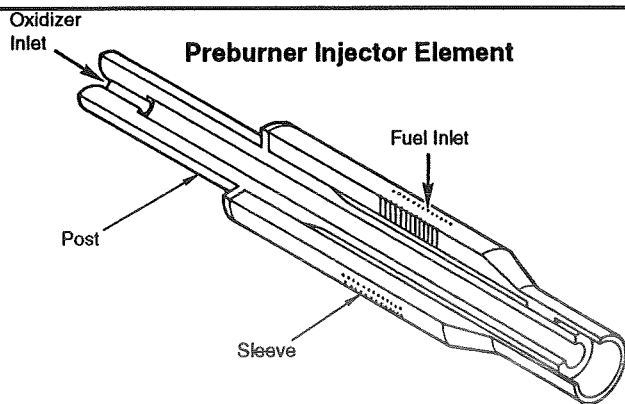
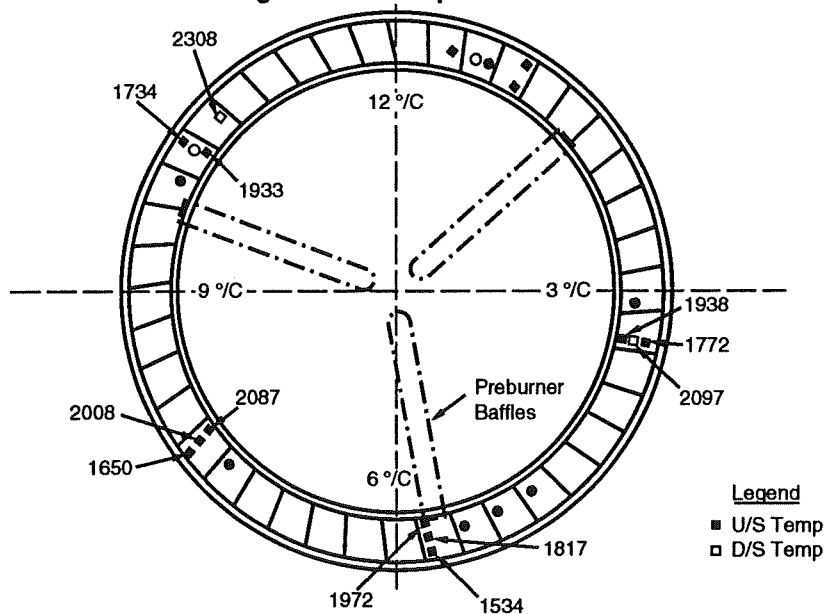


Figure 2

SMALL ROCKET RESEARCH AND TECHNOLOGY

Steven Schneider and James Biaglow

NASA Lewis Research Center

SUMMARY

Small chemical rockets are used on nearly all space missions. The small rocket program provides propulsion technology for civil and government space systems. Small rocket concepts are developed for systems which encompass reaction control for launch and orbit transfer systems, as well as on-board propulsion for large space systems and Earth orbit and planetary spacecraft. Major roles for on-board propulsion include apogee kick, delta-V, de-orbit, drag makeup, final insertions, north-south station-keeping, orbit change/trim, perigee kick, and reboost. The program encompasses efforts on Earth-storable, space storable, and cryogenic propellants. The Earth-storable propellants include nitrogen tetroxide (NTO) as an oxidizer with monomethylhydrazine (MMH) or anhydrous hydrazine (AH) as fuels. The space storable propellants include liquid oxygen (LOX) as an oxidizer with hydrazine or hydrocarbons such as liquid methane, ethane, and ethanol as fuels. Cryogenic propellants are LOX or gaseous oxygen (GOX) as oxidizers and liquid or gaseous hydrogen as fuels. Improved performance and lifetime for small chemical rockets are sought through the development of new predictive tools to understand the combustion and flow physics, the introduction of high temperature materials to eliminate fuel film cooling and its associated combustion inefficiency, and improved component designs to optimize performance. Improved predictive technology is sought through the comparison of both local and global predictions with experimental data. Results indicate that modeling of the injector and combustion process in small rockets needs improvement. High temperature materials require the development of fabrication processes, a durability data base in both laboratory and rocket environments, and basic engineering property data such as strength, creep, fatigue, and work hardening properties at both room and elevated temperature. Promising materials under development include iridium-coated rhenium and a ceramic composite of mixed hafnium carbide and tantalum carbide reinforced with graphite fibers. Component designs to optimize performance indicate that gains of 10 to 20 seconds specific impulse are possible with Earth-storable propellants. Further gains of 5 to 10 seconds are expected with designs which operate at high chamber pressure such that frozen flow losses in the nozzle are minimized and combustion efficiency possibly increases. Components designed for space-storable propellants are expected to provide an additional 15 to 20 seconds specific impulse over Earth-storables due to the more energetic nature of these propellants. Small cryogenic rockets are proposed only for those systems where integration is possible. Systems analyses indicate a significant payload benefit for vehicles with integrated propulsion systems. Both LOX/liquid hydrogen and GOX/gaseous hydrogen are candidate propellants. Tests with GOX/gaseous hydrogen are conducted for materials tests and predictive

technology development as a matter of convenience as well as to supply performance data on these high performance propellants. This program provides the opportunity to study fundamental rocket phenomena in testbed, as well as, prototype engines, not just subscale models, and may be an economical approach to providing subscale data of general value to all rockets.

EARTH STORABLE ROCKET DESIGN, FABRICATION, AND TEST

Small rocket chambers are usually radiation-cooled for simplicity. Radiation-cooled operation, in general, requires extensive fuel film cooling with its associated combustion/performance losses. This design practice reduces chamber temperature and limits thermal soakback to the injector. Small rockets require larger percentages of their fuel for cooling than large rockets because of their larger surface-to-volume ratios. They, therefore, stand to benefit the most from high temperature material technology. Design issues which must be addressed in the use of iridium-coated rhenium for rocket chambers include

- a) thermal management of the high temperature chamber, especially at the injector interface
- b) injector design to minimize oxidizer contact with the iridium
- c) chamber design to accommodate launch induced stresses in heavy annealed material
- d) basic material property data
- e) metallurgical joining techniques for rhenium with other materials

Radiation-cooling of the rhenium chamber is accomplished by the application of a high emissivity coating of dendritic rhenium to the outside surface by CVD. Thermal management of the injector-chamber interface is accomplished through the use of film coolant along with increased thermal resistance or path lengths in the rhenium material. Alternatively, fuel regenerative cooling of the interface is also used. Injectors are designed such that oxidizer momentum is either axial or away from the walls. Iridium has a finite oxidation rate and material loss escalates in the presence of oxidizer and at elevated temperatures. Combustion interactions with iridium is the subject of great uncertainty in the design process. Both liners fabricated from platinum-10rhodium and stainless steel regenerative sections were successfully used to prevent iridium oxidation at the head end of the combustion chamber. At the throat, where temperatures require the use of iridium (melting point 2720 K), increased iridium thickness is the only route to additional life, but lack of oxidation data makes this design purely empirical. Designing the chamber for adequate strength at operating temperature and fatigue life during launch is crucial. The former requires elevated temperature (2200 K) strength, creep, and low cycle fatigue data. The latter requires room temperature strength, fatigue, and work hardening data. These data are presently the subject of considerable contractor and NASA efforts. Designing the chamber to survive the launch loads is accomplished either by using lighter materials such as silicide coated niobium or ceramic composites for nozzle skirts, where temperatures permit, or by increasing material thickness at the throat. Investigations of metallurgical joining techniques required for flight type hardware yielded furnace brazing with Palcusil 25 or Nicro filler metals as a suitable technique. A form of electron beam (EB)

welding called parent metal braze is suitable for joining rhenium to stainless steel. Joining techniques are the subject of continuing investigations.

Performance and life tests of 22, 62, and 440 N thrust class rockets using this technology were conducted with NTO/MMH propellants. Both steady state and pulse testing was performed and thermal management issues were successfully addressed. Performance and life results are shown in the following table.

THRUST CLASS (N)	PROPELLANTS	AREA RATIO	PERFORMANCE (sec)	TOTAL TIME (hr)	CYCLES	COMMENT
22	NTO/MMH	150:1	310	1.7	100,311	100,000 @ 20% duty
62	NTO/MMH	75:1	305	0.2	263	240 @ 10% duty
440	NTO/MMH	286:1	321	6.2	93	
550	NTO/AH	200:1	330			

The Earth storable liquid rocket technology developed to date uses relatively low system pressures compared to recent DOD programs aimed at short lived rockets. A program is currently underway to develop long-life, high-pressure rocket technology which takes advantage of the BMDO investment in high pressure propellant management and industry investment in high pressure tanks. High pressure tests of small rockets will be used to determine their combustion chamber efficiency when designed with high temperature materials. These materials may offer the thermal margin necessary to withstand the increased heat fluxes associated with high pressure rocket chambers, without paying a performance penalty for film cooling. Operation at high pressure also allows a reduction in size of rockets, which is potentially of value to microsatellites.

SPACE STORABLE ROCKET TECHNOLOGY PROGRAM

Efforts to improve the performance of small rockets through the use of more energetic propellants have focused on a class of propellants called space storables. These propellants are those which can be passively stored in space, within mission constraints, without active cooling or refrigeration. Space storable propellant candidates include liquid oxygen (LOX) and hydrocarbon fuels such as liquid methane, ethane, propane, and ethylene. Other candidate fuels are storable on Earth as well as space and include hydrazine and ethanol. Based on system analysis, LOX/hydrazine was chosen for rocket development at TRW using their pintle injector design. In addition, a facility is under construction at LeRC to test LOX/hydrocarbons in the event toxic propellants such as hydrazine fall out of favor. TRW's space storable pintle injector concept is shown in figure 1. LOX is injected as a film along the outside of

the pintle and impinges on hydrazine, which is injected radially outward from slots in the pintle tip. Injector geometry is varied with shims, which alter the injection port geometry of both the fuel and oxidizer. In the initial tests, six fuel geometries were evaluated yielding lower than expected performance. A hybrid design injecting some fuel along the engine axis was then tested with better results, showing that the core flow was oxidizer rich. Tests to date have produced a maximum specific impulse of 346 seconds based on a 200:1 area ratio nozzle. They provide basic engineering information on combustion performance, thermal characteristics, stability, and ignition of LOX and hydrazine. Incorporation of high temperature materials is planned for the next phase of this development program and engine performance is expected to exceed 350 seconds specific impulse.

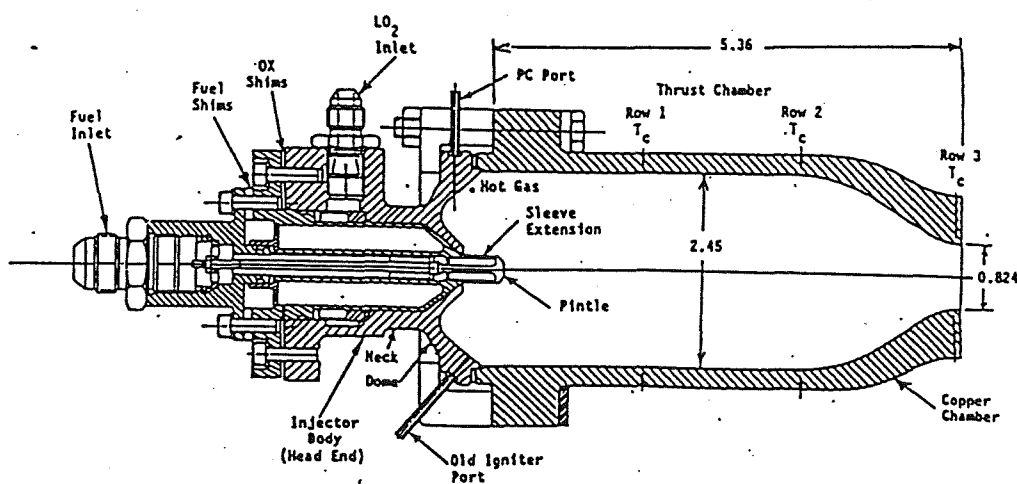


Figure 1. Baseline Injector with Workhorse Thrust Chamber

REFERENCES

- 1) Schneider, S.J., "Low Thrust Chemical Rocket Technology", IAF Paper 92-0669, 43rd Congress of the International Astronautical Federation, Washington, DC, September 1992
- 2) Rosenberg, S.D. and Schoenman, L., "High Performance Bipropellant Engines for Orbit Transfer and Attitude Control Propulsion", IAF Paper 91-249, 42nd Congress of the International Astronautical Federation, Montreal, Canada, October 1991.
- 3) Chazen, M.L., Mueller, T., Casillas, A.R., and Huang, D., "Space Storable Rocket Technology Program, Final Report-Basic Program", NASA-CR-189131, May 1992.
- 4) Chazen, M.L., Mueller, T., and Rust, T., "Space Storable Rocket Technology Program, Final Report-Option 1", NASA-CR-191171, August 1993.

FUNDAMENTAL ROCKET INJECTOR / SPRAY PROGRAMS AT THE PHILLIPS
LABORATORY

D.G. Talley, USAF Phillips Laboratory
OLAC PL/RKFA, 9 Antares Rd.
Edwards AFB, CA 93524-7660

INTRODUCTION

The performance and stability of liquid rocket engines is determined to a large degree by atomization, mixing, and combustion processes. Control over these processes is exerted through the design of the injector. Injectors in liquid rocket engines are called upon to perform many functions. They must first of all mix the propellants to provide suitable performance in the shortest possible length. For main injectors, this is driven by the tradeoff between the combustion chamber performance, stability, efficiency and its weight and cost. In gas generators and preburners, however, it is also driven by the possibility of damage to downstream components, for example piping and turbine blades. This can occur if unburned fuel and oxidant later react to create hot spots. Weight and cost considerations require that the injector design be simple and lightweight. For reusable engines, the injectors must also be durable and easily maintained. Suitable atomization and mixing must be produced with as small a pressure drop as possible, so that the size and weight of pressure vessels and turbomachinery can be minimized. However, the pressure drop must not be so small as to promote feed system coupled instabilities. Another important function of the injectors is to ensure that the injector face plate and the chamber and nozzle walls are not damaged. Typically this requires reducing the heat transfer to an acceptable level and also keeping unburned oxygen from chemically attacking the walls, particularly in reusable engines. Therefore the mixing distribution is often tailored to be fuel-rich near the walls. Wall heat transfer can become catastrophically damaging in the presence of acoustic instabilities, so the injector must prevent these from occurring at all costs. In addition to acoustic stability (but coupled with it), injectors must also be kinetically stable. That is, the flame itself must maintain ignition in the combustion chamber. This is not typically a problem with main injectors, but can be a consideration in preburners, where the desire to keep turbine inlet temperatures as cool as possible can make it advantageous for the preburners to operate as far from stoichiometry as can be tolerated. For some missions such as Single Stage To Orbit, all of the above requirements must be maintained over a throttleable range, for example 5:1 to 10:1. Finally, the injectors must be ignitable during startup where pressures and temperatures are far from design conditions, and ignition transients must be minimized in order to avoid damage to engine components.

In order to satisfy these various constraints, the injector designer must be able to perform design tradeoff studies, and it is important that this be done with minimal time and costs. In fact, it can easily be argued that reducing engine development time and costs is essential to maintaining U.S. competitiveness in space. The Propulsion Directorate of the Phillips Laboratory has invested in a number of programs to advance liquid rocket engine technology, and several of these are directed at improving design tools for liquid rocket injectors. The purpose of the presentation will be to describe some of these latter programs.

OVERALL APPROACH

The overall approach of the design-oriented programs is to first give consideration to fundamental mechanisms, and to initiate programs to study these mechanisms if they are not sufficiently well understood. The results are incorporated into models, and the models are validated using suitable subscale experiments. The validated models are then incorporated into design-oriented CFD codes. This includes efforts to make these codes user-friendly, such as equipping them with graphical user interfaces. Although priority is given to Air Force customers, in many instances the technology developed has broader commercial or other applications, and efforts are made to make the technology available to these other applications where appropriate. The ultimate goal is to reduce engine development time and costs by a factor of two. The overall program is accomplished by a mixture of in-house programs, externally funded programs, and cooperative efforts with other industry, government, and academic laboratories. A representative sample of these is summarized below.

INJECTOR CHARACTERIZATION AT HIGH PRESSURES

Engine development programs have typically had to resort to a large number of expensive large subscale and full scale hot fire tests. Although the need for these cannot be entirely eliminated, cold flow testing is by comparison much cheaper, and useful for providing initial conditions for code predictions, as well as for performing comparative studies of different injector designs. The Phillips Lab injector characterization facility is capable of performing cold flow testing of full scale single injector elements at chamber pressures up to 2000 psi. The injector chamber is equipped with four sapphire windows for optical access, and is supported by an array of optical diagnostics including an Aerometrics phase doppler particle analyzer (PDPA), a Malvern Fraunhofer diffraction instrument, a Greenfield image-based sizing instrument, and the coaxial beam particle analyzer of Grissom [1]. In addition, the vessel is equipped with a 27 element traversable linear patternator for mass distribution measurements. The facility is currently being used to study manifold effects on the atomization characteristics of a single orifice, as shown in Fig. 1. The manifold upstream of the orifice is designed to produce a well characterized turbulent cross flow, and the effects of cross velocity, orifice size, orifice L/D, chamber pressure, and injector ΔP are being studied.

PRIMARY AND SECONDARY ATOMIZATION AND DROPLET COMBUSTION

A number of programs have been directed at improving the understanding of these fundamental mechanisms as they apply to liquid rocket engines. Much of the work has been concerned with the effect of acoustic waves and the ability to couple with combustion instabilities, but steady state effects are also of concern. External programs have used shock tubes to study the effect shock strength and wave shape on liquid jets [2] and droplets [3]. Anderson and Winter [3] have applied the time and sub-micron resolution capability of the Morphology Dependent Resonant (MDR) drop sizing technique to effectively perform instantaneous vaporization rate measurements of droplets behind a shock wave. The results in Fig. 2 show

the diameter decrease in fractions of a micron as a function of time in microseconds for different shock strengths and different fluids. Vaporization rates are shown to increase with increasing shock strengths and more volatile fluids, as expected, and the rates measured are found to be substantially higher than steady state models would predict. These programs compliment an internal program to experimentally study the vaporization and combustion behavior of supercritical droplets. Injection in many liquid rocket engines occurs at pressures exceeding the critical pressure of the propellant. Liquid oxygen, for example, is typically injected at a supercritical pressure, but at a subcritical temperature. It then undergoes a transition to a supercritical state as it is heated in the combustion chamber. The mechanism by which this occurs is not well understood; consequently most rocket CFD codes still use correlations based on subcritical studies. The approach will be to study droplets in free fall in a supercritical environment. Figure 3 shows the droplet generator developed for this project. The generator was designed to produce a monodisperse stream of widely spaced droplets (>100 diameters), using a variety of fluids including cryogenic fluids, at pressures up to 1500 psi. The piezoelectric droplet generator is theoretically capable of operating either in an acoustically excited breakup mode, a drop-on-demand mode, or with a shroud in an aerodynamic stripping mode in the absence of excitation. Most likely operation in a hybrid fashion combining two or more modes will produce the most success. The generator is currently undergoing testing. This project will also use a high pressure acoustic driver developed under an SBIR grant to acoustically excite the droplets. Unlike alternative methods such as using a rotating toothed wheel at the exit of a choked orifice, the acoustic driver is piezoelectrically driven and is capable of operating with no mean flow. Initial tests in a high pressure impedance tube show that sound pressure levels reaching 160 dB (1 atm. ref.) can be produced at 1000 psi. Efforts are underway to increase the output of the driver.

ADVANCED LIQUID ROCKET ENGINE MEASUREMENTS

This program is designed to cultivate recent developments in combustion diagnostics and determine the extent to which they can be "hardened" to apply to more realistic rocket environments, including high pressures and high temperatures. Such techniques would serve to validate codes under more realistic conditions, as well as to provide tools for diagnosing problems that may be encountered during testing. Efforts to date have been largely limited to planar laser sheet Mie scattering, but future efforts will seek creative, innovative approaches to obtain badly needed realistic data.

1. Grissom, W.M., "A Coaxial Beam Drop Sizing Instrument for Dense Sprays," Proceedings of the 5th International Conference on Liquid Atomization and Spray Systems, paper 69, July 1991.
2. Ateshkadi, A., Eastes, T.W., and Samuelson, G.S., "Primary Breakup of a Liquid Jet in a Transverse Shock-Induced Flow," AIAA/SAE/ASME/ASEE 29th Joint Propulsion Conference & Exhibit, paper 93-2335, June 1993.
3. Anderson, T.J., and Winter, M., "Measurements of the Effect of Acoustic Disturbances on Droplet Vaporization Rates," AIAA 30th Aerospace Sciences Meeting & Exhibit, paper 92-0108, January 1992.

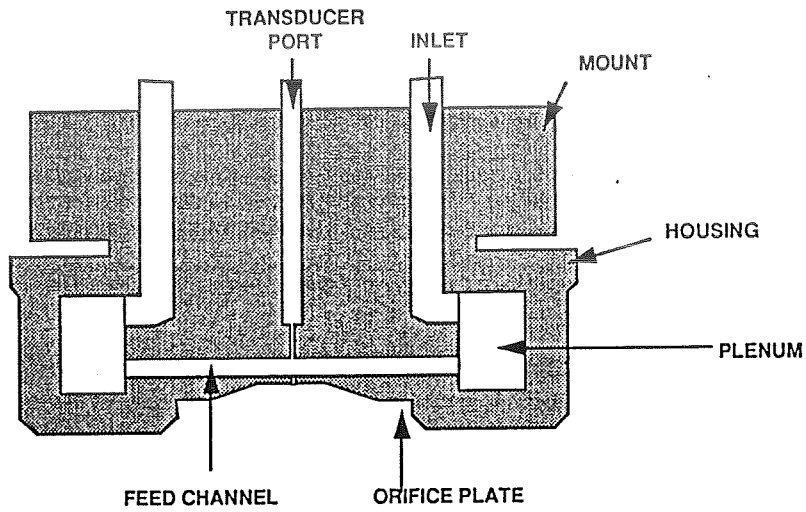


Figure 1.
Apparatus to study the effect of manifold cross flow on an orifice injector.

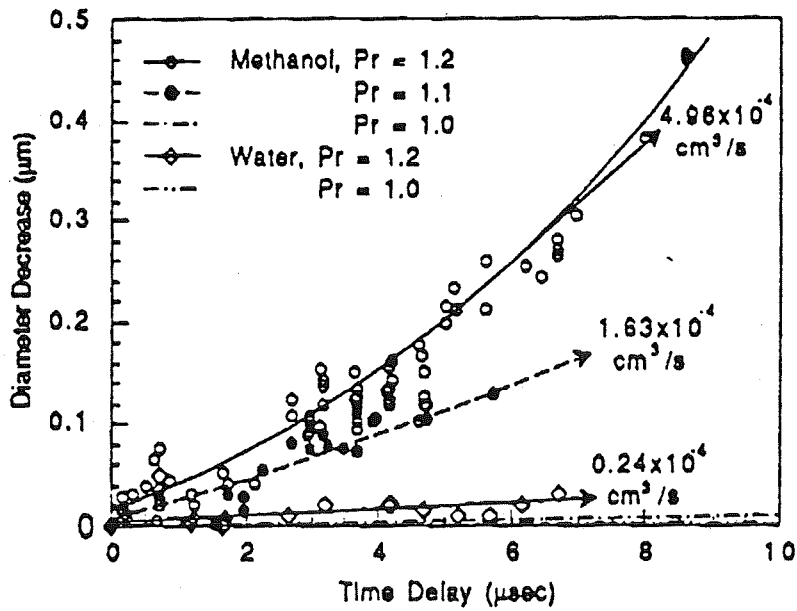


Figure 2.
Droplet vaporization rate measurements behind a shock wave (Winter/UTRC).

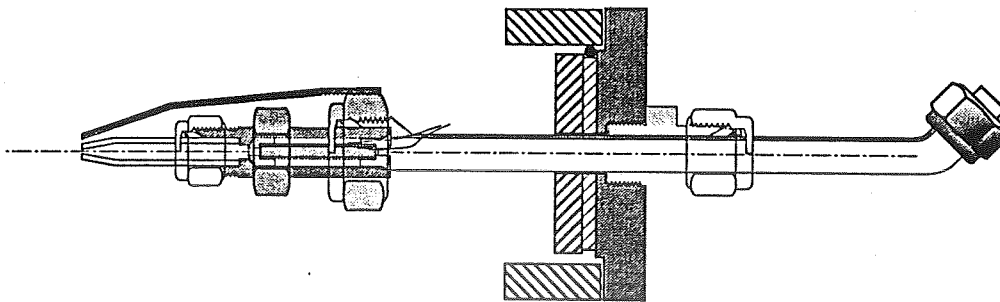


Figure 3.
Hybrid droplet generator for cryogenic fluids at high pressures.

AN EXPERIMENTAL STUDY OF CHARACTERISTIC
COMBUSTION-DRIVEN FLOWS FOR CFD VALIDATION

S. Pal, J. J. Merenich, M. D. Moser and R. J. Santoro

Propulsion Engineering Research Center
and
Department of Mechanical Engineering
The Pennsylvania State University
University Park, PA 16802

SUMMARY/OVERVIEW

The application of laser-based diagnostic techniques has become commonplace to a wide variety of combustion problems (for example, Ref. 1). New insights into combustion phenomena at a level previously unattainable has been made possible by non-intrusive measurements of velocity, temperature, and species. However, due to the adverse conditions which exist inside rocket engines, relatively few studies have addressed these combustion environments.²

The high pressure, high speed, combusting environment in a rocket engine prohibits the application of several measurement techniques. However, in the rocket community, there is a critical need for rocket flowfield data to validate Computational Fluid Dynamic (CFD) codes. Currently at Penn State, there is an effort to obtain flowfield measurements inside a rocket engine. Velocity measurements have been made inside the combustion chamber of a uni-element (shear coaxial injector) optically accessible rocket chamber at several axial locations downstream of the injector. These measurements, combined with future measurements, will provide benchmark data for CFD code validation.

TECHNICAL DISCUSSION

The velocity measurements were made in an optically accessible rocket chamber at Penn State's Cryogenic Combustion Laboratory. This facility is capable of supplying gaseous hydrogen (GH_2) and gaseous oxygen (GO_2) at mass flow rates up to 0.11 kg/s (0.25 lbm/s) and 0.45 kg/s (1.0 lbm/s), respectively. The uni-element rocket chamber used is modular in design and can be easily configured to provide optical access along the chamber length. A cross-sectional view of the rocket assembly is shown in Fig. 1. The rocket chamber is comprised of several interchangeable sections which include the injector assembly, igniter, window and blank sections, and a nozzle assembly. The windows are protected from the hot combustion gases by a gaseous nitrogen (GN_2) curtain purge which flows across the interior window surfaces.

A shear coaxial injector was used to introduce the propellants into the combustion chamber. The nominal mass flow rate of GH_2 through the annulus of the shear coaxial injector was 0.011 kg/s (0.025 lb/s), while the GO_2 mass flow rate through the central tube of the injector was 0.045 kg/s (0.1 lb/s), resulting in an O/F mass flow rate

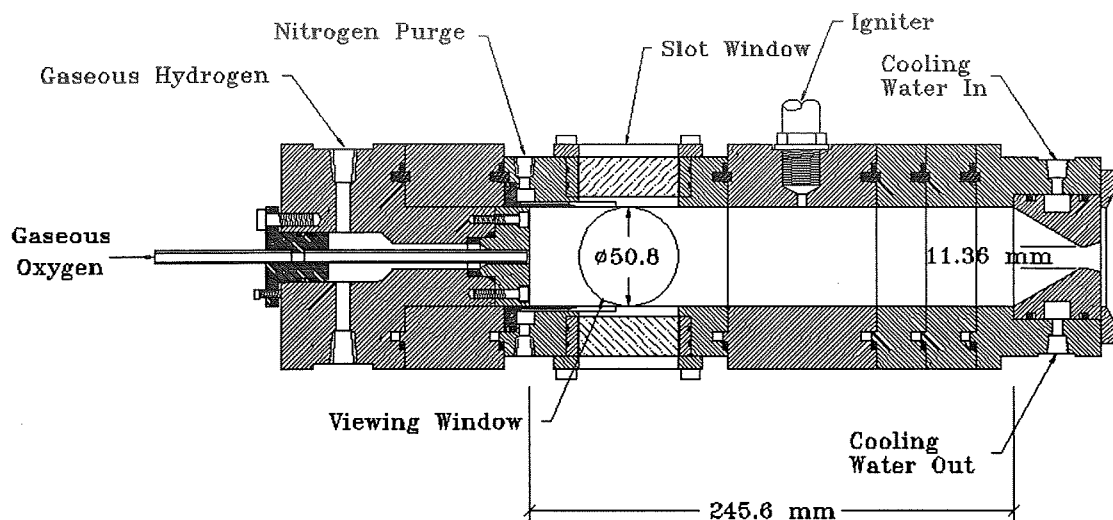


Fig. 1. Cross-sectional view of the optically accessible rocket chamber. The chamber is modular in design and allows for varying the chamber length, injector assembly, window-section location and nozzle assembly. The interior of the chamber is 50.8 x 50.8 mm. For the results presented here, a shear coaxial injector was used. The GO_2 post has an inner diameter of 7.75 mm (0.305 in.) and is not recessed with respect to the injector face. The fuel annulus has an inner diameter of 9.53 mm (0.375 in.) and an outer diameter of 12.7 mm (0.5 in.). The chamber length and nozzle throat diameter are 245.6 mm and 11.36 mm, respectively.

ratio of four. The corresponding mean injection velocities of GO_2 and GH_2 into the rocket chamber were 57 m/s (187 ft/s) and 194 m/s (636 ft/s), respectively. The combination of these mass flow rates with a nozzle having a throat diameter of 11.36 mm (0.447 in.) produced a chamber pressure of 1.31 MPa (190 psia). A rocket firing was four seconds in duration. Velocity measurements were taken from 1.4 to 3.9 seconds into the rocket firing to avoid measuring velocities during the start up and shut down transient periods.

Laser Doppler Velocimetry (LDV) was used to measure the velocity field in the rocket. The LDV system consists of a transmitter and receiver, each of which was inclined at an angle of 15° with respect to the horizontal plane to avoid problems with reflections. A probe volume was formed inside the rocket chamber by splitting an argon ion laser beam ($\lambda = 514.5$ nm) into two beams and focusing them to an intersection. The optics were mounted on translation stages to allow the probe volume to be traversed vertically through the flowfield. In order to reject light from the luminous flame of the GH_2/GO_2 flow, a 10 nm bandpass filter centered around 514.5 nm was placed in front of the receiving optics. Fluidized bed seeders were used to introduce aluminum oxide (Al_2O_3) seed particles into the GH_2/GO_2 flows. A small portion of the main gas flow is diverted into the seeder and flows through a porous plate (this plate traps particles greater than $5 \mu\text{m}$) on which seed particles are placed. This secondary flow entrains seed particles as it exits through the top of the seeder to recombine with the primary flow. The GH_2 and GO_2 flows were seeded individually.

The measured radial velocity profiles, along with the visible flame front, at the three axial measurement locations downstream of the injector face, viz., 25.4, 50.8 and 127 mm (1, 2 and 5 in.), are presented in the three inset graphs in Fig. 2. The radial velocity profile at the closest axial measurement location, 25.4 mm (1 in.), shows that in the shadow of the central GO_2 post of the injector, the mean velocity at the centerline is the same as the injection GO_2 mean velocity, i.e. about 57 m/s (187 ft/s), suggesting that the core of the GO_2 flow has not been affected by shear from the higher velocity GH_2 flow. Only the GO_2 flow was seeded for velocity measurements in this central region. For increasing radial distance in both directions, the mean velocity increases to a peak of about 120 m/s (394 ft/s), and then decreases. For velocity measurements in this outer region, only the GH_2 flow was seeded. The peak velocity is significantly lower than the injection GH_2 velocity (194 m/s) and occurs radially outward from the shadow of the injector's annulus, suggesting that the GH_2 flow is diffusing with radial distance and mixing with both GO_2 and the net outward mass flux of the combustion product, gaseous H_2O . Further inspection of the velocity profile at the 25.4 mm (1 in.) location also shows that in the mixing layer between the two flows, the measured mean velocity at a point differs depending on which flow was seeded. This is a reflection of the unsteady nature of the flame front and will be discussed later.

The radial velocity profile at the middle axial measurement location, 50.8 mm (2 in.), shows that the mean velocity in the central core is still the same as the injection GO_2 mean velocity, i.e. about 57 m/s (187 ft/s); however, here the velocity profile is more uniform suggesting that the wall effects on the turbulent velocity profile from the central GO_2 tube have relaxed with axial distance. Away from the central core, the mean velocity peaks at a maximum of about 80 m/s (262 ft/s) at a greater radial location than for the 25.4 mm (1 in.) axial measurement location, and then decreases with radial distance. Mean velocities at this axial location were measured radially up to about 20 mm (0.79 in.), as compared to about 15 mm (0.59 in.) for the 25.4 mm (1 in.) axial location, showing that the flowfield expands with axial distance. In terms of seeding, seed in the GH_2 flow was sufficient for making mean velocity measurements in the shadow of the central tube. The seed particles can be viewed to represent a passive scalar,³ i.e. the GH_2 flow seeding marks locations where hydrogen is present either as H_2 or H_2O , the combustion product. This indicates that at this axial location, hydrogen in the form of reactant GH_2 or product, gaseous H_2O is present in the central regions of the flowfield. Conversely, radial locations where velocity measurements are made by just seeding the GO_2 flow marks the presence of either GO_2 or gaseous H_2O .

The third velocity profile shown in Fig. 2 is for the 127 mm (5 in.) axial position. Here, the velocity in the central core is still about the same as the mean GO_2 injection velocity. However, unlike the velocity profiles at the other two axial measurement locations, the peak velocity is maximum at the centerline and relaxes with radial distance. Near the wall, the velocity profile shows a small increase from 25 m/s (82 ft/s) at a radial distance of -21 mm (0.83 in.) to almost 30 m/s (98 ft/s) at the next radial location. This is probably due to the nitrogen (GN_2) purge flow at the bottom of the combustion chamber for the slot windows. Note that the entire velocity profile was measured by just seeding the GH_2 flow.

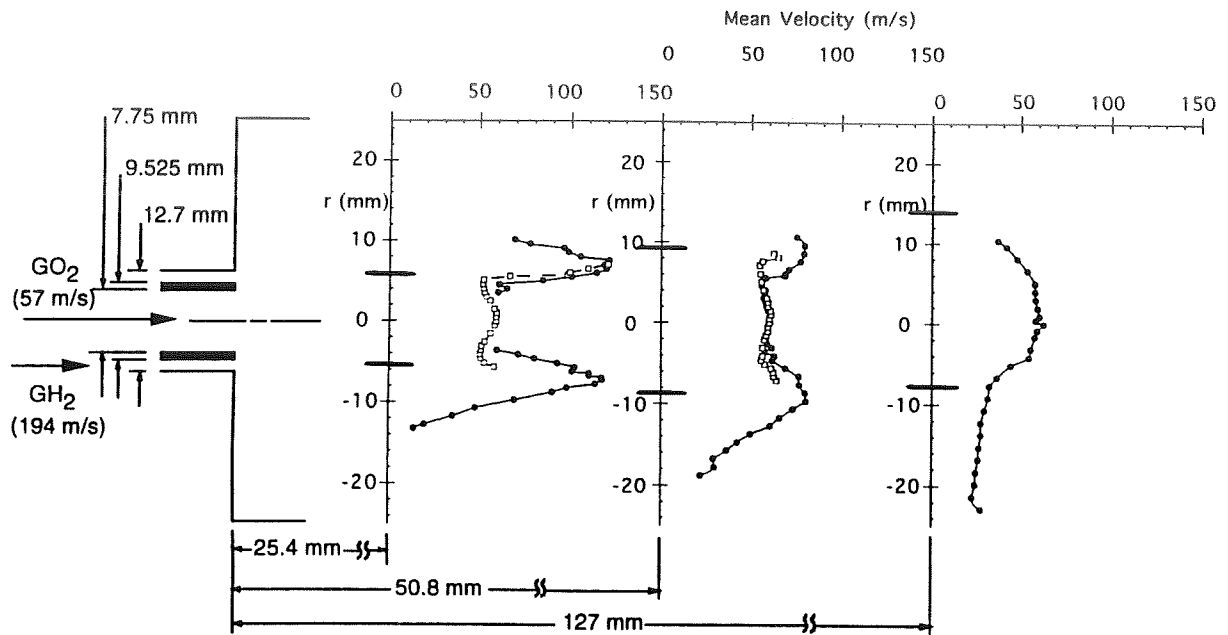


Fig. 2. Mean velocity profile measurements at three axial locations, 25.4, 50.8, and 127 mm (1, 2, and 5 in.), downstream of the injector face. The visible flame front (measured from 35 mm photographs) at each axial measurement location is indicated by the lines marked on the radial axes. The injector housing is also shown for reference. Note that the axial distances are not to scale. The hollow square (\square) and solid circle (\bullet) symbols correspond to GO_2 and GH_2 flow seeding, respectively.

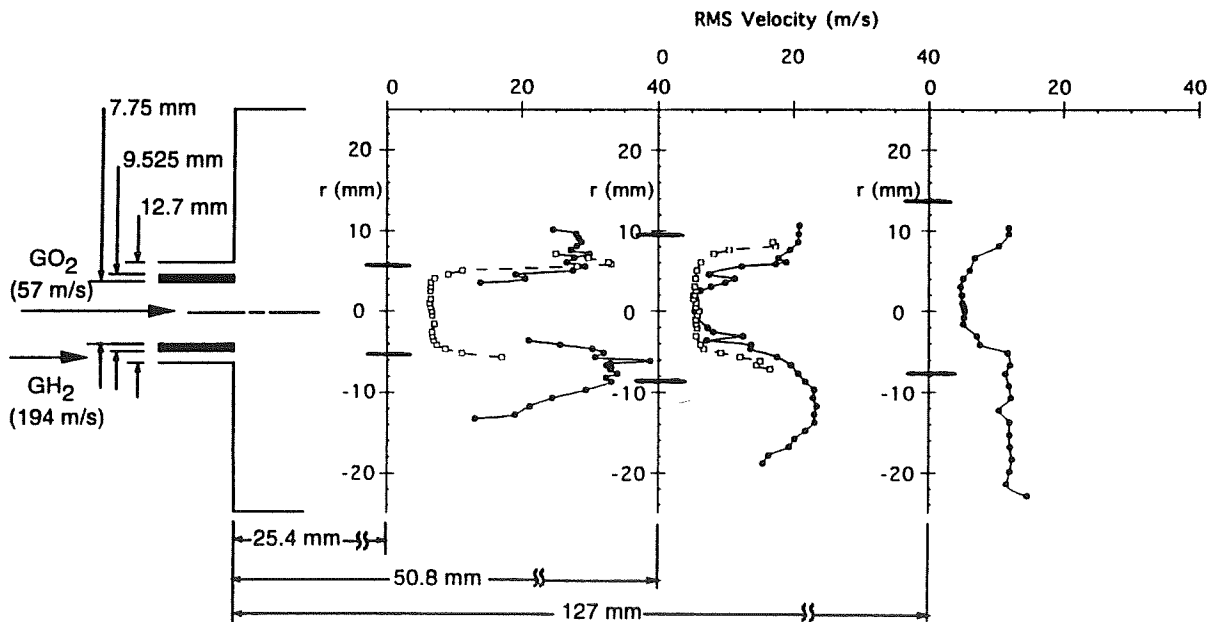


Fig. 3. Root mean square velocity profile measurements at three axial locations, 25.4, 50.8, and 127 mm (1, 2, and 5 in.), downstream of the injector face. The visible flame front (measured from 35 mm photographs) at each axial measurement location is indicated by the lines marked on the radial axes. The injector housing is also shown for reference. Note that the axial distances are not to scale. The hollow square (\square) and solid circle (\bullet) symbols correspond to GO_2 and GH_2 flow seeding, respectively.

The corresponding root mean square (RMS) velocities are plotted in a similar manner in Fig. 3. In the central core, the root mean square velocity is about 6 m/s at all three axial measurement locations yielding a turbulent intensity value of about 0.1, or 10%. Fully developed pipe flow turbulent intensities are about 0.05, or 5%,⁴ indicating that the incoming flow has a higher turbulent energy content and/or the combustion enhances the turbulence levels. In the peak velocity region at the first measurement location, the mean velocity is about 120 m/s (394 ft/s) with a corresponding root mean square velocity of about 30 m/s (98 ft/s) resulting in a turbulent intensity of about 0.25 or 25%. The higher turbulent intensity value here is probably a result of both combustion and the unsteady nature of the flow. A similar value of turbulent intensity is also obtained for the peak velocity region at the second axial location (mean velocity and RMS velocity are 80 m/s (262 ft/s) and 20 m/s (66 ft/s), respectively). At the outer regions of the furthest axial measurement location, both the mean velocity and the RMS velocity drop off in comparison to the other measurement locations; however, the rate of drop off is significantly higher for the mean velocity, resulting in a turbulent intensity of about 0.4 or 40% (mean velocity and RMS velocity are 25 m/s (82 ft/s) and 10 m/s (33 ft/s), respectively).

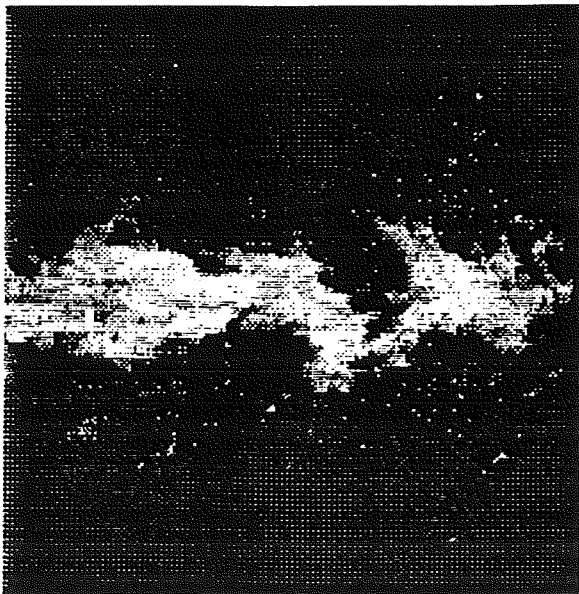


Fig. 4. Image of light scattered from seed particles originally entrained in the GO_2 flow. A laser light ($\lambda=532$ nm) sheet introduced into the rocket chamber was used to illuminate the seed material.

Images were also taken with a CCD camera of the scattered light from the seed particles inside the rocket chamber under conditions in which only the GO_2 flow was seeded. A typical image is shown in Fig. 4. In the figure, white areas represent locations where oxygen is present either as GO_2 or H_2O . The image (and other similar images) clearly shows that the oxygen region does not have smooth edges, but is characterized by highly irregular protuberances. This suggests that the mixing region is characterized by large scale turbulent structures that seem to eject from the central oxygen rich region in a manner analogous to bursts in the near wall region of a turbulent boundary layer. Single point velocity measurements in this type of mixing layer will therefore vary depending on the seeding method, i.e., seed in GH_2 or GO_2 flow, and is observed to be true for the velocity profile measurements described earlier. Similar observations regarding the effects of seeding on velocity measurements have been reported for turbulent diffusion flame studies.⁵

SUMMARY

Initial measurements on the evolution of the velocity field in a rocket-like chamber are reported. These results demonstrate that laser-based diagnostics can be effectively applied to *in-situ* measurements for uni-element rocket chamber geometries. The velocity measurements indicate that the evolution of the reacting flowfield for the shear coaxial flow studied involves a highly unsteady turbulent combusting flow.

Comparisons between the rocket flowfield and turbulent diffusion flame studies conducted at atmospheric pressure conditions indicate that the turbulent intensities and unsteady nature of the flows are similar. Additional velocity measurements, involving two dimensions, as well as other measurements, including temperature and species, will provide a better understanding of this complex combusting flowfield.

ACKNOWLEDGEMENTS

Funding by NASA Marshall Space Flight Center, Contract NAS 8-38862 and the Penn State Propulsion Engineering Research Center, Contract NAGW 1356 Supplement 5, is acknowledged. The authors would also like to thank Mr. L. Schaaf for his assistance in conducting the experiments.

REFERENCES

- [1] Eckbreth, A. C., Bonczyk, P. A. and Verdick, J. F., "Combustion Diagnostics By Laser Raman and Fluorescence Techniques," Prog. Energy Combust. Sci., 5, 1979, p. 253.
- [2] Pal, S., Moser, M. D., Ryan, H. M., Foust, M. J. and Santoro, R. J., "Flowfield Characteristics in a Liquid Propellant Rocket," AIAA 93-1882, AIAA/SAE/ASME/ASEE 29th Joint Propulsion Conference and Exhibit, Monterey, CA, June 28-30, 1993.
- [3] Kennedy, I. M. and Kent, J. H., "Measurements of a Conserved Scalar in Turbulent Jet Diffusion Flames," Seventeenth Symposium (International) on Combustion, The Combustion Institute, Pittsburgh, PA, 1979, pp. 279-287.
- [4] Schlichting, H., Boundary Layer Theory, McGraw Hill Publishing Company, New York, New York, 1979.
- [5] Stepowski, D. and Cabot, G., "Laser Mie Scattering Measurements of Mean Mixture Fraction Density and Temperature by Conditional Seeding in a Turbulent Diffusion Flame," Twenty-Second Symposium (International) on Combustion, The Combustion Institute, Pittsburgh, PA, 1988, pp. 619-625.

NUMERICAL PARAMETRIC STUDIES OF SPRAY COMBUSTION INSTABILITY

by
M.Z. Pindera
CFD Research Corporation
3325 Triana Blvd.
Huntsville, AL 35805

1. INTRODUCTION

It has long been recognized¹ that spray characteristics and droplet vaporization physics play a fundamental role in determining the stability behavior of liquid fuel rocket motors. Such instabilities are generated by in-phase interactions of rocket acoustics with combustion fields. This paper gives some results of numerical parametric studies conducted to investigate the interactions of reacting and non-reacting sprays with acoustic waves. The results were obtained using a multi-dimensional algorithm which couples gas and liquid phase physics. The algorithm includes a new treatment for spray injection through direct solution of equations for the spray producing liquid core. A brief outline of the methodology is given in the next section.

2. TECHNICAL DISCUSSION

2.1 General Approach

The mathematical formulation provides for solution of the interaction between the liquid spray droplets and the surrounding gas. The formulation used in this study is based on a Lagrangian/Eulerian approach. Here, gas phase behavior is treated on a fixed (Eulerian) mesh. Behavior of liquid droplets such as heating, evaporation, and displacement is treated in a Lagrangian manner. Interaction physics is contained in the source terms evaluated during the droplet-phase calculations, and subsequently introduced into the gas-phase formulation.

Droplets are introduced into the computational domain following a separate computation of the liquid jet. Liquid jet equations are solved on a separate grid embedded in the main computational domain. The jet motion and shape depends on a separately specified mass stripping rate, a semi-empirical formulation simulating the atomization process. Droplet sizes are specified using a semi-empirical expression based on linear stability theory. In order to conserve computational effort, droplets are treated as a "droplet cloud" with a number density dependent on the droplet mass and the stripping rate. The liquid droplets are allowed to evaporate and provide a source of fuel to the combustion calculations.

The final results for liquid and gas phases are obtained by combining the Eulerian and Lagrangian calculations using the fractional step technique with operator splitting. Details of the model are given below.

Gas Dynamics

Gas phase equations of motion can be written in the general conservation form:

$$\frac{\partial \mathbf{U}}{\partial t} + \nabla \cdot \mathbf{F}_c - \nabla \cdot \mathbf{F}_d = \dot{S}_{evap} + \dot{S}_{comb} \quad (1)$$

where \mathbf{U} , \mathbf{F}_c , and \mathbf{F}_d represent the conserved variables, and the convective and diffusive fluxes, respectively. The source term vectors \dot{S}_{evap} and \dot{S}_{comb} are due to droplet evaporation and combustion processes, respectively.

Equation (1) is solved using the method of fractional steps where each of the convective, diffusive and source fluxes are solved for separately. The fractional steps are,

$$\frac{\partial \mathbf{U}}{\partial t} + \nabla \cdot \mathbf{F}_c = 0 ; \frac{\partial \mathbf{U}}{\partial t} - \nabla \cdot \mathbf{F}_d = 0 ; \frac{\partial \mathbf{U}}{\partial t} = \dot{\mathbf{S}}_{\text{evap}} ; \frac{\partial \mathbf{U}}{\partial t} = \dot{\mathbf{S}}_{\text{comb}} \quad (2)$$

If each fractional step is solved using a second order scheme, second order accuracy of the complete algorithm can be maintained by using Strang-type operator splitting.² Thus if L_E , L_D , L_{evap} , and L_{comb} are the individual solution operators which advance the solutions through a time increment Δt , the solution at new time level can be expressed as,

$$U^{n+2} = (L_E^{\Delta t} L_D^{\Delta t} L_{\text{evap}}^{\Delta t} L_{\text{comb}}^{2\Delta t} L_{\text{evap}}^{\Delta t} L_D^{\Delta t} L_E^{\Delta t}) U^n \quad (3)$$

Such a solution procedure is widely used in combustion simulations; examples of its application can be found in Oran and Boris.³ Note that first order solution requires only one sweep of the solution operators.

2.2 Liquid Phase Equations

Solution of liquid phase equations forms one fractional step on the overall computational scheme. These equations themselves are solved in fractional steps; the two main ones being formation and transport of liquid jets and spray droplets.

Liquid Core

The liquid core equations are solved on a separate mesh embedded in the main computational domain. Assuming an incompressible flow of liquid with negligible variations in velocity across the thickness, the equations describing the motion of an isothermal liquid core can be cast in the standard conservative form given by:

$$\frac{\partial \mathbf{U}}{\partial t} + \frac{\partial \mathbf{F}}{\partial x} = \dot{\mathbf{S}} ; \mathbf{U} = \begin{pmatrix} h \\ uh \\ vh \end{pmatrix} ; \mathbf{F} = \begin{pmatrix} uh \\ u^2h \\ uvh \end{pmatrix} ; \dot{\mathbf{S}} = \frac{1}{\rho} \begin{pmatrix} \dot{m} \\ \dot{m}u + f \\ \dot{m}v + g \end{pmatrix} \quad (4)$$

Note that the v-momentum equation is independent of the solution for h or u .

The source vector $\dot{\mathbf{S}}$ contains terms due to mass loss \dot{m} caused by stripping of droplets, as well as external forcing functions f and g . Function f represents the effects of axial viscous drag, and g accounts for acoustic forcing caused by sound waves impinging on the liquid/gas jet interface. This formulation temporarily ignores the effects of surface tension and the axial pressure gradient, and introduces a mass stripping rate \dot{m} to account for losses due to droplet production. Both the stripping rate and the resultant droplet diameters are specified using semi-empirical correlations which depend on the local relative velocity, gas and liquid densities, and surface tension.⁴ Figure 1 below illustrates the development of a typical jet.

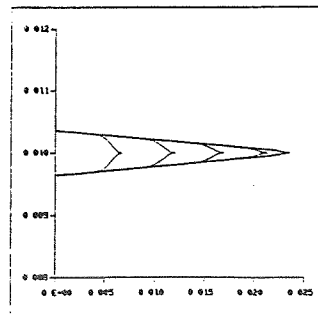


Figure 1. Development Time-History of a Typical Jet. The succeeding profiles are separated by 50 timesteps.

Since Equation (4) is hyperbolic, it may be solved using techniques similar to those employed in the gas-phase fractional step. However, since by ignoring the axial pressure gradient only one characteristic exists for the system, the solution is much simpler.

Given droplets produced by the liquid core, droplet physics are computed using the spray model.

Spray Model

The spray model used in this study is based on the Particle-In-Cell (PIC) formulation first proposed by Crowe *et al*⁵ and used with some variations by Moldavi and Sirignano.⁶ In this approach, the droplet motion and evaporation are found by integrating the individual droplet Lagrangian equations of motion. Determination of source terms denoting droplet-gas exchange of mass, momentum, and energy is subsequently obtained from general balance equations at each computational cell. An extended form of this model accounts for:

- viscous and pressure drag on a droplet, including droplet deformation;
- quasi-steady droplet heatup; and
- quasi-steady vaporization.

This fractional step convects and vaporizes the individual droplets and calculates the gas/liquid interaction source terms which are used in gas-phase calculations. This completes the description of the model.

3. RESULTS

Numerical experiments were performed to determine the effects of various parameters on spray characteristics and combustion response. The parameters included droplet size, stripping rate, spray angle, and chemical kinetics. A sample of the findings is given below.

3.1 Effect of Droplet Size

Droplets are inserted into the computational domain at the left, with initial velocity of 10 m/s. Transverse velocity is chosen at random to give a specified mean spray angle. Figure 2 shows unreacting spray shape and penetration for two drop at time $t = 0.02s$. This corresponds to droplet transit time in an inviscid flow. Note the difference in penetration length of the two sprays.

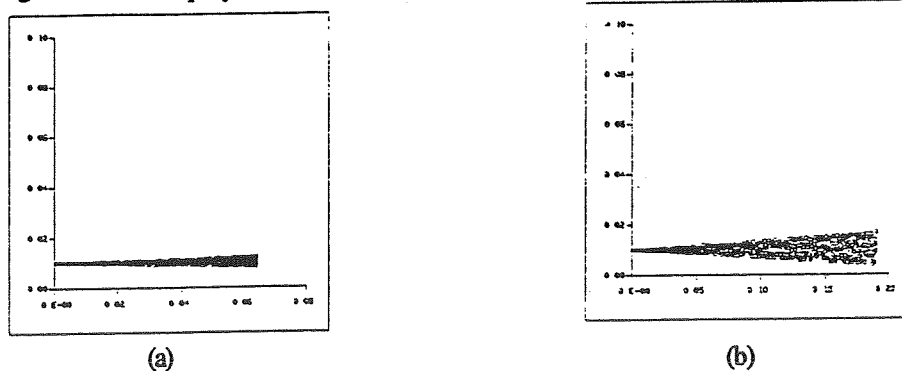


Figure 2. Penetration into Quiescent Medium of Spray Composed of (a) 150 μ drops; and (b) 1500 μ drops

3.2 Spray Formed from a Jet Liquid Core

Liquid core is introduced into the domain at left. The core develops in time until it reaches steady state. At each time step, droplets are stripped from the core and introduced into the domain. Initial drop velocity is that of the core with a random transverse component selected for a specified spray angle. Spray shapes are given in Figure 3 for a 100 m/s jet producing 70 μ drops, at time $t = .001$ s, for three spray angles.

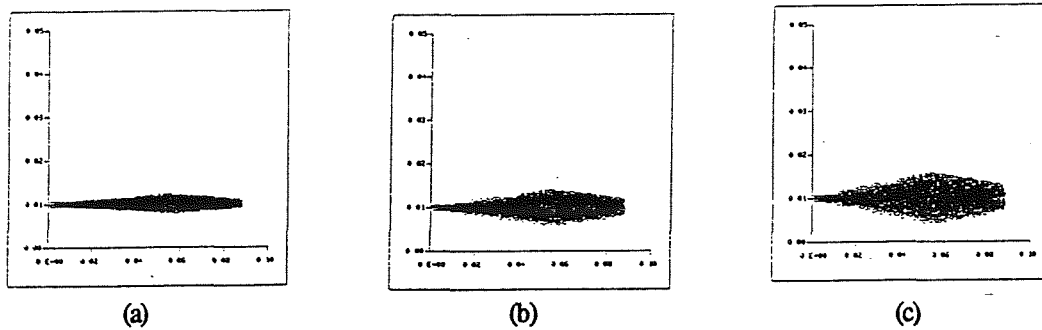


Figure 3. Spray Shape and Penetration for Spray with a Liquid Core for Spray Angles of (a) 2°; (b) 4°; and (c) 6°

Note the presence of the characteristic bulge. In the above calculations, the core extended to .06 m.

3.3 Acoustics-Reactive Spray Interactions

This simulation is similar to that given in 3.2 above, except that the domain is now treated as a resonant tube with a 20% cosine initial pressure perturbation, and the spray is allowed to react. Two reaction mechanisms for hydrogen-oxygen reaction: (a) instantaneous kinetics; and (b) one step finite rate kinetics. In this simulation, liquid oxygen is injected into a hydrogen atmosphere. During the injection, the initial pressure inhomogeneity in the gas phase repeatedly traverses the domain, forms a shock and interacts with the spray. Figure 4 shows the effect of shock interaction of spray and the liquid core.

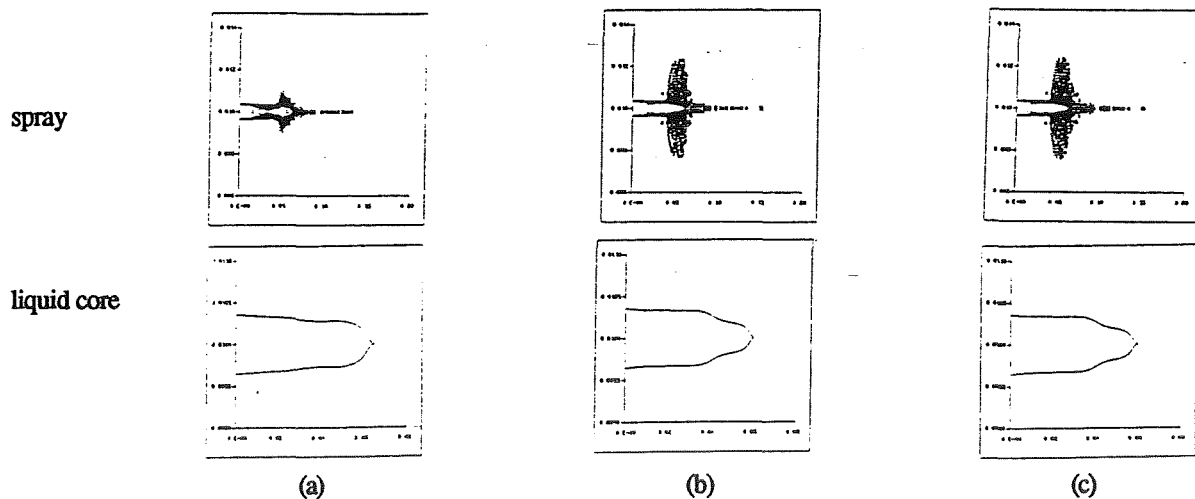


Figure 4. Spray and Associated Liquid Core Profiles for: (a) non-reacting spray; (b) reacting with infinite rate chemistry; and (c) reacting with one step finite rate model

Note the large spray deformations in the reacting case. These deformations are caused by the compressive effects of shock impinging on the spray coupled to the combustion generated expansion process. The figure also indicates the presence of disturbances on the surface of the liquid core.

Figure 5 shows some typical end-wall pressure traces. Along with Figure 4, this figure shows that there is little difference in results for the two simple kinetic models used in this study. A more sophisticated chemistry model is needed to quantify the combustor sensitivity to chemical kinetics.

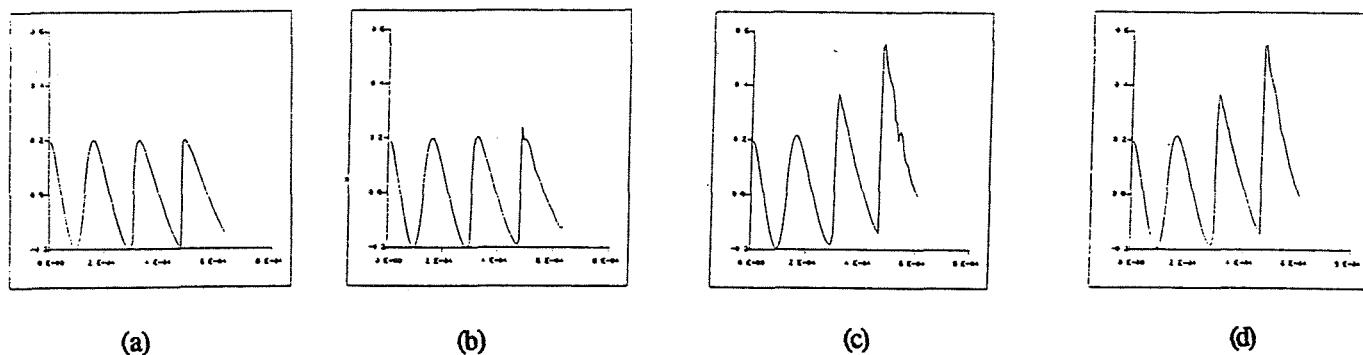


Figure 5. End Wall Pressure Time Histories: (a) base flow (no spray); (b) cold spray; (c) instantaneous kinetics; and (d) one step finite rate kinetics

4. CONCLUSIONS

A coupled numerical algorithm has been developed for studies of combustion instabilities in spray-driven liquid rocket engines. The model couples gas and liquid phase physics using the method of fractional steps. Also introduced is a novel, efficient, methodology for accounting for spray formation through direct solution of liquid phase equations. Preliminary parametric studies show marked sensitivity of spray penetration and geometry to droplet diameter, considerations of liquid core, and acoustic interactions. Less sensitivity was shown to the combustion model type although more rigorous (multi-step) formulations may be needed for differences to become apparent. Numerical studies are now planned to fully quantify these effects.

5. REFERENCES

1. Levine, L.S., COMBUSTION AND PROPULSION, Third AGARD Colloquium, Palermo, March 17-21, 1958.
2. Strang, G., SIAM J. Numerical Analysis, Vol.5, No.3, September
3. Oran, E.S. and Boris, J.P., Elsevier Science Publishing Co., 1987.
4. Sutton, R.D., Shuman, M.D., Chadwick, W.D., NASA CR-129031, April 1974.
5. Crowe, C.T., Sharm, M.P., Stock, D.E., *J. Fluids Eng.*, vol. 99, pp. 325, 1977.
6. Moldavi, K., and Sirignano, W.A., AIAA Paper 88-2856, Presentation at the 24th Joint Propulsion Conference, July 1988.

SPRAY FORMATION PROCESSES OF IMPINGING JET INJECTORS

W.E. Anderson, H.M. Ryan, S. Pal, and R.J. Santoro

Propulsion Engineering Research Center

and

Department of Mechanical Engineering

The Pennsylvania State University

University Park, PA 16802

SUMMARY:

A study examining impinging liquid jets has been underway to determine physical mechanisms responsible for combustion instabilities in liquid bi-propellant rocket engines. Primary atomization has been identified as an important process. Measurements of atomization length, wave structure, and drop size and velocity distribution were made under various ambient conditions. Test parameters included geometric effects and flow effects. It was observed that pre-impingement jet conditions, specifically whether they were laminar or turbulent, had the major effect on primary atomization. Comparison of the measurements with results from a two-dimensional linear aerodynamic stability model of a thinning, viscous sheet were made. Measured turbulent impinging jet characteristics were contrary to model predictions; the structure of waves generated near the point of jet impingement were dependent primarily on jet diameter and independent of jet velocity. It has been postulated that these impact waves are related to pressure and momentum fluctuations near the impingement region and control the eventual disintegration of the liquid sheet into ligaments. Examination of the temporal characteristics of primary atomization (ligament shedding frequency) strongly suggests that the periodic nature of primary atomization is a key process in combustion instability.

TECHNICAL DISCUSSION:

The present study is concentrated on defining the operative mechanisms of combustion instability in rocket engines that use impinging jet injectors. General information regarding the combustion process in rocket engine combustors of all types is also an important byproduct of this research. A review and characteristic time analysis¹ identified the combustion processes of primary atomization, secondary atomization, inter-propellant mixing, and droplet heating and vaporization as potential key mechanisms of combustion instability. Most of the effort to date has centered around an extensive characterization of primary atomization under cold-flow and atmospheric pressure conditions, with recent work emphasizing high-pressure and forced oscillatory conditions. A parallel effort in developing an accurate model of primary atomization is ongoing. More detail of the work can be found in References 1, 2, and 3.

There are two clear reasons for emphasizing atomization at the outset of the study: (1) atomization provides the initial conditions for subsequent combustion processes by its determinant effect on drop size and velocity; and (2) the periodic nature of primary atomization (ligament shedding) has pronounced similarities to combustion oscillations in rocket engines in terms of both frequency range and the way in which the frequencies of both combustion instability and ligament shedding are dependent on injector operational and geometric parameters.

The three classical cases of jet flow, namely fully-developed laminar jet flow, fully-developed turbulent jet flow, and "plug" jet flow have been studied because of their well-characterized velocity and turbulence intensity profiles. Fully-developed laminar flows could be obtained at high Reynolds by carefully contouring the orifice inlet. Absolute plug flow conditions were approached by using orifices with length-to-diameter ratios of five. Orifice length-to-diameter ratios used in practical injectors are typically about three. Undeveloped flows through the short orifices were observed to have either laminar or turbulent characteristics. In addition to changing flow condition and L/d_o , other test parameters varied included half-impingement angle, θ , orifice diameter, and free jet length prior to impingement.

The flow condition of the jet before impingement, i.e., whether it was laminar or turbulent, had the major effect on atomization. To illustrate the importance of the initial conditions of the liquid jet, consider the instantaneous images of the sheets formed by laminar and turbulent impinging jets shown in Fig. 1. These images were taken under quiescent conditions and at atmospheric pressure. Although the jet Reynolds numbers for both the laminar and turbulent cases are similar, the resultant sheets are distinctively different.

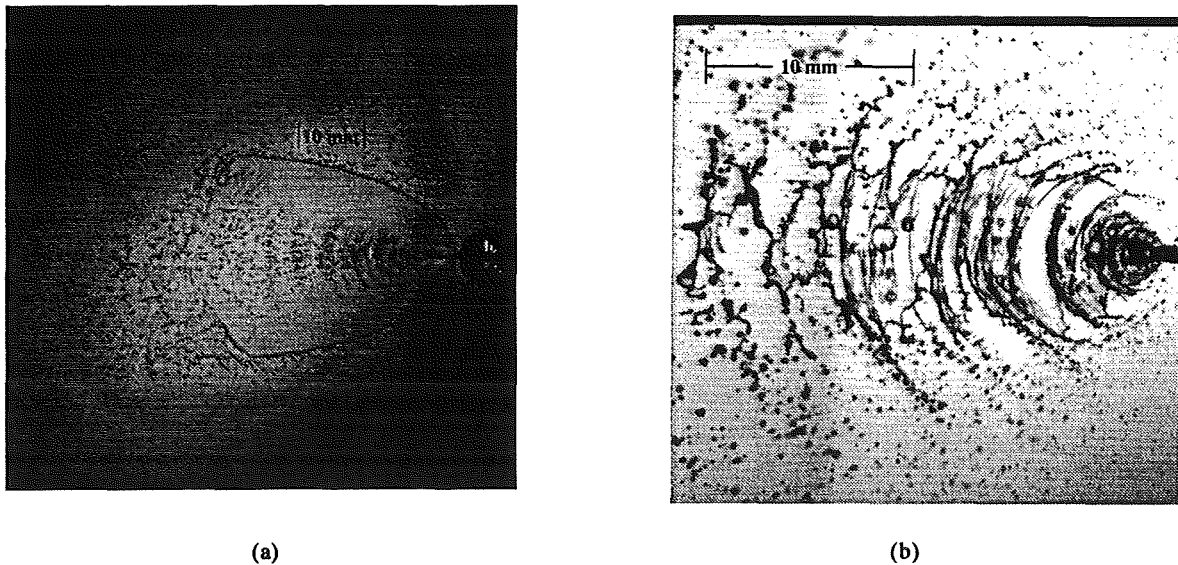


Fig. 1. Instantaneous images of sprays formed by two impinging water jets injected through precision bore glass tubes at full impingement angles, 2θ , of 60° . (a) Resultant sheet formed by two laminar impinging jets emanating from 0.51 mm inner diameter, $L/d_o=375$ tubes. The jet velocity was 13.1 m/s and the jet Reynolds number was 6680. (b) Resultant sheet formed by two turbulent impinging jets emanating from 0.64 mm inner diameter, $L/d_o=80$ tubes. The jet velocity was 12.2 m/s and the Reynolds number was 7810.

In the laminar case, Fig. 1a, small ripples on the surface of the sheet are seen near the impingement point, and after some distance the sheet suddenly disintegrates into droplets. In many of the images of laminar impinging jets, incipient breakup occurred at mid-span of the sheet. Drops are also seen shedding off the edge of the sheet.

In the turbulent case, Fig. 1b, larger waves are apparent at jet impact. Downstream, the sheet disintegrates into ligaments, with incipient breakup consistently occurring at the edges, where the sheet is thinnest. Periodicity is indicated by waves on the liquid sheet and by the spacing between the detached ligaments. Examination of the detached liquid structures reveals irregular liquid shapes that contract into roughly cylindrical ligaments. The cylindrical ligaments appear to contract further into irregularly-shaped drops that will eventually take a nearly spherical shape. The ligament-to-droplet formation process is most likely controlled by surface tension-driven instabilities. The turbulent sheet is not as symmetric as the laminar sheet, and, by comparing upstream and downstream points near the edge of the turbulent sheet there appears to be relatively large-scale displacement of the sheet in the image plane, indicating large scale jet unsteadiness. Examination of opposite edges at the same downstream location leads to the same conclusion regarding asymmetry and large-scale jet unsteadiness. Thus, this phenomena is in all probability three-dimensional.

A mechanistic model of primary atomization that can accurately predict the effects of injector design and operation on breakup length, atomization frequency, and drop size and velocity distributions is critically needed by engine designers. The theoretical model that has been used to date by most researchers in this area^{4,5,6} is based on linear stability analysis of aerodynamically-induced wave growth on the surface of a thinning, viscous liquid sheet. This model can be used to predict breakup length, the periodic structure of breakup, and drop size. Details of our implementation of the model as well as a more detailed comparison with the present experimental results can be found in References 2 and 3.

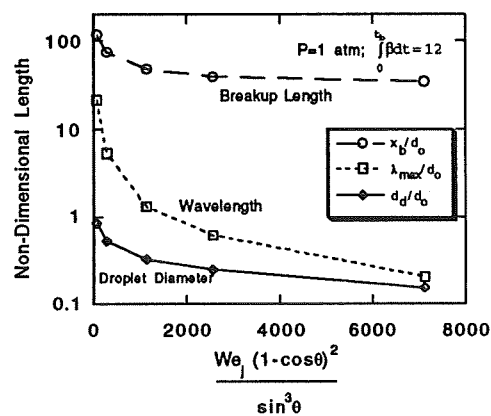


Fig. 2. Non-dimensional lengths as a function of geometrically scaled jet Weber number as predicted by aerodynamic instability model. Lengths normalized by orifice diameter.

In the course of analyzing results from the aerodynamic stability model, a non-dimensional scaling parameter based on the jet Weber number, $We_j = \rho_j v_j^2 d_o / \sigma$, and the half-impingement angle, θ , was identified: $We_j(1 - \cos\theta)^2 / \sin^3\theta$. Use of this parameter collapses the theoretical dependence of breakup length, fastest-growing wavelength, and drop size on orifice diameter, impingement angle, and velocity into a single curve dependent on the scaling parameter. Results from the model are shown in Fig. 2, where non-dimensional lengths, normalized by the orifice diameter, d_o , are plotted against the geometrically scaled jet Weber number.

Experiments were performed at atmospheric conditions using impinging jet injectors made of either precision bore glass tubes or twist-drilled orifices in a brass block. The latter injector unit was also used in experiments at high pressure and under oscillatory conditions forced by an acoustic driver. Length measurements of the intact sheet and of periodic structures were made from images such as

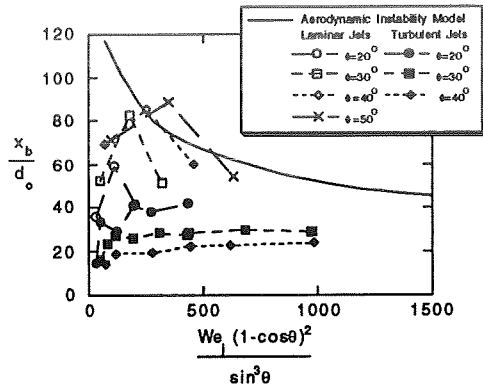


Fig. 3. Non-dimensional breakup length as a function of geometrically scaled jet Weber number. Comparison of measurements with aerodynamic instability model predictions.

breakup shows little dependence on the geometrically scaled jet Weber number. It appears that turbulent impinging jet breakup, which is clearly dependent on orifice diameter and impingement angle, is related to the sheet thickness, which also is determined by orifice diameter and impingement angle.

The measured distance of the separation between periodic structures for turbulent impinging jets normalized by orifice diameter is shown in Fig. 4 as a function of jet velocity. The "wavelength" appears to be primarily dependent on orifice diameter and independent of jet velocity. The observation of independence from jet velocity is contrary to the aerodynamic instability model predictions. The distance between detached ligaments is approximately constant at about four orifice diameters, and the distance between surface wave structures is constant at about two orifice diameters. There was a large spread in the data, with a standard deviation of +/- 35%.

The wavelength data was converted to atomization frequency simply by dividing the jet velocity by the measured wavelength; earlier studies showed that measured drop velocities were nearly equal to the jet velocity.² These atomization frequencies, as well as those obtained by Heidmann et al.⁷ using a different experimental method, are quite similar to the maximum possible combustion instability frequency given by the Hewitt Stability Correlation¹ in that the respective frequencies are linearly dependent on the parameter d_o/v_j and also have a similar magnitude. The similarity between the maximum possible instability frequency as indicated by the stability correlation and atomization frequency as indicated by measurement is significant and suggests that primary atomization is the key process in combustion instability.

The energy release process must certainly be considered in an analysis of combustion instability. In liquid rocket engine combustion, vaporization is the rate-limiting step. The vaporization process is controlled in large by the drop size. Accurate measurements of the drop size distribution are necessary to develop an accurate understanding of the problem of combustion instability. An argon-ion based, two-component Phase Doppler Particle Analyzer

those shown in Fig. 1. Results from breakup length measurements along with comparisons of the measured non-dimensional breakup length with predictions from the aerodynamic instability model are shown in Fig. 3. Again the differences between the turbulent impinging jet case and the laminar impinging jet case are evident. The non-dimensional breakup length of the turbulent impinging jets appears to have some dependence on impingement angle, but appears to be relatively independent of jet Weber number. There is a strong dependence on jet Weber number for the laminar impinging jet case. Laminar impinging jet breakup may be modeled relatively well by the aerodynamic instability model, but again, the turbulent impinging jet

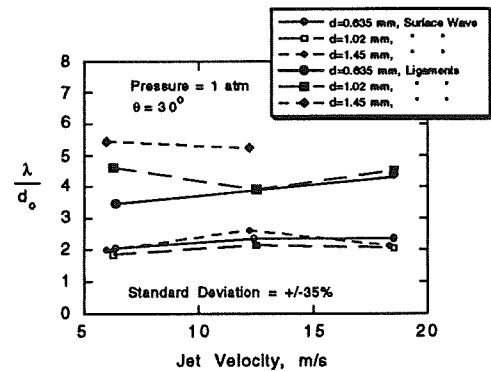


Fig. 4. Measured non-dimensional distance between adjacent surface wave structures and between adjacent ligaments.

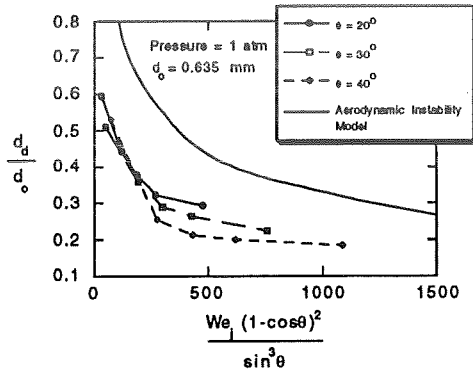


Fig. 5. Non-dimensional drop diameter as a function of geometrically scaled jet Weber number. Comparison of PDPA Measurements with predictions from aerodynamic instability model.

obtained with a correlation coefficient of 0.964: $\frac{d_D}{d_o} = 2.217 \cdot \{We_j f(\theta)\}^{-0.354}$.

Recent experimental work has focused on making spray measurements (e.g., breakup length and drop size/velocity distributions) in a rectangular, transparent acoustic chamber. The interior dimensions of the chamber are 254 mm in width, 305 mm in height and 102 mm in depth. A twist-drilled impinging injector is inserted into the chamber top-plate, while an Altec Lansing compression driver attaches to a chamber side-wall. Use of the compression driver allows for the excitation of the first (1W), second (2W) and third (3W) resonant modes in the 254 mm width dimension of the chamber at frequencies on the order of several thousand hertz under ambient temperature conditions for air and helium environments. These modes and frequencies were chosen because of their similarity to typical rocket instability characteristics. Visual access to the spray field formed by the impinging injector is primarily afforded by two clear plexi-glas side-walls.

Initial measurements of the breakup length have been made within the aforementioned acoustic chamber in a high-pressure environment. Specifically, the spray breakup length was measured from instantaneous images, much like the one shown in Fig. 1b, at chamber pressures of one and nine atmospheres. A plot of the non-dimensional breakup length, x_b/d_o , as a function of $We_g (= \rho_g v_j^2 d_o / \sigma)$ is shown in Fig. 6. The non-dimensional breakup length observed for the twist-drilled injector is quite similar to that of the glass tube breakup length data at a chamber pressure of one atmosphere, despite the fact that the glass tube length-to-diameter ratio is eight times greater than that of the twist-drilled injector. In both cases, the breakup length gradually increases with increasing gas Weber number. Also, the observed breakup length for the twist-drilled injector noticeably decreases with an increase in chamber pressure.

(PDPA) was used for making drop size and velocity measurements. A description of the theoretical and operating principles of the PDPA are given elsewhere.³ Non-dimensional arithmetic mean drop diameters (D_{10}) are presented in Fig. 5 for the turbulent impinging jet case. A comparison of measured D_{10} with the monodisperse drop size predicted by the aerodynamic instability model is also shown. The model predictions match the experimental trend quite well, and, as the model predicts, the measurements collapse into a single curve when plotted against the geometrically scaled jet Weber number. An empirical correlation for normalized drop size as a function of the geometrically scaled jet Weber number, $We_j f(\theta)$, was

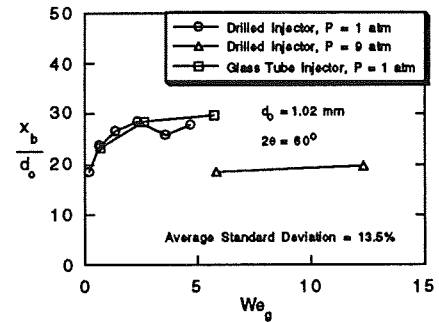


Fig. 6. Non-dimensional breakup length as a function of the gas Weber number and injector type. Breakup length measurements for the twist-drilled injector were taken at pressures of one and nine atm.

Ongoing work is focused on obtaining further drop size/velocity measurements using the Phase Doppler Particle Analyzer for various injector orientations within the acoustic chamber under high-pressure and oscillatory conditions. In addition, work continues on the development of an accurate primary atomization model that is able to account for the important physics occurring at the jet impingement point. After the completion of the high-pressure, acoustic cold-flow atomization and spray characterization studies, future efforts will focus on the initiation of experiments under combusting, high-pressure, and oscillating conditions.

ACKNOWLEDGEMENTS:

Funding for this work was provided by the Air Force Office of Scientific Research, Grant No. 91-0336, Dr. Mitat Birkan, Program Monitor, and by the Propulsion Engineering Research Center, Contract NAGW 1356 Supplement 5. The authors also gratefully acknowledge the help from Mr. Ross Hewitt of Aerojet Propulsion Division, Gencorp, and Mr. Jeffrey Phipps in identifying critical technical issues and initiating this cooperative project with Aerojet.

REFERENCES:

- [1] Anderson, W. E., Ryan, H. M., and Santoro, R. J., "Combustion Instability of Importance to Liquid Bi-Propellant Rocket Engines," 28th JANNAF Combustion Meeting, San Antonio, TX, Oct. 28 - Nov. 1, 1991.
- [2] Anderson, W. E., Ryan, H. M., Pal, S., and Santoro, R. J., "Fundamental Studies of Impinging Liquid Jets," AIAA paper 92-0458, 30th Aerospace Sciences Meeting, Reno, NV, Jan. 6 - 9, 1992.
- [3] Ryan, H. M., Anderson, W. E., Pal, S., and Santoro, R. J., "Atomization Characteristics of Impinging Liquid Jets," AIAA paper 93-0230, 31st Aerospace Sciences Meeting, Reno, NV, Jan. 11 - 14, 1993 (accepted for publication in Journal of Propulsion and Power).
- [4] Couto, H. S. and Bastos-Netto, D., "Modeling Drop Size Distribution from Impinging Jets," J. Propulsion, July-August 1991, pp. 654-656.
- [5] Dombrowski, N. and Johns, W. R., "The Aerodynamic Instability and Disintegration of Viscous Liquid Sheets," Chem. Eng. Science, Vol. 18, 1963, pp. 203-214.
- [6] Brodkey, R. S., Phenomena of Fluid Motions, Addison-Wesley Series in Chemical Engineering, 1967.
- [7] Heidmann, M. F., Priem, R. J. and Humphrey, J. C., "A Study of Sprays Formed by Two Impinging Jets," NACA Technical Note 3835, March 1957.
- [8] Hoover, D. V., Ryan, H. M., Pal, S., Merkle, C. L., Jacobs, H. R., and Santoro, R. J., "Pressure Oscillation Effects on Jet Breakup," Heat and Mass Transfer in Spray Systems, C. Presser and A.K. Gupta (eds.), HTD-Vol. 187, The American Society of Mechanical Engineers, New York, 1991, pp. 27 - 36.

INHERENT STABILITY OF CENTRAL ELEMENT COAXIAL
LIQUID-LIQUID INJECTORS

BY FRANK J. STODDARD
TRW APPLIED TECHNOLOGY DIVISION

Most TRW liquid bi-propellant rocket engines built over the past thirty-plus years have employed a central element coaxial pintle injector and have operated with liquid/liquid propellant injection. This injector is a patented design exclusive to TRW and has unique features that make the rocket engine combustion characteristics different from those of other types of injector engine designs. Its many benefits include excellent combustion performance, efficient deep throttling, adaptability to low cost manufacturing, and high reliability. Approximately 200 pintle injector engines of various sizes and operating on a variety of propellants have been flown without a single in-flight failure.

An especially important feature of the pintle injector engine is its apparent inherent combustion stability. In over thirty years of development, testing and production, TRW has never experienced combustion instability in any of its pintle injector engine designs. This has been true of engines operating over a range of thrust from 5 to 250,000 lbs. on earth-storable hypergolic propellants and a large number of smaller engines operating on a variety of propellants (21 combinations) in long duration-firing, pulsing (down to 2 msec) and deep throttling (as much as 19:1) modes. Operating chamber pressures have ranged from 10 to 3,500 psia.

This record is particularly impressive given that typical TRW design practice does not consider combustion instability as an issue and no pintle engine has ever employed stability-enhancing features, such as baffles or acoustically resonant chambers. In spite of this, TRW engines have operated stably in regimes not possible with other types of injectors.

Various physical explanations and combustion process models for this favorable stability characteristic have been postulated. However, a definitive study that unequivocally establishes the important stabilizing mechanisms still remains to be conducted.

The basic pintle injector concept is illustrated in Figure 1. It consists of a closed cylindrical element that projects into the combustion chamber and has ports machined into the cylindrical surface that allow the center propellant to flow radially into the chamber. The center propellant may be either oxidizer or fuel. The propellant port configurations typically range from discrete primary and secondary jet slots to a continuous gap. Selection of a particular configuration is governed by a number of factors including the propellants to be used, the required combustion chamber wall thermal environment, desired combustion performance, and whether the injector is intended to operate in continuous flow, throttling, or pulsing modes.

The other propellant enters the chamber flowing axially along the exterior of the cylindrical element. Mixing of the propellants occurs where this axial-flowing cylindrical sheet meets the radial flow issuing from the central propellant slots. The genesis of the pintle injector is traceable to the Apollo program. It provided a means to perform deep throttling, needed for a controlled descent to the lunar surface, while maintaining good stable combustion performance and mixture ratio control. Once Apollo got underway, TRW work on the pintle injector

attracted NASA interest and resulted in its selection for the Lunar Module Descent Engine (LEMDE). LEMDE was an ablative-cooled, pressure-fed engine having a maximum thrust of 10,500 lbs. with a chamber pressure of 100 psia and a 10:1 throttling range operating on NTO/A-50 propellants. This engine proved to be very stable throughout the development, qualification and flight phases of the Apollo program. It successfully landed on the moon six times and saved the crew of Apollo 13.

In the mid 1970's, a fixed thrust variant of the LEMDE was produced and designated as the TR201. It flew 75 successful missions as the second-stage engine on the Delta launch vehicle. During the late 1960's and early 1970's, the basic LEMDE concept was scaled up to 250,000 lbs. thrust and operated on NTO/UDMH propellants. In addition, 50,000 lbs. thrust engines were operated on IRFNA/UDMH, LOX/RP-1 and LOX/Propane. Smaller engines having 3000 lbs. thrust were tested on FLOX/LCH₄, FLOX/GCH₄ and FLOX/(LC₃H₈ + LCH₄) propellants. In all cases, explosive-induced disturbances were well damped and no evidence of spontaneous instabilities were observed even under liquid/liquid injection conditions.

In recent years, TRW pintle engines have also operated on gelled hypergolic propellants up to 1500 lbs. thrust and LOX/LH₂ up to 16,400 lbs. thrust. No spontaneous instabilities have been observed in either case. In the LOX/LH₂ tests, both propellants were injected at near normal-boiling point conditions for which conventional injectors are spontaneously unstable. Explosively produced disturbances were found to be well damped in this case.

Our current efforts in this area involve testing a 40,000 lbs. thrust (sea level) LOX/LH₂ demonstration engine at NASA LeRC. Tests are due to start in early September, 1993. Future plans include scaling this engine up to 400,000 lbs. thrust.

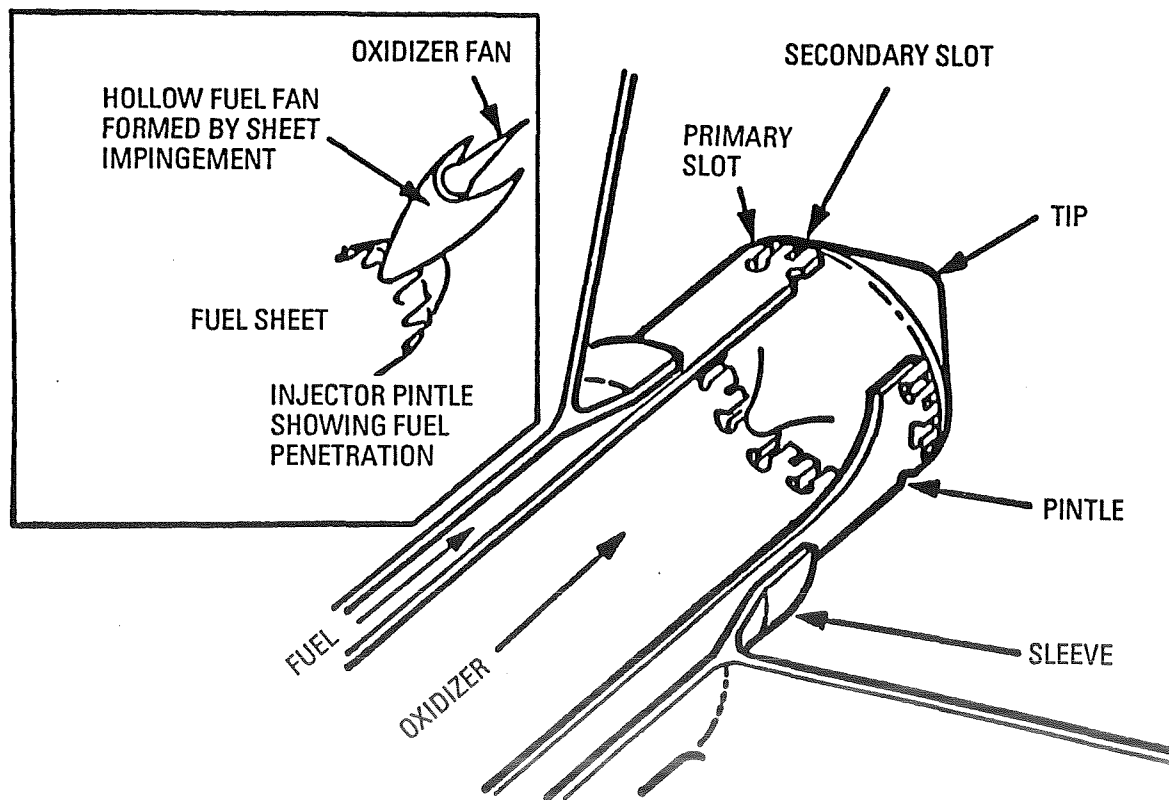


Figure 1. TRW Coaxial Pintle Injector Concept

**AXISYMMETRIC SINGLE SHEAR ELEMENT
COMBUSTION INSTABILITY EXPERIMENT**

Kevin J. Breisacher
NASA Lewis Research Center

SUMMARY

The combustion stability characteristics of a combustor consisting of a single shear element and a cylindrical chamber utilizing LOX and gaseous hydrogen as propellants are presented. The combustor geometry and the resulting longitudinal mode instability are axisymmetric. Hydrogen injection temperature and pyrotechnic pulsing were used to determine stability boundaries. Mixture ratio, fuel annulus gap, and LOX post configuration were varied. Performance and stability data were obtained for chamber pressures of 300 and 1000 psia.

INTRODUCTION

Currently, a rigorous calculation of the combustion stability of a large liquid rocket engine is not feasible. Computationally these calculations are infeasible due to the inherent three dimensionality of the most common instability mode shapes and the fact that flight engines typically contain several hundred injection elements. Parallel computing may offer some hope of resolving this computational dilemma. However, even if sufficient computational resources were brought to bear on the problem, the lack of validated models for atomization, droplet dynamics, and droplet combustion in a rocket combustor environment would still prevent a rigorous solution from being obtained. One of the problems of validating such models for combustion instability is that the majority of existing experimental data is for three dimensional, multi-element geometries. The ability to do "numerical experiments" to develop and validate new models without gross simplifications of the actual phenomena is severely limited by the existing experimental database. Complex multi-element geometries also make it difficult to apply diagnostics to obtain data for model validation. Finally, the cost of obtaining data from multi-element hardware is prohibitive.

TEST ENGINE

The test engine consisted of a single, coaxial injection element and a heat sink chamber (Figure 1). The chamber was 2.055" in diameter and was 18.25" in length from the injector face to the nozzle throat. The chamber consisted of a short injector section, a long main chamber assembly made of Hastalloy, and the throat section. A schematic representation of the engine is provided in Figure 1. The throat diameter was .592" and .296" for 300 and 1000 psia respectively. The chamber was instrumented with an array of seven high frequency, piezoelectric, pressure transducers. Three transducers were located circumferentially around the chamber 1.75" downstream of the injector face. The remaining four transducers were placed axially along the chamber. In addition to the high

frequency pressure transducers, an array of nine static pressure transducers were placed axially along the chamber.

The injection element consisted of a two piece LOX post assembly and a faceplate with an opening for the fuel annulus. The injection element was designed to be modular. Fuel annulus diameter (D_f) could be varied by changing the faceplate. LOX post orifice location and injection tip diameter could be varied by interchanging pieces of the two piece LOX post assembly. Three LOX post configurations were selected for testing (Figure 2.). All three configurations are 9.24" in length and are fed by a 1" diameter dome. This length was chosen so that the resonance of the LOX post would match the resonance of the chamber (approximately 1800 Hz).

LOX post configuration 1 in Figure 2 has a simple .9375" diameter tube with no orifice and was selected for its low LOX side pressure drop. Configuration 2 has a .0625" diameter orifice at the top of the tube. Configuration 2 represents the preferred configuration of engine manufacturers. Configuration 3 which has a .0625" diameter orifice at the bottom of the tube is similar to a design used in the Lewis LOX/H₂ instability test programs of the 1960's.

RESULTS

The most interesting stability behavior of this test program was encountered with configuration 3 (orifice at the bottom of the LOX post) and a fuel annulus diameter of .235". With this configuration, instabilities with amplitudes greater than 10% of chamber pressure were obtained. All of the instabilities encountered with this configuration were spontaneously unstable. The oscillations are present from the beginning of mainstage and persist throughout the run with little frequency shift. This can clearly be seen in Figure 3 which displays the frequency content and relative amplitude (pressure) of the oscillation as the test progresses (time axis). The second harmonic is clearly present and a trace of the third harmonic appears to be present also. To ensure that the two dimensionality of the oscillations was not being corrupted, Tests 286 and 292 were digitized at a sufficiently high rate to resolve the first tangential mode for this combustor (17,100 Hz). There was no indication that a tangential mode of oscillation was occurring.

The waveforms produced by the unstable test cases are fairly complex. For test 286, very pronounced beating occurred. Beating is occurring between oscillations at approximately 1780 Hz and 1858 Hz. These modes probably correspond to the natural modes of the chamber and the LOX post. A higher beat frequency also appears to be occurring and is produced by the first and second harmonics of the chamber oscillation. The oscillations appear to be limit cycle oscillations and do not appear to be very steep fronted. A number of the tests with this configuration had significant oscillation amplitudes but were not classically unstable. Figure 4. shows a plot of oscillation amplitude versus mixture ratio for configuration 3 with a fuel annulus diameter of

.235". Injector pressure drop or hydrogen injection temperature effects are not shown on the plot, resulting in some of the scatter. However, the appearance of distinct operation regimes is clear. In particular, a tuning region between a mixture ratio of approximately 5 to 6 exists in which classic instabilities occur. Retaining the same LOX post configuration but decreasing the fuel annulus diameter to .210" and .205" resulted in generally stable operation. Although an oscillation is present, its amplitude is between 3 and 5 percent of chamber pressure.

Configurations 2 and 3, both with orifices, had very high pressure drops. Eliminating the orifice, and utilizing a straight tube post (configuration 1) lowers the LOX side pressure drop. The tests are generally stable. While the LOX side pressure drop is down, the fuel side pressure drops as a percentage of chamber pressure for the configurations are relatively high (greater than fifteen percent). The only test with an oscillation approaching significant amplitude, also has the minimum fuel side pressure drop. It would have been interesting to test this configuration with a larger fuel annulus gap.

By changing the throat diameter from .592" to .296", tests were run at a nominal chamber pressure of a 1000 psi with the same injection element hardware and propellant flowrates that were used at 300 psi. A chamber pressure of 1000 psi was selected because it is above the critical pressure of pure liquid oxygen. When configuration 3 was run at 1000 psi the tests were very stable. In the majority of tests no organized oscillation is even detectable. It is interesting to note that when configuration 3 was tested at 1000 psi with a fuel annulus diameter of .235", the tests were stable. The same configuration was unstable at 300 psi. It is stable at 1000 psi even though the LOX and fuel side pressure drops as a percentage of chamber pressure are much lower than they were at 300 psi.

Bomb tests were performed during the test program (10 bomb tests are included in the tables). The bomb was triggered one half to one second before the end of a two second duration test. This timing provided ample time for a disturbance to organize and also permitted useful data to be taken before the bomb was triggered. Bomb overpressures ranged from 30 to 120 percent of chamber pressure. None of the bomb tests initiated an instability or altered the strength of an existing oscillation.

COMPUTATIONAL MODELS

A computational model of the test engine was made by modifying the KIVA II computer code.⁴ The LOX tube flow was modeled using the one-dimensional "water hammer" equations. The LOX tube model provided the spray velocity and mass flowrate boundary conditions. The fuel side was modeled using a lumped parameter approach with the property variations during hydrogen temperature ramping being taken into account. The fuel side model provided a velocity boundary condition for KIVA II. A constant mass flowrate was imposed

upstream of the LOX and fuel sides of the injection element. No attempt was made to resolve the atomization process computationally. A "blob" injection model with a droplet size correlation based on the work of Wu and Faeth⁵ and a stochastic breakup model was employed. Results from the model for a stable, ambient temperature test and an unstable low temperature test are presented in Figure 5. The simulation of the high temperature test case exhibits small amplitude pressure oscillations whose frequency content is dominated by the first longitudinal oscillation. The low temperature simulation produces first longitudinal oscillations of an amplitude similar to those obtained experimentally for Test 286. It also appears as if beating is beginning to occur between the first and second harmonics (between 4.5 and 5.5 milliseconds in Figure 5). While the preliminary results look encouraging, the simulation should be carried out for longer than a few milliseconds. The initial goal is to reproduce the stability (and corresponding performance) map shown in Figure 10. with a single droplet size correlation.

CONCLUDING REMARKS

The data obtained in this test program provide a unique set of test cases for the validation of combustion instability codes, particularly CFD based models. Ultimately, it is hoped that validated instability codes could be used to design and predict the stability characteristics of future single element tests, a step on the path to reliable stability design codes for large liquid rocket engines.

REFERENCES

1. Harrje, D. T. and Reardon, F. H., "Liquid Propellant Rocket Combustion Instability", NASA SP-194, 1972.
2. Harrje, D. T., Reardon, F. H., and Crocco, L., "Combustion Instability in Liquid Propellant Rocket Motors", Princeton Univ. Aero. Eng. Rept. No. 216, Nov 1960.
3. Auble, C. M., "A Study of Injection Processes for Liquid Oxygen and Gaseous Hydrogen in a 200-Pound-Thrust Rocket Engine", NASA RM E56125a, Jan. 1957.
4. Amsden, A. A., O'Rourke, P. J., and Butler, T. D., "KIVA II: A Computer Program for Chemically Reactive Flows with Sprays", LA-11560-MS, May 1989.
5. Wu, P. K., Hsiang, L. P., and Faeth, G. M., "Aerodynamic Effects on Primary and Secondary Spray Breakup", First International Symposium on Liquid Rocket Combustion Instability, Pennsylvania State University, University Park, Pa., Jan. 1993.

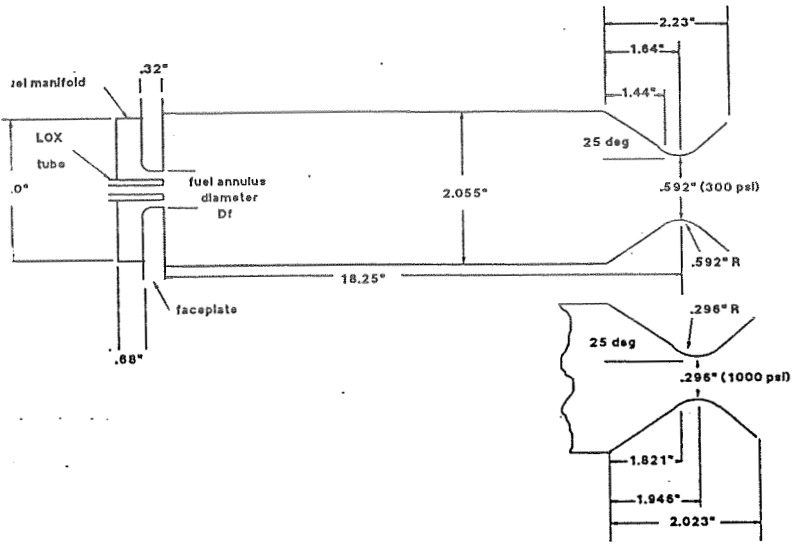


Figure 1. - Schematic Representation of Combustion Chamber Hardware

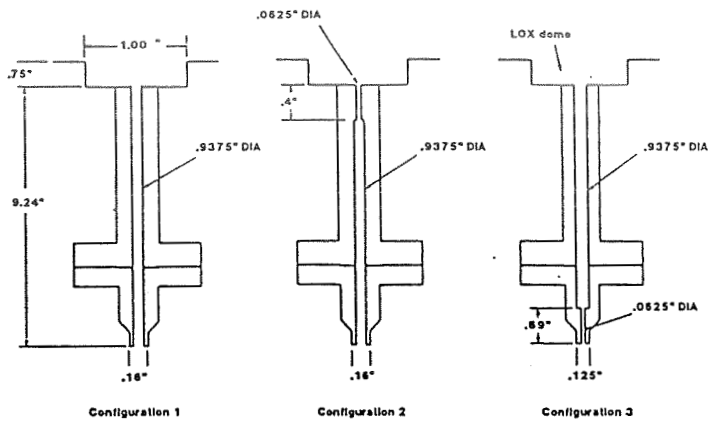


Figure 2. - Schematics of LOX Post Configurations

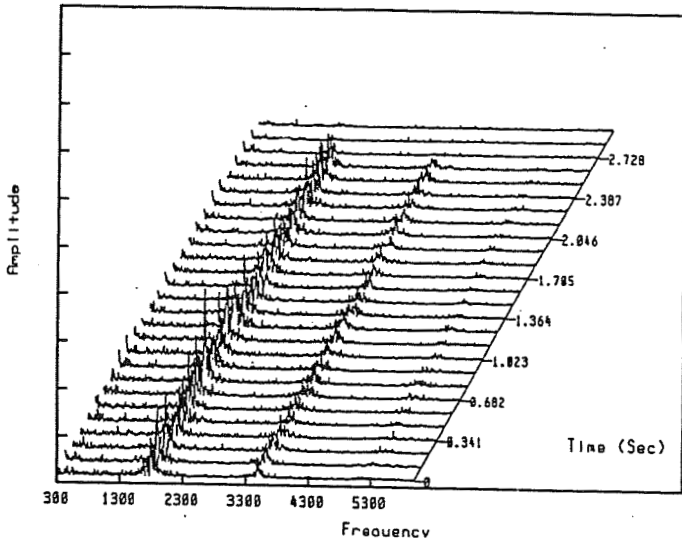


Figure 3. - Cascade Plot of Pressure for Unstable Test 292.

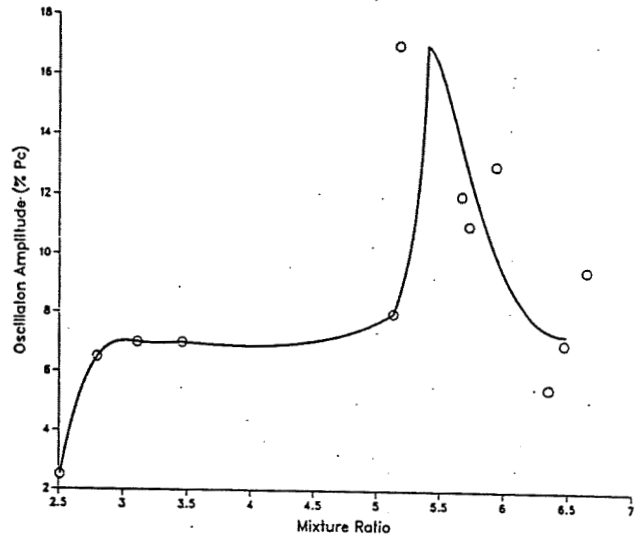


Figure 4. - Variation of Oscillation Amplitude with Mixture Ratio (Configuration 3, $D_f = .235$)

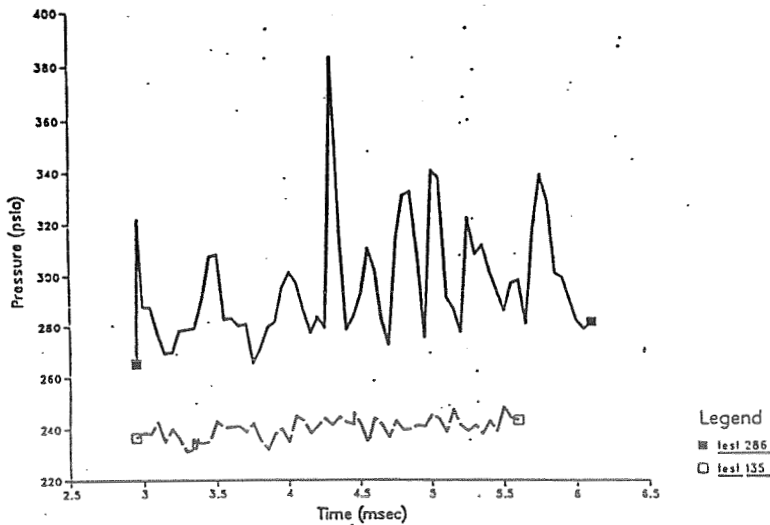


Figure 5. - Computed Pressure Trace for Stable and Unstable Test Cases.

DEVELOPMENT OF A DROPLET BREAKUP MODEL CONSIDERING
AERODYNAMIC AND DROPLET COLLISION EFFECTS

K. L. Wert and Dr. H. R. Jacobs
Propulsion Engineering Research Center
and
Department of Mechanical Engineering
The Pennsylvania State University
University Park, Pa 16802

SUMMARY:

A model is currently under development to predict the occurrence and outcome of spray droplet breakup induced by aerodynamic forces and droplet collisions. It is speculated that these phenomena may be significant in determining the droplet size distribution in a spray subjected to acoustic velocity fluctuations. The goal is to integrate this breakup model into a larger spray model in order to examine the effects of combustion instabilities on liquid rocket motor fuel sprays. The model is composed of three fundamental components: a dynamic equation governing the deformation of the droplet, a criterion for breakage based on the amount of deformation energy stored in the droplet and an energy balance based equation to predict the Sauter mean diameter of the fragments resulting from breakup. Comparison with published data for aerodynamic breakup indicates good agreement in terms of predicting the occurrence of breakup. However, the model significantly overpredicts the size of the resulting fragments. This portion of the model is still under development.

TECHNICAL DISCUSSION:

The work to be discussed here is part of an ongoing numerical study of several aspects of the interaction between transverse acoustic fluctuations and atomized liquid sprays. Therefore it is relevant to the study of combustion instabilities in liquid propellant rocket motors since it is known that these instabilities result from a coupling between the combustion and fluid dynamic processes of the motor and the chamber acoustic resonance modes. It has been conjectured that for a spray subjected to acoustic waves, the displacements of the droplets due to the acoustic velocity fluctuations may have a significant impact on the spray pattern and droplet size distribution downstream of the injector.

In a previous study [Wert (1992)], numerical solutions were obtained for a model of a nonevaporating, pressure-atomized spray subjected to a transverse, one-dimensional acoustic field. This model only examined potential droplet agglomeration. Examination of the results showed an increase in mean droplet size downstream of the injector compared to the same spray injected into a quiescent medium. An issue not addressed in this earlier work, however, is that of possible drop breakup downstream of the near-injector primary atomization zone. Just as acoustic velocity fluctuations were shown to enhance droplet coalescence, therefore increasing droplet size, so too may these fluctuations lead to enhanced droplet fragmentation.

Downstream drop breakup, or secondary atomization, can occur through two processes, both of which

are of potential importance for acoustically perturbed sprays:

1. Aerodynamic breakup where the relative velocity between the drop and the continuous phase is sufficient to fragment the drop.
2. Collision-induced breakup where the energy of the colliding drops is sufficient to fragment the drops.

To examine the importance of these two fragmentation modes, a breakup model is currently under development. When completed, this submodel will be integrated into the overall spray model. Previous efforts to model droplet breakup have focused on only the aerodynamic breakup mode [O'Rourke and Amsden (1987) and Ibrahim et al. (1990).] However, what is clearly needed is a model able to treat both aerodynamic and collision-induced modes. The remainder of this discussion will describe the droplet breakup model in its current state of development and provide some preliminary comparisons with experimental data.

The droplet breakup phenomenon was approached from the standpoint of energy conservation; thus, the analysis began by integrating the differential mechanical energy conservation equation over the volume of a drop of arbitrary shape. The velocity of a fluid element within the drop was then decomposed into two components: a mean velocity, equal to the velocity of the droplet mass center, and a fluctuating component that is nonzero for a deforming droplet. Substituting this decomposition into the energy equation and subtracting out the terms for the mean droplet energy (much like developing the turbulent kinetic energy equation), yielded an integro-differential equation governing the deformation velocity field of the droplet. This equation contains terms related to the temporal variation of the deformation kinetic energy, the surface tension energy generation rate, the dissipated energy due to viscous effects and an energy source term that must be constituted to account for aerodynamic surface forces and droplet collision.

While the energy equation gives a necessary condition that the deformation velocity components must satisfy in order to satisfy mechanical energy conservation, it is not possible to use this equation to solve for the deformation velocity field within the drop. To do this analytically would require the solution of the Navier-Stokes equations subject to the boundary conditions at the drop surface. Clearly a generalized analytical solution is not possible and a full numerical solution of the flow field within each spray droplet is not practical for implementation into an overall spray model. Thus it was necessary to specify an appropriate deformation velocity field. To do this, the droplet was viewed prior to breakup as deforming in one of two fundamental modes:

1. From a sphere to an oblate spheroid. This approximates the flattening of the droplet experienced initially in the aerodynamic breakup mode [Nigmatulin (1991) and Clift (1978).]
2. From a sphere to a prolate spheroid. When fragmentation occurs after the temporary coalescence of two colliding droplets, the droplet initially deforms into a shape much like a prolate spheroid before further deforming into a dumbbell shape and fragmenting [Ashgriz and Givi (1987) and (1989).]

By including both prolate and oblate deformation modes, the model can account for the initial stages of both aerodynamic and collision-induced breakup effects.

A velocity field was subsequently developed which not only satisfies both of the above mode shapes,

but which satisfies incompressible continuity as well. Substituting this field into the deformation mechanical energy equation yielded a second-order, nonlinear ordinary differential equation. This equation governs the temporal variation of the streamwise axis of the spheroid, $2b$:

$$\frac{\rho_d V_d}{10} \left[\left(2 + \left(\frac{a}{b} \right)^2 \right) \frac{db}{dt} \frac{d^2 b}{dt^2} - \frac{3}{2} \frac{a^2}{b^3} \left(\frac{db}{dt} \right)^3 \right] + 4\pi\sigma b S\left(\frac{b}{a}\right) \frac{db}{dt} + \frac{5}{2} \mu_d \frac{V_d}{b^2} \left(\frac{db}{dt} \right)^2 = E_i \quad (1)$$

where ρ_d is the drop density, V_d is the drop volume, $2b$ is the streamwise axis length, $2a$ is the cross-stream drop diameter, σ is the surface tension, $S(b/a)$ is a function of spheroid geometry, μ_d is the drop viscosity and E_i is the energy input source term. From left to right, the terms are: the deformation kinetic energy term, the surface tension energy term, the energy dissipation term and the energy input source term.

The development of a deformation velocity field allowed the explicit evaluation of all the terms of the deformation mechanical energy equation except one, the energy input source term, E_i . This term must incorporate both aerodynamic and collision effects. To evaluate the aerodynamic energy source term required knowledge of the pressure distribution on the droplet surface as a function of spheroid shape and relative velocity. In the paper of Masliyah and Epstein (1970), the authors reported numerically-determined surface pressure distributions at $Re = 1$ and $Re = 100$ for spheroids of various major to minor axis ratios. It should be noted that Reynolds numbers of the order of 100 are typical for sprays. Integration of the vector dot product between the surface pressure force and the surface velocity over the drop surface area yielded the aerodynamic energy input rate. At present, this has been done for the oblate data only ($b/a < 1$) as this is of most concern for aerodynamic-induced breakup. For simplicity, the derived points were correlated by the expression

$$\frac{E_{i,aero}}{\pi a^2 \left(\frac{1}{2} \rho_c U^2 \right) \frac{db}{dt}} = - \left[\left(1.037 - 0.388 \left(\frac{b}{a} \right) \right) f_1 + 0.854 f_2 \right] \left(\frac{Re}{6} \right)^{-0.11} \quad (2)$$

where $E_{i,aero}$ is the aerodynamic energy input term, ρ_c is the continuous phase density and U is the relative velocity while f_1 and f_2 are unit step functions such that $f_1=1$ for $b/a > 0.5$ and $f_2=1$ for $b/a < 0.5$. The Reynolds number is based on the cross-stream diameter, $2a$. Equation 2 correlates the data to within 2 % for the points at $Re = 100$. Note the weak Reynolds number dependence. The strongest dependence is on the spheroid geometry manifested through the axis ratio, b/a .

Equation 1 governs only the lowest-order deformation mode of a droplet prior to breakup. The final stages of droplet fragmentation are dominated by the development of higher-order modes (e.g. the dumbbell-shaped breakup of a droplet formed by two colliding droplets.) The reader is referred to Nigmatulin (1991) for a discussion of the various aerodynamic breakup modes. Since analytical treatment of these higher order modes was not desired for the sake of simplicity, the conditions under which a droplet fragments were specified in terms of a critical deformation energy level of the modeled fundamental modes. It is postulated that a single

critical deformation energy level for breakup exists for both collision and aerodynamic-induced breakup.

To estimate this critical energy level, the binary fuel droplet collision data of Ashgriz and Givi (1989) was used. In their work, the authors observed collisions of pairs of fuel droplets having various relative velocities and relative sizes. The critical energy level for breakup was derived by applying an energy balance to the test case in which the droplets just had sufficient relative velocity such that the droplet formed from the coalesced pair fragmented. From this energy balance, it was possible to derive the critical dimensionless energy:

$$\frac{E_{d,crit}}{\sigma D_o^2} = 1.48 \quad (3)$$

Here $E_{d,crit}$ is the critical deformation energy, which comprises the deformed kinetic and surface tension energies. This energy is nondimensionalized by the product of the drop surface tension and the square of the spherical diameter of the fragmenting drop, D_o .

Together, equations 1, 2 and 3 form the basis for predicting whether aerodynamic-induced breakup will occur. As a test, the model predictions were compared with droplet breakup data available in the literature. In the recent work of Hsiang and Faeth (1992), the authors conducted experiments on the properties of drop deformation and secondary breakup for shock wave initiated disturbances. To recreate the shock condition in the model, a step velocity change was specified. Noting that equation 1 is a second-order equation, the two specified initial conditions were that the drop was initially spherical and that it possessed no deformation kinetic energy ($b = 0$ and $db/dt = 0$, respectively.) Equations 1 and 2 were solved numerically using Heun's method. Care was taken to ensure a time step independent solution.

The model was used to determine what step change in velocity was necessary to bring about droplet breakup. This was done for several of the fluids considered by Hsiang and Faeth. Figure 1 shows the critical Weber number, $\rho_c U_o^2 D_o / \sigma$, necessary to bring about breakup of the drop as a function of the Ohnesorge number, $\mu_d / (\rho_d D_o \sigma)^{0.5}$ where U_o is the imposed step velocity change. The Ohnesorge number is a measure of the ratio of liquid viscous forces to surface tension forces. The points are the predictions of the model while the solid line is from the data presented by Hsiang and Faeth (1992), which includes data from past studies. For We above the line, the droplet is predicted to fragment; however, for We below the line, the drop merely undergoes deformation and oscillation. The model reasonably predicts the variation in the critical Weber

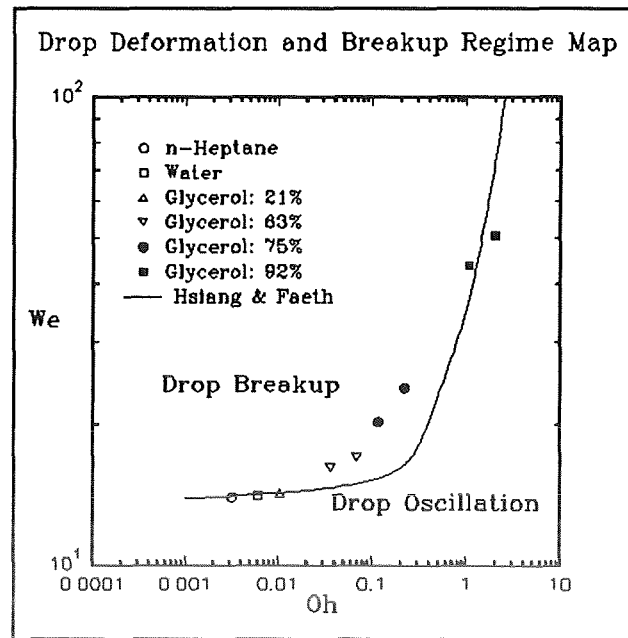


Figure 1. Deformation and breakup regime map.

number with increasing drop viscosity effects. The worst agreement is around $Oh = 0.2$, where the model predicts a critical We that is about 40 % high. It should be noted, however, that for sprays $Oh \leq 0.01$ is expected. For this range the agreement between the model and experimental data is excellent. Since the critical breakup energy was derived from considerations of drop collision data, its success in predicting aerodynamic breakup lends support to the hypothesis that, at least for small effects of viscosity, the critical breakup energy applies equally well to both collision and aerodynamic-induced fragmentation.

Having found the model able to adequately predict the occurrence of aerodynamic breakup, it was necessary to prescribe a method for predicting the outcome of breakup. For this, the simple energy balance method recommended by O'Rourke and Amsden (1987) and Ibrahim et al. (1990) was used. In this method, the deformation energy of the droplet (both kinetic and surface tension energy) is equated to the surface energy of a monodisperse group of spherical droplets. Thus the deformation energy is converted into surface energy of the fragments. Performing this energy balance allows the prediction of the size of the fragments, which is taken to be the Sauter mean diameter, SMD, of the fragments.

The results of using this method are shown in figure 2. The points are the model predictions, the solid line is the best-fit line provided by Hsiang and Faeth (1992) and the dashed lines represent the spread in their data. Examining figure 2 it is seen that the model predicts the trend of the data quite well, but significantly overpredicts the size of the SMD resulting from breakup. This was not unexpected. Recall that the oblate spheroid deformation model treats only the initial stages of droplet deformation. The higher-order deformation modes that ultimately lead to breakup are neglected in favor of the critical energy criterion of equation 3. Thus the model neglects the energy that enters the droplet through the aerodynamic forces acting on the higher-order deformation modes. It is believed that the neglect of this energy, which would be available to generate additional droplet surface area thus producing smaller fragments, is the source of the overprediction of the SMD. An attempt to account for the energy that enters the droplet as a result of these higher-order modes is under development.

Work that remains to be done on the model includes the derivation of E_i for droplet collision, further comparison of model predictions with available experimental data and integration of the breakup model into the larger spray acoustics model.

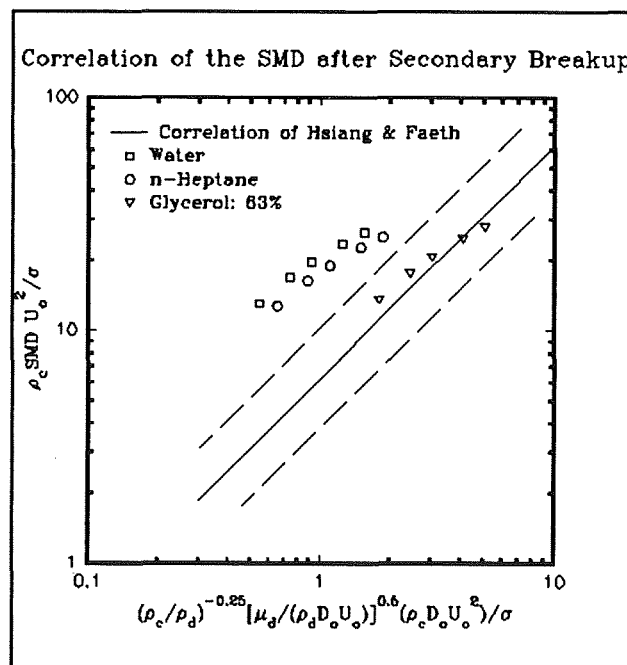


Figure 2. Correlation of the SMD after breakup.

CITED REFERENCES:

Ashgriz, N. and Givi, P., 1987. "Binary Collision Dynamics of Fuel Droplets," Int. J. of Heat and Fluid Flow, Vol. 8, No. 3, pp. 205-210.

Ashgriz, N. and Givi, P., 1989. "Coalescence Probabilities of Fuel Droplets in Binary Collisions," Int. Comm. Heat Mass Transfer, Vol. 16, No. 1, pp. 11-20.

Clift, R., 1978. Bubbles Drops and Particles, Academic Press.

Hsiang, L.-P. and Faeth, G. M., 1992. "Near-Limit Drop Deformation and Secondary Breakup," Int. J. Multiphase Flow, Vol. 18, No. 5, pp. 635-652.

Ibrahim, E. A., Yang H. Q. and Przekwas, A. J., 1990. "Modeling of Spray Droplets Deformation and Breakup," ASME Fluids Engineering Division, Vol. 99, pp. 475-479.

Masliyah, J. H. and Epstein, N., 1970. "Numerical Study of Steady Flow Past Spheroids," J. Fluid Mech., Vol. 44, part 3, pp. 493-512.

Nigmatulin R. I., 1991. Dynamics of Multiphase Media, Hemisphere Publishing Corporation.

O'Rourke, P. J. and Amsden, A. A., 1987. "The Tab Method for Numerical Calculation of Spray Droplet Breakup," SAE Paper 872089.

Wert, K. L., 1992. Drop Agglomeration in an Atomized Spray Subjected to a Transverse Acoustic Field, Applications to Combustion Instabilities in Liquid Propellant Rocket Motors, M.S. Thesis, The Pennsylvania State University.

DEVELOPMENT OF A COMPUTATIONAL TESTBED FOR NUMERICAL SIMULATION OF COMBUSTION INSTABILITY

Jeffrey Grenda*, Sankaran Venkateswaran†, Charles L. Merkle‡

Propulsion Engineering Research Center

and

Department of Mechanical Engineering

The Pennsylvania State University

University Park, PA 16802

SUMMARY:

A synergistic hierarchy of analytical and computational fluid dynamic techniques is used to analyze three-dimensional combustion instabilities in liquid rocket engines. A mixed finite difference/spectral procedure is employed to study the effects of a distributed vaporization zone on standing and spinning instability modes within the chamber. Droplet atomization and vaporization are treated by a variety of classical models found in the literature. A multi-zone, linearized analytical solution is used to validate the accuracy of the numerical simulations at small amplitudes for a distributed vaporization region. This comparison indicates excellent amplitude and phase agreement under both stable and unstable operating conditions when amplitudes are small and proper grid resolution is used. As amplitudes get larger, expected nonlinearities are observed. The effect of liquid droplet temperature fluctuations was found to be of critical importance in driving the instabilities of the combustion chamber.

TECHNICAL DISCUSSION:

Current understanding of liquid rocket combustion instability has been obtained through the implementation of two primary tools: experimental investigations and analytical models. Computational capabilities have recently advanced to the point where they provide a third potential investigative tool to complement these existing approaches. The dramatic progress in the field of computational fluid dynamics (CFD) over the past decade has demonstrated the ability to model highly complicated flow phenomena typical of combustion chambers. CFD methods offer a promising methodology to model not only the important subprocesses such as atomization and vaporization, but also to directly simulate and accurately capture the acoustical physics of the combustion chamber.

Research directed towards developing computational instability models for liquid propellant engines has been undertaken in several research groups. Early work using computational fluid dynamics in studying combustion instability was performed by Habiballah *et al.* [1] and Liang and Ungewitter [2], and followed later by Bhatia and Sirignano [3], Jeng and Litchford [4], Kim *et al.* [5], Wang *et al.* [6], as well as the current authors [7]. Typical results using these time-marching approaches have found that droplet size, mixture ratio, and mean chamber conditions are important physical parameters. Due to computational restrictions, most analyses have considered axisymmetric or

*Graduate Research Assistant

†Research Associate

‡Distinguished Alumni Professor

annular geometries, although some preliminary three-dimensional results for a thin or “collapsed” combustion zone have previously been reported by the current authors [7].

The current work develops a computational testbed for modelling a distributed vaporization zone by coupling CFD with available empirical and semi-empirical models of the dominant subprocesses in rocket engines. These solutions are then compared with closed-form analytical solutions to verify their accuracy. Although the solution of the unsteady, three-dimensional fluid dynamic equations is straightforward in principle, the required computational resources limit the quantity of solutions that can be obtained. This is the motivation for providing companion analytical procedures, which may be performed in a significantly more efficient manner. This approach permits important trends in relevant physical variables to be identified rapidly while simultaneously allowing a systematic assessment of the numerical issues involved.

The unsteady Euler equations are used to describe the fluid dynamics of the three-dimensional gas phase flowfield within the combustion chamber. Due to the substantial computational cost associated with finite difference solutions of the three-dimensional unsteady equations, a mixed character finite difference/spectral method is employed to decompose the primary variable Q in the circumferential direction into a Fourier series. The vector Q is given as a truncated series $Q = \sum_{m=0}^M [\hat{Q}_{m,c}(x, r, t)\cos m\theta + \hat{Q}_{m,s}(x, r, t)\sin m\theta]$ where $\hat{Q}_{m,c} = (\hat{\rho}_c, \hat{\rho}u_c, \hat{\rho}v_c, \hat{\rho}w_c, \hat{e}_c, 0, 0, 0, 0, 0)^T$ and $\hat{Q}_{m,s} = (0, 0, 0, 0, 0, \hat{\rho}_s, \hat{\rho}u_s, \hat{\rho}v_s, \hat{\rho}w_s, \hat{e}_s)^T$ are time-dependent functions of both the axial and radial finite-difference directions. A general equation governing the dynamics of the flowfield development in Fourier space can then be written as

$$\frac{\partial \hat{Q}_{m,T}}{\partial t} + \frac{\partial \hat{E}(\hat{Q}_{m,T})}{\partial x} + \frac{1}{r} \frac{\partial \hat{F}(\hat{Q}_{m,T})r}{\partial r} = -\frac{m}{r} \hat{G}(\hat{Q}_{m,T}) + \frac{1}{r} \hat{H}_{tot}(\hat{Q}_{m,T}) \quad (1)$$

where the vectors \hat{E} , \hat{F} , \hat{G} , and \hat{H}_{tot} are conservative flux vectors written in Fourier space [7]. The source term vector \hat{H}_{tot} contains the interphase coupling terms between the gas phase and liquid phase analyses including effects such as atomization, vaporization, and injector coupling. Representative vaporization models based upon the work of Priem-Heidmann and Abramzon-Sirignano are summarized in Table 1. These relationships are complicated nonlinear functions of the liquid and gas phase variables. Linearized versions of these expressions written in terms of an appropriate set of independent variables lead directly to a combustion response function for the instability. This combustion response function in turn allows analytical solutions to be obtained which may complement CFD approaches.

One appropriate set of functional variables governing the droplet vaporization rate can be written as $\dot{m}_{vap} = f(p, u, T_l)$ where T_l is the liquid droplet temperature. Since the pressure and velocity are fundamental flow quantities, the evaluation of the combustion response functions is greatly simplified if the liquid temperature fluctuation can be eliminated. By manipulating the vaporization expression and combining it with a linearized energy balance over the droplet surface, the two-parameter expression

$$\dot{m}'_{vap} = \bar{m}_{vap} \left[\alpha^* \frac{p'}{\bar{p}} + \beta^* \frac{u'}{\bar{u}} \right] \quad (2)$$

provides a relationship for the rate of vaporization from a liquid droplet with a fluctuating temperature as a function of the mean vaporization rate and the acoustic disturbances of pressure and velocity. The values of the complex linearization constants α^* and β^* are determined from the conditions within the combustion chamber. It is sufficient to note here that it is expected that the values of α^* and β^* will directly determine the stability of the combustor in the linearized case.

For a constant mean flow, a small amplitude version of Eqn. 1 can be solved analytically. When the vaporization zone is treated with physical models in the form of Eqn. 2, the problem can be reduced to an eigenvalue solution in

terms of the vaporization constants and mean flow parameters. The dispersion relationship for the eigenvalues are obtained by manipulating the equations of motion to provide a single wave equation in the chamber,

$$p'_{tt} + 2\bar{u}p'_{xt} + (\bar{u}^2 + \bar{c}^2)p'_{xx} = \bar{c}^2\bar{m}_v \left[\left(\alpha^* \frac{p'_x}{\bar{p}} + \beta^* \frac{u'_x}{\bar{u}} \right) + \left(\alpha^* \frac{p'_t}{\bar{p}} + \beta^* \frac{u'_t}{\bar{u}} \right) \right] \quad (3)$$

where the subscripts denote differentiation with respect to the particular variable. This expression also holds in regions where the mean volumetric vaporization term \bar{m}_v vanishes. Substitution of the classical acoustic form of solutions for pressure and velocity produces a dispersion relationship of the form

$$k^2(\bar{u}^2 + \bar{c}^2) + k \left(-2\bar{u}\omega + \frac{i\beta^* \bar{c}^2 \bar{m}_v}{\bar{\rho}\bar{u}} - \frac{i\alpha^* \bar{c}^2 \bar{u} \bar{m}_v}{\bar{p}} \right) + \omega^2 - \bar{c}^2\lambda + \frac{i\alpha^* \bar{c}^2 \bar{m}_v \omega}{\bar{p}} = 0 \quad (4)$$

Here, λ is the radial wavenumber, and k and ω are the complex wavenumber and frequency, respectively. Once these have been determined, the oscillatory flow quantities which determine the stability behavior can be evaluated. In this way, the analytical solutions provide a valuable means of validating and complementing the more general nonlinear numerical approaches described earlier. This capability plays an important role in establishing a validated testbed upon which more comprehensive physical modelling can be added.

RESULTS:

First, we consider the analytical dispersion relationship presented in Eqn. 4 for a uniformly distributed vaporization process. For simplicity, we neglect droplet production processes and instead specify an initial droplet size of 140μ and a total mass flow rate of 5 kg/sec (H_2 and LOX) entering the combustion chamber. This corresponds to a vaporization zone 95% of the length of the combustion chamber.

In the absence of droplet temperature fluctuations, α^* and β^* are real and depend on droplet Reynolds number and gas static pressure. A typical stability map for the constant liquid temperature case is presented in Fig. 1. The stability plane for the distributed vaporization model includes both stable and unstable regions depending on the values of the vaporization coefficients α^* and β^* . Positive contours indicate unstable growth of disturbances, and negative values indicate stable decay. The neutral stability curve is indicated by the dashed contour and separates the unstable and stable regions which are labelled U and S, respectively. For this typical example, unstable regions are centralized in the regions of positive α^* and negative β^* . This indicates that both pressure and velocity are important in determining the stability although pressure effects may be more important under certain conditions.

The estimated ranges of the two vaporization models are indicated by the shaded regions on the stability plane. These values are approximated by allowing possible variations in the properties and other constant terms in the vaporization expressions. The locations of the Priem-Heidmann and Abramzon-Sirignano models indicate that both lie in the stable region of the stability domain. These predicted results indicate that the coupling of the vaporization process alone for constant temperature liquid droplets is insufficient to sustain pressure oscillations characteristic of combustion instability. Similar stable behavior has also been found for a wide range of operating conditions. These generalized results confirm our previous numerical findings [7] that droplet vaporization without temperature fluctuations cannot account for unstable growth of pressure oscillations.

When liquid droplet temperature is permitted to fluctuate, the linearization coefficients in Eqn. 2 become complex numbers since they are functions of the complex frequency eigenvalue. Since both the real and imaginary components of α^* and β^* may be important, the stability diagram becomes a more complicated four-dimensional space. The overall result is that the presence of a temperature fluctuation drives both the Priem-Heidmann and Abramzon-Sirignano models more towards instability. Both stable and unstable modes are possible, depending on the physical operating conditions within the combustion chamber.

Although the effects of the gas phase and liquid phase flow variables are strongly coupled and not easily separated, experience has demonstrated that droplet diameter and droplet temperature are two critical parameters that influence stability behavior. Fig. 2 presents a stability contour which has been determined computationally by a parametric study of these variables. Here, we specify a total mass flow rate of 3 kg/sec with a mean chamber temperature of 3000 K and pressure of 40 atm. The triangular upper bound of the stability is determined by the constraint that the droplets must totally vaporize within the chamber. The neutral stability curve is again indicated by a dashed contour and separates the unstable and stable regions which are labelled U and S, respectively. The results indicate that smaller initial droplet sizes and colder initial droplet temperatures tend to result in destabilized combustor behavior.

In order to demonstrate the applicability of the two-zone analysis with fluctuating temperature droplets, the predicted analytical solution is compared with numerical results using a pure mode initial condition and tracking the temporal evolution of the flowfield in time. Fig. 3 presents a comparison of the analytical and numerical solutions for the gas phase pressure oscillation at the upstream centerline of the chamber for an initial droplet diameter and temperature of 130 μ and 130 K, respectively. Also shown is a comparison of the analytical and numerical predictions for the fluctuating liquid droplet temperature at a axial location one-fourth of the chamber length. The agreement is excellent for both cases.

The stability behavior of practical engines is often tested by bombing or pulsing the combustion chamber to induce pressure oscillations. The numerical pressure response to an pulsed initial condition can be validated by using the long-term analytically predicted growth rate. As shown in Fig. 4, the short-term temporal response contains a wide variety of modes within the chamber. In the long-term solution, however, we expect the most unstable mode (predicted by the analytical method) to dominate within the combustion chamber. Here, we have shown the pressure fluctuation at the upstream centerline of the combustion chamber. A comparison with the analytically predicted solution indicates that the growth rates correlate to within about 0.1%. It is evident that the numerical and analytical solutions demonstrate excellent agreement, thus validating the CFD results.

REFERENCES:

1. Habiballah, M., Lourme, D. and Pit, F., "A Comprehensive Model for Combustion Stability Studies Applied to the Ariane Viking Engine", AIAA-88-0086, AIAA 26th Aerospace Sciences Meeting, January 11-14, 1988, Reno, NV.
2. Liang, R., Ungewitter, R., "Multi-Phase Simulations of Coaxial Injector Combustion", AIAA-92-0345, AIAA 30th Aerospace Sciences Meeting, January 6-9, 1992, Reno, NV.
3. Bhatia, R., Sirignano, W., "A One Dimensional Model of Ramjet Combustion Instability", AIAA-90-0271, AIAA 28th Aerospace Sciences Meeting, January 8-11, 1990, Reno, NV.
4. Jeng, S.M. and Litchford, R.J., "Nonlinear Analysis of Longitudinal Mode Liquid Propellant Rocket Combustion Instability", AIAA-91-1985, AIAA/SAE/ASME/ASEE 27th Joint Propulsion Conference, June 24-27, 1991, Sacramento, CA.
5. Kim, Y.M., Chen, C.P., and Ziebarth, J.P. "Numerical Simulation of Combustion Instability in Liquid-Fueled Engines", AIAA-92-0775, AIAA 30th Aerospace Sciences Meeting, January 6-9, 1992, Reno, NV.
6. Wang, Z.J., Yang, H.Q., Pindera, M.Z., and Przekwas, A.J., "CFD Simulations of Nonlinear Acoustics in Liquid Rocket Combustors", Penn State Propulsion Engineering Research Center and MSFC Fourth Annual Symposium, September 9-11, 1992, MSFC, Huntsville, AL.
7. Grenda, J.M., Venkateswaran, S., and Merkle, C.L., "Multi-Dimensional Analysis of Combustion Instabilities in Liquid Rocket Motors", AIAA-92-3764, AIAA/SAE/ASME/ASEE 28th Joint Propulsion Conference, July 6-8, 1992, Nashville, TN.

Model	Vaporization	Heat Transfer
Priem-Heidmann	$\dot{m}_{vap} = \pi d \bar{\rho} D Sh \ln \left[\frac{p}{p-p_{v,s}} \right]$	$q_v = \frac{\dot{m}_{vap} c_{p,v}(T_g - T_{d,s})}{e^2 - 1}$
Abramzon-Sirignano	$\dot{m}_{vap} = \pi d \bar{\rho} D Sh^* \ln [1 + B_M]$	$q_v = \dot{m}_{vap} \left[\frac{c_{p,l}(T_g - T_{d,s})}{B_T} \right]$

Table 1: Summary of Typical Vaporization Models

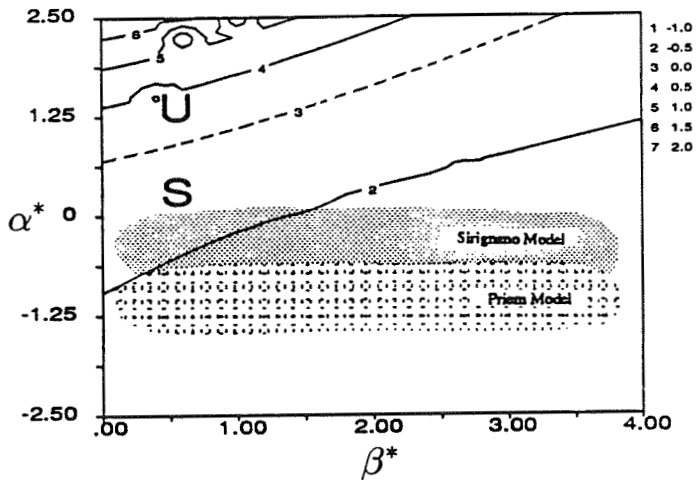


Figure 1: Distributed Vaporization Stability Plane; Constant Temperature Droplets With Initial Diameter 140 μ ; Most Unstable Growth Rate 1T,1R Instability Mode, Nondimensionalized Growth Rate.

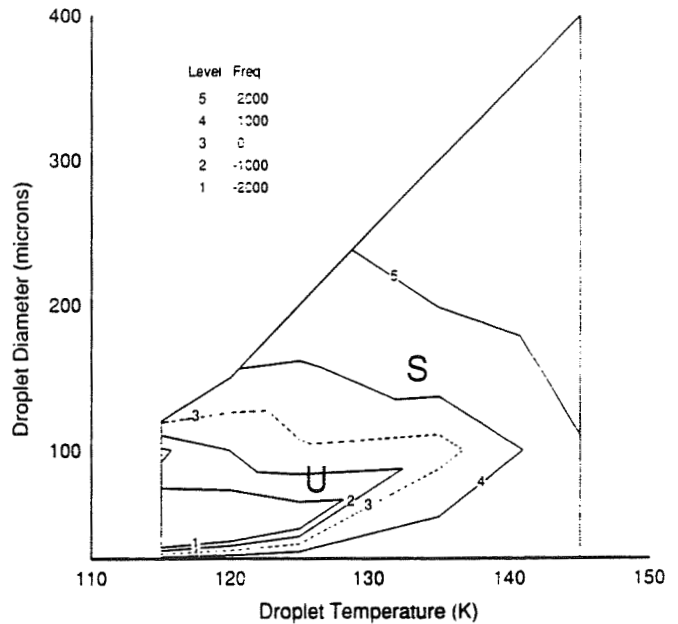


Figure 2: Distributed Vaporization Stability Plane as a Function of Droplet Diameter and Temperature; Variable Temperature Droplets; Most Unstable Growth Rate 1T,1R Instability Mode.

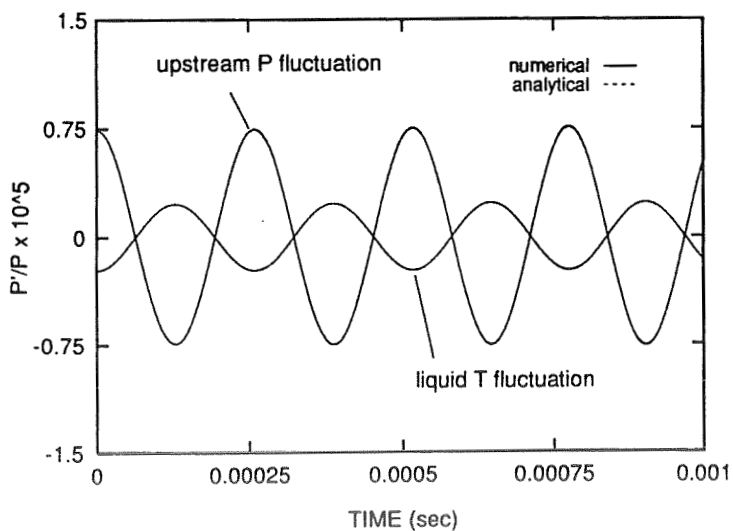


Figure 3: Pressure and Liquid Temperature Fluctuation vs. Time; Pure Mode 1T,1R Initial Condition.

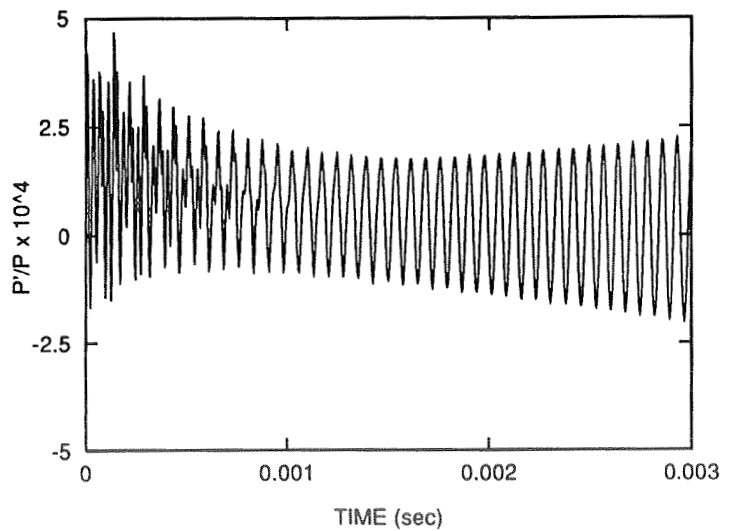


Figure 4: Upstream Centerline Pressure Fluctuation vs. Time; Pulsed (Mixed) Mode Initial Condition.

T. Kaltz, M. Glogowski, and M. M. Micci

Aerospace Engineering Department &
Propulsion Engineering Research Center
The Pennsylvania State University
University Park, PA 16802

SUMMARY/OVERVIEW:

Although stable operating regimes for cryogenic coaxial injectors have been empirically determined, there is no knowledge of the spray characteristics corresponding to stable operation, or the physical processes which produce the atomization patterns that result in stable or unstable operation. The current engineering method for determining the stable operating regime of a cryogenic coaxial injector is the 'hydrogen temperature ramping' method, however there is no definitive knowledge of whether the hydrogen temperature influences the chamber stability by decreasing the injected gas velocity, by affecting a recirculation region at the base of the LOX post, or by changing the pressure drop across the injector, allowing chamber pressure oscillations to couple to the fuel feed system. Results for the injector response from a linearized lumped-element model are presented as a function of temperature and frequency. LDV measurements in the recess region at the base of the LOX post show reverse flow indicative of a recirculation region. Finally, Phase Doppler Particle Analyzer (PDPA) measurements of droplet size and velocity distributions are discussed for a coaxial injector element similar to the SSME preburner element operating with water and air at atmospheric pressure and liquid and gaseous nitrogen at 20 bars.

TECHNICAL DISCUSSION:

In the 'hydrogen temperature ramping' test one or more injectors are placed in a combustion chamber and hot fired while the temperature of the gaseous hydrogen being injected is slowly reduced until a spontaneous instability occurs. The physical significance of the hydrogen temperature ramping technique comes from the atomization process occurring in coaxial injectors where the high velocity outer gaseous hydrogen flow strips droplets from the lower velocity inner liquid oxygen flow. Experiments at ONERA using water as the liquid oxygen simulant have shown that a higher relative velocity between the two flows, one gaseous and the other liquid, results in smaller droplets¹. Lowering the gaseous hydrogen temperature increases its density, thus lowering its injection velocity relative to the liquid in order to maintain the same mass flow and therefore the same fuel-to-oxidizer ratio. Wanhainen et al have shown that it is not the hydrogen temperature itself causing the transition to instability but

¹Vingert, L., "Coaxial Injector Spray Characterization for the Ariane 5 Vulcain Engine," 6th Annual Conference "Liquid Atomization and Spray Systems - Europe," July 4-6, 1990.

the ratio of the gas to liquid injection velocities². From this one might infer that the instability arises from a decline in droplet burning efficiency because of an increase in the liquid oxygen drop sizes along with an extension in the length of the atomization zone. A primary purpose of the experiments is to identify what effect the velocity ratio has on atomization and pressure drop across the injector to provide a better understanding of this common stability rating technique.

Another proposed explanation for the emergence of unstable operation in the hydrogen temperature ramping test is that a recirculation region acting as a flameholder exists downstream of the LOX post tip. Below a minimum relative velocity between the liquid oxygen and gaseous hydrogen, the recirculation region becomes too weak to act as a flameholder and the combustion zone moves away from the injector face to a location where it can interact more strongly with the chamber acoustic modes. Liang and Schumann have examined this idea with an experimental and computational investigation of gaseous oxygen and hydrogen coaxial injectors³. They examined several injectors designed to produce recirculation regions of different sizes but found that all injectors tested showed the combustion region anchored to the base of the injector. Whether this conclusion applies to liquid oxygen and gaseous hydrogen coaxial injectors has yet to be experimentally proven.

Some previous experimental evidence has indicated that the spontaneous instability condition for a hydrogen/oxygen rocket was determined by the hydrogen pressure drop through the injector^{4,5}. Below a critical minimum value for the pressure drop, chamber oscillations evidently can couple to the propellant feed system, causing a combustion instability in the chamber. However, the value of this critical pressure drop was a function of the injector and chamber design.

The first nine months of the grant period were spent designing a liquid nitrogen cooled heat exchanger to lower the temperature of the injected gas, either hydrogen or helium, from ambient down to 80K. The design has been completed and construction has begun. The heat exchanger will be used for the final series of experiments to simulate the hydrogen temperature ramping test.

An injector with the same dimensions as the SSME preburner injector has been constructed. The SSME preburner injector was selected because the test facility is capable of providing the required gas and liquid mass flow

²Wanhainen, J.P., Parish, H.C. and Conrad, E.W., Effect of Propellant Injection Temperature on Screech in 20,000-Pound Hydrogen-Oxygen Rocket Engine, NASA TN D-3373, April 1966.

³Liang, P.-Y. and Schumann, M.D., "A Numerical Investigation of the Flame-Holding Mechanism Downstream of a Coaxial Injector Element," Proceedings of the 24th JANNAF Combustion Meeting, CPIA Publication 476, Vol. 3, Oct. 5-9, 1987, pp. 599-610.

⁴Conrad, E.W., Bloomer, H.E., Wanhainen, J.P. and Vincent, D.W., Interim Summary of Liquid Rocket Acoustic-Mode-Instability Studies at a Nominal Thrust of 20,000 Pounds, NASA TN D-4968, Dec. 1968.

⁵Hannum, N.P., Russell, L.M., Vincent, D.W. and Conrad, E.W., Some Injector Element Detail Effects on Screech in Hydrogen-Oxygen Rockets, NASA TM X-2982, Feb. 1974.

rates for a full size injector and as large an injector as possible was desired to provide the possibility of optical access. The initial tests of the injector used air and water injecting into atmospheric ambient pressure. PDPA measurements were made of the droplet size and velocity as a function of axial and radial position. Both the magnitudes and the trends of the measured Sauter mean diameters and velocities agree well with results obtained by Zaller and Klem⁶ using a similar injector and air and water flow rates. The main purpose for this limited series of tests was to confirm the operation of the PDPA system as well as the injector. The effects of varying the PDPA PMT voltage and of taking measurements through plexiglass windows of varying thickness were quantified. A windowed cold flow high pressure chamber has been designed, constructed and pressure tested to 9 MPa. As an initial step in the investigation of the atomization behavior of cryogenic coaxial injectors, liquid nitrogen was selected as an appropriate simulant to liquid oxygen based on their similar thermophysical properties. The fuel simulant for these first tests was gaseous nitrogen. The LN₂/GN₂ flow rates were computed from the nominal exit velocities of LOX/GH₂ in the SSME fuel preburner injector. At a chamber pressure of 10 bar it was not possible to prevent cavitation at the lowest attainable supply temperature of the liquid nitrogen. Based on the vapor pressure of LN₂ at that temperature, a chamber pressure of approximately 20 bar was required to avoid this phenomenon. Tests were pursued in which the pressure was maintained above 20 bar but yielded a dense spray that could not be measured satisfactorily by the PDPA. To obtain acceptable spray data it will be necessary to move further downstream in the spray and/or reduce the mass flow rate. These actions will be pursued in future tests.

The original injector design was modified in order to allow LDV access into the recess region. This was accomplished by inserting a pyrex tube concentrically around the LOX post, such that the fuel annulus was defined by a transparent boundary 0.04 in. thick. The inner diameter of the fuel annulus is 0.197 in. Gaseous nitrogen and water at flow rates of 1.8 gm/s and 1 gm/s respectively were used. From Figure 1, it can be seen that recirculation does in fact exist within the recess region and the magnitudes of the axial velocities in this region appear consistent with the given flow conditions as does the trend on going from a high velocity gas to a low velocity liquid.

A simple model based on the Rayleigh criterion was constructed for the flow dynamics of several processes in the system to determine the effect of various design and operating parameters on combustion stability. The mechanisms included are the fuel flow through the injector, the vaporization of oxidizer in the chamber, and the flow of exhaust gases through the nozzle. Figures 2 and 3 show the effect of fuel temperature on the injector response for a chamber pressure of 21.4 bars and a gaseous fuel flow rate of 0.064 kg/s. Both graphs indicate that decreasing fuel temperature increases the response. At a frequency of 1 kHz significant variations in response occur. Figure 2 indicates that the injector response is positive over a wide frequency range while Figure 3 shows that the injector response for certain frequencies can abruptly switch from stabilizing to destabilizing as the fuel

⁶Zaller, M., and Klem, M., "Shear Coaxial Injector Spray Characterization," Proceedings of the First International Symposium on Liquid Rocket Engine Combustion Instability, Jan. 18-20, 1993, University Park, PA.

temperature is reduced. This supports the previous hypothesis that many low-frequency instabilities are due to the coupling of the feed system with the chamber acoustic modes. Results of this analysis will be compared to chamber high frequency pressure measurements. Measurements of the injector pressure drop as a function of the relative gas/liquid flow velocity and injector geometry are planned. The results of these measurements will be used as input to a stability model of the propellant feed system to determine the magnitude of the influence of the injector pressure drop on the combustion stability of the entire motor.

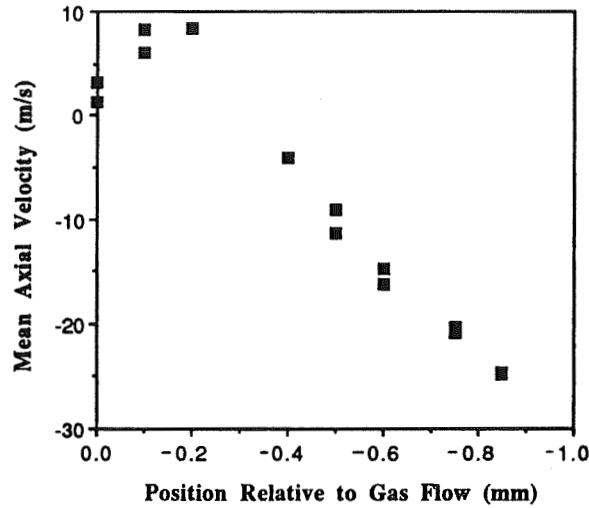


Fig. 1 LDV measurements of the mean axial velocity in the injector recess region showing reverse flow.

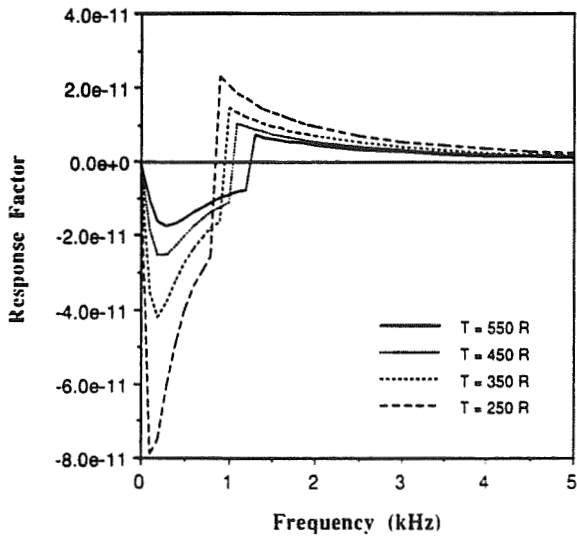


Fig. 2 Injector response as a function of frequency for several gaseous fuel temperatures.

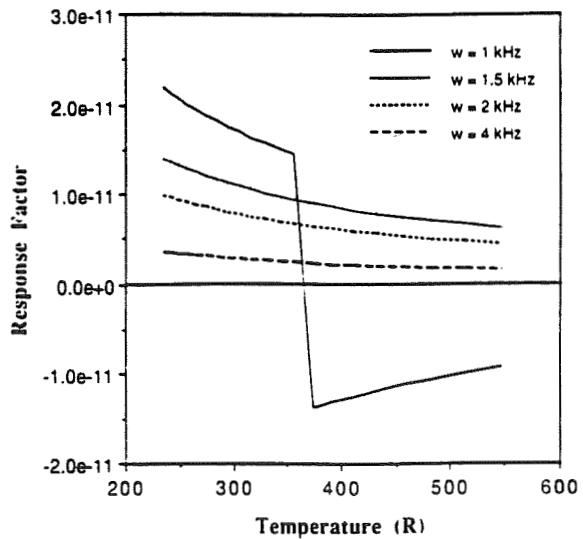


Fig. 3 Injector response as a function of gaseous fuel temperature for several frequencies.

NUMERICAL INVESTIGATION OF TWO- AND THREE-DIMENSIONAL
HEAT TRANSFER IN EXPANDER CYCLE ENGINES

Robert L. Burch and Fan-Bill Cheung
Propulsion Engineering Research Center

and

Department of Mechanical Engineering
The Pennsylvania State University
University Park, PA 16802

SUMMARY:

The concept of using tube canting for enhancing the hot-side convective heat transfer in a cross-stream tubular rocket combustion chamber is evaluated using a CFD technique in this study. The heat transfer at the combustor wall is determined from the flow field generated by a modified version of the PARC Navier-Stokes Code, using the actual dimensions, fluid properties, and design parameters of a split-expander demonstrator cycle engine. The effects of artificial dissipation on convergence and solution accuracy are investigated. Heat transfer results predicted by the code are presented. The use of CFD in heat transfer calculations is critically examined to demonstrate the care needed in the use of artificial dissipation for good convergence and accurate solutions.

TECHNICAL DISCUSSION:

The expander cycle has recently been considered one of the most desirable cycles for space propulsion applications. A liquid rocket engine operating on this cycle makes additional use of the fuel as the coolant. The performance of such an engine usually depends strongly on efficient combustor heat transfer to the coolant (i.e., fuel). By enhancing the rate of heat transfer in the combustion chamber, an increase in the chamber pressure can be achieved, leading to improved engine performance. One way to increase convective heat transfer is the use of round or oval coolant tubes, running longitudinally, to form the inner wall of the combustion chamber. This increases heat transfer by increasing the wall surface area, while providing relatively uniform heat fluxes. Berkopec [1992] reported wall heat transfer increases of up to 30% for some specific applications. One possible way to further increase the wall heat transfer is through tube canting in a coolant tube-lined combustion chamber. In this design concept, the coolant tubes are not parallel to the flow of combustion products. Rather, they are oriented at an angle α to the flow direction. With this arrangement, the surface contour varies continuously in the downstream locations. The boundary layer that would have been built up in the crevices is likely to be broken up or "tripped" by the angled tubes. This may result in increased local mixing of the flow, thus offering a potential for heat transfer enhancement over that of a non-canted tubular combustion chamber.

To evaluate the tube canting concept, a detailed numerical investigation of the flow and heat transfer in the combustion chamber of a split expander demonstrator cycle engine is conducted using a modified version of the PARC Navier-Stokes code. Both turbulent and laminar two- and three-dimensional flow fields were investigated. For the turbulent flow case, turbulence generated in the flow is approximated by using the Baldwin and Lomax algebraic model. The working fluid was assumed to be a non-reacting combustion gas using the physical properties that are consistent

with the actual case.

The portion of the engine which is of interest includes the combustion chamber before the throat area. The inner wall of the combustion chamber is made up of 350 oval coolant tubes. The interior shape of the engine wall is three-dimensional but periodic in the azimuthal direction. Using the assumption of axisymmetry, the wall geometry used in the two-dimensional cases is a longitudinal wall cut made from the three-dimensional configuration. This should provide the greatest effect or influence on heat transfer (i.e., best case) for any wall geometry or helical tube angle, since previous studies had shown that helical ribs at 90 degrees had the greatest effect on heat transfer [Gee and Webb 1980]. The two-dimensional cases provide information concerning overall trends which should hold true in the three-dimensional cases, such as the effect of flow separation on heat transfer and the rib angle required for flow separation. The results of the two-dimensional study were reported at the previous symposium [Burch and Cheung 1992]. Additional two-dimensional calculations were performed to provide reference data for comparison with the three-dimensional results. In the three-dimensional cases a periodic boundary condition was used allowing calculation of one sector (1/350 of the total flow field) made up of one coolant tube interval rather than the whole flow field.

The three-dimensional grid generation program written for this study uses a generated two-dimensional grid for each required downstream or streamwise location. A Steger-Sorenson [1979] elliptical smoother refines the grid produced by an algebraic grid model. This helps to insure grid orthogonality at the wall as well as allowing control of grid clustering along the wall. A close-up of the wall surface contour is shown in Figure 1.

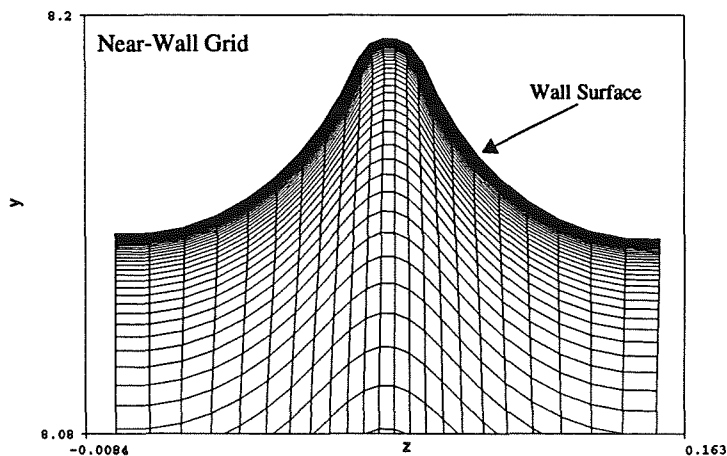


Figure 1. The near-wall region from an axial cut showing the wall grid structure

A three-dimensional test case was successfully run using a smooth wall combustion chamber to ensure the two- and three-dimensional versions of the PARC code produced the same results, once the implementation of the periodic boundary condition was corrected. The results of three-dimensional smooth wall case should be the same as the axisymmetric two-dimensional case. This case also allowed for check out of the three-dimensional versions of the programs used to calculate the wall heat transfer as well as other supporting post-processing programs.

The initial three-dimensional calculations used a zero degree canting angle, i.e., the coolant tubes run streamwise, in the baseline case. The turbulent heat transfer results ran counter intuitive, they do not seem to be physically

correct. Because of resource limitations on the PSC CRAY YMP C-90, a 1/6 length test case was developed to run in-house using a IBM RS6000. Upon further testing it was reaffirmed that the results were not physically acceptable. The error in the solution was initially speculated to be a problem with the turbulence model, the artificial dissipation, or a combination of both. The same grid was subsequently run with laminar flow in order to remove the effects of the turbulence model from the solution. Again, similar heat transfer results were obtained. The greatest heat flux was occurring in the crevice or gap between the two adjacent coolant tubes. Upon further examination, there seemed to be a correlation between the grid spacing at the wall and the heat flux; the larger the distance of the first point off the wall, the lower the heat transfer. The correlation seemed to override the seemingly natural heat flux suppression due to the larger thermal boundary layer developing in the crevice. This correlation was confirmed using two-dimensional test cases. The calculated wall heat flux was found to be dependent on the wall grid spacing rather than the amount of grid stretching.

The variation of the wall heat flux with wall grid spacing in the laminar case was traced to solution sensitivity to the artificial dissipation. The PARC codes use central differencing scheme which requires artificial dissipation to provide high frequency damping and good convergence properties [Tukel and Vatsa 1990]. Central difference schemes experience odd and even point decoupling that must be damped to achieve satisfactory convergence [Swanson and Turkel 1987]. The PARC codes use a Jameson-style scalar dissipation model with an anisotropic directional scaling factor as suggested by Swanson and Turkel [1987]. To demonstrate the solution sensitivity due to the artificial dissipation, several cases were run with varying values of the fourth-order dissipation coefficient. On a global scale the thermal boundary layer appears to be independent to the amount of fourth-order dissipation used except for a temperature overshoot that accompanies case A. This aspect can be seen in Figure 2a. However, close to the wall, the tem-

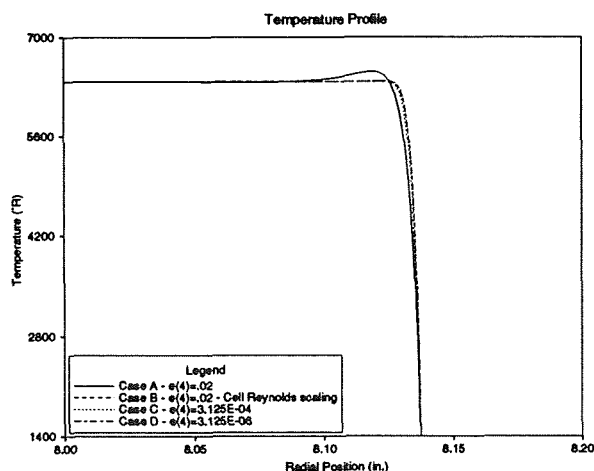


Figure 2a. The Thermal boundary layer

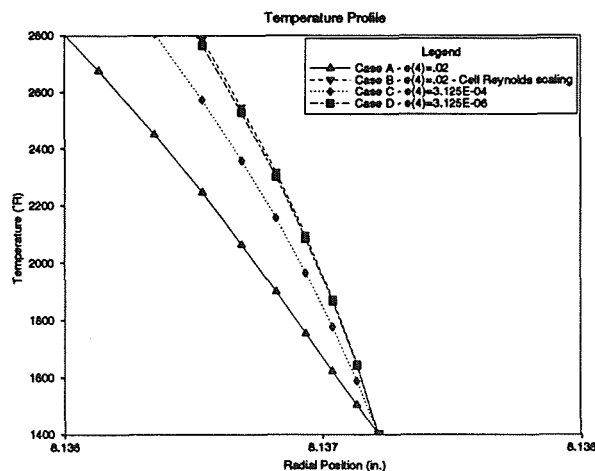


Figure 2b. The near-wall region of the thermal boundary layer.

perature profile shows marked differences in the wall temperature gradient, dT/dX , as seen in Figure 2b. Case A uses the recommended values for the fourth-order artificial dissipation coefficient ($\epsilon^{(4)}=.02$). Cases C and D use significantly smaller dissipation coefficient ($3.125E-04$ and $3.125E-06$, respectively). Case B uses a program option which scales the artificial dissipation coefficient with the cell Reynolds number. This effectively shuts the artificial dissipation off

in the radial direction since there is very little flow in this direction, but at the price of a much slower rate of convergence. This option was used for all the previously reported two-dimensional results [Burch and Cheung 1992]. For three-dimensional calculations, this scaling method did not provide enough artificial dissipation for efficient convergence and physically acceptable results.

This sensitivity has been documented by Jameson [1993], Swanson and Turkel [1992,1993], and Turkel and Vatsa [1993]. Alternatives to the previously described implementation of the artificial dissipation have included the scaling of the artificial dissipation in the direction normal to the surface boundary with the local Mach number [Swanson and Turkel 1987] and the implementation of the matrix artificial dissipation as suggested by Swanson and Turkel [1992]. The use of the local Mach number scaling did reduce the sensitivity of the solution to the artificial dissipation but did not eliminate it. The matrix artificial dissipation model is under evaluation using the two-dimensional test cases.

Turbulent cases are less sensitive to the artificial dissipation swamping the physical dissipation due to the fact that a larger physical dissipation exists due to the turbulent viscosity. Therefore, any improvement in the artificial dissipation as seen in the laminar test cases should be acceptable for turbulent test cases. With the sensitivity of the artificial dissipation resolved, attention can be given to the turbulence model if perceived problems persist in the solution. The adequacy of the Baldwin-Lomax turbulence model when used with this type wall surface contour can be evaluated. Particular attention must be given in the proper implementation of the local turbulent length scales.

REFERENCE

- Berkopec, F. D., 1992, "Space Vehicle Propulsion," NASA-Lewis Research Center, March 17 - Presentation.
- Burch, R. L. and Cheung, F.-B., 1992, "Numerical Study of Heat Transfer in Expander Cycle Engines," Fourth Annual PERC Symposium, NASA - Marshall Space Flight Center, Huntsville, AL, pp. 85-88.
- Gee, D. L. and Webb, R. L., 1980, "Forced Convection Heat Transfer in Helically Rib-Roughened Tubes," *Int. J. Heat Mass Transfer*, Vol. 23, pp. 1127-1136.
- Jameson, A., 1993, "Artificial Diffusion, Upwind Biasing, Limiters and their Effect of Accuracy and Multi-grid Convergence in Transonic and Hypersonic Flow," *AIAA Paper 93-3359*.
- Steger, J. L. and Sorenson, R. L., 1979, "Automatic Mesh-Point Clustering Near a Boundary in Grid Generation with Elliptic Partial Differential Equations," *Journal of Computational Physics*, Vol. 33, pp. 405-410.
- Swanson, R.C. and Turkel, E., 1987, "Artificial Dissipation and Central-Difference Schemes For the Euler and Navier-Stokes Equations," *AIAA Paper 87-1107*.
- Swanson, R.C. and Turkel, E., 1992, "On Central-Difference and Upwind Schemes," *Journal of Computational Physics*, Vol. 101, pp. 292-306.
- Swanson, R.C. and Turkel, E., 1993, "Aspects of a High-Resolution Scheme for Navier-Stokes Equations," *AIAA Paper 93-3372-CP*.
- Turkel, E. and Vatsa, V. N., 1990, "Effect of Artificial Viscosity on Three Dimensional Flow Solutions," *AIAA Paper 90-1444*.

FLOW VISUALIZATION STUDY IN HIGH ASPECT RATIO
COOLING CHANNELS FOR ROCKET ENGINES

Michael L. Meyer
NASA Lewis Research Center
Cleveland, Ohio 44135

James E. Giuliani
Ohio Aerospace Institute
Brook Park, Ohio 44142

INTRODUCTION:

The structural integrity of high pressure liquid propellant rocket engine thrust chambers is typically maintained through regenerative cooling. The coolant flows through passages formed either by constructing the chamber liner from tubes or by milling channels in a solid liner. Recently, Carlile and Quentmeyer¹ showed life extending advantages (by lowering hot gas wall temperatures) of milling channels with larger height to width aspect ratios ($AR > 4$) than the traditional, approximately square cross section, passages. Further, the total coolant pressure drop in the thrust chamber could also be reduced, resulting in lower turbomachinery power requirements. High aspect ratio cooling channels could offer many benefits to designers developing new high performance engines, such as the European Vulcain engine (which uses an aspect ratio up to 9)². With platelet manufacturing technology, channel aspect ratios up to 15 could be formed offering potentially greater benefits³.

Some issues still exist with the high aspect ratio coolant channels. In a coolant passage of circular or square cross section, strong secondary vortices develop as the fluid passes through the curved throat region. These vortices mix the fluid and bring lower temperature coolant to the hot wall. Typically, the circulation enhances the heat transfer at the hot gas wall by about 40% over a straight channel⁴. The effect that increasing channel aspect ratio has on the curvature heat transfer enhancement has not been sufficiently studied. If the increase in aspect ratio degrades the secondary flow, the fluid mixing will be reduced. Analysis has shown that reduced coolant mixing will result in significantly higher wall temperatures, due to thermal stratification in the coolant, thus decreasing the benefits of the high aspect ratio geometry⁵. A better understanding of the fundamental flow phenomena in high aspect ratio channels with curvature is needed to fully evaluate the benefits of this geometry.

The fluid dynamic and conjugate heat transfer problem of high aspect ratio rocket engine coolant channels are being investigated numerically, but these efforts have been hampered by a lack of validating data^{2,6}. Wall temperature data is available for the conjugate problem for channels without curvature and aspect ratio = 5.0¹, and unheated fluid dynamic data are available for square and circular cross section channels with curvature at Reynold's numbers up to 40,000^{7,8}. But the effects of aspect ratio on secondary flow development have not been experimentally studied.

To provide some insight into the effects of channel aspect ratio on secondary flow and to qualitatively provide anchoring for the numerical codes, a flow visualization experiment was initiated at the NASA Lewis

APPARATUS:

The experimental test rig, shown in figure. 1, was designed to permit visualization of the secondary flow structure that develops in a turning rectangular channel. The test rig consists of upper and lower plexiglass plates, which form the channel top and bottom, and two strips of plexiglass which make up the side walls. The plexiglass strips fit into grooves cut into the upper and lower plates. The grooves are spaced 1.25 in. apart and provide a constant channel width. Wall strips of varying heights may be placed into the grooves to change the height of the channel. Aspect ratios from 1.0 to 5.0 are possible and a wall height was selected for this experiment that gave the channel an aspect ratio of 5.0 (1.25 in. width x 0.25 in. height; NOTE: In this experiment, the channel is laying on its side so height and width are interchanged with respect to an actual cooling channel dimensions). The total length of the channel is 11.3 ft. and consists of two 5.0 ft. straight sections and a 180° bend in the center. Upon entering the channel, the flow first passes through a 5.0 ft. straight section where disturbances dissipate and the flow is allowed to develop. The channel then turns 180° with a 5.0 in. centerline radius of curvature. The channel continues straight for an additional 5.0 ft. to the flow outlet. Water is pumped through the system either by normal water supply pressure or by an additional pump. Reynolds numbers based on hydraulic diameter up to 40,000 can be obtained with the normal supply pressure and Reynolds numbers up to 100,000 are possible with the pump.

To visualize the flow structure in the turning section, the hydrogen bubble technique is used to provide a seedant for the flow^{9,10}. With this technique, hydrogen bubbles are formed on thin wires placed within the flow field. The wires form the cathode (negative) pole of a DC circuit and an additional wire, which is placed non-intrusively in the flow, forms the anode (positive) pole. When a current is applied to the circuit, electrolysis takes place forming oxygen on the anode and hydrogen on the cathode. As hydrogen bubbles form on the cathode wires, the flow strips them away. Five cathode wires are placed vertically across the width of the channel and 1.0" upstream of the turning section. The size of the bubbles generated is a function of the wire diameter, conductivity of the water, applied voltage and flowrate⁹. The power supply used to generate the hydrogen bubbles is a 160 V DC with a 100 mA current limit, and wire diameters of 0.002", 0.005" and 0.010" were interchanged.

A high intensity photographic spot light was used to illuminate the hydrogen bubbles from above as they flowed through the turning section. The beam from the light source was collimated with a series of slits so that only a thin plane of the flow was illuminated. A standard VHS camera and recorder were used to record the illuminated particle streaks. The camera was placed perpendicular to the plane of interest and to minimize the distortion caused by the camera focusing through the curved plexiglass wall, a triangular window was seated against the channel wall and filled with water. The side of the window provides a flat surface parallel to the focus plane and the water filled cavity provides a more uniform index of refraction. The optical compensating window was sealed to the test rig with RTV and could be removed, cleaned and re-attached at a different location. Video image data was recorded at 1 inch upstream of the bend, 3 inch downstream of the bend and at 0°, 30°, 60°, 90°, 120°, 150° and 180° from the start of the bend.

DATA ANALYSIS:

Analysis of the raw video images provided some insight into the flow structure, however, results were somewhat inconclusive. A problem with this type of flow visualization is that the particle streaks remain illuminated for only 2 to 3 video frames before passing out of the light sheet. Once a particle enters a particular region, only a brief view of the flow structure is given. To better understand where vortices and velocity gradients occur in the channel, a computer algorithm was developed to enhance the digitized raw video images, resolve vectors from particle streaks, and infer particle direction by analyzing several sequential frames.

Individual video frames were digitized to a 620 pixel wide by 160 pixel high image with a 15 pixel border surrounding the actual channel. Figure 2 shows a digitized image from a video frame taken at a Reynolds number of 6,800. The algorithm first scanned the digitized image looking for local gradients in pixel brightness to find particle streaks. Once a gradient was encountered, marking a particle streak, the algorithm searched along the gradient to find the two endpoints. Figure 3 shows the individual particle streaks that were calculated from the image in figure 2. Resolving the particle streaks by processing the brightness gradients worked well as many streaks were resolved that are too subtle for the unaided eye. Considering local gradients also eliminated the problem of resolving streaks in regions where glare on the plexiglass side wall was encountered. While glare on the side wall caused the background to be of differing intensity levels throughout the image, its change from pixel to pixel was small and was therefore invisible to local gradient calculations.

Once the particle streaks in individual frames are resolved, the algorithm compares sequential frames to see if a particle streak in frame 1 at time 0 continues in frame 2 at time Δt . For each vector in frame 1, frame 2 is searched to see if any endpoints match those in frame 1. If vectors in frame 1 and frame 2 have a matching endpoint, then a multiple frame particle streak has been found and the direction of the particle is inferred by the sequence of the frames. A circle is placed on the head of the vector to denote direction.

Figure 4 shows the results of processing 30 sequential frames from video taken at 30° from the start of the bend at a Reynolds number of 6,800 based on hydraulic diameter. Only resolved vectors with magnitudes greater than 20 pixels are considered. In this figure, the primary flow direction is out of the page, with the outer wall of the bend on the left and the inner wall on the right. Here the classical secondary flow can be seen, with the velocity on the upper and lower surfaces travelling towards the inner wall and the centerline velocity travelling towards the outer wall. This is the result of a pair of horizontally elongated vortices stacked on top of each other. It should be noted that the flow is not perfectly steady and some particle streaks represent momentary fluctuation in the flow structure. Some particles can also be seen being stripped from the centerline flow by the flow at the wall. As Reynolds number is increased, resolving the particle streaks becomes increasingly difficult. Improved experimental techniques will be required to capture the secondary flow structures at higher velocities.

REFERENCES

1. Carlile, J. A., Quentmeyer, R. J., "An Experimental Investigation of High-Aspect-Ratio Cooling Passages," NASA TM 105679, AIAA Paper 92-3154, 1992.

2. LeBail, F., Popp, M., "Numerical Analysis of High Aspect Ratio Cooling Passage Flow and Heat Transfer," AIAA Paper 93-1829, 1993.
3. Tobin, S., Mueggenburg, H., Burkhardt, W., "Formed Platelet Liner Concept for Regeneratively Cooled Chambers," AIAA Paper 90-2117, July 1990.
4. Hendricks, R. C., Simon, F. F., "Heat Transfer to Hydrogen in a Curved Tube," presented at the ASME Meeting, Philadelphia, November, 1963.
5. Kacynski, K. J., "Thermal Stratification Potential in Rocket Engine Coolant Channels," NASA TM 4378, 1992.
6. Yagley, J. A., Feng, J., Merkle, C. L., "CFD Analyses of Coolant Channel Flowfields," AIAA Paper 93-1830, June 1993.
7. Taylor, A. M. K. P., Whitelaw, J. H., Yiannakis, M., "Measurements of Laminar and Turbulent Flow in a Curved Duct with Thin Inlet Boundary Layers," NASA Contractor Report 3367, 1981.
8. Humphrey, J. A. C., Launder, B. E., "Developing Turbulent Flow in Strongly Curved Passages of Square and Circular Cross Section," Final Technical Report for the Office of Naval Research, AD-A143 279, 1984.
9. Davis, W., Fox, R. W., "An Evaluation of the Hydrogen Bubble Technique for the Quantitative Determination of Fluid Velocities Within Clear Tubes," Journal of Basic Engineering, Trans. ASME, December 1967, pp. 771-781.
10. Tory, A. C., Haywood, K. H., "The Hydrogen Bubble Technique of Flow Visualization: Factors Affecting Bubble Size and Buoyancy," Fluids Engineering Conference, ASME Paper 71-FE-36, May 1971, Pittsburgh, Pa.

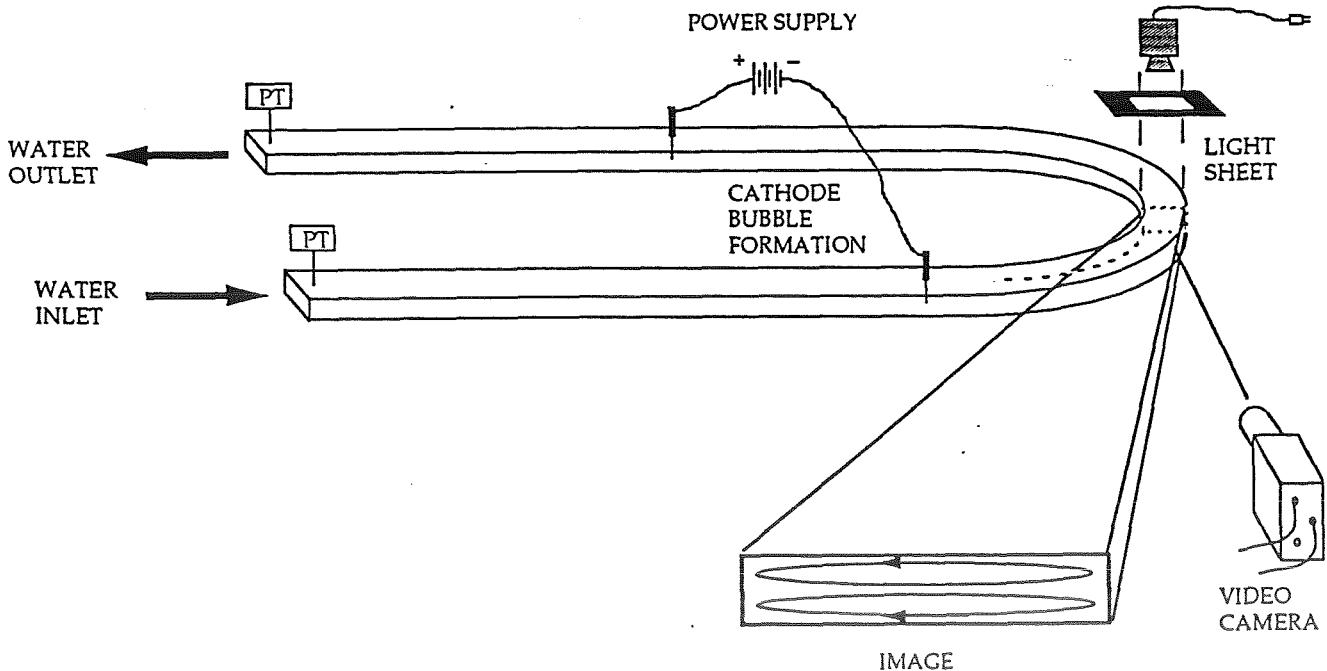


Figure 1. Experimental setup of the channel flow visualization rig.

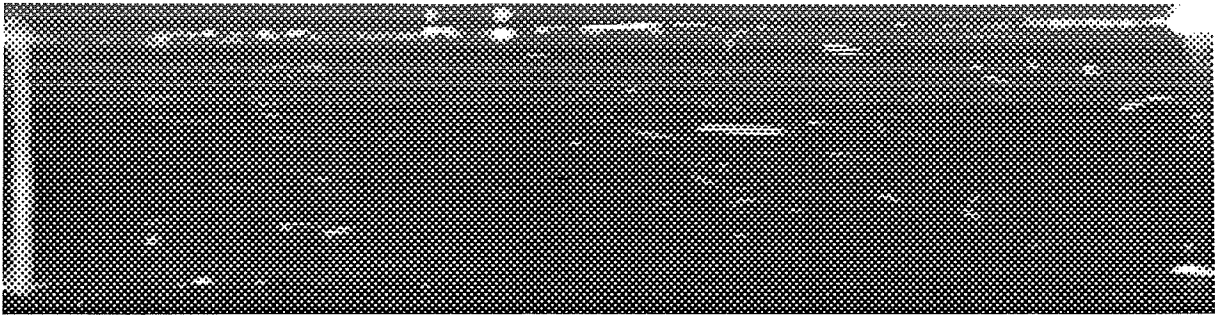


Figure 2 - Digitized video image

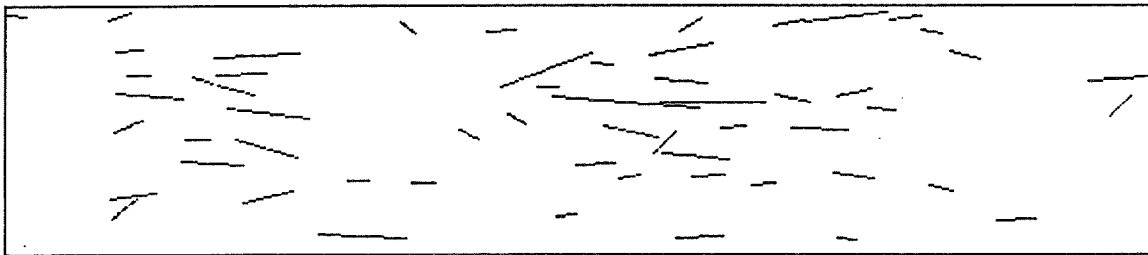


Figure 3 - Single frame particle streaks

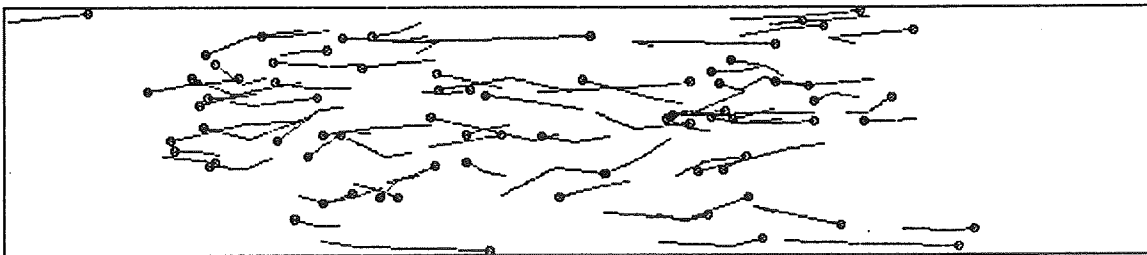


Figure 4 - Multiple frame particle streaks at $Re=6,800 @ 30^\circ$

CFD ANALYSES OF COOLANT CHANNEL FLOWFIELDS

Jennifer A. Yagley[†], Jinzhang Feng[‡], and Charles L. Merkle[§]
 Propulsion Engineering Research Center
 Department of Mechanical Engineering
 The Pennsylvania State University
 University Park, PA 16802

SUMMARY

The flowfield characteristics in rocket engine coolant channels are analyzed by means of a numerical model. The channels are characterized by large length to diameter ratios, high Reynolds numbers, and asymmetrical heating. At representative flow conditions, the channel length is approximately twice the hydraulic entrance length so that fully developed conditions would be reached for a constant property fluid. For the supercritical hydrogen that is used as the coolant, the strong property variations create significant secondary flows in the cross-plane which have a major influence on the flow and the resulting heat transfer. Comparison of constant and variable property solutions show substantial differences. In addition, the property variations prevent fully developed flow. The density variation accelerates the fluid in the channels increasing the pressure drop without an accompanying increase in heat flux. Analyses of the inlet configuration suggest that side entry from a manifold can affect the development of the velocity profile because of vortices generated as the flow enters the channel. Current work is focused on studying the effects of channel bifurcation on the flow field and the heat transfer characteristics.

TECHNICAL DISCUSSION

Regenerative cooling is normally used in rocket engine combustors to protect the walls from the severe thermal environment of the combustion process. In most cases, the coolant passages are rectangular in shape and run the length of the combustor with the coolant entering at the supersonic end, passing through the throat region, and exiting near the injector face. In cryogenic engines, the coolant is generally liquid hydrogen, and the elevated pressures are sufficient to ensure that the fluid remains supercritical over the entire length of the cooling passage.

Although the design of these coolant passages is critical to the operation and life of the engine, their heat transfer characteristics are only poorly understood. To maximize our understanding of the fluid dynamics and the associated heat transfer characteristics of the coolant passages, the limiting case of a straight rectangular channel (which is currently being tested at NASA LeRC) is studied. Even with straight geometries, the flowfield inside the tubes remains quite complex because of the asymmetrical heating, the fin effect, the presence of a supercritical coolant with its characteristically strong property variations and the high Reynolds numbers. Because of the complex three-dimensional flow patterns in these coolant passages, it is anticipated that an optimum channel aspect ratio exists, and a validated CFD code is an important tool in assessing where this optimum occurs under different conditions.

At supercritical conditions all fluid properties (density, viscosity, thermal conductivity and specific heat) become strong functions of both pressure and temperature [1]. These variations are particularly strong near the critical

[†] Graduate Research Assistant

[‡] Research Associate

[§] Distinguished Alumni Professor

point. Temperature dependence is especially significant in the present problem because of the strong temperature gradients near the hot wall of the coolant passage.

In the presence of property variations, the Navier-Stokes equations and the energy equation are coupled and must be solved simultaneously. The corresponding system of governing equations is:

$$\Gamma \frac{\partial Q}{\partial \tau} + \frac{\partial}{\partial \xi} (E - E_v) + \frac{\partial}{\partial \eta} (F - F_v) + \frac{\partial}{\partial \zeta} (G - G_v) = 0$$

$Q=(P,u,v,w,T)^T$ is the vector of dependent variables; (ξ, η, ζ) represents a general non-orthogonal coordinate system; Γ is a pre-conditioning matrix; $E, F,$ and G are the conservative flux vectors while E_v, F_v and G_v are the viscous flux vectors [2]. The equation set is completed by a tabular equation of state relating the density to the local temperature and pressure. Additionally, auxiliary equations for the pressure and temperature dependence of the viscosity, thermal conductivity and specific heat are also specified. The Baldwin-Lomax algebraic turbulence model [3] is used to accommodate turbulent flow. The turbulent Prandtl number is chosen as 0.9 throughout the calculation.

Although our interest is in steady flow, the equations of motion are written in unsteady form for computational purposes and are solved by a four stage Runge-Kutta explicit scheme [4]. All derivatives of the Navier-Stokes equations are represented by centered differences. Local time stepping is used to achieve maximum convergence and a small amount of fourth order artificial dissipation is added to prevent odd-even splitting. Since the time derivatives disappear in the steady state, some license may be taken with them to counter the stiffness caused by the low Mach numbers in the supercritical fluid. This stiffness is circumvented using an artificial compressibility expression [5,6]. During the process of convergence, all the time derivatives approach zero and the numerical solution satisfies the proper steady state Navier-Stokes equations.

As boundary conditions for the present calculations, we specify the velocity and temperature profiles at the inlet, and uniform pressure at the exit plane. The remaining flow variables at the inlet and outlet are computed from the Riemann variables determined from the method of characteristics [4]. The velocity boundary conditions on the passage wall are the traditional no-slip conditions. These are augmented by enforcing the normal momentum equation to obtain the wall pressure.

Heat transfer conditions representative of those in combustor coolant passages are simulated by selecting appropriate Dirichlet (temperature) boundary conditions around the periphery of the duct. Uniform temperature conditions are assigned on both the inner (combustor) and outer (ambient) sides of the passage while a linear distribution of temperature is used on the side walls to simulate the fin effect. The inlet temperature is specified as 40 K. Future plans are to couple the present fluids solution with a heat conduction formulation for the combustor walls to obtain the coupled solution.

The straight duct study was conducted to give an understanding of the fundamental physical effects of variable properties, turbulence modeling, high length to diameter ratios and inlet conditions. The next step in the study is to investigate the effects of channel bifurcation on the flow and temperature fields. A representative geometry is shown in Figure 1.

RESULTS

The geometry and flow conditions for this study were chosen to parallel an experimental study currently being conducted at NASA LeRC [7]. The length of the experimental channel is 137 mm which corresponds to 112 hydraulic diameters. The Reynolds number based on the inlet conditions and hydraulic diameter is 500,000. For the current study we also studied channels of shorter lengths and flow at the lower Reynolds number of 10,000. Computations have also been completed for both constant and variable (supercritical hydrogen) property flows.

One of the important issues in the straight tube studies is the effect of variable properties on the pressure drop and heat transfer characteristics of the channels. The property variation of super-critical hydrogen significantly alters the flow field characteristics and it is important to assess its effect on the channel cooling. To evaluate the nature of these differences a comparison of the flowfields based upon constant and variable properties was conducted. This comparison was made at a Reynolds number of 10,000.

The mid-plane, streamwise direction contour plots of the pressure, the axial velocity and the temperature variations are shown in Figure 2. The constant property results are shown on the right while the variable property results are shown on the left. The cross-stream direction has been stretched by a factor of five in these figures. As can be seen, the variable properties cause the velocity profiles to be very non-uniform across the tube, and in addition, lead to an acceleration by a factor of about two. The higher flow speeds cause a lesser, but noticeable effect on the temperature.

A comparison of the flow fields for the two different Reynolds numbers 10,000 and 500,000 shows the viscous and thermal boundary layers were significantly thinner at the higher Reynolds number. Despite the fact that the thermal effect are limited to a small portion of the flowfield there is still an acceleration of the flow due to the density variations although not as significantly as in the lower Reynolds number.

Another issue studied was the effect of inlet velocity profiles on the downstream fluid dynamics and heat transfer. The inlet conditions studied were slug flow, fully developed velocity profiles and entry through a 90 degree bend (constant property). The first two represents a bounding study between two extremes in inlet profiles. The last condition represents an approximation to the type of entry that is used in the experimental configuration. A comparison of fully developed velocity profile with the slug flow velocity profile shows that the inlet condition has a measurable effect on the velocity contours in the exit plane (Fig. 3). The contours in the exit plane are qualitatively similar, but the results for the slug flow inlet show a peak velocity of 4.0 m/s in the exit plane whereas those for the fully developed inlet show a peak of 3.3 m/s. The corresponding pressure drop for the slug flow inlet is about 15 percent larger than that for the fully developed inlet profile. By contrast, the fluid temperatures at the exit plane for both cases are about the same. Both calculations show that the fluid has been heated to the point where the minimum temperature in the exit plane is 45 K, although more of the fluid appears to have been heated in the slug flow inlet case. In agreement with this latter observation, computation of the heat flux through the walls shows that the heat addition is larger (by about 15 percent) for the slug flow inlet case. These differences between the two calculations are not major, but they do suggest that care should be taken in defining the inlet conditions to be sure to obtain maximum accuracy in the coolant channel predictions.

The results for the second inlet condition, the inlet with a 90 degree bend are presented in Figure 4. The velocity contours are quite similar in magnitude, although the profiles for the 90 degree bend inlet are slightly asymmetric. Similar comparison of the temperature profiles shows the presence of the bend in the inlet increases the minimum temperature from 90 K to 110 K, suggesting that the vortex created by the turn at the inlet has some effect on the heat flux.

Comparisons of the streamwise development of the various flow characteristics are given on Figs. 5 and 1. The pressure drop predictions for the two cases is nearly identical (not counting the pressure drop across the inlet bend itself), suggesting that the strength of the vortices developed by the bend in the inlet was not sufficient to affect the downstream pressure gradient. The velocity profile in the bent inlet calculation shows a dramatic thickening of the boundary layer downstream of the inside portion of the curved inlet. This arises from a flow separation near the bend. The presence of flow separation and the vortex generated by the curved inlet suggests that the type of connection between the manifold and the coolant channels can have an effect on the downstream heat transfer.

REFERENCES

- [1] McCarty, R.D., "Hydrogen Technological Survey-Thermophysical Properties", NASA SP-3089, 1975, Washington D.C.
- [2] Yagley, J.A., Feng, J. and Merkle, C.L., "CFD Analyses of Coolant Channel Flowfields", AIAA/SAE/ASME/ASEE 29th Joint Propulsion Conference, AIAA-93-1830, June 1993, Monterey, CA.
- [3] Baldwin, B.S. and Lomax H., "Thin Layer Approximation and Algebraic Model for Separated Turbulent Flows", AIAA 16th Aerospace Sciences Meeting, AIAA Paper 78-257, January 1978, Huntsville, AL.
- [4] Merkle, C.L. and Tsai, Y.L. Peter, "Application of Runge-Kutta Schemes to Incompressible Flows", AIAA-86-0553, AIAA 24th Aerospace Sciences Meeting, January 1986, Reno, NV.
- [5] Merkle, C.L. and Athavale, M., "Time-accurate Unsteady Incompressible Flow Algorithms based on Artificial Compressibility", AIAA 8th Computational Fluid Dynamics Conference, AIAA Paper 87-1137, June 1987, Honolulu, HA.
- [6] Choi, Y.-H. and Merkle, C.L., "The Application of Preconditioning in Viscous Flows", Journal of Computation Physics, Vol 105, No2, April 1993.
- [7] Carlile, J.A. and Quentmeyer, R.J., "An Experimental Investigation of High-Aspect-Ratio Cooling Passages", AIAA-92-3154, AIAA/SAE/ASME/ASEE 28th Joint Propulsion Conference, July 1992, Nashville, TN.

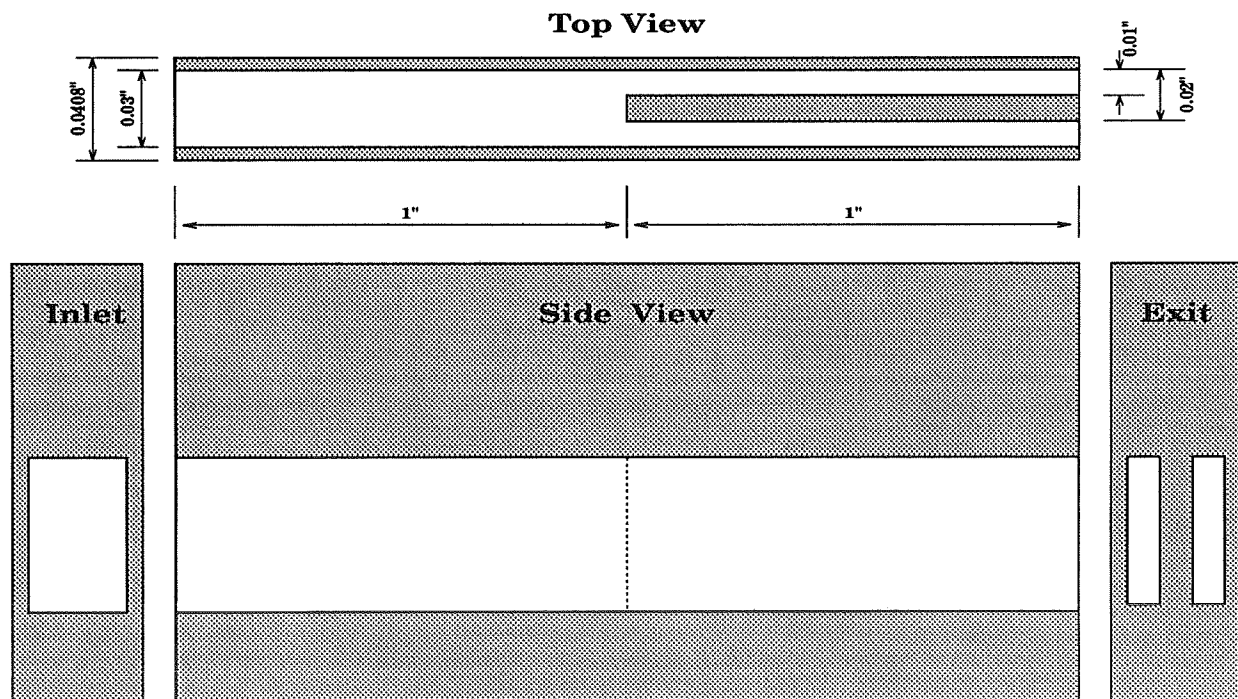


Figure 1: Representative sketch of channel bifurcation geometry.

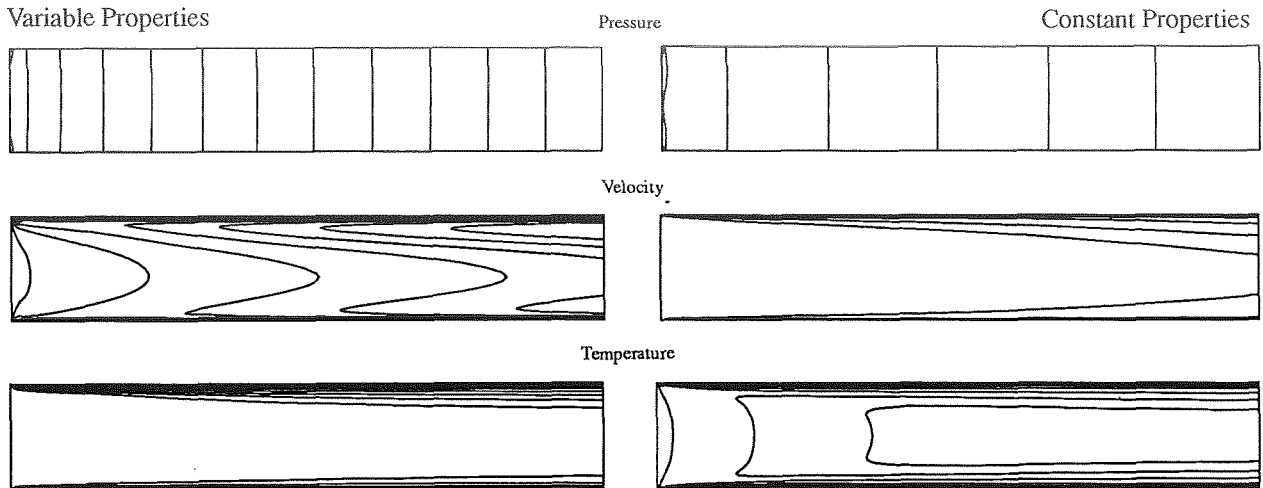


Figure 2: Steamwise contours of the pressure, velocity, and temperature on the centerplane for an L/D_h of 28. Variable Properties: $P_{inc} = 20.$, $P_{max} = 220.$; $u_{inc} = 0.5$, $u_{max} = 4.0$; $T_{inc} = 70$, $T_{max} = 600$ (top wall). Constant Properties: $P_{inc} = 6.$, $P_{max} = 42.$; $u_{inc} = 0.17$, $u_{max} = 1.4$; $T_{inc} = 70$, $T_{max} = 600$ (top wall).

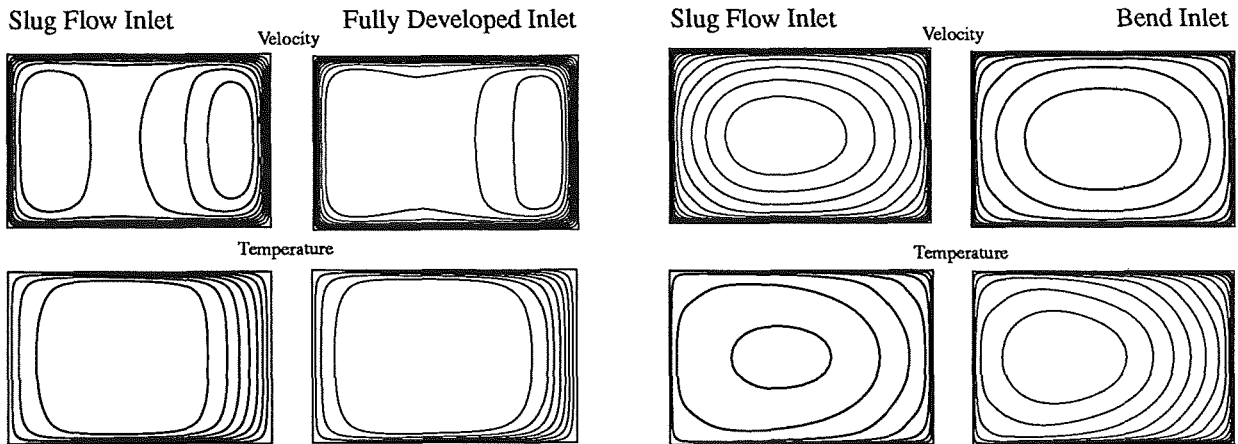


Figure 3: Contour of axial velocity and temperature at the exit plane ($L/D_h = 28$) for slug flow and fully developed inlet with variable properties. Slug: $u_{inc} = 0.4$, $u_{max} = 4.0$, $T_{inc} = 70$, $T_{min} = 45$. Fully Developed: $u_{inc} = 0.4$, $u_{max} = 3.3$; $T_{inc} = 70$, $T_{max} = 600$ (right wall).

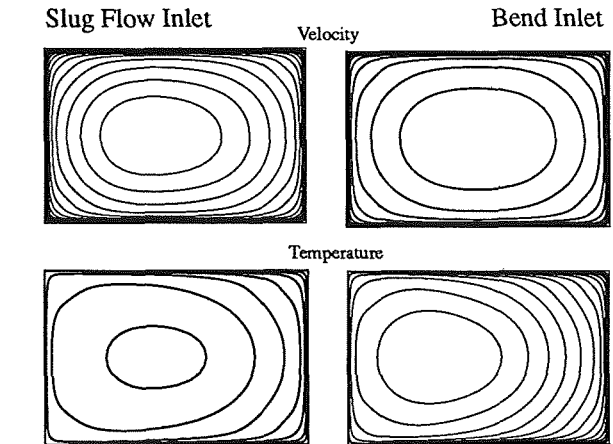


Figure 4: Contour of axial velocity and temperature in the exit plane ($L/D_h=28$) for slug flow and bend entrance inlet with constant properties. Slug: $u_{inc} = 0.4$, $u_{max} = 4.0$, $T_{inc} = 70$, $T_{min} = 45$. Bend Inlet: $u_{inc} = 0.4$, $u_{max} = 3.3$; $T_{inc} = 70$, $T_{max} = 600$ (right wall).

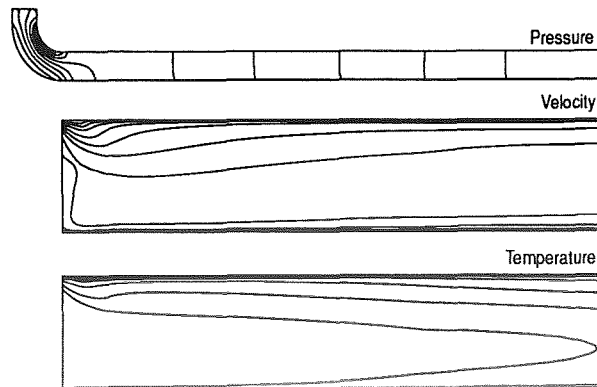


Figure 5: Effects of bend on flowfield (constant properties). There are 28 hydraulic diameters after the bend. $P_{inc} = 0.5$, $P_{max} = 5$; $u_{inc} = 0.1$, $u_{min} = -0.1$, $u_{max} = 1.5$; $T_{inc} = 70$, $T_{max} = 600$ (at bottom wall), $T_{min} = 40$ (at inlet).

HEAT TRANSFER IN ROCKET COMBUSTION CHAMBERS

P. Anderson, G. Cheng, and R. Farmer

SECA, Inc., Huntsville, AL

Complexities of liquid rocket engine heat transfer which involve the injector faceplate and film cooled walls are being investigated by computational analysis. A conjugate heat transfer analysis was used to describe localized heating phenomena associated with particular injector configurations and film coolant flows. These components were analyzed, and the analyses verified when appropriate test data were available. The component analyses are being synthesized into an overall flowfield/heat transfer model. A Navier-Stokes flow solver, the FDNS code, was used to make the analyses. Particular attention was given to the representation of the thermodynamic properties of the fluid streams. Unit flow models of specific coaxial injector elements have been developed and are being used to describe the flame structure near the injector faceplate.

The FDNS code was modified to compute through the two orders of magnitude density variation encountered in the region where the hot exhaust gases and cold oxygen mix at the exit of a coaxial injector. A thermal equation of state based on a modified principle of corresponding states was used to represent the real fluid properties of the propellants.

The flowfield and heat transfer for a main injector element of the Space Shuttle Main Engine were simulated; the resulting temperature field is presented in Fig. 1. The oxygen, entering the LOX post as a liquid at 200 °R, reaches temperatures of 240 °R (still a liquid) along the element axis, and 304 °R (dense gas) at the wall in the exit plane of the LOX post, prior to mixing with the hot exhaust gases. The exhaust gases have been cooled from 1500 to around 1440 °R. A similar analysis for a baffle element has also been made. For this case, the oxygen remains a liquid as it emerges from the LOX post, reaching temperatures of 223 to 230 °R. The lower heating, compared to the main injector element, is due to the use of coolant hydrogen with a temperature range of 465 to 450 °R. Both analyses provide a good approximation to the flowfield where the propellants leave the injector elements and enter the combustion chamber.

To investigate the effects of film cooling, a Rocketdyne RP-1/ O₂ test motor which utilized slightly film cooled walls was simulated and compared to the same motor operated at uniform O/F ratio. The analysis for the constant O/F ratio case matched the test results very closely. Wall heat flux prediction for the film cooled case are shown in Fig. 2. The dotted line prediction indicates that even though the film is initially cold enough to provide the correct wall heating, the film mixes too fast to match the measured wall heat flux distribution. Apparently, the turbulent mixing, which is based on an incompressible K-ε turbulence model, is too fast. This phenomena has been observed repeatedly in variable density flowfield predictions. A thicker film specification on the startline would have a similar effect, but such a specification is not physically realistic. Delays associated with RP-1 droplet vaporization could also cause such effects. This is not thought to be the case, but vaporization effects are still under investigation. The problem was further analyzed by using the temperature correction to the incompressible K-ε turbulence model which was successfully used by these investigators to predict a dump combustor flowfield. The

improvement in the predicted wall heat flux distribution, shown by the solid line in Fig. 2, is dramatic. Although the experiment did not provide enough detailed data to verify this analysis, the qualitative features of the film cooling were well predicted.

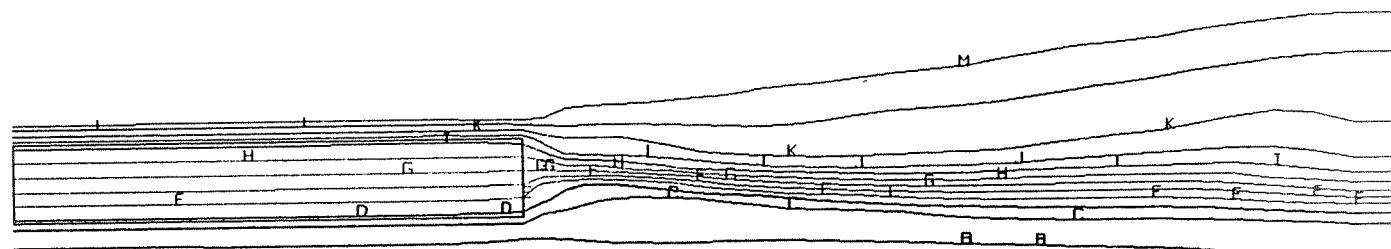
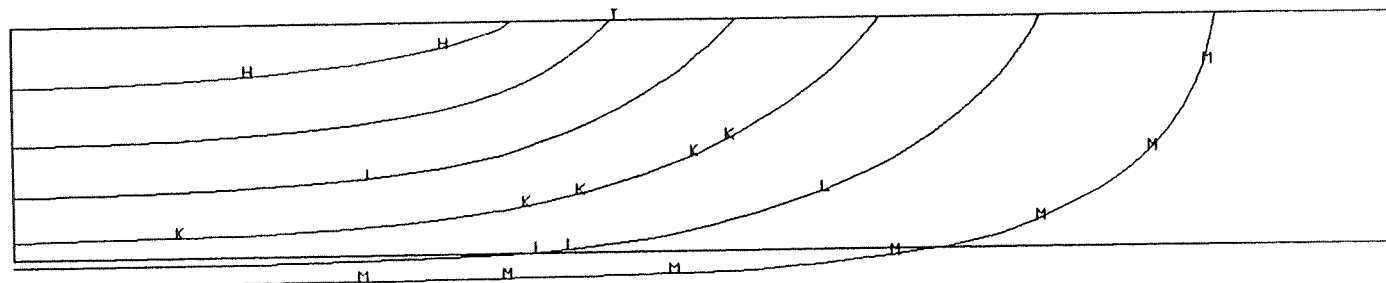
The results of the main injector element flow and heat transfer analysis are now being used as upstream boundary conditions to continue the analysis into the combustion chamber. The combustion chamber analysis is still in progress.

This work was sponsored by NASA/MSFC under Contract NAS8-38961.

Figure 1

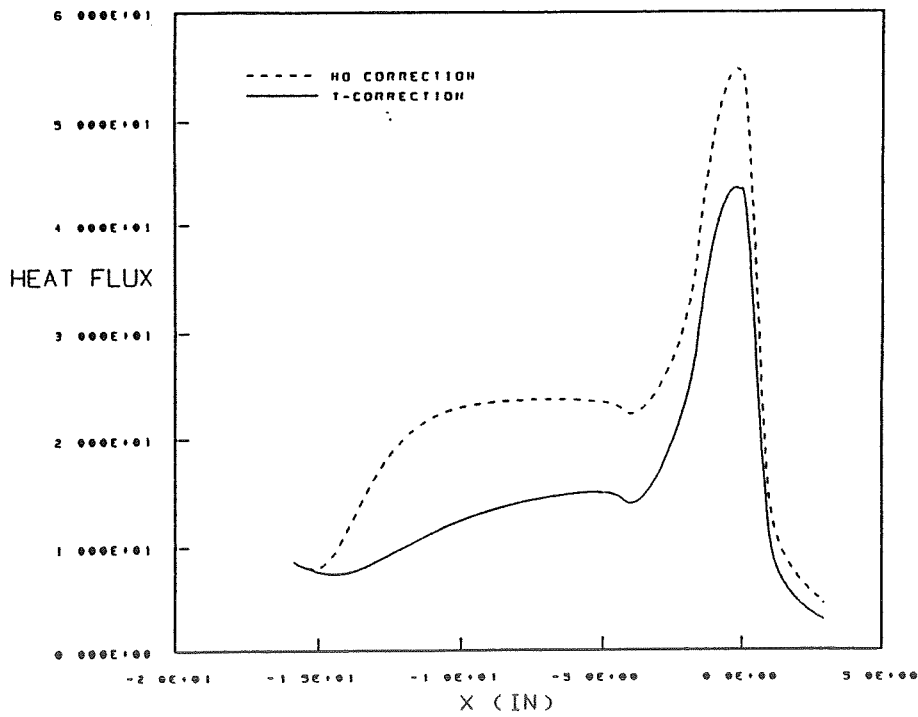
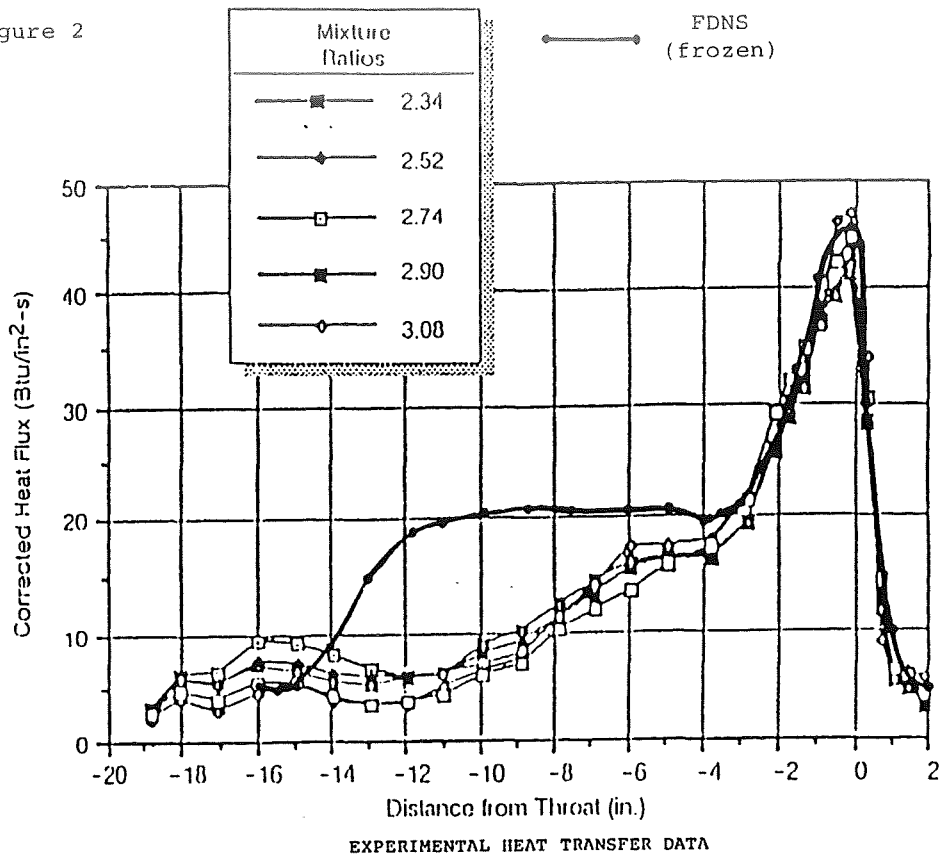
TEMPERATURE
(DEG R)

0.20000E+03	A
0.30000E+03	B
0.40000E+03	C
0.50000E+03	D
0.60000E+03	E
0.70000E+03	F
0.80000E+03	G
0.90000E+03	H
0.10000E+04	I
0.11000E+04	J
0.12000E+04	K
0.13000E+04	L
0.14000E+04	M
0.15000E+04	N
0.16000E+04	O
0.17000E+04	P
0.18000E+04	Q
0.19000E+04	R
0.20000E+04	S



TEMPERATURE IN MAIN INJECTOR ELEMENT EXIT

Figure 2



ADVANCED MATERIALS FOR RADIATION-COOLED ROCKETS

Brian Reed, James Biaglow and Steven Schneider
NASA Lewis Research Center

SUMMARY

The most common material system currently used for low thrust, radiation-cooled rockets is a niobium alloy (C-103) with a fused silica coating (R-512A or R-512E) for oxidation protection. However, significant amounts of fuel film cooling are usually required to keep the material below its maximum operating temperature of 1370 °C, degrading engine performance. Also the R-512 coating is subject to cracking and eventual spalling after repeated thermal cycling. A new class of high-temperature, oxidation-resistant materials are being developed for radiation-cooled rockets, with the thermal margin to reduce or eliminate fuel film cooling, while still exceeding the life of silicide-coated niobium. Rhenium coated with iridium is the most developed of these high-temperature materials. Efforts are on-going to develop 22 N, 62 N, and 440 N engines composed of these materials for apogee insertion, attitude control, and other functions. There is also a complimentary NASA and industry effort to determine the life limiting mechanisms and characterize the thermomechanical properties of these materials. Other material systems are also being studied which may offer more thermal margin and/or oxidation resistance, such as hafnium carbide/tantalum carbide matrix composites and ceramic oxide-coated iridium/rhenium chambers.

IRIDIUM/RHENIUM

A technology program¹ was conducted to find a chamber material system that could operate for long life in a 2200 °C environment. After a literature and vendor survey, iridium-coated rhenium (Ir/Re) was selected. In the same technology program, a 22 N Ir/Re chamber was operated for 15 hours at 2200 °C on monomethylhydrazine (MMH) and nitrogen tetroxide (NTO) propellants with negligible internal erosion. A flighttype 22 N chamber was then fabricated and tested for 1.77 hours on MMH/NTO before a coating failure at the throat. An alteration in the contour design gave a sharp radius of curvature at the throat, which proved to be a stress concentrator. A flighttype 440 N chamber has been successfully tested for 6.3 hours on MMH/NTO. There has been further testing of flighttype 22 N, 62 N, and 440 N Ir/Re engines on MMH/NTO and hydrazine/nitrogen tetroxide (N₂H₄/NTO) by various rocket companies.^{2,3} A 22 N Ir/Re chamber has also been tested for over 14 hours on gaseous hydrogen/gaseous oxygen (GH₂/GO₂) propellants.

The life limiting mechanisms of Ir/Re chambers were investigated.⁴ It was found that rhenium slowly diffuses along grain boundaries into the iridium coating during high temperature operation, so that the concentration of rhenium at the inner surface slowly increases. Oxidation testing at 1500 °C has shown that the iridium oxidation rate increases significantly above a rhenium concentration of 20 percent. Rhenium diffusion into iridium and oxidation of the resulting iridium-rhenium alloy had been identified as the life limiting mechanism for Ir/Re rockets, with 20 percent rhenium concentration at the inner wall surface determined as the failure criterion. Further oxidation testing of iridium/rhenium alloys is being performed to more clearly define the rhenium concentration level where iridium oxidation accelerates.

A potentially more rapid failure mechanism for Ir/Re rockets has been identified in recent testing of Ir/Re

rockets. All of the Ir/Re rocket testing in the initial technology programs were performed with either a cooled section between the chamber and injector or with a platinum/rhodium liner installed in the head end region of the chamber. No problems were experienced with the chambers tested in this manner. However, where Ir/Re chambers were directly welded to injectors, erosion or pitting of the iridium occurred in the head end region of the chamber.^{2,5,6} The reasons for this degradation of the iridium coating are not yet certain, but the phenomenon would pose a threat to the long-life, high-temperature advantages offered by this material system. The coating degradation has occurred in the head end, relatively low temperature region of the chamber, where the flowfield was probably still mixing and where oxidizers and combustion radicals may be present at the wall. In the instances when Ir/Re chambers were run with a cooled-section or liner, the iridium was not exposed to the flowfield until it was probably well mixed and nearly completely combusted. It is suspected, based on circumstantial evidence, that the iridium degradation is a result of iridium reactivity with combustion radicals, oxidation of the underlying rhenium through the iridium grain boundaries, or high partial pressures of oxidizers at the wall directly oxidizing the iridium.

Testing of 22 N chambers on GH2/GO2 would seem to support this line of reasoning. One chamber was tested for over 14 hours at mixture ratios from 3 to 8, but with the overwhelming majority of time at mixture ratios between 3 and 4. Testing stopped because of a facility-related failure and posttest material analysis indicated that the chamber could have run for much longer. Another Ir/Re chamber was run at mixture ratio 6, but had a coating failure after 2.6 hours. The iridium had ruptured in the barrel section of the chamber. Both chambers were run with a water-cooled section between the injector and chamber, so they were exposed to well mixed flows. The mixture ratio 6 environment, however, had high partial pressures of oxygen, atomic oxygen, and hydroxyl compared to the low mixture ratio environment. Material analyses of these chambers and of as-fabricated samples of Ir/Re, along with experiences in industry and any required laboratory scale testing, will be used to determine the mechanisms for this iridium degradation phenomenon.

The majority of Ir/Re chambers tested to date have been fabricated using chemical vapor deposition (CVD).⁷ The CVD process involves the passing of a gaseous compound of the desired material over a heated mandrel. The material is deposited on the mandrel due to thermal decomposition of the gas at the mandrel surface. Iridium and then rhenium is deposited on the molybdenum mandrel, with the mandrel chemically etched out after the CVD processing. Alternate methods of fabricating Ir/Re chambers are being explored including powder metallurgy rhenium, electrodeposition of rhenium and iridium, arc plasma spraying of rhenium, and the use of a rolled, welded iridium liner.

The ability of the Ir/Re engine to survive the launch vibration environment after being hot fired in acceptance tests is critical to the eventual use of the material system. The thermomechanical property database for rhenium, as fabricated by CVD and other methods, is limited, therefore a program is underway to procure rhenium samples fabricated through various means and by various manufacturers and conduct testing to determine the ultimate strength, yield strength, modulus, low cycle fatigue, and creep properties at room and elevated temperatures. It is particularly important to determine the thermomechanical properties of annealed rhenium samples, as this will most closely simulate the behavior of a chamber that has been through acceptance testing. The ability to join the Ir/Re chambers to injectors and nozzle extensions composed of other materials is also a concern.

CERAMIC OXIDE/IRIDIUM/RHENIUM

Ceramic oxide coatings for Ir/Re chambers are being investigated⁸ as a way to significantly extend thruster lifetimes and allow operation in more aggressively oxidizing environments, such as stoichiometric (or higher mixture ratio) hydrogen/oxygen. The oxide coatings would serve as a thermal and diffusion barrier for the iridium coating, lowering the temperature at the iridium surface, while also preventing the ingress of oxidizers and egress of iridium oxides. The oxide coatings could also serve as a protector against iridium degradation (assuming that iridium reactivity with combustion radicals or oxidation is the cause). The primary issue with these coatings is their ability to withstand the thermal shock of combustion and repeated thermal cycling.

Seven Ir/Re chambers with yttria-stabilized zirconia and yttria-stabilized hafnia coatings were tested.⁹ The chamber structures, coating thicknesses, and fabrication techniques are proprietary to the manufacturer. The purpose of the yttria stabilization is to suppress a phase transformation that occurs at 1650 °C and 1100 °C for hafnia and zirconia, respectively. The nominal test matrix began with short duration (5 and 15 second) tests at mixture ratio 4. This testing was performed to determine the ability of the coating to withstand the thermal shock of combustion, with little or no oxidizers present. Testing was then performed at mixture ratio 6 and 8 (stoichiometric), increasing both the temperature and oxygen partial pressure of the flowfield. At each of these mixture ratios, short (5 and 15 second) and longer duration (300 second) testing were performed. This gave a nominal time of 14 firings and 22 minutes for each chamber.

All seven chambers survived the initial testing intact. In five of the chambers there was cracking, but no spalling of the oxide coating. The other two chambers did not experience cracking or any evidence of coating degradation. Six of the chambers were further tested in a series of ten, 60-second duration runs at mixture ratio 11. Though temperature does not increase at mixture ratios above stoichiometric, the amount of oxygen, atomic oxygen, and hydroxyl increases significantly. The high mixture ratio testing, then, determined the ability of the coating to operate in an aggressively oxidizing environment. Two of the chambers began to show evidence of spalling at the front end in the high mixture ratio testing. Another chamber lost its coating from the throat downstream. The seventh chamber was tested at mixture ratio 16. After 30 firings and 29.2 minutes at mixture ratio 16, burn-through occurred in the converging section of the thruster. The chambers will be sectioned for material analyses. The most promising structures will be fabricated and tested further.

CERAMIC MATRIX COMPOSITES

Ceramic matrix composite (CMC) chambers are also being investigated as a high-temperature material system for radiation-cooled rockets. CMC materials are a lightweight alternative to Ir/Re and also have the advantage of being chemically compatible with the combustion products of hydrazine/chlorine pentafluoride, a propellant combination under consideration for apogee and planetary propulsion applications. There has been extensive development of CMC chambers for divert and similar type propulsion systems. These chambers were always porous to a degree, however in the divert propulsion application, reduction of weight and volume were the primary design drivers and lifetimes were usually under a minute. For the longer life apogee and attitude control propulsion functions, densification of these engines is a major technology issue to be resolved.

Composites composed of silicon carbide fibers and silicon carbide matrix are the most developed chamber

materials for apogee and attitude control applications, with extensive testing of 22 N and 2000 N engines at 1595 °C.¹⁰ A higher temperature CMC option is a composite composed of graphite fibers and a refractory carbide matrix. Hafnium carbide doped with tantalum carbide is a very promising matrix for this material system.¹¹ Oxidation protection for the graphite fibers are dependent on the in-situ formation of the oxide from the matrix. Hafnia, as mentioned above, undergoes a phase transformation at 1100 °C, which results in a significant volume change and subsequent spalling of the coating after repeated thermal cycling. The presence of tantalum carbide in the matrix leads to a mixed hafnia/tantala layer being form. The technology issue needed to be resolved is the proper percentage of tantalum carbide in the matrix in order to assure the in-situ formation of a stable oxide.

OTHER CANDIDATE MATERIALS

There are other material systems that could be considered (depending on the application) for radiation-cooled rockets. A chamber fabricated from pure iridium would eliminate the rhenium/iridium diffusion mechanism, but there are concerns about its structural integrity as a rocket engine. Tantalum-10% tungsten alloy and woven carbon-carbon fibers could serve as high-temperature substrates, but requires a suitable oxidation-resistant coating for any type of long life applications. Platinum-10% rhodium alloy and grain-stabilized platinum are excellent oxidation-resistant materials that could be considered for very long life (tens of hours), but relatively low temperature (1650 °C) applications. Cermets and intermetallic compounds have also been considered for high temperature rocket operation, but there is a very limited experience base with them.

REFERENCES

1. Wooten, J.R. and Lansaw, P.T., "High-Temperature, Oxidation-Resistant Thruster Research", Final Report, Contract NAS3-24643, NASA CR-185233, February 1990.
2. Schneider, S.J., "Low Thrust Chemical Rocket Technology", IAF Paper 92-0669, NASA TM-105927, September 1992.
3. Schoenman, L., "4000 °F Materials For Low Thrust Rocket Engines", AIAA Paper 93-2406, June 1993.
4. Hamilton, J.C., et. al., "Diffusion Mechanisms in Iridium-Coated Rhenium for High-Temperature, Radiation-Cooled Rocket Thrusters", AIAA Paper 91-2215, June 1991.
5. Wood, R., "Development Experience With 22N Bipropellant Using Columbium and Rhenium Thruster", AIAA Paper 92-3801, July 1992.
6. Wood, R., "Experiences With High Temperature Materials For Small Thrusters", AIAA Paper 93-1963, June 1993.
7. Harding, J.T., et. al., "Iridium-Coated Rhenium Thrusters by CVD", NASA TM-101309, September 1988.
8. Tuffias, R.H., et. al., "Enhanced Oxidation Protection For Iridium-Lined Rhenium Thrust Chambers", Final Report, Contract NAS3-25468, June 1990.
9. Reed, B.D., "Testing and Evaluation of Ceramic Oxide-Coated Iridium/Rhenium Chambers", to be presented at the 1993 JANNAF Propulsion Meeting, November 1993.
10. Mathieu, A.C., et. al., "Ceramic Matrix Composite Materials For a Low Thrust Bipropellant Rocket Engine", AIAA Paper 90-2054, July 1990.
11. "Hafnium-Tantalum Carbide Composite Rocket Thruster Development", Final Report, Contract NAS3-26243, October 1991.

MOLECULAR GAS DYNAMICS APPLIED TO LOW-THRUST PROPULSION

Donna Zelesnik
Ohio Aerospace Institute

Paul F. Penko
NASA Lewis Research Center

Iain D. Boyd
Cornell University

SUMMARY

The Direct Simulation Monte Carlo method is currently being applied to study flowfields of small thrusters, including both the internal nozzle and the external plume flow. The DSMC method is employed because of its inherent ability to capture nonequilibrium effects and proper boundary physics in low-density flow that are not readily obtained by continuum methods. Accurate prediction of both the internal and external nozzle flow is important in determining plume expansion which, in turn, bears directly on impingement and contamination effects.

INTRODUCTION

An important consideration in placing small electric thrusters on satellites is the effect the plumes may have on contamination and heating of solar arrays, instrumentation and other subsystems, as well as disturbance torques that may be induced by impingement on various spacecraft surfaces. Assessment of interactions between the spacecraft and thruster requires an accurate description of the expanding plume from the nozzle using the appropriate fluid dynamic models.

The current work is specifically directed at applying gas dynamics on the molecular level to the phenomena associated with viscous flows in nozzles and plumes of small electrothermal thrusters, such as arcjets and high-temperature resistojets, designed for satellite stationkeeping and attitude control. Of particular interest is the prediction of plume expansion, especially in the off-axis region where the plume may impinge on spacecraft surfaces. A continuum code based on the Navier-Stokes' equations is also applied, with the results used to scale the grid and provide inflow conditions for the molecular model.

In prior work,^{1,2} the flow of nitrogen in and from a nozzle was computed with two numerical techniques: one based on continuum theory that numerically solved the Navier-Stokes equations for compressible flow,³ and one based on a stochastic model of kinetic theory that used the direct-simulation Monte Carlo (DSMC) method pioneered by Bird⁴ and modified by Boyd.⁵ Each was applied to solution of a low-density, viscous gas flow in a converging-diverging nozzle of conical shape that simulated flow in a resistojet. This work demonstrated that the numerically intensive DSMC technique could be applied readily to a low-density nozzle flow, where the flow varied from continuum at the throat to rarefied at the

exit plane and also demonstrated that results from the DSMC method matched well with experimental measurements of Pitot pressure and flow angle made in the plume.

The DSMC code developed by Boyd is employed in the current study to assess the effect of nozzle shape on plume expansion and surface impingement. Nozzles of conical, trumpet, and bell shapes are considered with flow rates of nitrogen at 6 mg/s and helium at 2.4 mg/s. The nozzle geometries and flow conditions are given in Tables 1 & 2. To demonstrate the utility of DSMC to predict potential impingement effects and to assess the validity of a semi-empirical model commonly used for impingement analysis, comparisons are made of density contours produced by the DSMC code with those obtained from Simons' method.⁶

THE DSMC METHOD

The DSMC code applied in this study simulates the flowfield in two-dimensional, axisymmetric coordinates and utilizes the VHS gas model for determination of collisional cross-sections. Rotational energy exchange is computed with the probability model of Boyd.⁷ The flows are assumed to be both chemically and vibrationally frozen.

The computational grids used in the current study are based on continuum flowfield solutions from RKRPLUS.⁸ The mesh for the nozzle flow consists of 250x88 cells and 800,000 particles are used in the simulation. The nozzle flow simulation begins just downstream of the throat, in the diverging section, and uses results from the continuum code for the inflow surface. The performance of the DSMC code on a Cray/YMP for this case is 1.08×10^{-6} CPU seconds/particle/time step.

The nozzle and plume flows are simulated separately due to the large variation in density between the two regions. A mesh consisting of 130x96 cells is used for the plume simulation with 48 particles per cell. An inverse-squared relation for density with distance from the nozzle exit plane is used to scale the cell dimensions. The plume simulations require 14.4×10^{-6} CPU seconds/particle/time step on an IBM RS/6000 workstation.

SAMPLE OF RESULTS

Isograms of Mach Number are given in Fig. 1 for the internal flow of nitrogen for each of the three nozzle shapes. The nozzles have the same exit-to-throat area ratio of 225:1 but differ in length because of the contour. The figure illustrates the distinct flow structure of each shape. The conical shape gives the maximum expansion contrasted to the bell contour, derived from the classical Rao design methodology, that restricts expansion of the flow to the point of causing viscous deceleration from a maximum Mach Number of about 6 in the internal portion of the nozzle to a Mach Number of about 5 at the exit plane.

To quantify differences in plume expansion for the various nozzle shapes, density contours along

arcs of various radii originating from the center of the exit plane are given in Fig. 2. The curves are normalized by the density on the plume axis (0°) for each case. In Fig. 2a (arc radius = one exit dia.) the density for the trumpet nozzle is higher than for the cone and bell nozzles. The effect of nozzle contour on plume shape, however, diminishes with arc radius as is readily apparent by the similarity of the curves in Fig. 2b (arc radius = 5 exit dia.).

Comparison of density contours for the conical nozzle from the DSMC method with the Boynton-Simons' model⁶ for the expansion of the nozzle core flow are compared in Fig. 3 along a radial line 30° off the plume axis extending from the centerline of the nozzle exit plane to 0.1 m into the plume. The Boynton-Simons' model predicts a plume density about an order of magnitude higher than the DSMC simulation.

CONCLUSIONS

The DSMC technique is a practical tool for prediction of nozzle and plume flow, and assessing the effect of plume expansion on surface impingement for small thruster nozzles characterized by low-density, highly viscous flow. The prediction of plume density from the DSMC method for the conical nozzle of this study is substantially lower than from the widely used Boynton-Simon model. As the results are preliminary and significant, they will be investigated further in continuation of this work.

REFERENCES

1. Boyd, I.D., et al., "Experimental and Numerical Investigations of Low-Density Nozzle and Plume Flows of Nitrogen," *AIAA Journal*, Vol. 30, No. 10, October 1992, pp. 2453-2461.
2. Penko, P.F., et al., "Measurement and Analysis of a Small Nozzle Plume in Vacuum," *J. of Propulsion and Power*, Vol. 9, No. 4, July-August 1993, pp. 646-648.
3. Cline, M.C., "Computation of Two-Dimensional, Viscous Nozzle Flow," *AIAA Journal*, Vol. 14, No. 3, 1976, pp. 295-296.
4. Bird, G.A., *Molecular Gas Dynamics*, Oxford University Press, London, 1976.
5. Boyd, I.D., "Vectorization of a Monte Carlo Simulation Scheme for Nonequilibrium Gas Dynamics," *J. Computational Physics*, Vol. 96, 1991, pp. 411-427.
6. Legge, H., "Plume Impingement Forces on Inclined Flat Plates," Proc. 17th International Symposium on Rarefied Gases, Aachen, Germany, July 1990, pp. 955-962.
7. Boyd, I.D., "Rotational-Translational Energy Transfer in Rarefied Nonequilibrium Flows," *Physics of Fluids A*, Vol. 2, March 1990, pp. 447-457.
8. Weiss, J.M., "Analysis of Reacting Flowfields in Low-Thrust Rocket Engines." Ph.D. Dissertation, December 1992, Dept. of Mechanical Engineering, The Pennsylvania State University, University Park, PA.

Table 1: Nozzle Geometries

	Cone	Trumpet	Bell
Throat Diameter	0.635 mm	0.635 mm	0.635 mm
Exit Diameter	9.526 mm	9.526 mm	9.526 mm
Area Ratio, (A/A*)	225	225	225
Exit Half-Angle	20°	40°	10°
Diffuser Length	12.301 mm	12.301 mm	16.04 mm

Table 2: Nozzle Flow Conditions

Propellant	Nitrogen	Helium
Flow Rate	6.0×10^{-6} kg/s	2.4×10^{-6} kg/s
Total Pressure, P_0	9100 Pa	10360 Pa
Total Temperature, T_0	294 K	297 K
Wall Temperature	298 K	298 K
Throat Reynolds Number	700	250

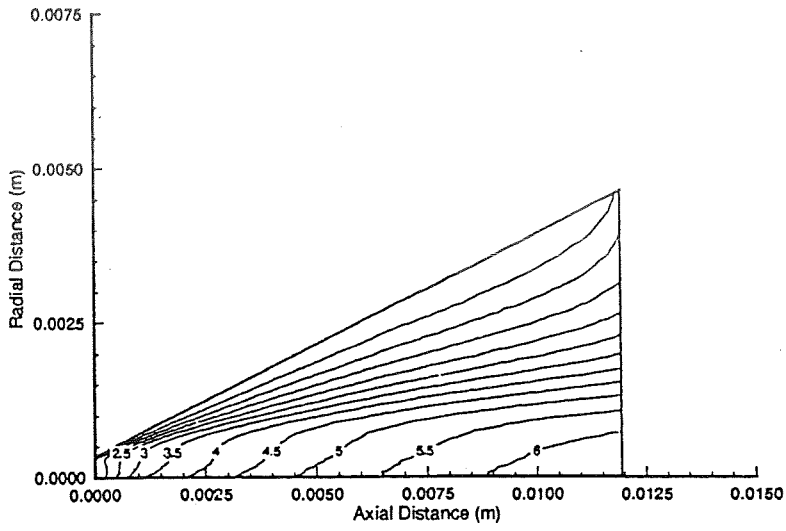


Fig. 1a. Mach no. contours of N_2 flow through conical nozzle

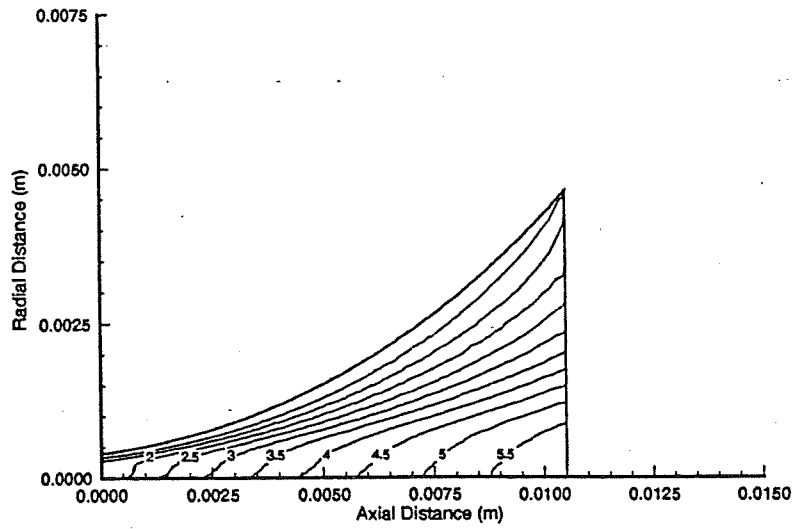


Fig. 1b. Mach no. contours of N_2 flow through trumpet-shaped nozzle

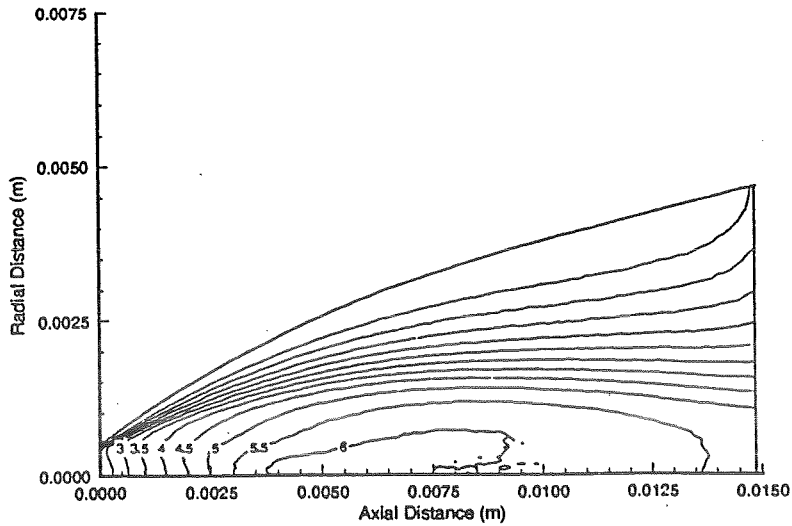


Fig. 1c. Mach no. contours of N_2 flow through bell-shaped nozzle (short)

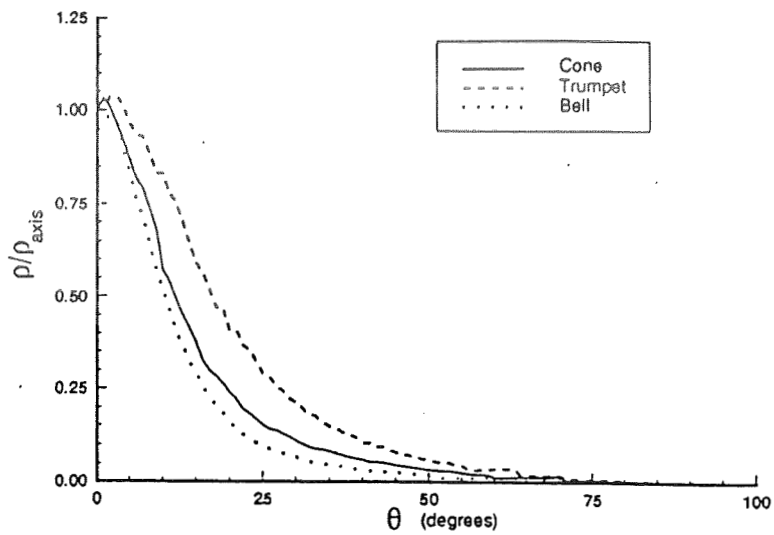


Fig. 2a. Normalized density vs. theta at arc radius = 1 exit diameter

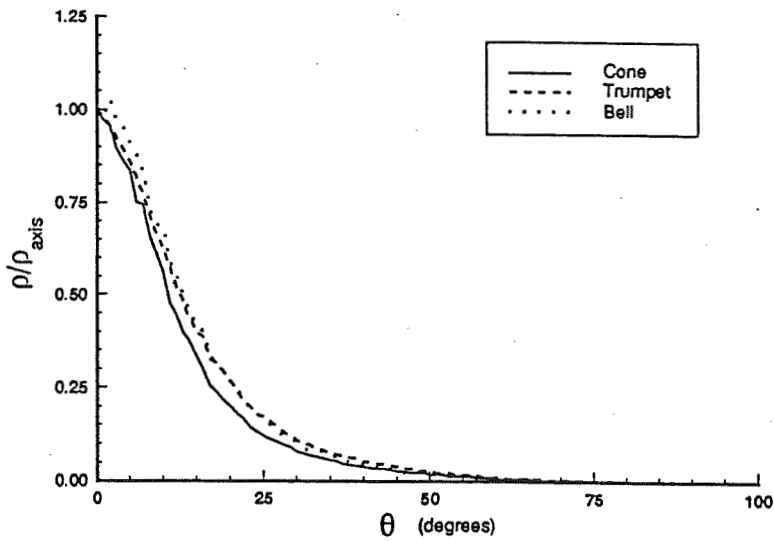


Fig. 2b. Normalized density vs. theta at arc radius = 5 exit diameters

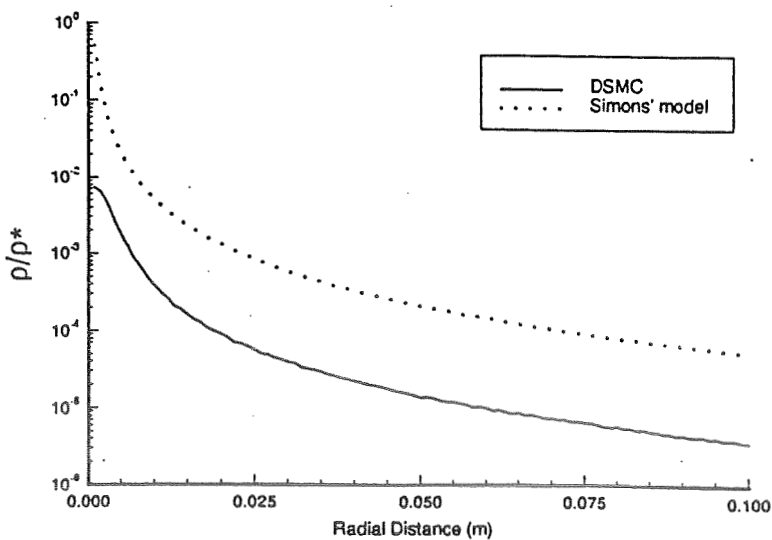


Fig. 3. Normalized density vs. radial distance at theta = 30°

COMPUTATIONAL FLUID DYNAMICS (CFD)
APPLICATIONS IN ROCKET PROPULSION ANALYSIS AND DESIGN

P. K. McConnaughey, R. Garcia, L. W. Griffin, J. H. Ruf
NASA George C. Marshall Space Flight Center

ABSTRACT

CFD has been used in recent applications to affect subcomponent designs in liquid propulsion rocket engines. This paper elucidates three such applications for turbine stage, pump stage, and combustor chamber geometries. Details of these applications include the development of a high turning airfoil for a gas generator (GG) powered liquid oxygen (LOX) turbopump single-stage turbine using CFD as an integral part of the design process. CFD application to pump stage design has emphasized analysis of inducers, impellers, and diffuser/volute sections. Improvements in pump stage impeller discharge flow uniformity have been seen through CFD optimization on coarse grid models. In the area of combustor design, recent CFD analysis of a film cooled ablating combustion chamber has been used to quantify the interaction between film cooling rate, chamber wall contraction angle, and geometry and their effects of these quantities on local wall temperature. The results are currently guiding combustion chamber design and coolant flow rate for an upcoming subcomponent test. Critical aspects of successful integration of CFD into the design cycle includes a close-coupling of CFD and design organizations, quick turnaround of parametric analyses once a baseline CFD benchmark has been established, and the use of CFD methodology and approaches that address pertinent design issues. In this latter area, some problem details can be simplified while retaining key physical aspects to maintain analytical integrity.

INTRODUCTION

A crucial challenge for CFD has been the application and integration of CFD analysis methods into the rocket propulsion system design process. Several factors encourage intensive analysis in support of the engine design process (e.g., the high cost of testing). Historically, geometric and flow process complexity has precluded efficient and timely analysis to support the design process. This paper briefly highlights three applications that advanced the design process and hardware concept through judicious application of CFD codes. These three applications include turbine stage design, impeller design optimization, and parametric assessment of a low cost ablative combustion chamber design. Discussion of these CFD design applications will be followed by a summary of analytical guidelines that allow for integration of CFD into the design process, and an assessment of future needs to further mature CFD for rocket engine design applications.

TURBINE STAGE DESIGN

Griffin and Huber (ref. 1) summarize advancements in the turbine design process that include the application of a range of CFD codes to both the fuel and LOX turbine stages of a GG engine. Huber, et al, (ref. 2) gives details of

the design process and how integration of several codes, approaches, and organizations contributed to the design of the LOX turbine for the Space Transportation Main Engine (STME). Coordination of these activities was through the CFD Consortium for Applications in Propulsion Technology (CAPT) as discussed by McConnaughey and Schutzenhofer (ref. 3), which allowed for efficient technology transfer from NASA and industry research efforts to a hardware development program.

Results of applying CFD codes to the fuel turbine (denoted G³T) as compared to conventional design methods can be seen in table 1. To achieve this increase in efficiency and decrease in blade count, airfoil camber was increased from 140 to 160 degrees. Analytical refinements to a preliminary design that led to such a highly loaded blade were made through the application of a multi-stage Euler analysis with a surface drag force model, an inverse design code for blade leading edge definition, full Navier-Stokes analysis of both the stator and nozzles (decoupled steady), and two-dimensional (2D) unsteady Navier-Stokes analysis of the first stage. It is with this latter analysis that the axial gap was adjusted to preclude a predicted unsteady shock between the stator and rotor. Optimal axial gaps based on unsteady CFD analysis led to a 24 percent decrease in blade dynamic and loading and a predicted efficiency gain of 1 percent relative to the preliminary design (ref. 1).

The development of the G³T turbine showed how CFD could be used to extend the design envelope of subsonic turbines used in GG engines, and these lessons and hardware design concepts were then applied to the STME LOX turbine. This turbine stage preliminary design was predicted to have an efficiency increase of two points relative to conventional meanline design methods, and further refinement of the design was a result of CFD analysis. This analysis includes multi-stage Euler analysis, steady three-dimensional (3D) Navier-Stokes analysis, and 2D unsteady Navier-Stokes analysis. As in the G³T turbine, unsteady stage analysis was used to adjust axial spacing of the stator and rotor, and both the modified Euler and 3D Navier-Stokes analysis predicted a flow separation downstream of the rotor that was removed by changing blade lean until the analysis predicted elimination of the separation region (refs. 1 and 2). A grid used for inviscid analysis of the design is seen in figure 1.

To summarize the impact of CFD on turbine stage design for rocket propulsion systems, the incorporation of Euler and both steady and unsteady Navier-Stokes analyses have led to advanced designs that extended the design envelope with increased performance and turning angle such that turbine part count and stage number are decreased.

PUMP STAGE DESIGN

CFD analysis of the STME fuel pump impeller has led to comparable advances in both hardware concepts and design methodology comparable to the turbine stage design. Prior to this design effort, a significant effort in benchmarking CFD codes for inducer and impeller flows was completed, and continues to be in progress. As seen in Garcia, et al, (refs. 4 and 5), a preliminary design of the STME fuel impeller was completed using current design methodology,

and then optimized using 3D Navier-Stokes analysis. The impeller was designed to minimize exit flow distortion, and hence, unsteady diffuser loads while maintaining or increasing impeller performance. Variation in impeller exit flow velocities for a range of CFD code predictions can be seen in figure 2. This optimized impeller design was then used to evaluate non-standard impeller design changes that would lead to further reduction in flow distortion and enhanced stage performance. Design changes evaluated included tandem (or offset) bladed impellers, length and location of partial blades, the use of pressure side/suction bleed holes at the shroud, and significant blade lean that limits the flow overturning that contributes to the exit distortion level. The latter design incorporating a change of blade lean was seen to be most effective in reducing impeller exit flow distortion.

The net result of this CFD-based pump stage design activity (also through the CFD CAPT) has been the development of advanced impeller hardware concepts and the integration on CFD into the pump stage design cycle. Even though computational grids may be coarse by some standards, both inviscid and viscous CFD analyses are routinely used to support inducer and impeller design for rocket engines at the major manufacturers and design organizations. It is in the use of benchmarked codes for parametric design assessment that CFD has and will continue to play a key role in advanced pump stage design.

COMBUSTION CHAMBER DESIGN

A recent example of CFD used to support combustion chamber design is assessment of both injection coolant schemes and chamber geometry for an ablative insert chamber design. This combustion chamber design is associated with the Advanced Technology Low Cost Engine (ATLCE) where parametric assessment of coolant injection mass, injection velocity, and chamber geometry and their effect on wall temperature was completed using a Navier-Stokes code. In this advanced engine, simplicity is maximized and cost is minimized through the use of radiatively cooled composites and ablative liner materials. New materials (such as silica phenolics) have lower ablation rates, but material behavior and properties at higher temperatures are not well characterized. Thus, the objectives of this analysis were to support a preliminary design for a hot-fire chamber characterization test while minimizing risk through lowering wall temperatures to below a known acceptable value (3800 degrees R). The code used in this study was previously benchmarked for coolant jet injection heat transfer (ref. 6), and a similar approach was used for this design application with the exception of some turbulence model modifications. The chamber geometries considered are seen in figure 3, with the range of parameters for injection and predicted maximum wall temperatures seen in table 2. A Taguchi approach was used in the parametric assessment, and the 'best' design was predicted to be the constant contraction chamber geometry with a 'low' coolant injection velocity and a coolant mass flow rate of 3.6 lbm/sec. Parametric analysis indicates this flow rate could be reduced to 2.6 lbm/sec while providing some margin relative to the chosen material limit. These results were provided to the designer to then complete the combustion chamber design from a system perspective. It is expected that the chamber will be fabricated and tested at NASA/Marshall Space Flight Center in the near future.

SUMMARY AND FUTURE NEEDS

Key aspects in these analyses that allowed for timely completion of design parametrics include the use of benchmarked Navier-Stokes codes for the chosen range of applications, close coupling between the design group and CFD analyst, and an understanding of key physical aspects of the flow problem. The latter point allows for the CFD analyst to assess important design issues and not overcomplicate the CFD analysis. Continued development and maturation of this philosophy should lead to further integration of CFD methods into subcomponent design organizations.

Future requirements for CFD methodology and applications development to support design integration include the following: (1) The use of unstructured grids and/or expanded multiblock interface capabilities (e.g., chimera or patched) to address more complicated domains, (2) increasingly robust and efficient solution algorithms, (3) solution algorithms that are efficient and port to either moderate or massively parallel computer architectures, (4) design optimization techniques, (5) an assessment of the level of physical modeling necessary for a given design application, and (6) coupling of various discipline codes to support integrated engineering analysis. It is in this latter area that the unstructured approach allows for flexibility, albeit with some cost in code efficiency.

REFERENCES

1. Griffin, L. W., and F. W. Huber, "Advancement of Turbine Aerodynamics Design Techniques," ASME Paper No. 93-GT-370.
2. Huber, F. W., P. D. Johnson, X. A. Montesdeoca, R. J. Rowey, and L. W. Griffin, "Design of Advanced Turbopump Drive Turbines for National Launch System Application," AIAA Paper No. 92-322.
3. McConnaughey, P. K., and L. A. Schutzenhofer, "An Overview of the NASA/Marshall Space Flight Center Consortium for Applications in Propulsion Technology," AIAA Paper No. 92-3219.
4. Garcia, R., E. D. Jackson, and L. A. Schutzenhofer, "A Summary of the Activities of the NASA/Marshall Space Flight Center Pump Stage Technology Team," Proceedings of the 4th International Symposium on Transport Phenomena and Dynamics in Rotating Machinery.
5. Garcia, R., P. McConnaughey, and A. Eastland, "Activities of the Marshall Space Flight Center Pump Stage Technology Team," AIAA Paper No. 92-3222.
6. Tucker, P. K. and M. Croteau-Gillespie, "Combustion Devices Technology Team: An Overview and Status of STME-Related Activities," AIAA Paper No. 92-3224.

Table 1 - Comparison of Conventional Design and G³T (as predicted by meanline analysis)

	Conventional	G ³ T
No. of Stages	2	2
Work Split	70/30	50/50
Blade Turning	2.36 rad	2.79 rad
Max. Blade Mach No.	1.32	0.87
Efficiency	base	+9.8%
Airfoil Count	base	-55%

Table 2 - Maximum Temperature (degrees R) of ATLCE Combustion Chamber Wall from Parametric Study

	Geometry 1		Geometry 2		Geometry 3	
	low	high	low	high	low	high
Boundary Layer Injection Vel.						
Mass Injection Rate						
1.0 lbm/sec	5400	5500	5200	-	-	-
2.6 lbm/sec	4000	-	3540	-	-	-
3.6 lbm/sec.	3400	3900	2950	-	3550	-

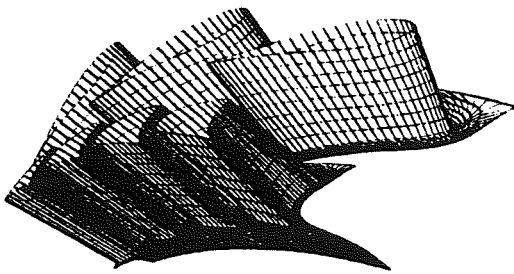
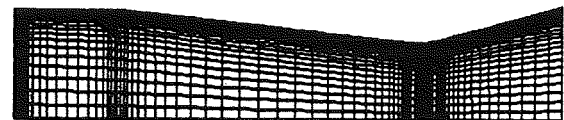
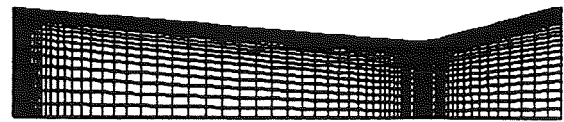


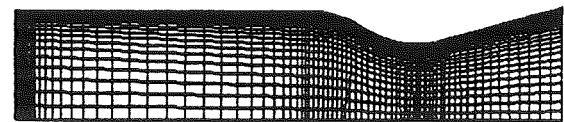
Figure 1 - STME LOX Turbine Geometry and Grid (Ref. 1)



Geometry 1



Geometry 2



Geometry 3

Figure 2 - Geometries Analyzed for Ablative Combustion Chamber Design

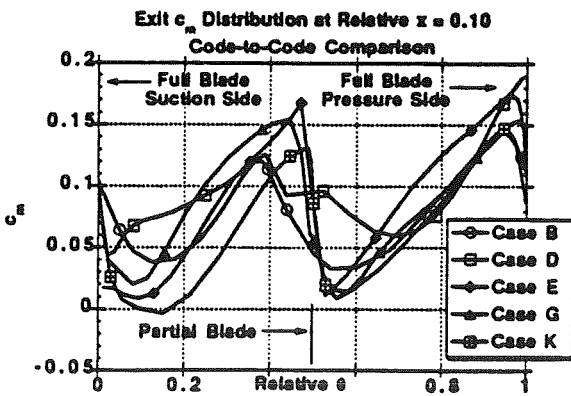


Figure 3 - STME Impeller Blade-to-Blade Exit C_m Distribution Near Shroud ($x = 0.10$) (Ref. 5)

EFFICIENCY AND RELIABILITY ENHANCEMENTS IN PROPULSION FLOWFIELD MODELING

Philip E.O. Buelow*, Sankaran Venkateswaran†, Charles L. Merkle‡
Propulsion Engineering Research Center
Department of Mechanical Engineering
The Pennsylvania State University

SUMMARY:

The implementation of traditional CFD algorithms in practical propulsion related flowfields often leads to dramatic reductions in efficiency and/or robustness. The present research is directed at understanding the reasons for this deterioration and finding methods to circumvent it. Work to date has focussed on low Mach number regions, viscous dominated regions and high grid aspect ratios. Time derivative preconditioning, improved definition of the local time stepping, and appropriate application of boundary conditions are employed to decrease the required time to obtain a solution, while maintaining accuracy. A number of cases having features typical of rocket engine flowfields are computed to demonstrate the improvement over conventional methods. These cases include laminar and turbulent high Reynolds number flat plate boundary layers, flow over a backward-facing step, a diffusion flame, and wall heat-flux calculations in a turbulent converging-diverging nozzle. Results from these cases show convergence that is virtually independent of the local Mach number and the grid aspect ratio, which translates to a convergence speed-up of up to several orders of magnitude over conventional algorithms. Current emphasis is in extending these results to three-dimensional flows with highly stretched grids.

TECHNICAL DISCUSSION:

Propulsion flowfields contain a rich variety of physical processes. The combustion process in a rocket engine takes place at low flow speeds and is accompanied by very high rates of energy release and species generation. Although the Reynolds numbers are high, mixing and diffusion are critical to achieving combustion, and recirculation regions are often present near the injector face. Following combustion, the flow accelerates through the nozzle to supersonic speeds, where the Reynolds numbers are typically very high and there is little heat release, but recombination effects are important for performance predictions. This wide variety of physical processes and conditions presents a formidable challenge for CFD codes.

In order to design an efficient and reliable CFD code to solve these flowfields, one needs to address the issues which lead to a deterioration in code performance. Convergence rates and code robustness often suffer in practical problems due to any number of factors. For example, the initial conditions may be poorly specified, the grid resolution may be inadequate, very high grid stretching will generally be present, or there may be flow regimes present for which the algorithm was not designed to converge efficiently. An example of this latter issue occurs for traditional density-based algorithms in the presence of very low Mach numbers, as occurs in the combustion chamber. Density-based algorithms were designed for transonic and supersonic Mach number flows, but typically have difficulty computing low Mach number flows. The convergence rates of these algorithms decrease dramatically because of the wide disparity

*Graduate Research Assistant

†Research Associate

‡Distinguished Alumni Professor

between fluid particle and acoustic wave propagation speeds. Various researchers, including the present authors, have negated these detrimental effects through the use of time-derivative preconditioning [1-6] so that such schemes are now routinely used at low speeds. A related issue at low Reynolds numbers occurs where the disparity between wave propagation speeds and viscous diffusion rates controls the convergence. This has also been effectively addressed through time-derivative preconditioning [2,3,6].

The details of the preconditioning techniques used herein can be found in References [2],[3] and [7]. The basic technique is to premultiply the time derivative by an appropriate preconditioning matrix. For flows dominated by inviscid effects, the preconditioning matrix is designed to alter the acoustic speed of the governing system so that each of the inviscid time scales is of the same order. This allows a larger time step than the unaltered system. The preconditioned density-based system closely resembles a ‘pressure-based’ system at low Mach numbers, while reverting to the traditional density-based system at transonic and supersonic Mach numbers [8]. For viscous flows, there exists a time-scale disparity between the diffusive and the convective processes. At low Reynolds numbers, this disparity becomes strong enough to deteriorate the convergence rate. Typically the difficulty arises when the cell Reynolds number (*e.g.* $Re_{\Delta x} = u\Delta x/\nu$) becomes less than unity. Such Reynolds numbers are encountered in boundary layers, shear layers, recirculation regions, or anywhere the flow gradients are strong. In this case the previous preconditioning matrix is slightly altered so that the acoustic time scale is of the same order as the diffusive time scale [2].

It is also well known that the presence of large grid aspect ratios decreases the performance of conventional algorithms. Large grid aspect ratios are often required to resolve the steep gradients that occur in turbulent boundary layer calculations. Flow calculations in long, narrow ducts also give rise to large grid aspect ratios. The decreased performance in the presence of large grid aspect ratios occurs because of a wide disparity in the cell crossing times in the different coordinate directions. The difficulties caused by the large grid aspect ratios have been addressed by the present authors [7], and resulted in improvements that yield convergence rates that are orders of magnitude faster than the conventional algorithms in highly stretched grids for two-dimensional problems. Presently, these improvements only apply to the 2-D ADI scheme. In order to obtain enhanced convergence, three issues must be addressed. The choice of the local time step should be based on the minimum CFL number

$$\Delta t = \text{Max} \left[\frac{\text{CFL}\Delta x}{\lambda_x}, \frac{\text{CFL}\Delta y}{\lambda_y} \right]$$

where λ_x and λ_y are the acoustic eigenvalues in each of the coordinate directions. The boundary conditions should be applied before the governing equations are approximately factored, and the viscous preconditioning should be based upon the maximum von Neumann number, VNN (see Ref. [7]).

RESULTS:

To demonstrate the efficiency and reliability of the improved algorithm, the following test cases are presented: 1) turbulent flat plate boundary layer, 2) H_2/O_2 diffusion flame, 3) 2-D backward facing step, 4) turbulent rocket nozzle heat flux computation. Additional cases have been calculated; however, they are not presented here because of space limitations.

The first case is a Mach 0.1 turbulent flat plate boundary layer computation. The Reynolds number for this case is 8×10^5 , and the maximum grid aspect ratio (located adjacent to the wall) is 8000. The k- ϵ turbulence model was used for closure. Figure 1 displays the convergence history for the enhanced ADI algorithm (preconditioning + grid aspect ratio enhancements), and for the standard ADI algorithm. The enhanced algorithm converges in under 2000 steps, whereas the convergence for the standard algorithm flattens after a three order of magnitude drop in the residual and would require over 50,000 steps to converge to machine accuracy.

The H_2/O_2 diffusion flame consists of a central core flow of pure oxygen (Reynolds number of 200). The outer gas flow is pure hydrogen. The grid size used is 71×61 . Both reacting and nonreacting cases were computed, and the convergence for both cases using the enhanced algorithm are shown in Figure 2. For the reacting case, the reaction rates were reduced for initial start-up and gradually increased to their full level, which is represented by the initial portion of the convergence curve. Once the reactions are at the full level, the convergence rate is the same as the nonreacting case. Figure 3 shows contours of temperature and water mass fractions for the reacting case.

The geometry for the 2-D backward facing step corresponds to the one studied experimentally by Armaly *et al.* [9]. The length and width of the duct are 10 cm and 1 cm respectively, and the step height is 0.5 cm. A uniform grid of 101×61 is used. Convergence results are shown in Figure 4 for $Re = 100, 200, 300$ and 400. The residuals are shown sequentially because each case is used as the initial condition for the subsequent case. All Reynolds number cases converge at about the same rate of 7 orders of magnitude in 1000 steps. Table 1 shows the predicted primary recirculation zone lengths, normalized by the step height. Agreement between computations and measurements is excellent.

The final case shown is high Reynolds number turbulent flow through a converging-diverging nozzle with cooled walls. The incoming gas is at a stagnation temperature of 3500 K and the wall is maintained at 700 K. The grid size is 141×121 . For accuracy in heat flux predictions it is necessary to maintain a minimum y^+ of about one along the wall. The strong wall stretching results in grid aspect ratios that are as high as 2×10^6 in this region. Figure 5 shows the convergence for the standard algorithm and the enhanced algorithm. The enhanced algorithm converges in 2000 steps, whereas the standard algorithm would require over 50,000 steps to reach machine accuracy. Even though the standard algorithm converges about five orders of magnitude in 4000 steps, Figure 6 reveals that the wall heat flux is far from converged. In fact, even after 20,000 steps the wall heat flux is not quite fully converged in the throat region. This is because the convergence in the near wall region is much slower than the core flow due to the extremely large aspect ratios near the wall. Examination of the wall heat fluxes from the enhanced algorithm reveals that a fully converged solution is reached in just 400 iterations, indicating the flowfield in the near wall region and the core region converge at similar rates.

REFERENCES:

1. Turkel, E., "Review of Preconditioning Methods for Fluid Dynamics," NASA Contractor Report 189712, ICASE Report No. 92-47.
2. Choi, Y.-H. and Merkle, C. L., "The Application of Preconditioning to Viscous Flows," *Journal of Computational Physics*, Vol. 105, No. 2, April, 1993, pp. 207-223.
3. Venkateswaran, S., Weiss, J.M., Merkle, C. L. and Choi, Y.-H., "Propulsion-Related Flowfields Using the Preconditioned Navier-Stokes Equations," AIAA Paper 92-3437, July, 1992.
4. Shuen, J.-S., Chen, K.-H. and Choi, Y.-H., "A Time-Accurate Algorithm for Chemical Non-Equilibrium Viscous Flows at All Speeds," AIAA 92-3639, July, 1992.
5. van Leer, B., Lee, W. T. and Roe, P. L., "Characteristic Time-Stepping or Local Preconditioning of the Euler Equations," AIAA Paper 91-1552, June, 1991.
6. Godfrey, A. G., Walters, R. W. and van Leer, B., "Preconditioning for the Navier-Stokes Equations," AIAA Paper 93-0535, January, 1993.
7. Buelow, P.E.O., Venkateswaran, S. and Merkle, C. L., "The Effect of Grid Aspect Ratio on Convergence," AIAA Paper 93-3367, July, 1993.
8. Merkle, C. L., Venkateswaran, S. and Buelow, P. E. O., "The Relationship Between Pressure-Based and Density-Based Algorithms," AIAA 92-0425, 30th Aerospace Sciences Meeting, January, 1992, Reno, NV.

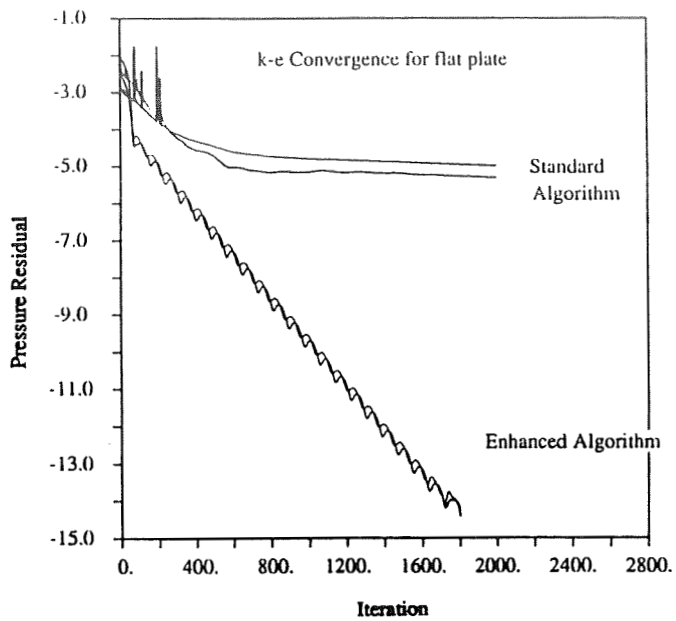


Figure 1: Convergence for turbulent flat plate boundary layer for standard and enhanced algorithm

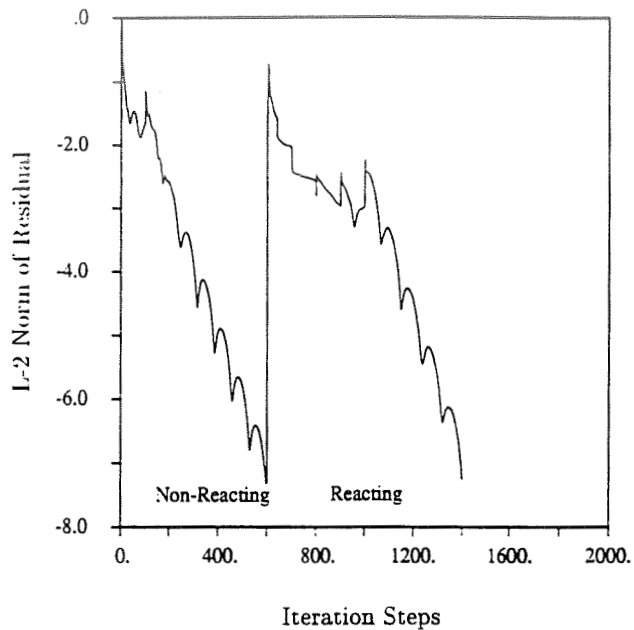


Figure 2: Convergence for nonreacting and reacting multi-species shear layer

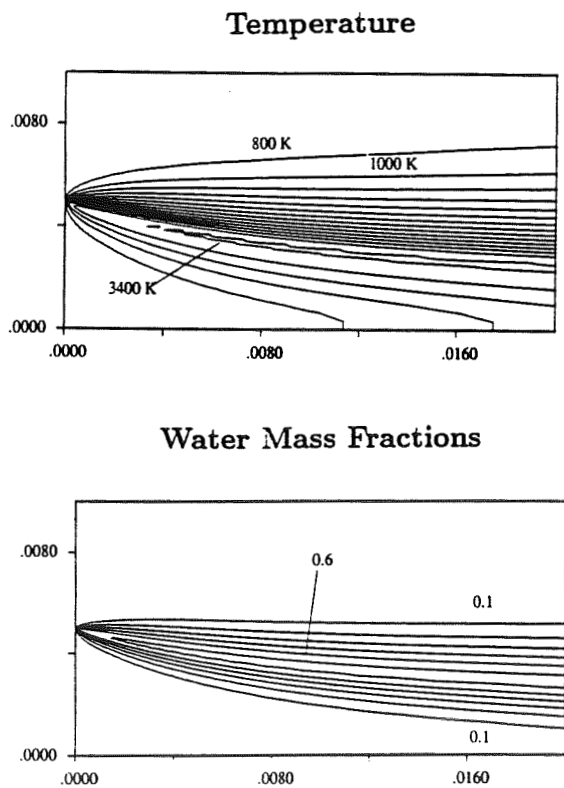


Figure 3: Contours of temperature and H_2O mass fractions for the reacting shear layer

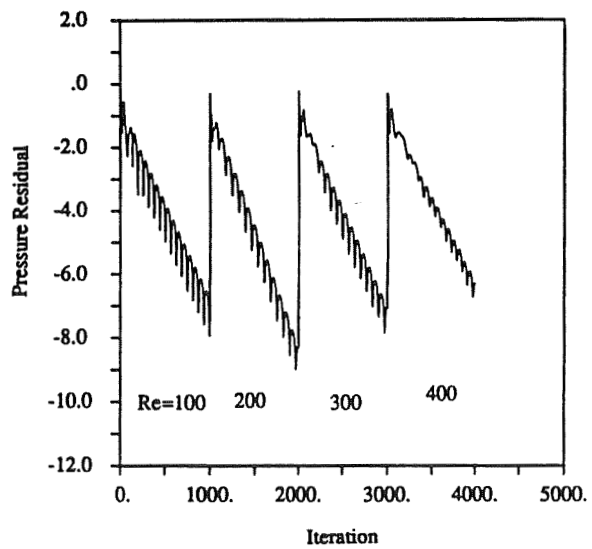


Figure 4: Convergence for backward facing step at various Reynolds numbers

Table I.
Reattachment Length vs. Reynolds Number
for Backward Facing Step

Reattachment Length, X_r/S

<u>Reynolds No.</u>	<u>Experiment [22]</u>	<u>Implicit</u>
100	3.0	3.0
200	5.0	5.0
300	6.8	6.6
400	8.6	8.0

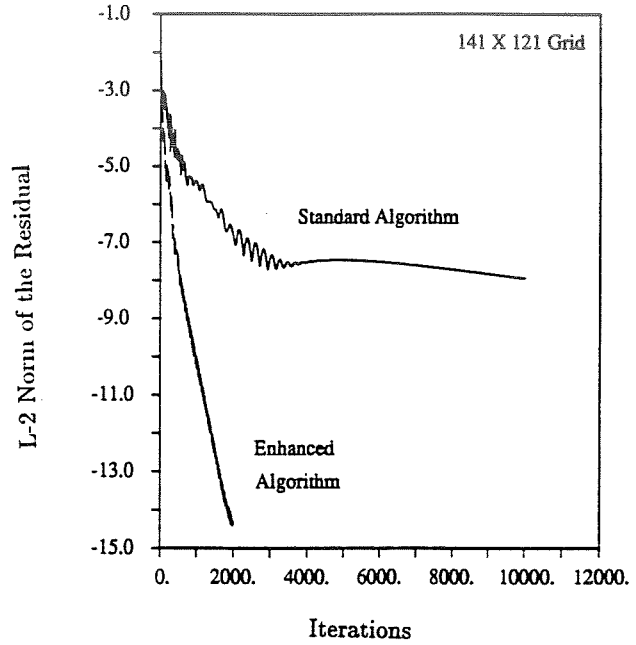


Figure 5: Convergence for turbulent nozzle computations for standard and enhanced algorithms

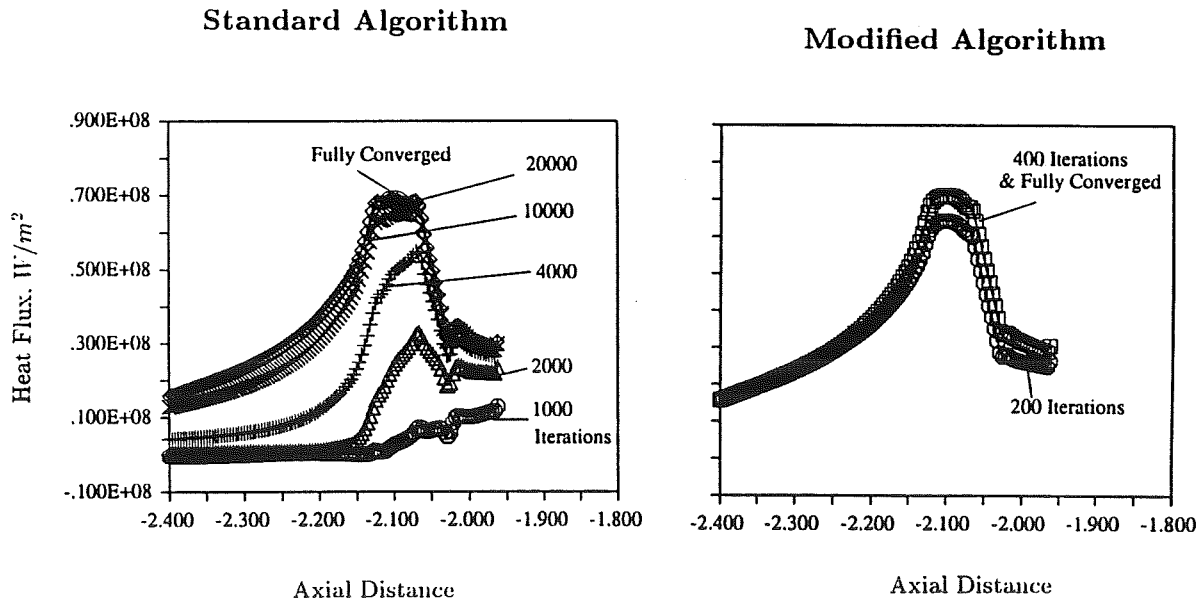


Figure 6: Wall heat flux results for standard and enhanced algorithms

COMPUTATION OF PROPULSION-RELATED FLOWFIELDS USING
UNSTRUCTURED ADAPTIVE MESHES

Jonathan M. Weiss and Jayathi Y. Murthy
Fluent, Inc.
10 Cavendish Ct.
Lebanon, NH 03766

Overview

In this paper, we describe a computational fluid dynamics (CFD) technique based on unstructured triangular/tetrahedral meshes. A finite-volume scheme is used in conjunction with a multi-stage Runge-Kutta algorithm. Convergence enhancements in the form of dual time-stepping and time-derivative preconditioning are used to overcome the limitations of conventional multi-stage schemes. The method is applied to propulsion-related flows and shown to perform satisfactorily.

Technical Discussion

Governing Equations and Discretization

The equations governing the unsteady flow of a multi-species fluid mixture may be written in integral Cartesian form for an arbitrary control volume, V , with surface, S , as follows:

$$\frac{\partial}{\partial t} \iiint W \, dV + \iint F \cdot dS + \iint G \cdot dS = \iint H \, dV \quad (1)$$

where

$$\begin{aligned} W &= [\rho, \rho v_x, \rho v_y, \rho v_z, \rho e, \rho Y_l]^T \\ F &= [\rho v, \rho v_x v + p \hat{i}, \rho v_y v + p \hat{j}, \rho v_z v + p \hat{k}, \rho e v + p v, \rho v Y_l]^T \\ G &= [0, \tau_{xi}, \tau_{yi}, \tau_{zi}, \tau_{ij} v_j + q, \rho \hat{v}_l Y_l]^T \\ H &= [0, 0, 0, 0, \dot{\omega}_l]^T \end{aligned}$$

Here ρ , v , e , and p are the density, velocity, total energy, and pressure of the fluid mixture, respectively. Y_l and $\dot{\omega}_l$ are the mass fraction and rate of production of the l -th chemical species. τ , q and \hat{v}_l are the viscous stress tensor, and the heat flux and diffusion velocity vectors, respectively.

The domain is divided into triangular/tetrahedral volumes and the governing equations discretized over these volumes using a cell-centered finite-volume approach.⁵ Odd-even decoupling due to the use of central-difference operators is damped by adding fourth difference artificial dissipation;² a first-order dissipative term is selectively added near discontinuities.

Preconditioning for Convergence Enhancement

The performance of the time-marching scheme at low Mach numbers is enhanced by using time-derivative preconditioning^{1, 4, 7} in the context of unstructured meshes. Equation (1) is modified as follows:

$$\Gamma \frac{\partial}{\partial t} \iiint \hat{W} \, dV + \iint F \cdot dS + \iint G \cdot dS = \iint H \, dV$$

where \hat{W} are a new set of primary dependent variables: $\hat{W} = [p, v_x, v_y, v_z, T, Y_l]^T$, and Γ is the preconditioning matrix:

$$\Gamma = \begin{bmatrix} \frac{1}{U_r^2} & 0 & 0 & 0 & 0 & 0 \\ \frac{v_x}{U_r^2} & \rho & 0 & 0 & 0 & 0 \\ \frac{v_y}{U_r^2} & 0 & \rho & 0 & 0 & 0 \\ \frac{v_z}{U_r^2} & 0 & 0 & \rho & 0 & 0 \\ \frac{h + \frac{\mathbf{v}^2}{2}}{U_r^2} - 1 & \rho v_x & \rho v_y & \rho v_z & \rho C_p & \rho(h_l - h_N) \\ \frac{Y_l}{U_r^2} & 0 & 0 & 0 & 0 & \rho \end{bmatrix}$$

Here U_r is a reference velocity, $U_r < \text{Min}(|\mathbf{v}|, U_c)$, where U_c is a characteristic speed of the flow such as the local speed of sound or a maximum velocity within the domain.

In the preconditioned system, time-step definition is based on the modified eigenvalues: λ_{\pm} , $|\mathbf{v}|$, $|\mathbf{v}|, \dots$ where

$$\begin{aligned} \lambda_{\pm} &= \frac{1}{2} \left[|\mathbf{v}| \left(1 + \kappa \beta U_r^2 \right) \pm c' \right] \\ c' &= \sqrt{|\mathbf{v}|^2 \left(1 - \kappa \beta U_r^2 \right)^2 + 4U_r^2} \\ \beta &= \left(\frac{\partial \rho}{\partial p} \Big|_T + \frac{\frac{\partial \rho}{\partial T} \Big|_p}{\rho C_p} \right) \end{aligned}$$

The parameter κ is included to provide time-step control at low Reynolds numbers.¹ When viscous effects become important, the preconditioning scheme alters the acoustic speed such that the CFL number is of the same order of magnitude as the von-Neumann number; thus optimal wave propagation speeds as well as optimum von-Neumann numbers result.⁷

Dual Time-Stepping for Unsteady Flows

To provide for efficient, time accurate solution of the governing equations, we employ dual time-stepping,³ adapted for use with an explicit multi-stage scheme. Here we introduce a preconditioned pseudo-time derivative term into (1) as follows:

$$\Gamma \frac{\partial}{\partial \tau} \iiint \hat{W} dV + \frac{\partial}{\partial t} \iiint \mathbf{W} dV + \iint \mathbf{F} \cdot d\mathbf{S} + \iint \mathbf{G} \cdot d\mathbf{S} = \iiint \mathbf{H} dV \quad (2)$$

Note that as $\tau \rightarrow \infty$, the first term on the LHS of (2) vanishes and (1) is recovered.

The time-dependent term in (2) is discretized in an implicit fashion by means of a second order accurate, three-point backwards difference in time and the pseudo-time derivative is driven to zero by means of the following multi-stage algorithm:

$$\begin{aligned} \hat{W}^{(0)} &= \hat{W}^{(k)} \\ \left[\Gamma + \frac{3}{2} \frac{\Delta \tau}{\Delta t} \frac{\partial \tilde{W}}{\partial \hat{W}} \right] (\hat{W}^{(i)} - \hat{W}^{(0)}) &= -\alpha_i \Delta \tau \left\{ \mathbf{R} \tilde{W}^{(i-1)} + \frac{1}{2\Delta t} (3\tilde{W}^{(i-1)} - 4\tilde{W}^{(n)} + \tilde{W}^{(n-1)}) \right\} \\ \hat{W}^{(k+1)} &= \hat{W}^{(m)} \end{aligned} \quad (3)$$

Here $i = 1, 2, \dots, m$ is the stage counter for the m -stage scheme, and k and n represent any given pseudo-time and physical-time level, respectively. Throughout the iterations on k , $\tilde{W}^{(n)}$ and

$\tilde{W}^{(n-1)}$ are held constant. As $\tau \rightarrow \infty$, $\tilde{W}^{(k+1)} \rightarrow \tilde{W}^{(n+1)}$. Note that the matrix on the LHS of (3) is inverted in a point-wise fashion and its inverse is readily derived analytically and need not be computed numerically. Note also that the physical time step, Δt , is limited only by the level of desired temporal accuracy. And the pseudo time-step, $\Delta \tau$, is determined by the multi-stage scheme, which here employs local time stepping and preconditioning for convergence enhancement.

Results

Rocket Engine Flowfield

To demonstrate the viability of using unstructured solution-adaptive meshes to compute transonic, internal, viscous flows typically found in space propulsion applications, the finite-volume, multi-stage method presented here is used to compute a transonic, converging/diverging nozzle flowfield. Figure 1 shows the unstructured triangular mesh used in these computations. This mesh consists of 6,877 cells. It has been adapted to gradients of velocity in order to resolve the boundary layer along the nozzle walls, and to gradients of pressure in order to better capture the oblique shock in the divergent section. Pressure contours within the nozzle, plotted on a logarithmic scale in Figure 2, depict the oblique shock that develops as the expanding flow is turned inward by the nozzle walls.

Flow Past Circular Cylinder

The time accurate, dual time-stepping scheme described above is applied to solve the unsteady, two-dimensional flow over a circular cylinder in crossflow at a Reynolds number, $Re = Ud/\nu = 75$. At this Reynolds number the flow is laminar and exhibits periodic unsteady behavior as vortices shed from the cylinder to form a Karman vortex street in the wake. The computational domain for this problem is chosen to extend 5 diameters upstream and 20 diameters downstream of the cylinder, with symmetry boundaries placed 5 diameters above and below. Details of the unstructured mesh in the vicinity of the cylinder are shown in Figure 3(a). The specified fluid is air at standard conditions with $U = 11.5 \text{ m/s}$ ($M = 3 \times 10^{-4}$) and $d = 1 \text{ cm}$. The predicted shedding frequency, f , is 1.67 s^{-1} , resulting in a Strouhal number, $St = fd/U = 0.146$. This compares reasonably with the measured value⁶ of 0.147. Contours of stream function in the vicinity of the cylinder at several times during the shedding cycle are shown in Figure 3(b). The physical time step, Δt is chosen to be 0.025 s and time periodic behavior is achieved in roughly 5 s beginning from an impulsive start from rest at $t = 0$. Twenty-five inner iterations are performed at each time level to achieve three orders of magnitude decrease in the x-momentum residual using the preconditioned, multi-stage scheme with a CFL of 2.7. Thus 600 iterations are required to resolve one time period of 0.6 s . This represents a 1000 time speed-up over global time stepping which, for this grid and these flow conditions, would have restricted the time step in each cell to roughly $1 \times 10^{-6} \text{ s}$.

Conclusions

A finite-volume, multi-stage algorithm based on an unstructured grid topology is presented. The use of solution adaption is demonstrated in the calculation of a typical space propulsion application. Dual time-stepping and time-derivative preconditioning are shown to provide efficient solution of unsteady, low speed flow on an unstructured mesh. The benefits of extending this method to low Mach number flows with heat release, and to incompressible flows with variable density are evident, and our efforts continue in that direction.

References

- ¹ Choi, Y.-H., and Merkle, C. L., "Time-Derivative Preconditioning for Viscous Flows," AIAA Paper 91-1652, June 1991.
- ² Jameson, A., Schmidt, W. and Turkel, E., "Numerical Solution of the Euler Equations by Finite Volume Methods Using Runge-Kutta Time Stepping Schemes," AIAA Paper 81-1259, June 1981.
- ³ Merkle, C.L. and Athavale, M.M., "Time-Accurate Unsteady Incompressible Flow Algorithms Based on Artificial Compressibility," AIAA Paper 87-1137.
- ⁴ Shuen, J.S., Chen, K.H. and Choi Y.H., "A Time-Accurate Algorithm for Chemical Non-Equilibrium Viscous Flows at All Speeds," AIAA Paper 92-3639, July 1992.
- ⁵ Smith, W., "Multigrid Solution of Transonic Flows on Unstructured Grids," *Recent Advances in Computational Fluid Dynamics, ASME Fluids Engineering Division, FED Vol. 103, ASME, NY, 1990.*
- ⁶ Tritton, D., "Experiments on the flow past a circular cylinder at low Reynolds numbers," *J.Fluid.Mech.*, Vol. 6, pp. 547-657.
- ⁷ Venkateswaran, S., Weiss, J.M. and Merkle, C.L., "Propulsion Related Flowfields Using the Preconditioned Navier-Stokes Equations," AIAA Paper 92-3437, July 1992.

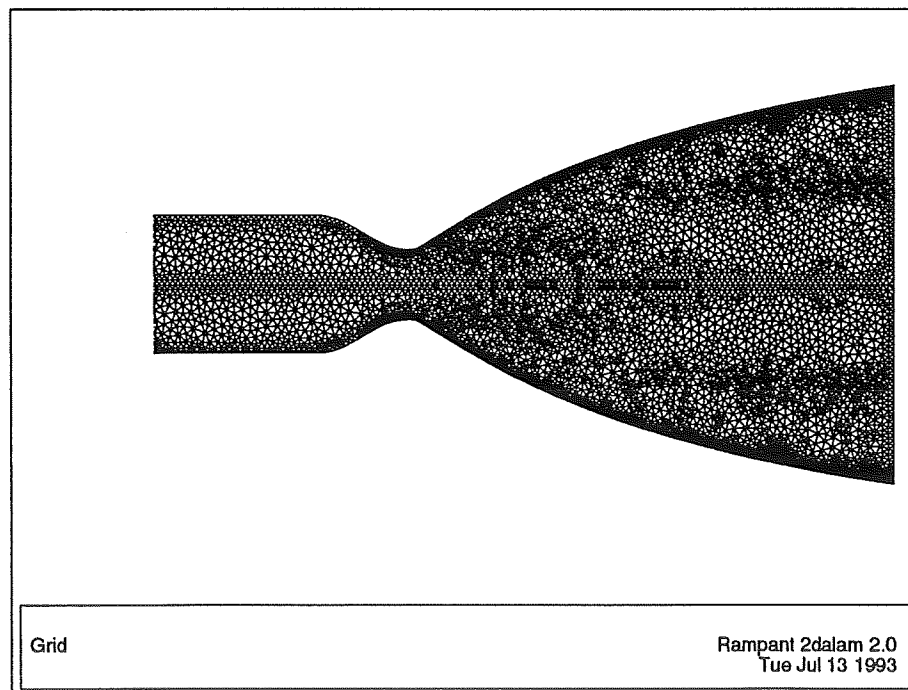


Figure 1: Unstructured, triangular mesh used for transonic, converging/diverging nozzle calculations.

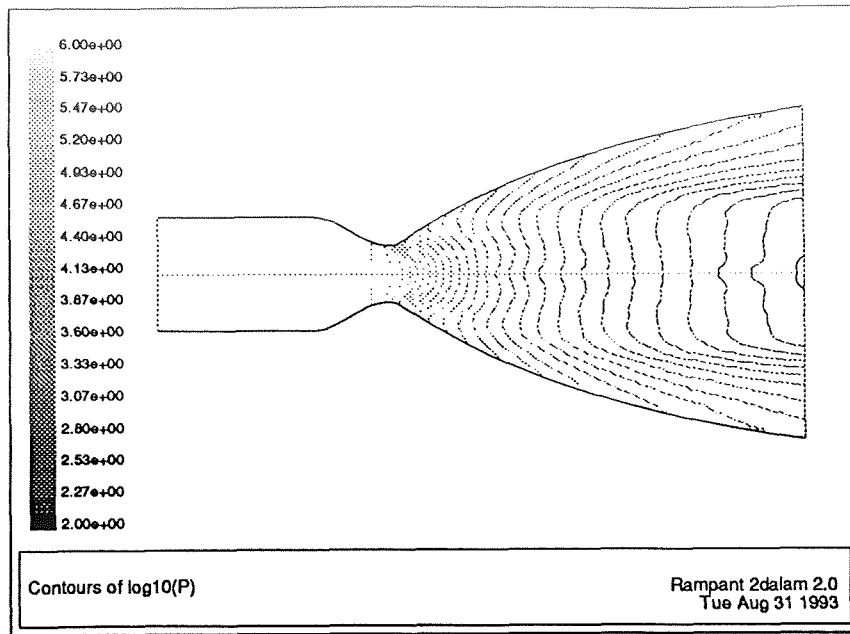


Figure 2: Pressure contours in convergent/divergent nozzle (plotted on logarithmic scale) computed using unstructured, triangular mesh.

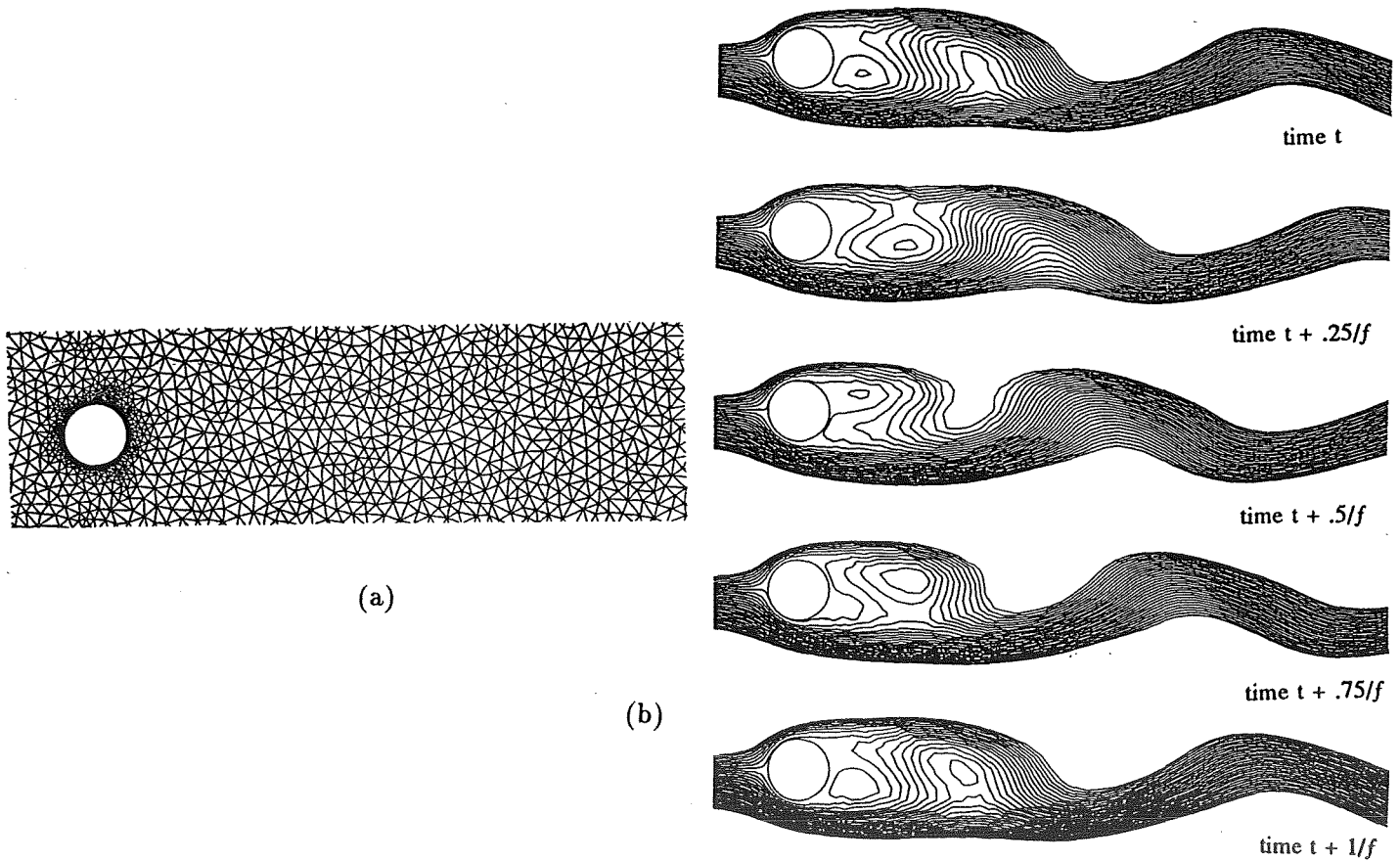


Figure 3: (a) Detail of unstructured mesh, and (b) contours of stream function about circular cylinder.

DUAL-BELL ALTITUDE COMPENSATING NOZZLES

M. Horn and S. Fisher

Rocketdyne Div., Rockwell International

BACKGROUND

All large liquid rocket booster engines in use today rely on fixed geometry bell nozzles. These nozzles limit engine performance, since they operate at optimal efficiency at only one point along the flight trajectory. Thus, during the design process, a compromise must be made between sea level and vacuum performance in order to best meet the demands of the mission within the nozzle performance limitations. An additional constraint is the nozzle expansion ratio, which must be limited to prevent the nozzle flow from separating at sea level, resulting in separation sideloads. Engine lift-off thrust requirements, weight and packaging issues may also limit the nozzle size. These factors all contribute to the limitations in the vacuum performance of an engine.

Conversely, a nozzle capable of varying effective expansion area ratio can optimize delivered impulse throughout the entire flight trajectory, resulting in dramatic performance gains. The ideal Altitude Compensating Nozzle (ACN) would continuously vary nozzle exit area ratio such that the nozzle is always pressure matched. In pursuit of these performance gains, ACN's have been investigated numerous times, but always, weight, cost, mechanical complexity and cooling issues have precluded their implementation on a real vehicle.

One ACN concept which avoids many of these design difficulties is the dual bell nozzle. The dual bell nozzle relies on an inflection point in the nozzle to force the flow to separate from the nozzle wall at the desired location, thus increasing sea level thrust. Since the flow separation is symmetrical and controlled, no sideloads are generated by the flow separation. During the ascent profile, the plume gradually expands until it finally attaches to the nozzle wall downstream of the inflection point, as depicted in Figure 1. Once the flow is attached and the nozzle exit pressure exceeds ambient pressure, the higher effective area ratio results in increased performance for the remainder of the ascent. For the ideal case, the net effect is that of having two nozzles, each optimized for a different portion of the flight trajectory. Mission studies have demonstrated that the performance of this two-stage ACN comes very close (within 1 to 3%) to the optimal efficiency for an ideal ACN of a given maximum area ratio.

In reality, however, the dual bell nozzle concept has several inherent inefficiencies which reduce its performance from the theoretical optimum. Figure 2 compares the actual performance of a dual bell nozzle to the optimum dual bell. The optimum dual bell nozzle, for this case, would follow the 16:1 Rao optimum nozzle thrust coefficient curve as the vehicle ascended, and then, at the performance cross-over point, switch to the 40:1 Rao optimum nozzle thrust coefficient curve for the remainder of the mission. However, during sea level operation with an actual dual bell nozzle, the separated region of the nozzle results in "aspiration drag". The relative impact of this aspiration drag on nozzle performance is evident in region A on the graph. By lowering the effective wall pressure

at the inflection point, this aspiration effect also triggers transition before the optimum performance cross-over point, as seen in region B. Then, once transition occurs and the flow is fully attached in the nozzle, the inflection point results in losses due to a non-optimal contour, illustrated by region C on the graph.

Despite these losses, the dual bell nozzle still provides a significant net impulse gain relative to either the 16:1 or the 40:1 fixed Rao optimum nozzles. It should also be noted that most ACN concepts suffer from similar losses due to non-optimal contours, induced drag, etc.

DISCUSSION OF TESTING

The primary objective of this cold flow test effort was to assess the performance characteristics of dual bell nozzles and to obtain preliminary design criteria by testing a number of configurations. Characteristics of interest included low altitude performance, high altitude performance and the flow transition process. In combination with this performance data, other factors such as cost, weight, fabricability and vehicle related issues could then be traded to establish the feasibility of the concept.

The testing was carried out in Rockwell's altitude test chamber located in El Segundo, California. Figures 3 and 4 show the layout of the facility. The test chamber is approximately 5'x5'x16', with 3' diameter windows on either side of the test section to allow viewing of the flow field. Air flow is supplied to the chamber by an air compressor capable of an output of 12 lb/sec at 300 psia. Altitude chamber evacuation occurs through a variable supersonic diffuser connected to a 26,000 cu ft vacuum sphere. The vacuum sphere is continuously evacuated by five vacuum pumps and an air ejector. Additionally, the flow through the model at the exit plane acts as a jet pump, further reducing the ambient pressure in the altitude chamber.

The nozzle configurations were mounted on a balance to measure axial thrust loads. Pressures and temperatures were also measured along the length of the nozzle. Schlieren imaging was used to visualize the plume flow field at the exit of the nozzle. This allowed real time evaluation of the flow field to determine nozzle transition characteristics.

Four different dual bell nozzle configurations were tested in this effort, along with two baseline nozzles to allow for performance comparisons. Figures 5 and 6 compare the contours tested. The baselines were 16:1 and 40:1 Rao optimum nozzles, which represented the low and high area ratios of the dual bell nozzles tested.

The 16:1 Rao optimum nozzle was used as the base nozzle for all of the dual bell contours. All of the extensions were of the same axial length, with an exit area ratio of 40:1. The test matrix varies the pressure gradient in the extension, since this is known to be the primary factor affecting both nozzle performance and flow transition characteristics. The conical extension provides a negative pressure gradient, as does the Rao optimum extension. The constant pressure extension has a zero pressure gradient, while the overturned extension provides a positive pressure gradient. Figure 5 illustrates the nozzle wall pressure gradients as a function of contour. Controlling the pressure gradient along the nozzle also controls the contour turn angle at the inflection point. The greater the turn

angle, the better the anticipated transition performance; however, this benefit comes at the cost of decreased high altitude performance. The exploration of this trade was a primary goal of this activity.

RESULTS OF TESTING

During testing, it was observed that the conical and Rao optimum dual bells did not provide smooth flow transition from the low to high area ratio mode. In both cases, the flow attachment was unsteady over a range of pressure ratios. The constant pressure and the overturned extensions, however, both exhibited excellent transition characteristics, with transition occurring in less than 30 msec* and at repeatable nozzle pressure ratios. The high altitude and low altitude performance of the configurations were also quantified using the test results.

Based on these results, the constant pressure extension was selected as the baseline dual bell nozzle contour, since it provided the best high altitude performance of the two contours with acceptable transition characteristics. The high altitude performance of the overturned contour was degraded by the more severe nozzle geometry.

Figure 7 depicts the nozzle thrust coefficient versus the pressure ratio for the constant pressure dual bell nozzle. At low pressure ratios, the nozzle flow separates at the inflection point. This separation results in a higher thrust coefficient than for the full flowing nozzle, until the flow transitions. The flow transition consistently occurred at the same pressure ratio, although, as expected, the transition takes place before the optimum performance cross-over point. At higher pressure ratios, the full flowing constant pressure dual bell nozzle provides improved performance relative to the baseline 16:1 nozzle, as illustrated by region C in figure 2.

Figure 8 illustrates the nozzle pressure profiles in both the separated and attached flow cases. In the case of separated flow in the extension, it is seen that the relative pressure in the extension is lower than the ambient pressure due to aspiration of the nozzle extension by the flow. This results in the observed performance loss relative to the 16:1 nozzle case. In the attached flow cases, it can be seen that when the nozzle is underexpanded, the nozzle pressure profiles all lie on top of each other, as predicted by basic nozzle theory. However, in the case of overexpansion with attached flow in the extension, it is seen that nozzle wall pressure in the extension increases with increasing ambient pressure. This behavior is attributed to the zero pressure gradient condition along the nozzle wall, and is believed to be a contributing factor in the excellent transition characteristics of this contour.

Low altitude performance losses due to aspiration drag, high altitude performance losses due to a non-optimal contour and early transition all reduce the dual bell nozzle's efficiency below the theoretical optimum. Even with these losses, however, the dual bell nozzle has shown significant gains over a single bell nozzle in mission studies. For a three engine SSTO vehicle based on the SSME engine, the use of a dual bell nozzle of the same area ratio as the baseline SSME nozzle resulted in a 12.1% increase in payload to L.E.O. The use of a larger area ratio

* (Framing speed of video camera)

nozzle yields even more significant payload gains, with the added advantage of allowing a larger area ratio nozzle to be used at lift-off without suffering undue transient sideloads due to flow separation.

CONCLUSIONS

While certain inefficiencies are inherent in the dual bell nozzle concept, it is seen that there are still clear performance advantages to using a dual bell nozzle for certain mission applications. While other altitude compensating nozzle concepts offer similar advantages, they typically suffer from mechanical complexity, difficulty of cooling and ultimately, high weight and cost. The dual bell nozzle offers a unique combination of performance, simplicity, low weight and ease of cooling, and thus warrants continued investigation.

RECOMMENDATIONS

Follow on testing is planned which will provide more detailed information on the performance and flow transition process for the dual bell nozzle. In addition to this testing, analytical modeling to investigate detailed aspects of the flow field and assist in design optimization is also desirable. While the attached flow case is readily addressed using a variety of currently available codes, modeling of the separated flow case and the flow transition process will likely require significant effort. The experimental data will allow validation of the models developed, so that they may be used as design tools for the dual bell nozzle and other separated, transient nozzle cases of interest.

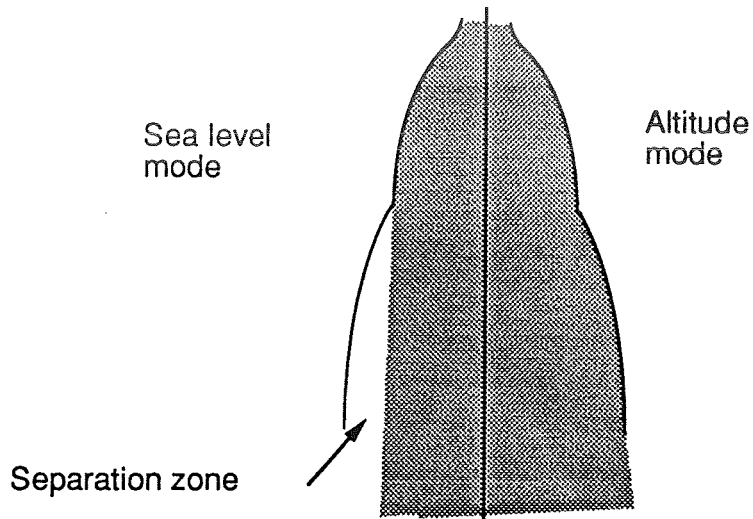


Figure 1 - Flow separation at the inflection point provides increased sea level thrust

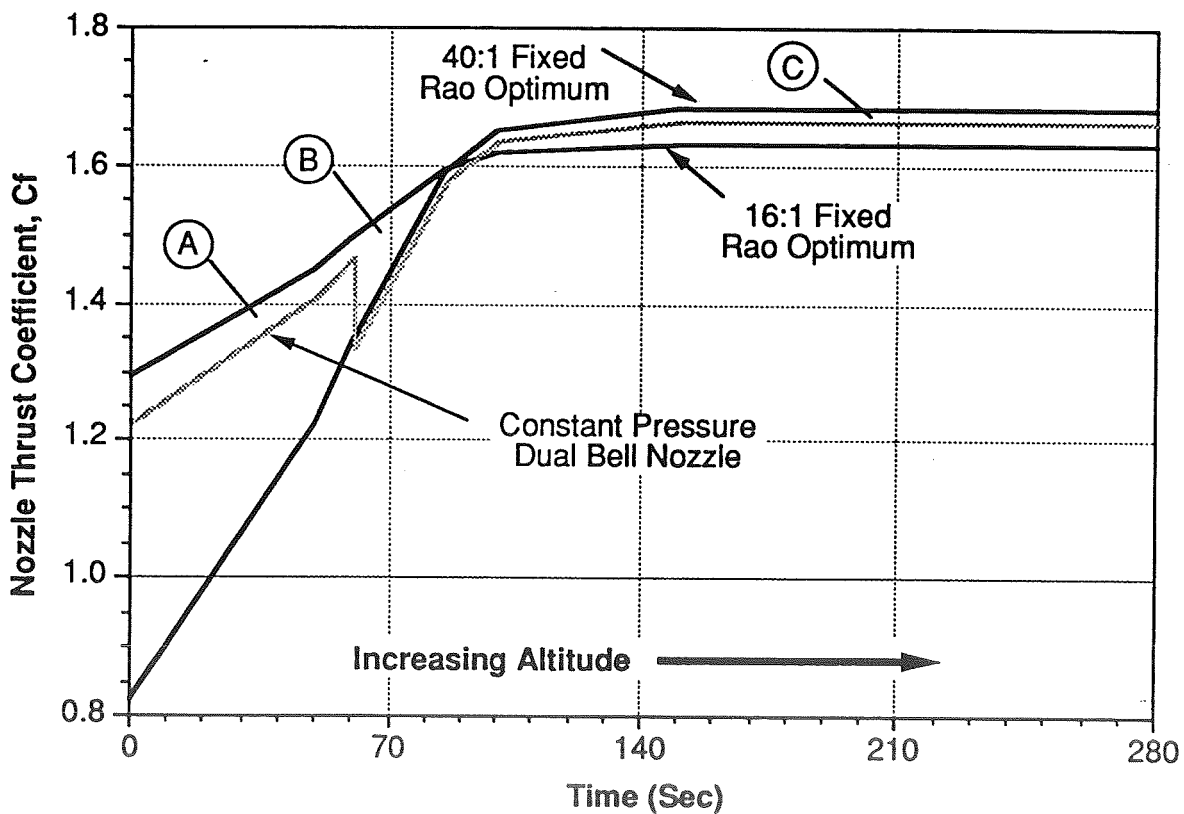


Figure 2 - Comparison of nozzle thrust coefficient vs time for a typical mission using a dual bell nozzle

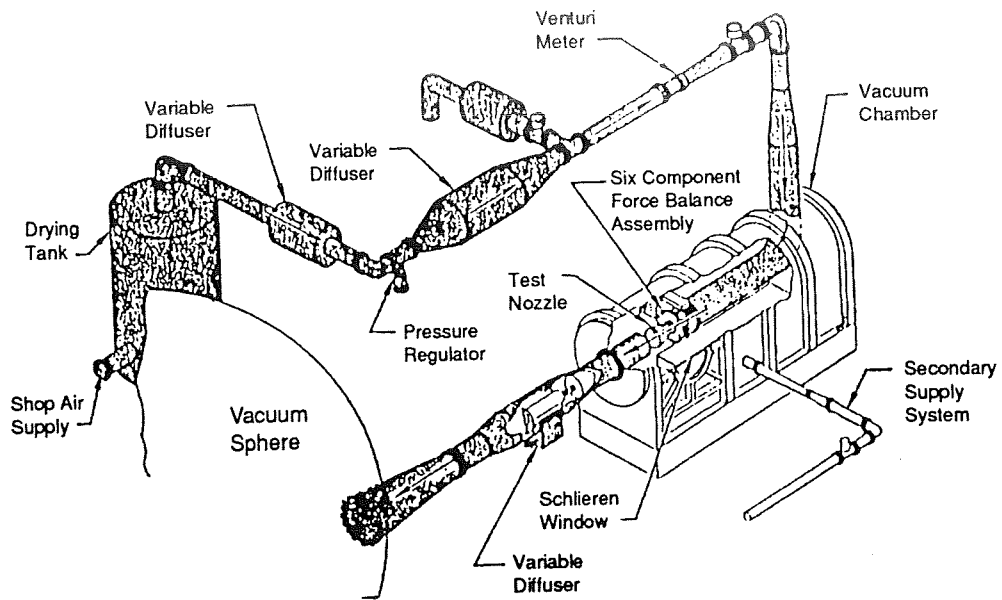


Figure 3 - Schematic of altitude test facility at NAA

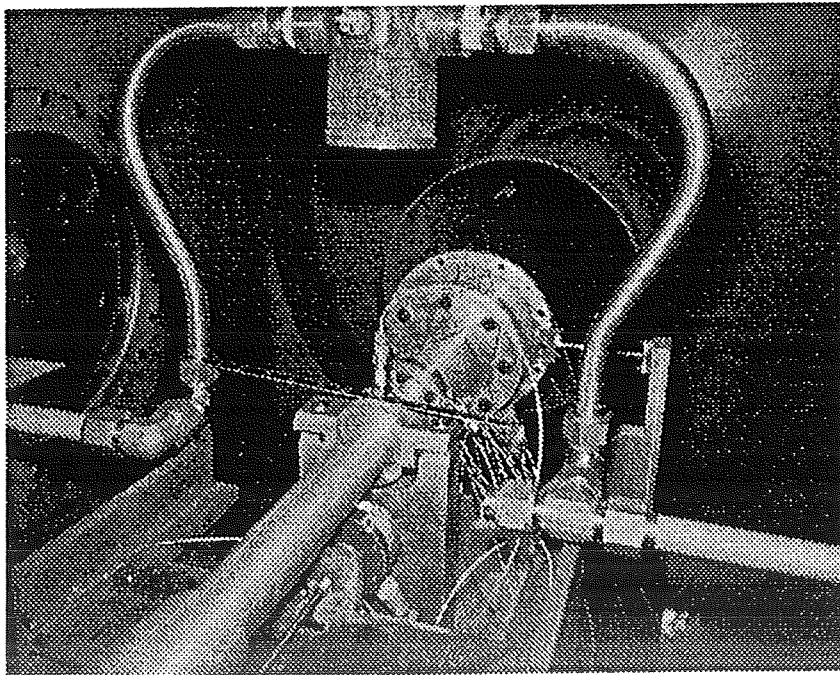


Figure 4 - Dual bell nozzle test hardware installed in altitude test chamber

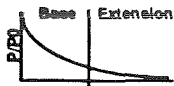
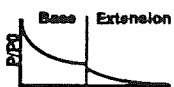
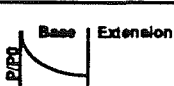
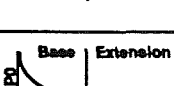
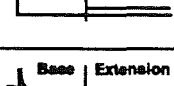
Configuration	θ Turn	Pressure Profile
16:1 Rao Optimum (baseline)	—	
40:1 Rao Optimum (baseline)	—	
16:1 Rao Opt Base, 40:1 Conical Extension	14.5°	
16:1 Rao Opt Base, 40:1 Rao Opt Extension	18.5°	
16:1 Rao Opt Base, 40:1 Constant Press Extension	22.5°	
16:1 Rao Opt Base, 40:1 Overturned Extension	26.5°	

Figure 5 - Dual bell nozzle configurations tested

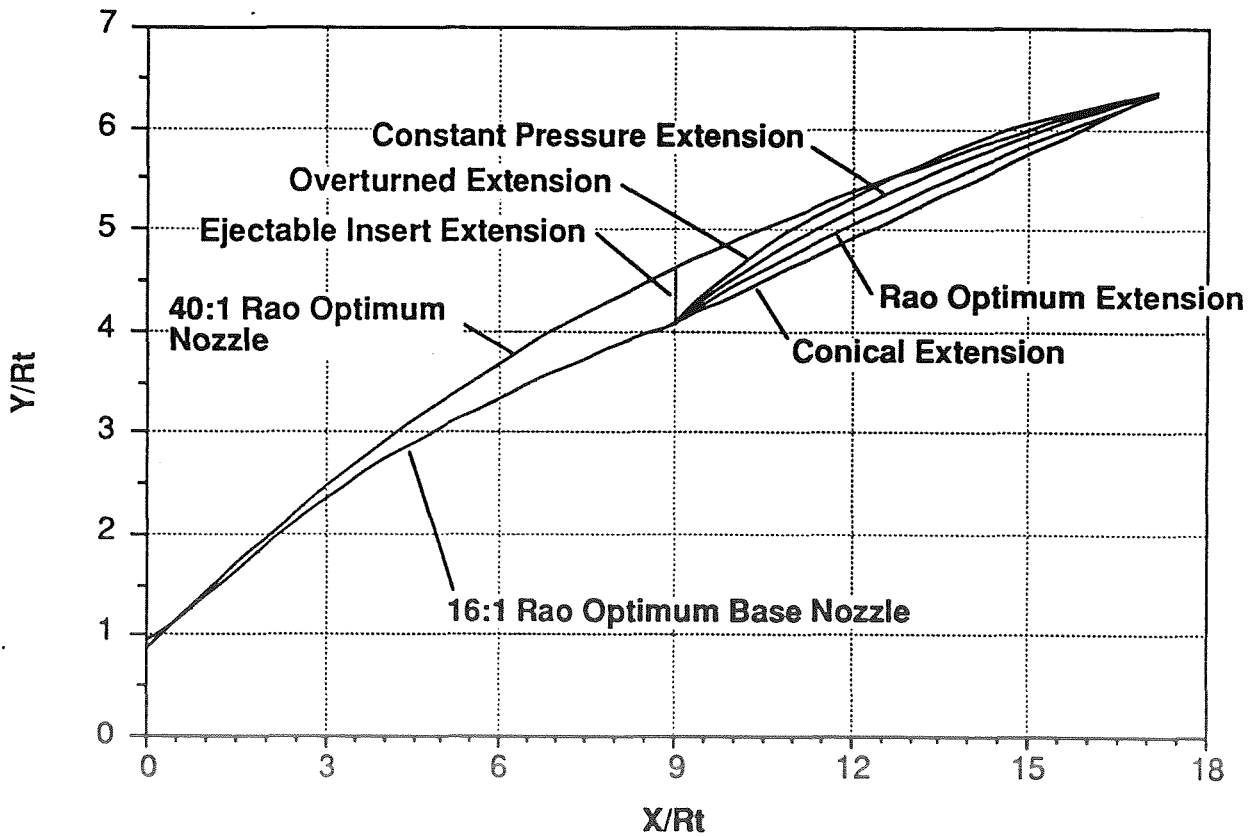


Figure 6 - Comparison of dual bell nozzle contours

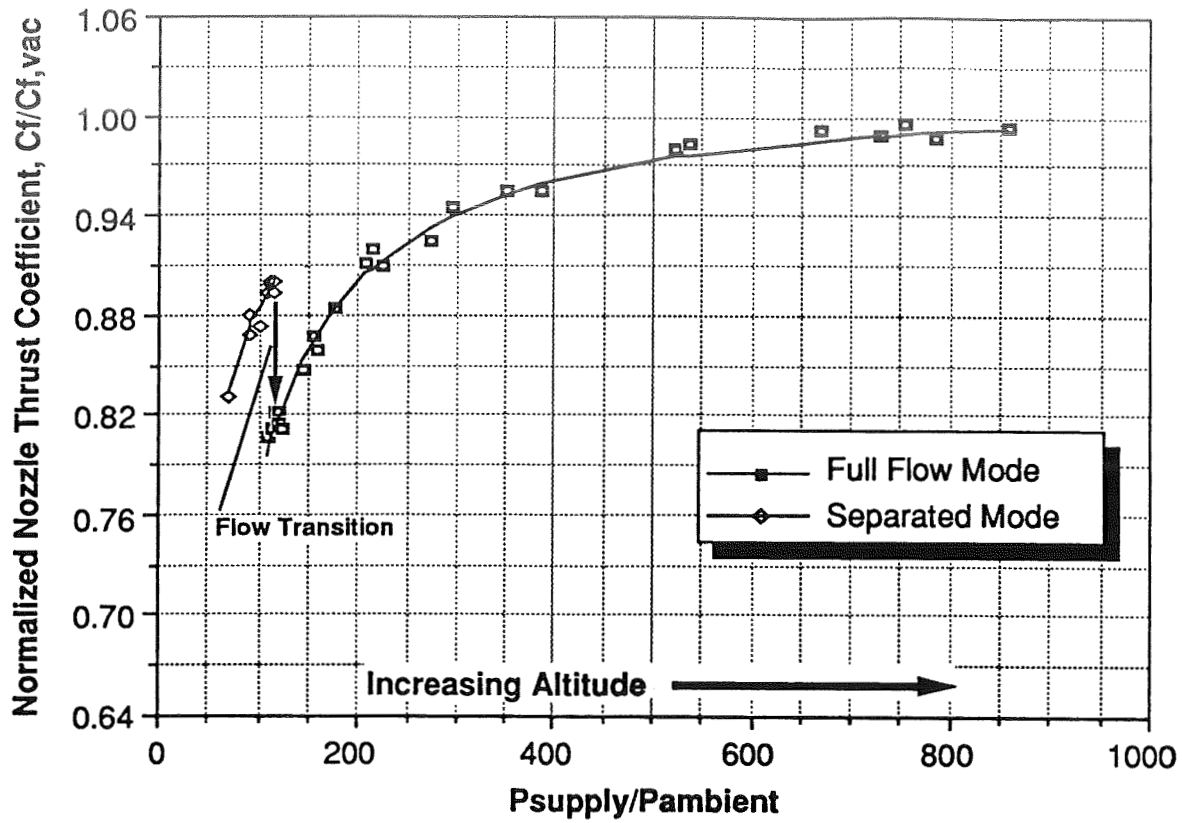


Figure 7 - Thrust coefficient vs pressure ratio for a constant pressure dual bell nozzle

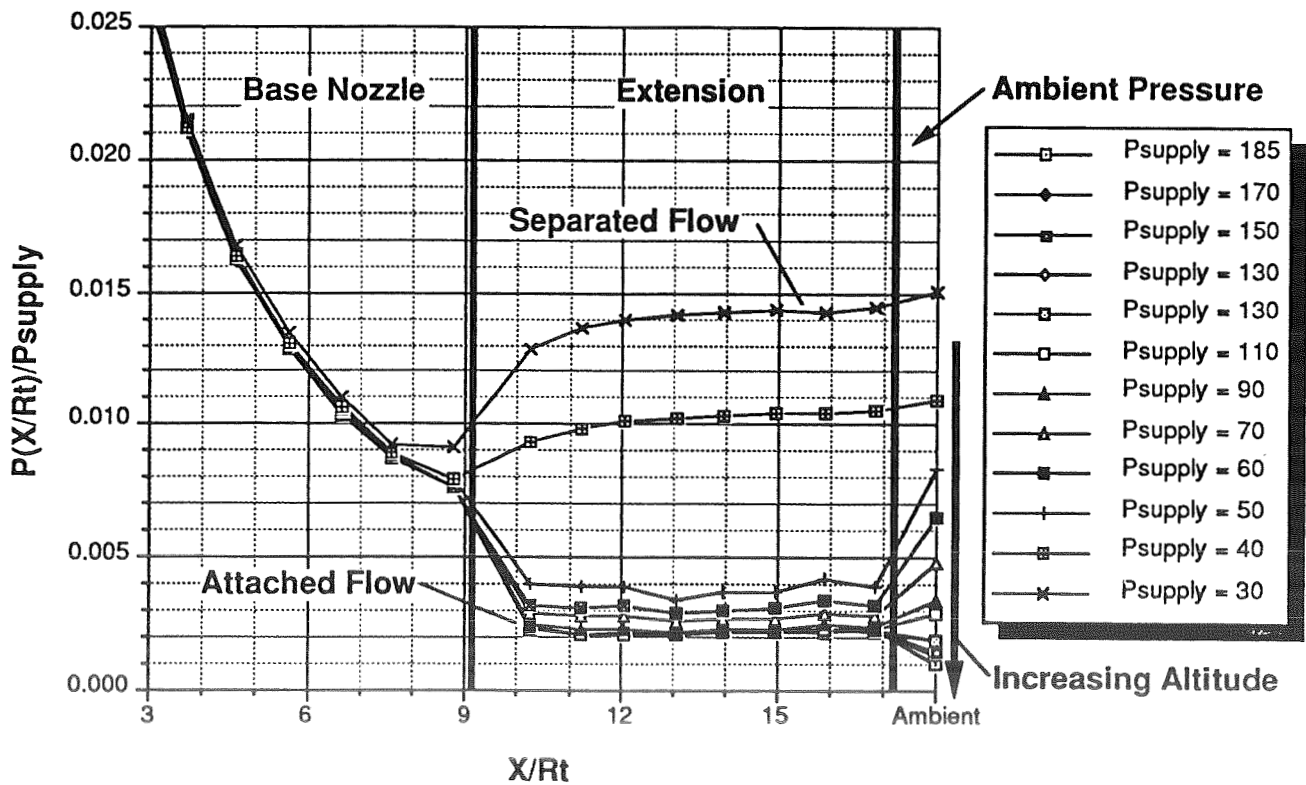


Figure 8 - Nozzle pressure ratio vs axial distance from throat for constant pressure dual bell nozzle

FOIL BEARING RESEARCH AT PENN STATE

Marc Carpino
Department of Mechanical Engineering
The Pennsylvania State University
University Park, PA 16802

SUMMARY

Foil journal bearings consist of a compliant metal shell or foil which supports a rigid journal by means of a fluid film. Foil bearings are considered to be a potential alternative to rolling element or traditional rigid surface bearings in cryogenic turbomachinery applications. The prediction of foil bearing performance requires the coupled solution of the foil deflection and the fluid flow in the bearing clearance between the rotor and the foil. The investigations being conducted in the Department of Mechanical Engineering at Penn State are focused in three areas: theoretical prediction of steady state bearing performance, modeling of the dynamic bearing characteristics to determine performance in rotor systems, and experimental verification of analysis codes. The current status and results from these efforts will be discussed.

BACKGROUND

Foil journal bearings are considered to be an alternative to rolling element bearings, and to rigid surface hydrostatic, hydrodynamic, or hybrid journal bearings for rotor support in cryogenic turbomachinery applications such as rocket propulsion engines. Foil bearings offer several advantages[1]: compliance which can compensate for misalignment and deflection of rotors and machinery casings; reduced thermal distortion due to the thin shell structures of the bearing; tolerance of dirt and debris in the lubricant flow; and enhanced dynamic performance.

A foil bearing is generally constructed of a foil or thin shell which supports a rotor by any combination of bending, membrane, or elastic foundation effects. Two basic foil bearing configurations are of general interest in turbomachinery applications; first the elastically supported bearing, and second, the leaf type of foil bearing(see figure 1). The foil surface in the elastically supported foil bearing configuration resists deflection by means of the elastic foundation in back of the foil. The elastic foundation can be constructed from other structural shells, polymers, or springs. The foils in the leaf type bearing support load primarily by the resistance of the foils to bending.

The investigations at Penn State have the following broad objectives aimed at the development of general design tools for foil bearings: (1) develop general physical models of foil journal bearings which will predict steady state and dynamic behavior in rotor systems; (2)investigate the performance of foil bearing configurations which are of significance in rotordynamic applications; and (3) validate the results of predictive codes with basic experimental investigations.

STEADY STATE BEARING PERFORMANCE

The development of robust design tools for the predictive design of foil bearings requires that analyses be able to address different bearing configurations, misalignment of the bearing, geometric defects, and the broad range

of fluids which can occur. These requirements have led to the selection of a direct iteration approach to the solution of the coupled lubricant fluid flow/foil deflection problem. In the direct iteration approach, deflections and pressure distributions are calculated iteratively from displacement and fluid flow formulations. At the completion of the deflection calculation, the new clearance is computed from the rotor location, the nominal foil location, and the foil deflection. The clearance is then under-relaxed before the next calculation of the pressure distribution. The finite element method has been used to calculate both pressure distributions and deflections in the results to be discussed here[2,3].

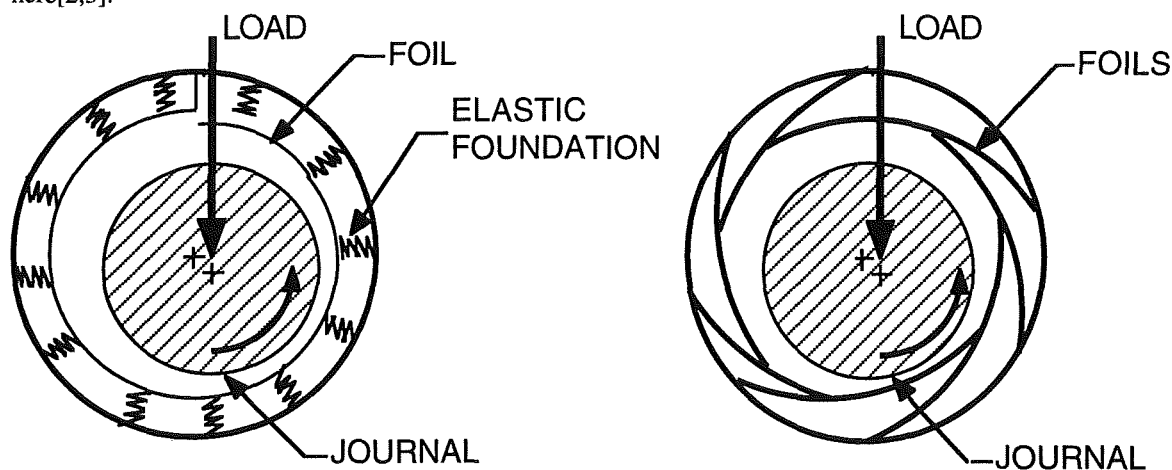


Figure 1- Elastically supported and leaf type foil journal bearings.

This analysis approach has been applied to an elastically supported split shell foil bearing (often referred to as a Hydresil bearing configuration). In this configuration, the foil is not continuous in the circumferential direction. As with the complete shell foil bearing, the foil is treated as perfectly flexible and inextensible. The foil is allowed to lift off of the elastic foundation if the pressure on the foundation becomes negative. Typical clearance and pressure results are shown in figure 2. The clearance distribution in figure 2 demonstrates the importance of membrane effects in the analysis by the virtually constant clearance across the width of the bearing. These results are in contrast to earlier analyses[1] wherein the clearance varied in the axial direction. The clearance in the exit region of the bearing remains virtually constant in the circumferential direction as the foil lifts off of the elastic foundation.

TRANSIENT BEARING PERFORMANCE

The design and development of high speed rotor systems requires detailed dynamic analyses of the rotor-bearing system. Although the dynamic system performance is one of the most important factors in rotor operation, the transient performance of foil bearings has received very little attention. A common approach to the dynamic performance of a bearing in a rotor system is to characterize the bearing in terms of stiffness and damping coefficients by perturbing the operation of the bearing about the nominal operating state. These coefficients are then used in a larger simulation of the dynamics of the rotor system. In a traditional rigid surface bearing, the bearing stiffness and damping are attributed solely to the behavior of the fluid film. In a foil bearing, the stiffness and

damping are dependent on the stiffness and coulomb friction of the foil structure in addition to the fluid film between the foil and the rotor.

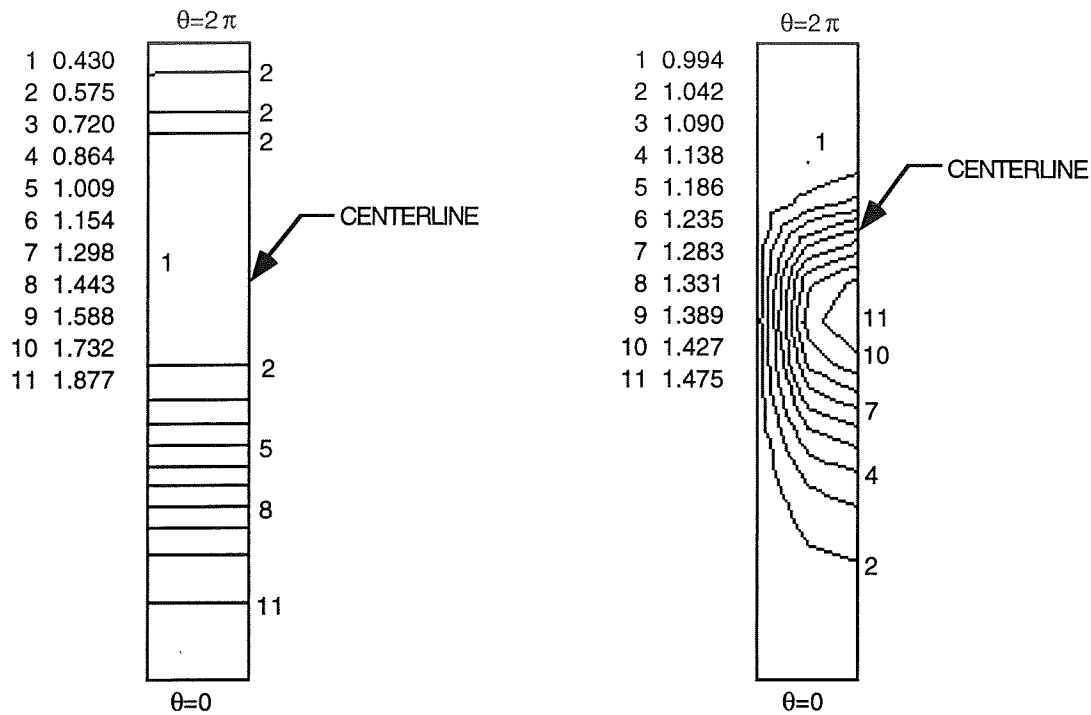


Figure 2 - Clearance and pressure distributions for split foil configuration, Eccentricity ratio, $\epsilon = 0.9$, Bearing number, $\Lambda = 1.0$, Bearing compliance, $\alpha = 1.0$, Eccentricity angle = π radians, $L/d = 1$.

Results from a finite difference analysis predicting the stiffness and damping coefficients for the Hydresil bearing configuration[4,5] are presented in figure 3. In the analysis, the foil is supported on an elastic foundation from which it can detach if the force in the foundation becomes tensile. Membrane and bending effects in the foil have been neglected. A compressible fluid was used. The effects of Coulomb friction are included. These results at high speeds demonstrate that as the Coulomb friction is increased, the effective viscous damping will increase. A general finite element based approach has been developed which incorporates a complete three dimensional structural model.

EXPERIMENTAL INVESTIGATION

An foil bearing testbed has been built to verify the steady-state prediction of loads, film thickness distributions, and pressure distributions in an elastically supported foil bearings operating with incompressible lubricants at low speeds. The bearing has a nominal diameter equal to 5 inches and operates at 100 to 1000 RPM using SAE 30 oil as the lubricant. To facilitate accurate measurements, the nominal bearing clearance equals 0.020 inches. Detailed clearance and pressure measurements are made by transducers which have been installed in the journal.

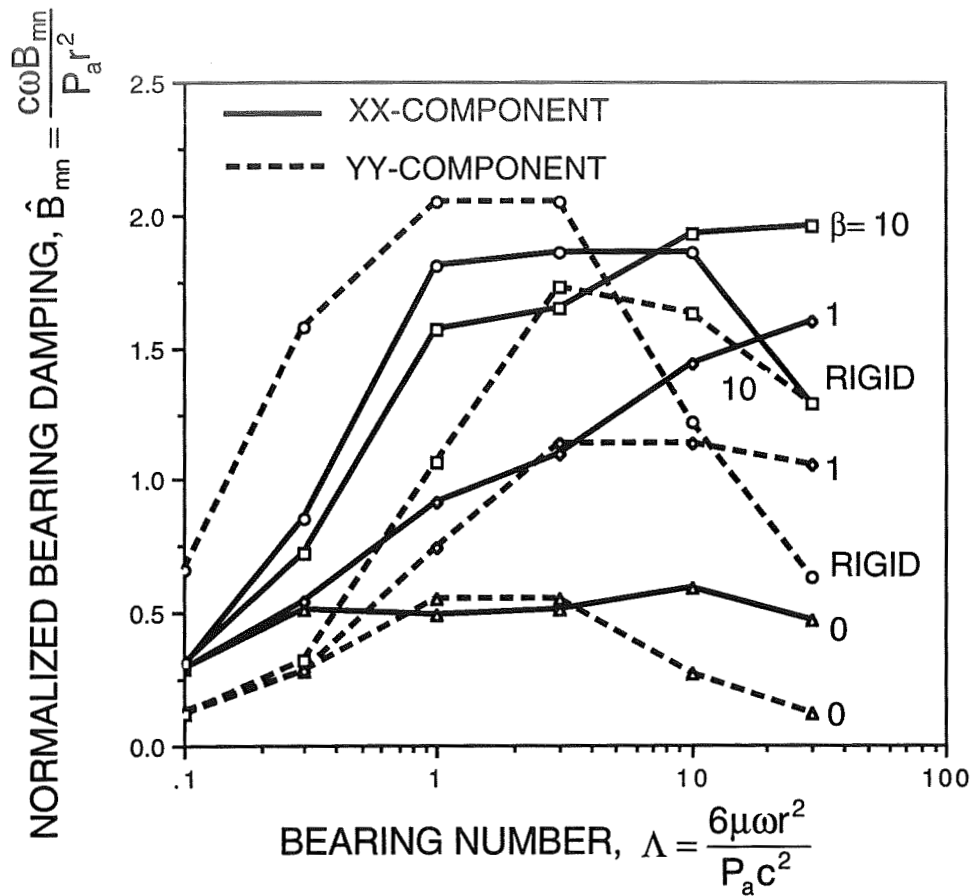


Figure 3 - Effect of bearing compliance, α , on normalized bearing damping \hat{K}_{xx} , $L/d = 1.0$, $\epsilon = 0.5$. Numbers denote bearing compliance.

ACKNOWLEDGMENT

The author would like to acknowledge the continued support from the NASA Lewis Research Center under NASA Grant No. NAG-3-1052 and the Pennsylvania State University Propulsion Engineering Research Center.

REFERENCES

1. Heshmat, H., Walowit, J. A., and Pinkus, O., 1983, "Analysis of Gas-Lubricated Foil Journal Bearings," *ASME Journal of Lubrication Technology*, Vol. 105, pp. 647-655.
2. Carpino, M., and Peng, J.-P., 1991, "Theoretical Performance of Foil Journal Bearings," Presented at the AIAA/SAE/ASME/ASEE 27th Joint Propulsion Conference, paper no. AIAA-91-2105.
3. Carpino, Marc, J.-P. Peng, and L. Medvetz, 1992, "Misalignment in a Complete Shell Gas Foil Journal Bearing," to be published in *STLE Transactions*.
4. Peng, J.-P. and Carpino, M., 1992, "Calculation of Stiffness and Damping Coefficients for Elastically Supported Gas Foil Bearings," *ASME Journal of Tribology*, Vol. 115, pp 20-27.
5. Peng, J.-P. and Carpino, M., 1993, "Calculation of Stiffness and Damping Coefficients for Elastically Supported Gas Foil Bearings," STLE preprint no. 93-AM2E-2, to be published in *STLE Transactions*.

TWO STAGE TURBINE FOR ROCKETS

Joseph P. Veres
NASA Lewis Research Center
Cleveland, Ohio 44135
(216) 977-7527

ABSTRACT

The aerodynamic design and rig test evaluation of a small counter-rotating turbine system is described. The advanced turbine airfoils were designed and tested by Pratt & Whitney. The technology represented by this turbine is being developed for a turbopump to be used in an advanced upper stage rocket engine. The advanced engine will use a hydrogen expander cycle and achieve high performance through efficient combustion of hydrogen / oxygen propellants, high combustion pressure and high area ratio exhaust nozzle expansion. Engine performance goals require that the turbopump drive turbines achieve high efficiency at low gas flow rates. The low mass flow rates and high operating pressures result in very small airfoil heights and diameters. The high efficiency and small size requirements present a challenging turbine design problem. The shrouded axial turbine blades are 50% reaction with a maximum thickness to chord ratio near 1. At 6 degrees from the tangential direction, the nozzle and blade exit flow angles are well below the traditional design minimum limits. The blade turning angle of 160 degrees also exceeds the maximum limits used in traditional turbine designs.

INTRODUCTION

Studies at NASA have identified the need for a new propulsion system that can be utilized for a variety of missions. The goal of NASA's Advanced Chemical Engine (ACE) program is to develop key technologies required for the propulsion system of space vehicles such as upper stages, orbit transfer vehicles and landers. The new system will be an oxygen / hydrogen expander cycle engine that will rely on efficient components in order to achieve high performance. The range of missions demand that the engine should be capable of a high degree of throttling and operate over a wide range of propellant mixture ratios. In order to develop an engine with these qualities, several component technologies must first be demonstrated. The Advanced Expander Test Bed (AETB) described in references 1 and 2 has been designed by Pratt & Whitney in order to develop and demonstrate advanced components in an expander engine environment. Key technologies to be validated include the performance levels of the advanced turbopumps and system interaction effects at off-design operating conditions. A key part of the turbopump overall performance is the aerodynamic performance of the small, but high energy density two stage counter-rotating turbine. The aerodynamic performance of the counter-rotating turbine concept within the hydrogen turbopump has been demonstrated early in the AETB program. Pratt & Whitney has designed and tested a two stage turbine in a full scale rig at equivalent engine operating conditions using air as the test fluid (references 3 and 4).

TURBINE DESIGN

The turbines are required to have high efficiency in order to meet the performance goals of the AETB and future liquid space propulsion engines. The AETB hydrogen turbopump cross-section in Figure 1 shows the dual spool configuration. The two stage counter-rotating turbines use warm gaseous hydrogen as the working fluid to drive the primary and the secondary liquid hydrogen pumps.

The aerodynamic design process for the turbines was initiated with flow path parametric optimization studies using a meanline analysis and is described in reference 3. The design configuration that resulted from the optimization studies are two full admission 50% reaction turbines. The full admission turbine flow path allowed the use of efficient high reaction rotor blading. The selection of a full admission turbine configuration required a primary turbine blade turning angle of 160.6° , well above the traditional limit of 140° . Streamline analyses using a 3-D multi-stage Euler flow solver were used to analyze the complete turbine system. After numerous iterations, satisfactory airfoil contours were obtained that resulted in acceptable static pressure distribution along the airfoil surfaces, while minimizing the axial flow reversal due to the low axial thru-flow component of velocity. The resulting turbine airfoil shapes and the flow path are shown in Figure 2. The nozzle inlet angle is set at 22° to take advantage of the swirl produced by the tangential inlet volute. In this way, the reduced turning required through the nozzle vane results in reduced aerodynamic losses. Similarly, the flow exiting the second stage rotor has a high degree of swirl for reduced turning losses in the exit volute. The predicted velocity triangles during engine operation (hydrogen driven) are shown in Figure 3. While this two stage turbine is the result of numerous engine cycle design iterations, it is not the final turbine configuration that will be used in the AETB, but is very similar in overall dimensions and performance.

TURBINE TEST RIG

In order to verify the performance of the turbine in the engine, a turbine test rig using room temperature air at reduced pressure as the working fluid was designed and built. The design point aerodynamic performance requirements for both the primary and the secondary turbine stages in the engine and in the turbine rig are shown in Table I. With the exception of Reynolds number, all of the key operating parameters can be simulated in the rig. The variation in efficiency between the engine and the rig is based on a predicted Reynolds number correction using turbulent boundary layer correlations. The predicted velocity triangles during testing in air at the referred conditions of Table I are shown in Figure 4. Rig instrumentation includes total pressure and temperature rakes, flow angle seeking cobra probes, wall static pressure taps and shaft torquemeters. The instrumentation has circumferentially traversable rings for measuring pressure and temperature contours in the inlet and exit flow fields.

Table I
Engine and Rig Operating Parameters

<u>Parameter</u>	<u>Engine</u>	<u>Rig</u>
Working Fluid	Hydrogen gas	Air
P inlet (psia)	3500.	100.
T inlet (°R)	985.	575.
Flow Rate (lbm/sec)	3.49	0.50
<u>Primary Turbine</u>		
RPM	100,000.	20,000.
Press. Ratio (T-T)	1.48	1.48
Predicted η (T-T)	79.0	76.8
Um / Co	0.45	0.45
Horsepower (HP)	1365.9	8.0
Work Δh (BTU/lbm)	276.7	11.3
γ	1.39	1.40
Reynolds No. (avg.)	3.75xE6	3.95xE5
<u>Secondary Turbine</u>		
RPM	100,000.	20,000.
Press. Ratio (T-T)	1.35	1.35
Predicted η (T-T)	86.1	84.3
Um / Co	0.515	0.515
Horsepower (HP)	1050.0	6.2
Work Δh (BTU/lbm)	212.7	8.8

PERFORMANCE TESTING

The test program was performed at Pratt & Whitney using warm air at 100 psia turbine inlet pressure. Test point conditions of inlet pressure and pressure ratio were controlled by the rig inlet and exit valves. The primary turbine stage was evaluated first over a wide range of Reynolds numbers as possible, being limited by maximum allowable rig inlet pressure. The primary turbine efficiency at the design pressure ratio as a function of mean velocity ratio is shown in Figure 5 and is in excellent agreement with the expected level. In the next series of tests, the primary and secondary turbine stages were tested together with and without the vane in the secondary turbine stage. The best performing configuration was the two stage turbine with a vaneless secondary stage. The measured overall two stage counter-rotating turbine efficiency (vaneless secondary stage) is shown in Figure 6 for operation over a range of velocity ratios at design point pressure ratio.

CONCLUSIONS

The aerodynamic design and rig testing of the two stage counter-rotating turbine for an advanced upper stage rocket engine turbopump has been completed. The turbine configuration is unconventional in that it utilizes a full admission design in an application region that traditionally has used a partial admission turbine. The two stage full admission turbine having high blade turning and low exit angles has performed satisfactorily in an extensive series of rig tests. Measured efficiency levels of the primary and the vaneless secondary turbines are in close agreement with the predictions.

ACKNOWLEDGEMENTS

The author wishes to thank Pratt & Whitney and F.W. Huber and his team at Pratt & Whitney for the support of this program and in achieving the high quality turbine design and test data.

REFERENCES

1. Masters, A.I., Tabata, W.K., "Design of an Advanced Expander Test Bed," AIAA 91-3437
2. Davidson, D.P., Finke, A.K., "The Design and Fabrication of a Small Highly Instrumented Counterrotating Turbine Rig," ASME 93-GT-396
3. Huber, F.W., Branstrom, B.R., Finke, A.K., Johnson, P.D., Rowey, R.J., Veres, J.P., "Design and Test of a Small Two Stage Counter-Rotating Turbine for Rocket Engine Application," AIAA 93-2136

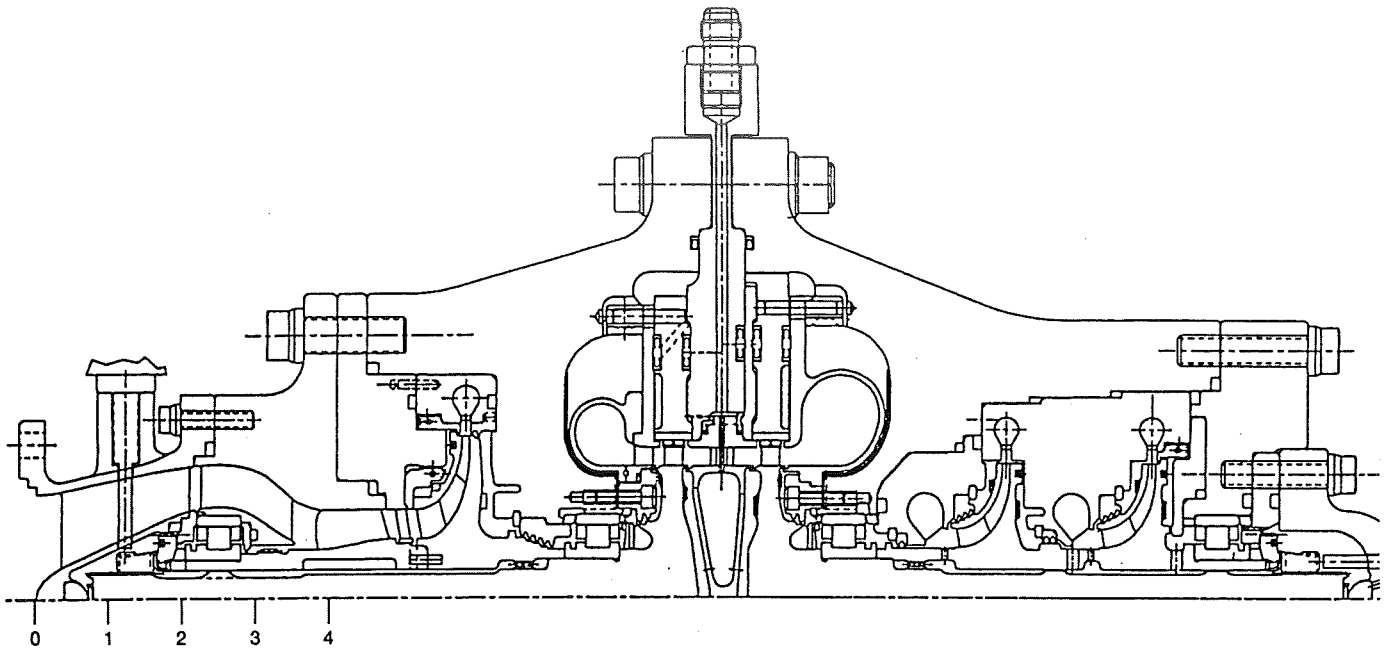


Figure 1 Liquid Hydrogen Turbopump Utilizing Two Stage Counter-Rotating Turbines.

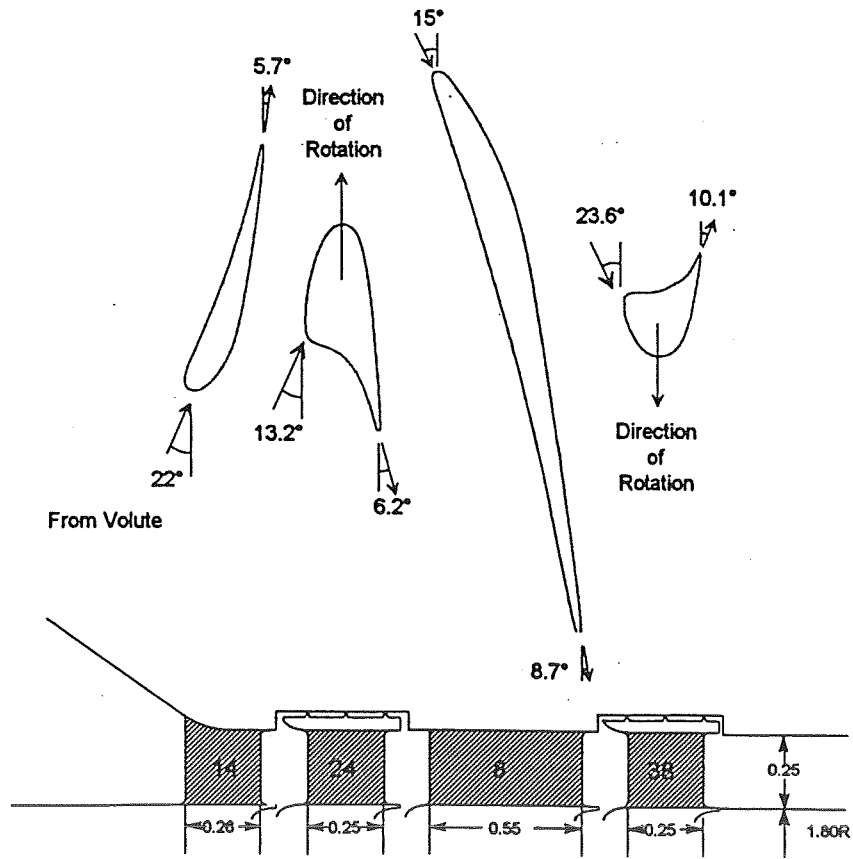


Figure 2 Pump Drive Turbine Airfoil Shapes and Flow Path Elevation.

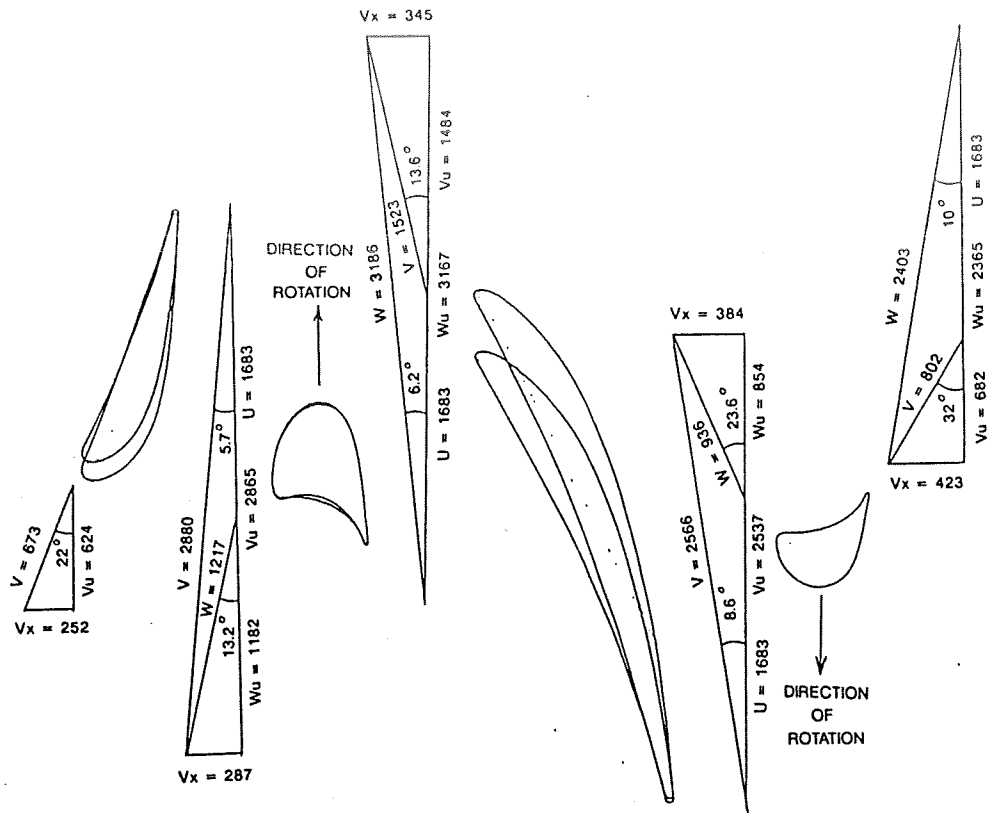


Figure 3 Engine Design Point Gaseous Hydrogen Driven Turbine Meanline Velocities.

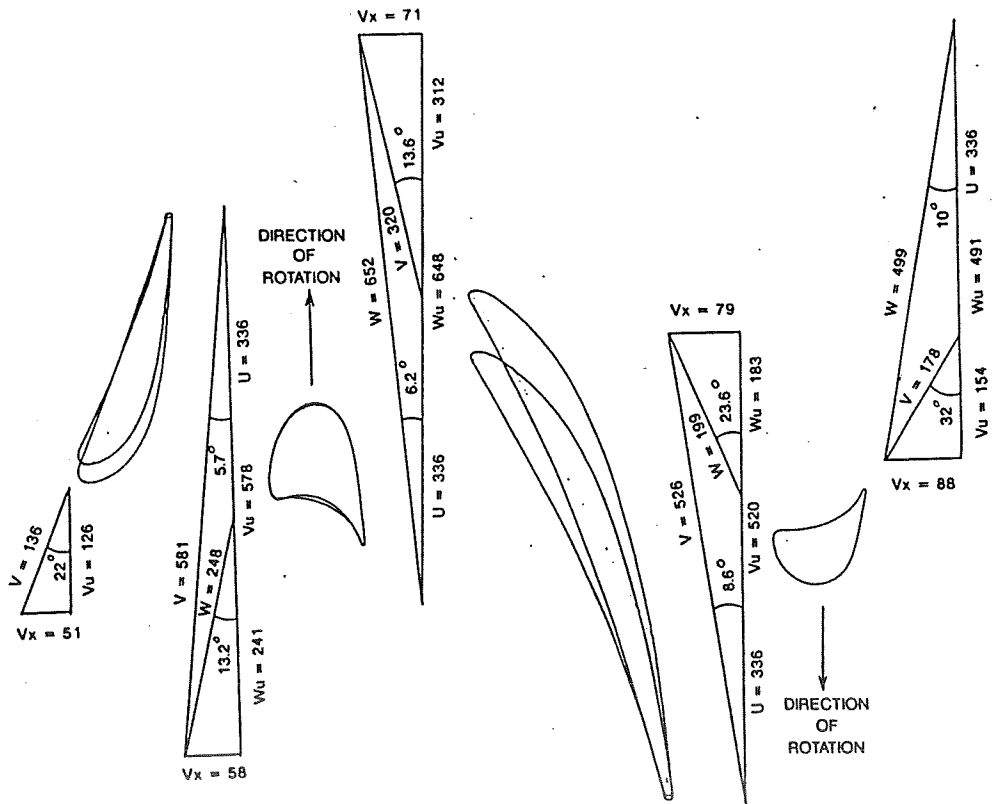


Figure 4 Meanline Velocity Triangles, Air Driven at Referred Conditions

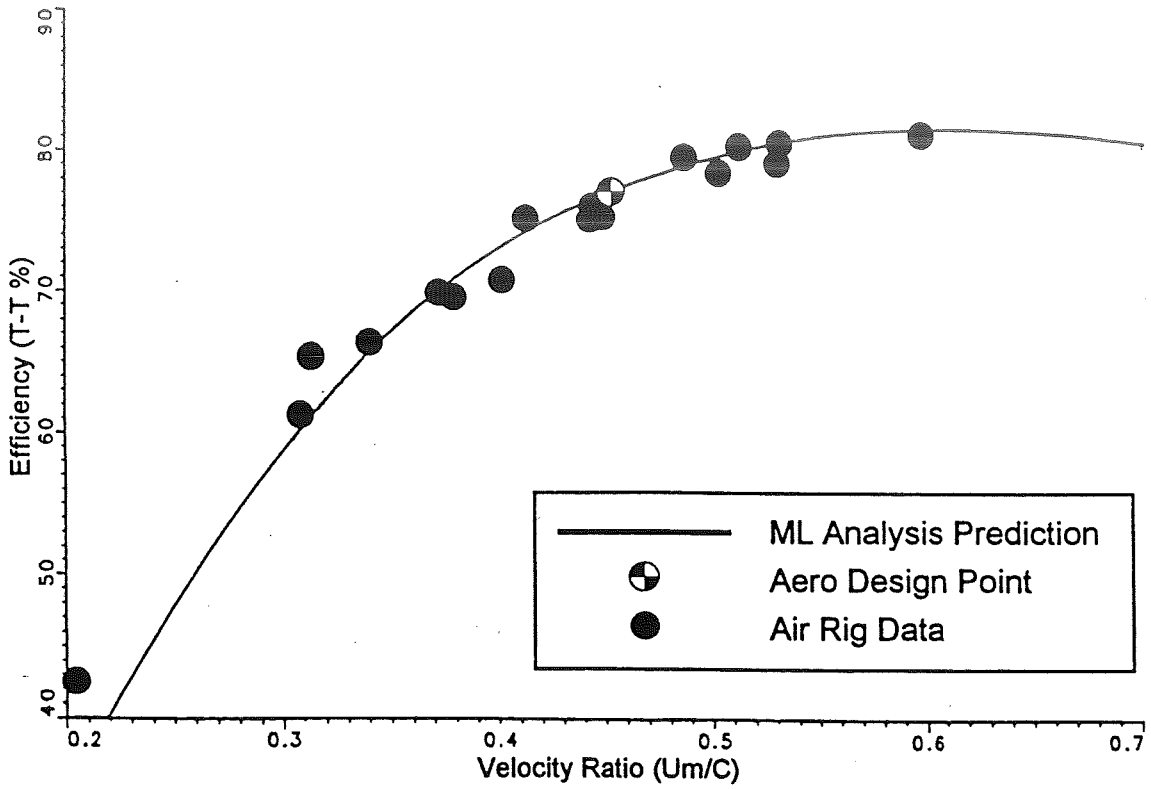


Figure 5 Primary Turbine Stage Efficiency. (Ref. 3)

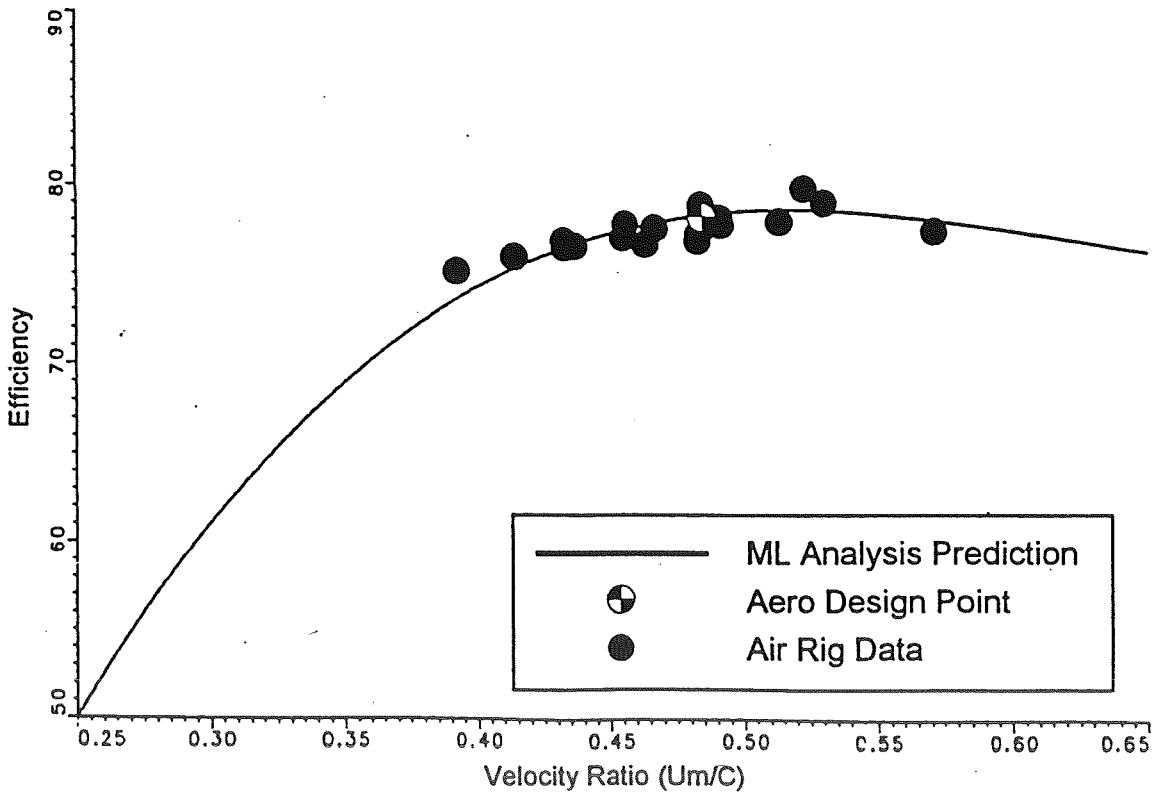


Figure 6 Overall Two Stage (Primary & Vaneless Secondary) Turbine Efficiency. (Ref. 3)

COMPUTATIONAL FLUID DYNAMIC MODELLING OF CAVITATION

Manish Deshpande[†], Jinzhang Feng[‡], Charles L. Merkle*

Propulsion Engineering Research Center
 Department of Mechanical Engineering
 The Pennsylvania State University

SUMMARY

Models in sheet cavitation in cryogenic fluids are developed for use in Euler and Navier-Stokes codes. The models are based upon earlier potential-flow models but enable the cavity inception point, length and shape to be determined as part of the computation. In the present paper, numerical solutions are compared with experimental measurements for both pressure distribution and cavity length. Comparisons between models are also presented. The CFD model provides a relatively simple modification to an existing code to enable cavitation performance predictions to be included. The analysis also has the added ability of incorporating thermodynamic effects of cryogenic fluids, into the analysis. Extensions of the current two-dimensional steady state analysis to three-dimensions and/or time-dependent flows are, in principle, straightforward although geometrical issues become more complicated. Linearized models, however offer promise of providing effective cavitation modeling in three-dimensions. This analysis presents good potential for improved understanding of many phenomena associated with cavity flows.

COMPUTATIONAL MODEL

Cavitation is a persistent problem in many fluid mechanical devices and has received much attention in the past several decades [1, 2]. In many cases cavitation occurs in flows that include rotational effects, viscous effects and heat transfer. Existing models based on potential flow theory are relatively limited in the ability to analyze these more complex flowfields. The objective of the present research is to extend the potential flow analyses to solutions of the Euler/Navier-Stokes equations to predict the geometrical characteristics of the cavity. It requires no presumptions of either the cavity length or cavity inception point and satisfies the cavity pressure as well as normal velocity condition on the cavity surface.

The steady state Navier-Stokes equations when written in a strongly conservative form in generalized coordinates using the unsteady artificial compressibility formulation become

$$\Gamma \frac{\partial Q}{\partial \tau} + \frac{\partial}{\partial \xi} (E - E_v) + \frac{\partial}{\partial \eta} (F - F_v) = 0 \quad (1)$$

where Q is the vector of primary dependent variables, E and F are the convective fluxes in the ξ and η directions respectively and E_v and F_v are the viscous fluxes. The Euler equations are obtained from the above by dropping the viscous flux terms. Turbulence effects are calculated from the Baldwin-Lomax algebraic turbulence model [3].

[†] Graduate Research Assistant

[‡] Research Associate

^{*} Distinguished Alumni Professor

An explicit time-marching Runge-Kutta algorithm is used to advance the Navier-Stokes/coupled energy system of equations in pseudo-time. Center-differencing is used for all spatial derivatives. Local time-stepping is used to improve convergence. A fourth-order artificial viscosity [4] is used to prevent odd-even splitting in the numerical solution.

The inviscid portion of the coupled equations becomes hyperbolic with the addition of the artificial time derivative. This enables the use of the Method of Characteristics (MOC) procedure to formulate the inflow and outflow boundary conditions, analogous to compressible flow. The application of MOC to the above problem dictates that the inflow be determined by three boundary conditions and one characteristic equation and the outflow by one boundary condition and three characteristics. Here the total pressure, the inflow angle and the temperature are specified at the inlet, while the static pressure is specified at the downstream boundary. These are complemented by information obtained from outrunning characteristics.

Boundary conditions at the body surface in the absence of cavitation are the no-slip condition for the NS equations and inviscid wall conditions for the Euler equations, and a specified wall temperature or heat flux condition. These are augmented by applying the normal momentum equation on the surface. Boundary conditions on the cavity interface are discussed in the next section.

CAVITATION MODEL

The cavity is modeled as a region of constant pressure, corresponding to the liquid vapor pressure. The location of the cavity interface is determined by over-specifying the boundary relations on it, analogous to procedures used in potential flow models. For the Navier-Stokes equations the boundary conditions include flow tangency, continuity of shear stress at the interface and the cavity pressure. These conditions replace the usual two no-slip conditions ($u = v = 0$), and enable the computation of the interface location as a part of the marching process. In the Euler model the cavitation pressure and the total pressure are specified along with one characteristic.

In keeping with the potential flow models, both a linear and a nonlinear procedure can be used to enforce the cavity conditions. In the linear case the cavity conditions are applied on the airfoil surface, under the assumption of a thin cavity, so that the computational domain does not change. For the nonlinear procedure, the cavity conditions are applied directly on the cavity interface. As a consequence the computational domain adjacent to the cavity evolves and needs to be updated.

During the computational procedure the pressure distribution is checked against the specified cavitation pressure. If the pressure at any point drops below the local vapor pressure that point is switched from a 'solid wall' point to a 'cavity' point with a corresponding switch in the boundary conditions. Subsequent iterations then allow the normal velocity on the cavitating interface to deviate from zero. The finite normal velocity on the interface can then be used to update the cavity interface.

The cavity profile is fixed by ensuring positive cavity thickness at every cavitating point. Any points with negative cavity thickness are reset to non-cavitating points in the next iteration regardless of their pressure level. This enables the cavity to shrink if required by the iterative procedure. If the cavity ends with a finite non-negative thickness the cavity is artificially closed by adding an afterbody [5, 6], which is treated as inviscid. The afterbody shape chosen here is a cubic profile that merges tangentially with the body surface.

In the nonlinear analysis the grid is then updated to incorporate the change in the airfoil/cavity boundary. In the next iteration the computations are performed over the modified grid. The non-cavitating points are treated as standard, while the interface points are treated as constant pressure points. This procedure is then repeated. The cavity surface then converges to a unique solution satisfying both flow tangency and pressure conditions. In the linear analysis, the solution is obtained in exactly the same manner as above, without updating the grid.

THERMODYNAMIC ANALYSIS

The thermal effects of cavitation result from the continuous vaporization process that is needed to sustain the cavity on the body surface. The heat for this vaporization must be extracted from the bulk liquid, and as a result, the temperature of the liquid in the immediate vicinity of the liquid-vapor interface is depressed below the free-stream temperature. An energy balance at the cavity interface yields the numerical conditions required for incorporating the thermal effects into the cavitation model. The evaporation rate and the temperature depression is determined by the thermal boundary layer at the liquid-vapor interface. The local temperature depression reduces the local vapor pressure of the fluid, which leads to a lower observed cavity pressure. As a result, the cavity size is smaller with temperature depression effects present.

Thermodynamic effects of cavitation are generally more significant in cryogenic fluids than in room temperature fluids such as water, because they are typically operated closer to their critical point. In addition, the slope of the vapor pressure-temperature curve of cryogenic fluids is much steeper than that for water. As a result, the change in vapor pressure is more significant.

RESULTS AND DISCUSSION

The cavitation model and the computational procedures presented above are discussed in greater detail elsewhere [7, 8, 9]. Comparisons of the Euler and Navier-Stokes models with experiments and potential flow calculations and with each other as well as parametric studies of cavitation are also presented in the above references. Some representative results are shown here.

Figure 1 compares the predicted pressure distribution over a NACA66(MOD) airfoil for the Euler and Navier-Stokes nonlinear analyses with experiment. Although there are some differences, the predictions from both the Navier-Stokes and the Euler analyses agree quite well with experiment and qualitatively with each other.

The cavity length for both the Euler and Navier-Stokes models is plotted as a function of cavity pressure in Fig. 2. The two models predict similar cavity lengths for the shorter cavities but the Euler predictions are slightly larger than the NS predictions at the longer cavity lengths. The obvious implication is that the presence of viscous and turbulent diffusion decreases the cavitation region slightly. One possible explanation is the fact that the fluid over the cavity interface in the viscous case has less energy than the inviscid case, due to viscous effects. The viscous fluid therefore tends to reattach earlier, in comparison to the inviscid fluid. These comparisons though justify the use of either velocity potential or Euler methods in a design model, where cavitation regimes are required to be identified.

A similar comparison between the linear and nonlinear Navier-Stokes cavitation models is shown in Fig. 3, for a NACA0012 airfoil at five degrees angle of attack. The much simpler linear model consistently provides an excellent prediction of the cavity length. The effectiveness of placing the cavity boundary conditions on the body along with the ability to use a fixed grid suggest that the linear analysis is best for design purposes, although periodic checks with the nonlinear model are recommended. The predictions agree quite well for the short cavities. However as the cavity length increases the predictions deviate, as the inaccuracies in the linearization become more significant.

The prediction of midchord cavitation is another advantage of the CFD solution over the velocity potential. For devices where the shape of the pressure distribution resembles a rooftop, the absence of a sharply defined minimum pressure location makes it difficult to identify a cavitation inception point for velocity potential solutions. In the CFD analysis such a pre-specification is not necessary. The prediction of midchord cavitation becomes straightforward, presented in Fig. 4 for a NACA66 hydrofoil at one degree angle of attack, compared with experiments from [10]. The predictions are in good agreement with experiments both with respect to the location of the cavity inception point as well as the length of the cavity. The expected stagnation pressure at the termination of the cavity can also be clearly

seen in the computations. This capability for predicting midchord cavitation represents an important advantage of the model.

As noted before the model needs no presumptions about either the pressure distribution or cavity length. Therefore we next turn to predictions of pressure level (cavitation number) for a computed cavity length. For this, we compare predicted pressure distributions with the data from Hord [11] for liquid hydrogen for a tapered plate airfoil. To compare our predictions we select a cavity length and present in Fig. 5, computed and measured pressure distribution on the airfoil surface. In this case the cavity length is about half the chord. The agreement between the calculation and the experiment is quite satisfactory in terms of the cavitation pressure level.

To evaluate the thermodynamic effects of cavitation, we compare temperature depression predictions with measurements from Hord [11] for liquid hydrogen in Fig. 6. as a function of cavity length. The calculated temperature depressions correspond to three different upstream velocities are shown. The experimental data for hydrogen, which are for a velocity range of about 25 to 55 m/s show non-dimensional temperature depressions up to 0.18. The analysis predicts similar magnitudes (up to 0.16). In addition, the analysis predicts an increase in $\Delta T/T$ with velocity, which is to be expected on theoretical bases, but which cannot be discerned clearly from the experimental data. Similar results were obtained for nitrogen [8].

REFERENCES

- [1] Tulin, M. " Steady two-dimensional cavity flows about slender bodies," Tech. Rep. 834, David Taylor Model Basin, 1953.
- [2] Wu, T. " Cavity and Wake Flows," *Annual Review of Fluid Mechanics*, vol. 4, 1972.
- [3] Baldwin, B., and Lomax, H. " Approximate and Algebraic Model for Separated Turbulent Flows," AIAA Paper 78-257, AIAA, 16th Aerospace Sciences Meeting Huntsville, AL. January 1978.
- [4] Kwak, D., Chang, J., Shanks, S., and Chakravarthy, S. " A Three-Dimensional Navier-Stokes Flow Solver Using Primitive Variables," *AIAA Journal*, vol. 24, 1986, 390–396.
- [5] Tulin, M., and Hsu, C. " New Applications of Cavity Flow Theory," Proc. 13th Symposium on Naval Hydrodynamics, Tokyo 1980.
- [6] Buist, J., and Raven, H. " A Consistently Linearized Approach for the calculation of Partial Sheet Cavitation," *Cavitation and Multiphase Flow Forum, ASME, FED*, vol. 98, 1990.
- [7] Deshpande, M., Feng, J., and Merkle, C. " Cavity Flow Predictions Based on the Euler Equations," *Journal of Fluids Engineering*, to appear, 1993.
- [8] Deshpande, M., Feng, J., and Merkle, C. " Numerical Modeling of the Thermodynamic Effects of Cavitation," 3rd International Conference on Cavitation, Cambridge, U.K. December 1992.
- [9] Deshpande, M., Feng, J., and Merkle, C. " Navier-Stokes Analysis of 2-D Cavity Flows," *Cavitation and Multiphase Flow Forum*, Washington, D.C. June 1993.
- [10] Shen, Y., and Dimotakis, P. " The influence of surface cavitation on hydrodynamic forces," Proc. 22nd ATTC, St. Johns 1989.
- [11] Hord, J. " Cavitation in Liquid Cryogenics : 2-Hydrofoils," Tech. Rep. CR-2156, NASA, 1972.

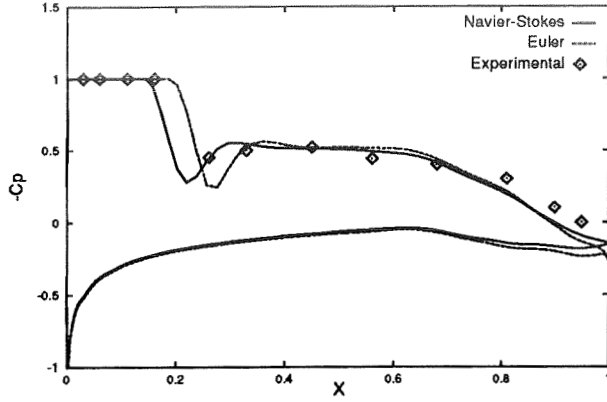


Figure 1: Comparison between Euler and Navier-Stokes analyses for NACA66(MOD) airfoil at $\alpha = 4$ deg. and $\sigma = 1.0$

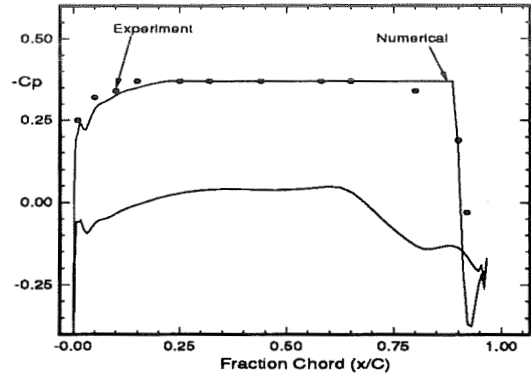


Figure 4: Mid Chord Cavitation for NACA66(MOD) airfoil at $\alpha = 1.0$ and $\sigma = 1.0$.

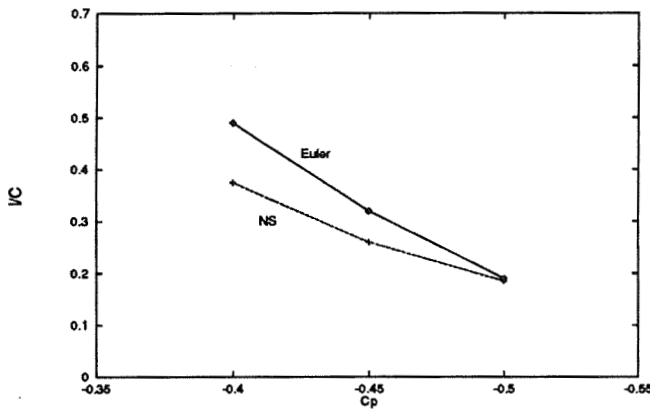


Figure 2: I/C vs C_p for Navier-Stokes and Euler models for a NACA66(MOD) airfoil at four degrees angle of attack

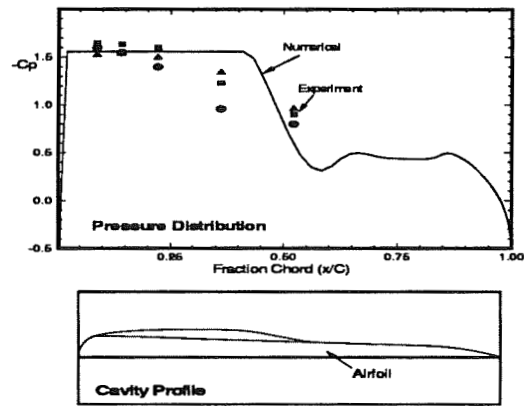


Figure 5: Comparison of cavitation pressure level with measurements from Hord.

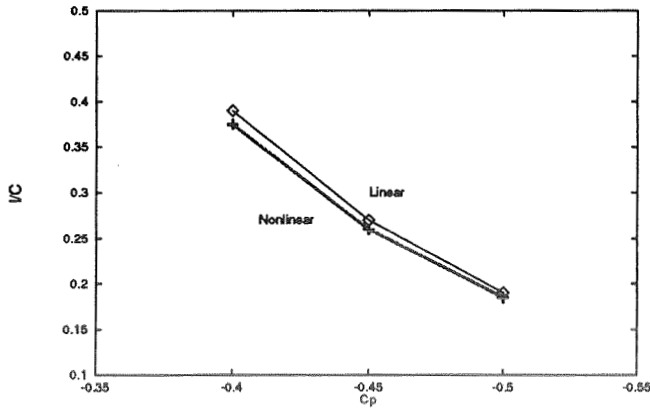


Figure 3: I/C vs C_p for linear and Nonlinear Navier-Stokes Models for NACA0012 Airfoil

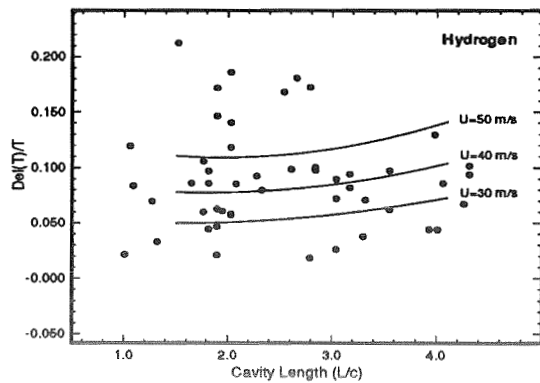


Figure 6: Temperature Depression as a function of Cavity Length for Hydrogen Comparison with Hord

A TECHNIQUE TO MEASURE ROTORDYNAMIC COEFFICIENTS IN HYDROSTATIC BEARINGS

Russell J. Capaldi
NASA Lewis Research Center

ABSTRACT

An experimental technique is described for measuring the rotordynamic coefficients of fluid film journal bearings. The bearing tester incorporates a double-spool shaft assembly that permits independent control over the journal spin speed and the frequency of an adjustable-magnitude circular orbit. This configuration yields data that enables determination of the full linear anisotropic rotordynamic coefficient matrices. The dynamic force measurements were made simultaneously with two independent systems, one with piezoelectric load cells and the other with strain gage load cells. Some results are presented for a four-recess, oil-fed hydrostatic journal bearing.

INTRODUCTION

New-generation rocket engine turbopumps will make greater use of fluid film journal bearings. This type of bearing has potential for long life and can use the engine's propellants as lubricant. Part of the design process for a turbopump involves rotordynamic analysis of the rotor-bearing system. As part of the rotor dynamic analysis, bearing coefficients, in the form of stiffness, damping and inertia, are necessary inputs. While rotor mechanics is well-characterized and relatively straightforward, determination of accurate bearing coefficients is not so well-established. Lund's review of the concept of fluid film bearing coefficients has a comprehensive reference list that includes experimental and analytical work (1). Taken as a whole, these references reveal the general difficulties in measuring bearing coefficients and the lack of uniform agreement between measured and analytical coefficients. The data base for rocket engine-type fluid film bearings is extremely small. The turbopump requires a bearing that operates at high speed, with small clearance and with low viscosity fluid. These parameters make experimental coefficient determination especially challenging. Butner and Murphy's report, as an example, reveals the added research and operational complexities of measuring coefficients for such a bearing (2).

As part of NASA's effort to develop fluid film bearings for rocket engine turbopumps, it has an ongoing program with Case Western Reserve University (CWRU) to develop a reliable and accurate measurement technique for bearing coefficients that can be ultimately applied to high-speed, low-viscosity bearings. The current experimental setup tests a hydrostatic oil journal bearing, but can accommodate other types of fluid film bearings. Coefficients have been extracted at low static eccentricity ratios and compare well with theory. In addition, the tester's unique load measuring system gives a high level of confidence in the data.

EXPERIMENTAL FACILITY

The linear anisotropic bearing model is shown in Figure 1, where K , C and D designate respectively stiffness, damping and inertia. In addition, the two fundamental methods to extract the coefficients from a dynamic system (i.e. fluid film bearing) are shown. The coefficient extraction method used at CWRU, and fully explained in reference 3., is the linear impedance model.

The test facility is located at CWRU and is fitted with independent air, water and oil systems. The bearing tester, shown in Figure 2, consists of a double-spool shaft assembly supported by rolling element bearings, and overhung test section. The double-spool shaft assembly is configured so that the orbital eccentricity of the inner shaft (relative to the outer shaft) can be accurately set from zero to 0.060 inch. This is achieved by having the outer spindle shaft comprised of two closely fitted cylindrical portions, with their respective mating surfaces eccentric to their respective centering surfaces. Each spindle shaft is independently driven by a variable speed drive and can be driven in either forward or backward rotation. The net result is a controlled circular orbit of the journal, with an orbit frequency independent of the journal spin speed. The resulting dynamic force signals exerted upon the test bearing are then measured by the load support system.

Figure 3 shows a lobe bearing installed in the tester. In this earlier version of the tester, the load support system consisted of only four piezoelectric load cells. Figure 4 shows the current load support system. Each load path consists of a strain-gaged load link in series with a piezoelectric load cell. This arrangement provides simultaneous measurement of the dynamic forces by two independent systems. The strain-gaged system also permits measurement of static radial forces. Both systems are calibrated in place. Journal displacements are measured by eddy current proximity probes.

The outer spindle, which produces the orbit frequency, is equipped with a timing disk at its drive end. The timing disk contains 360 equally spaced slots that interrupt a light beam, triggering an A-to-D converter as an external clock to the data acquisition PC. Eight channels of data are taken A-to-D, which include four force signals and four displacement signals. Thus, 45 digitized data points are taken from each channel per cycle of orbit. Typically, data is taken for 50 consecutive cycles and time-averaged. Data is taken at sufficiently off-synchronous frequencies so that extraneous signals not coherent with the orbit frequency are essentially filtered out (i.e. mechanical and electrical runout and 60 Hz). The eight time-averaged signals are then Fourier decomposed to extract the fundamental orbit frequency signal components, which provide the inputs to extract the bearing coefficients.

SAMPLE OF RESULTS

The test bearing details are given in Figure 5. A typical example of comparison between the dynamic load signals of the two independent systems is shown in Figure 6. The two signals shown are time-averaged over 50 consecutive cycles, and show very few harmonics. Numerical comparison between the fundamental

frequency components shows only a 1.8 % difference in amplitude and 0.3 degree difference in phase.

Figure 7 is a typical example of comparison between experimental and analytical stiffness and damping coefficients. This test condition was run at zero static eccentricity. As expected, the measured bearing coefficients are close to being isotropic. Direct coefficients are approximately equal in x - and y - directions. Cross-coupled stiffness in y - direction is equal in magnitude and opposite in sign to that in x -direction. Cross-coupled damping is close to zero. Predictions agree quite well with measured values. The biggest discrepancy is in over-prediction of direct stiffness. This is probably due to not including the effects of oil compressibility in the relatively deep (0.1875 inch) bearing recesses.

CONCLUDING REMARKS

The experimental results obtained so far with the CWRU tester have agreed quite well with analytical predictions. The self-checking nature of the dual load measurement system provides for greater accuracy in measuring fluid film forces, which has always been a difficult and uncertain aspect of coefficient determination.

A new test bearing holder is currently being fabricated so that tests can be performed at static eccentricity ratios up to 0.9, and the eccentricity can be quickly and accurately adjusted. This will allow for tests over a wide range of operating conditions and also for quicker setup and testing of a given bearing.

Testing to higher eccentricities will also verify over what range of eccentricities the linear impedance model can be expected to hold, as fluid film bearing coefficients should theoretically become nonlinear when the bearing becomes highly eccentric.

REFERENCES

- 1.) Lund, J.W., "Review of the Concepts of Dynamic Coefficients for Fluid Film Journal Bearings," ASME Journal of Tribology, Vol. 109, 1987, pp. 37 - 41.
- 2.) Butner, M., Murphy, B.T., "SSME Long-Life Bearings," NASA CR179455, 1986.
- 3.) Adams, M.L., Sawicki, J.T., Capaldi, R.J., "Experimental Determination of Hydrostatic Journal Bearing Rotordynamic Coefficients," IMechE Proceedings of 5th Rotating Machinery Symposium, C432/145, 1992.

Anisotropic Model

$$\begin{Bmatrix} f_x \\ f_y \end{Bmatrix} = - \begin{bmatrix} K_{xx} & K_{xy} \\ K_{yx} & K_{yy} \end{bmatrix} \begin{Bmatrix} x \\ y \end{Bmatrix} - \begin{bmatrix} C_{xx} & C_{xy} \\ C_{yx} & C_{yy} \end{bmatrix} \begin{Bmatrix} \dot{x} \\ \dot{y} \end{Bmatrix} - \begin{bmatrix} D_{xx} & D_{xy} \\ D_{yx} & D_{yy} \end{bmatrix} \begin{Bmatrix} \ddot{x} \\ \ddot{y} \end{Bmatrix}$$

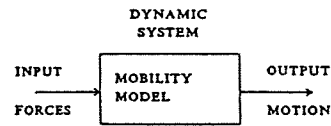
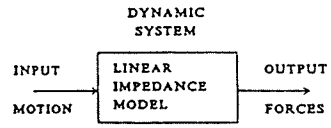
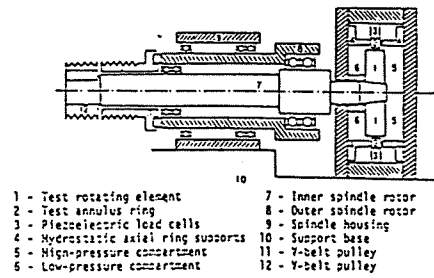
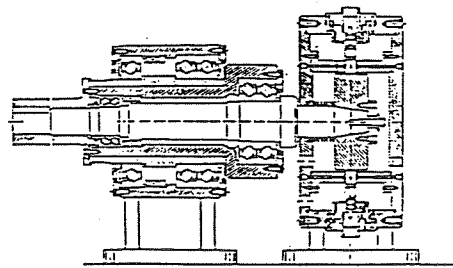


Figure 1. The Linear Anisotropic Bearing Model



Conceptual Sketch of Rotor Support Component Test Apparatus



Assembly Layout of Rotor Support Component Test Apparatus

Figure 2. CWRU Bearing Tester

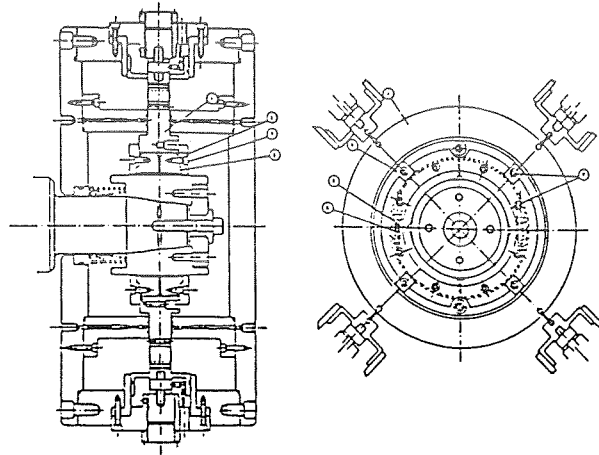
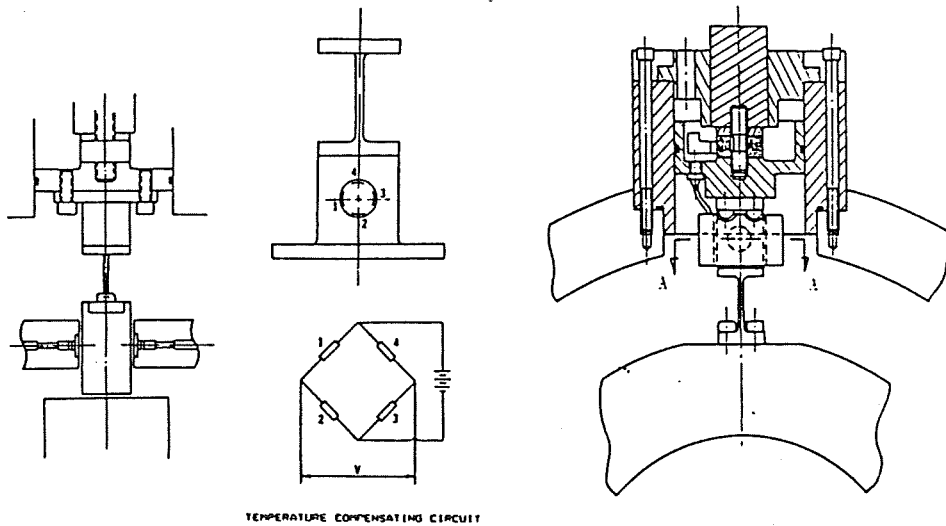
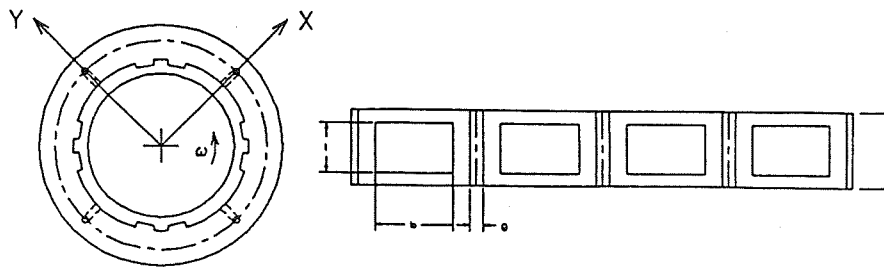


Figure 3. Arrangement for Bearing Test



TEMPERATURE COMPENSATING CIRCUIT

Figure 4. Dual Piezoelectric-Strain Gage Load Measurement System



LUBRICANT:

Motor Oil SAE 30
 Viscosity @ 100°F:
 14.212 micro-reyns
 (97987 micro-Pa·s)
 Operating Temperature 100-110°F

GOMETRY:

Diameter 4.516 in. (114.71 mm)
 Length 2.125 in. (53.98 mm)
 Recess (l) 1.40 in. (35.56 mm)
 Recess (b) 2.21 in. (56.13 mm)
 Recess Depth 0.1875 in. (4.763 mm)
 Groove (g) 0.375 in. (9.525 mm)
 Radial Clearance 0.0083 in. (0.211 mm)

Figure 5. Test Bearing and Parameters

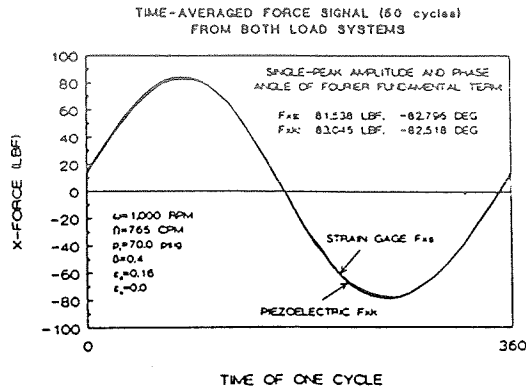


Figure 6. Total Time-Averaged Force Signal from Both Load Measuring Systems

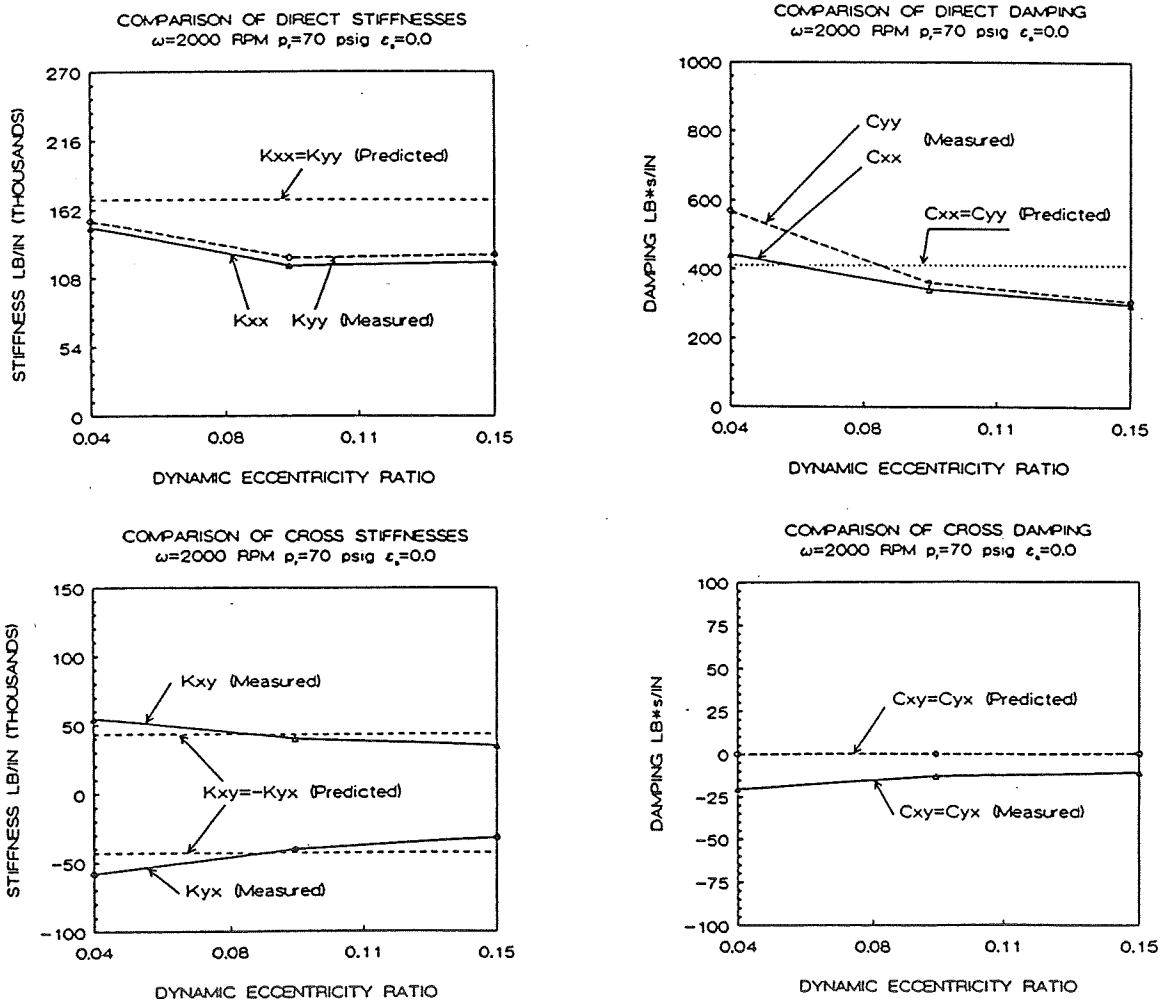


Figure 7. Comparisons of Test Results with Computations for Hydrostatic Oil Journal Bearing

Computation of Flows in a Turn-Around Duct and a Turbine Cascade
Using Advanced Turbulence Models

B. Lakshminarayana and J. Luo
Department of Aerospace Engineering
The Pennsylvania State University
University Park, PA 16802

Summary

Numerical investigation has been carried out to evaluate the capability of the Algebraic Reynolds Stress Model (ARSM) and the Nonlinear Stress Model (NLSM) to predict strongly curved turbulent flow in a turn-around duct (TAD). The ARSM includes the near-wall damping term of pressure-strain correlation ($\phi_{ij,w}$), which enables accurate prediction of individual Reynolds stress components in wall flows. The TAD mean flow quantities are reasonably well predicted by various turbulence models. The ARSM yields better predictions for both the mean flow and the turbulence quantities than the NLSM and the k - ϵ (k =turbulent kinetic energy, ϵ =dissipation rate of k) model. The NLSM also shows slight improvement over the k - ϵ model. However, all the models fail to capture the recovery of the flow from strong curvature effects. The formulation for $\phi_{ij,w}$ appears to be incorrect near the concave surface.

The hybrid k - ϵ /ARSM, Chien's k - ϵ model and Coakley's q - ω ($q = \sqrt{k}$, $\omega = \epsilon/k$) model have also been employed to compute the aerodynamics and heat transfer of a transonic turbine cascade. The surface pressure distributions and the wake profiles are predicted well by all the models. The k - ϵ model and the k - ϵ /ARSM model provide better predictions of heat transfer than the q - ω model. The k - ϵ /ARSM solutions show significant differences in the predicted skin friction coefficients, heat transfer rates and the cascade performance parameters, as compared to the k - ϵ model. The k - ϵ /ARSM model appears to capture, qualitatively, the anisotropy associated with by-pass transition.

Numerical Technique

An explicit two-dimensional Navier-Stokes solver -- RK2D (Kunz & Lakshminarayana, 1992) was used in the computation. The RK2D uses a standard 4-stage Runge-Kutta scheme. The fourth-order artificial dissipation is included to damp high wave number errors and the second-order artificial dissipation is used to improve the shock capturing. Anisotropic scaling of artificial dissipation terms was used. By the use of local velocity scaling, the smoothing was reduced to zero near the wall to avoid contamination of the solution by excessive dissipation. Local variable timestepping was also used to improve convergence. In the near wall viscous sublayer and buffer layer, the low Reynolds number k - ϵ model is used. The matching point for ARSM (or NLSM) and k - ϵ model is at $y^+ = 50$ ($y^+ = yu_\tau/\nu$, y =distance from the wall, u_τ =friction velocity, ν =kinematic viscosity).

Results and Discussion

1) Computation and Analysis of the Flow in a Turn-Around Duct

Most rocket engine components operate at very high pressures and Reynolds numbers and the flows are fully turbulent. These flows are often subjected to very large strain-rates such as those arising from the strong streamline curvature. There have been many studies on the effects of streamline curvature, however, most deal with mild curvature. Bradshaw (1973) reviewed the literature prior to 1973. Recently, Monson et al. (1990) reported detailed measurements in a two-dimensional TAD air tunnel at Mach no.=0.1 and $Re=10^5$ or $Re=10^6$. They also calculated this TAD flow using several different versions of $k-\epsilon$ models and found that only one extended model gave reasonable predictions. The present investigation has been carried out with more advanced turbulence models, namely, the ARSM, which was derived from Gibson & Launder (1978) Reynolds Stress Model (RSM) by invoking the ARSM assumption, and the NLSM of Shih et al. (1992). A 201×101 (streamwise x normal direction) H-grid is generated by algebraic method.

The $k-\epsilon$ /ARSM model was validated against a flat plate boundary layer. The computed values of turbulence intensities are in good agreement with Klebanoff's data (1954) for a flat plate boundary layer, as shown in Fig. 1. For the TAD flow, all the three turbulence models predict the static pressure coefficients very well on both the inner and the outer walls along the bend, as can be seen in the Fig. 2. The pressure loss and static pressure downstream of the bend are also predicted reasonably well by all the three models. However, the NLSM predicts a larger separation region on the inner wall than the measurement, which can be seen from the underprediction of the pressure coefficient near the exit of the bend.

Fig. 3(a) shows longitudinal velocity profiles predicted by the $k-\epsilon$ model (with Chien's near wall function slightly modified), NLSM and ARSM models. All the models underpredict the velocity near the outer wall. However, the turbulent kinetic energy (TKE) and turbulent shear stress (TSS) profiles are predicted reasonably well by all the models. As shown in Fig. 3(b) and 3(c), the reduction of turbulent shear stress near the convex (inner) wall is predicted well. The predicted enhancement of turbulence near the concave (outer) wall is in agreement with the experiment (Fig. 3(c)). As shown in the figures, prediction of turbulence quantities from the ARSM is consistently better than those from the NLSM and $k-\epsilon$ models.

At the exit of the bend ($\theta=180$ deg), the data indicate that the flow is separated on the convex wall (Fig. 4(a)). All the models predict separation, but underpredict the height of the separation bubble. The prediction of mean velocity by the ARSM is slightly better than those from the NLSM and the $k-\epsilon$ models. The TKE level near the mid-channel was underpredicted significantly by all the models (Fig. 4(b)), this is due to underprediction of the radial component of normal stresses near the outer wall. It could be due to the breakdown of the ARSM assumption, i.e., the $u_i u_j / k$ is constant in the flowfield, or the deficiency of the present formulation for the pressure-strain correlation and the dissipation rate of k (i.e., ϵ).

2) Computation of the transonic turbine cascade flow

The aerodynamics and blade heat transfer data of the VKI transonic linear turbine guide vane cascade measured by Arts, et al. (1990) was selected as the primary test case for present work. The turbine blade shape tested was optimized for a downstream isentropic Mach number of 0.9. The downstream isentropic Reynolds number (based on chord length) varied from 0.6×10^6 to 2.1×10^6 . The total temperature in the free stream was around $410(^{\circ}\text{K})$ and the blade surface temperature was constant at about $300(^{\circ}\text{K})$ for all the test runs. The freestream turbulence intensity varied from 1% to 6%. The inlet flow

angle was $\beta_1=0$ (deg), chord length $C=67.65$ (mm), pitch/chord=0.85, stagger angle=55 (deg), axial chord length $C_{ax}=37.0$ (mm), design outlet angle $\beta_2=74$ (deg). For numerical details, see Luo & Lakshminarayana (1993).

A 129x71 H-grid is used. Blade surface pressure distributions, blade wake, aerodynamic losses and exit flow angles are captured very well by all the three models. The blade isentropic Mach no., including the effect of shock wave, is captured accurately by all the models, as shown in Fig. 5. Fig. 6 shows the comparison of computed and measured wake profiles. The agreement is very good from all the three models. The semi-wake width is shown in Fig. 7. Sudden increase in wake width at downstream locations A and B is attributed to shock/wake interaction. It is clear that the correlation shown in Fig. 7 is not valid when shock waves are present at the cascade exit. Except for the shock/wake interaction region the wake width follows the correlation. In Fig. 8, the predictions of heat transfer by all the models are shown and these are in good agreement with the data. The transition is triggered by the shock wave and this has been captured by all the models. The boundary layer code (TEXSTAN) underpredicts the heat transfer on the pressure surface and the solution is terminated on the suction surface near the inception of separation. Sharma et al. (1982) have observed that most of the disturbance energy is contained in the streamwise component of turbulence intensity before transition. During the transition, both the streamwise and the normal components grow with the latter component growing at a faster rate than the former, resulting in a decrease of the relative magnitude of the streamwise intensity. As can be seen from Fig. 9, this evolution of streamwise and normal turbulence intensity within the boundary layer during transition appears to have been simulated qualitatively by the k- ϵ /ARSM model.

Acknowledgements

This work was supported by the NASA through contract NAS 8-38867 monitored by Lisa Griffin of Marshall Space Flight Center, and by the Penn State - NASA Propulsion Center. The authors wish to acknowledge NASA for providing the supercomputing resources at NASA Lewis and Marshall Research Centers.

References

- Arts, T., Rouvroit, M. L. and Rutherford, A. W., 1990, "Aero-thermo Investigation of a Highly Loaded Transonic Linear Turbine Guide Vane Cascade," Von Karman Institute TN 174. Also, *Journal of Turbomachinery*, Vol. 114, pp. 147-154.
- Bradshaw, P., 1973, "Effects of Streamline Curvature on Turbulent Flow," *AGARD-AG-169*.
- Chien, K. Y., 1982, "Prediction of Channel and Boundary-Layer Flows with a Low-Reynolds Number Turbulence Model," *AIAA Journal*, Vol. 20, No. 1.
- Coakley, T.J., 1983, "Turbulence Modeling Methods for the Compressible Navier-Stokes Equations", *AIAA Paper 83-1693*.
- Gibson, M. and Launder, B., 1978, "Ground Effects on Pressure Fluctuations in the Atmospheric Boundary Layer," *J. Fluid Mech.*, vol. 86, pp.491.
- Klebanoff, P., 1954, "Characteristics of Turbulence in a Boundary Layer with Zero Pressure Gradient," *NACA TN-3178*.
- Kunz, R. and Lakshminarayana, B., 1992, "Explicit Navier-Stokes Computation of Cascade Flows Using the k- ϵ Model," *AIAA Journal*, Vol. 30, No. 1.
- Luo, J. and Lakshminarayana, B., 1993, "Navier-Stokes Analysis of Turbine Aerodynamics and External Heat Transfer," *ISABE paper*, Tokyo.
- Monson, D. J., Seegmiller, H.L., McConnaughey, P. K. and Chen, Y. S., 1990, "Comparison of Experiment with Calculations Using Curvature-Corrected Zero and Two Equation Turbulence Models for a Two-Dimensional U-Duct," *AIAA paper 90-1484*.
- Sharma, O. P., Wells, R. A., Schlinker, R. H. and Bailey, D. A., 1982, "Boundary Layer Development on Turbine Airfoil Suction Surfaces," *Journal of Engineering for Power*, Vol. 104, pp. 698-706.
- Shih, T., Zhu, J. and Lumley, J. L., 1992, "A Realizable Reynolds Stress Algebraic Equation Model," *NASA TM 105993*.

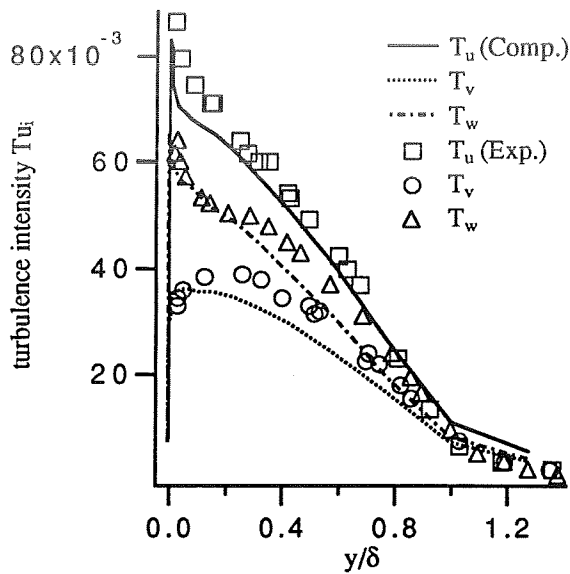


Fig. 1 Turbulence intensity profiles in the flat-plate turbulent boundary layer: experiment by Klebanoff; computation by 2-layer $k-\epsilon$ /ARSM; y =normal distance to the wall, δ =boundary layer thickness, Tu_i =turbulence intensity components.

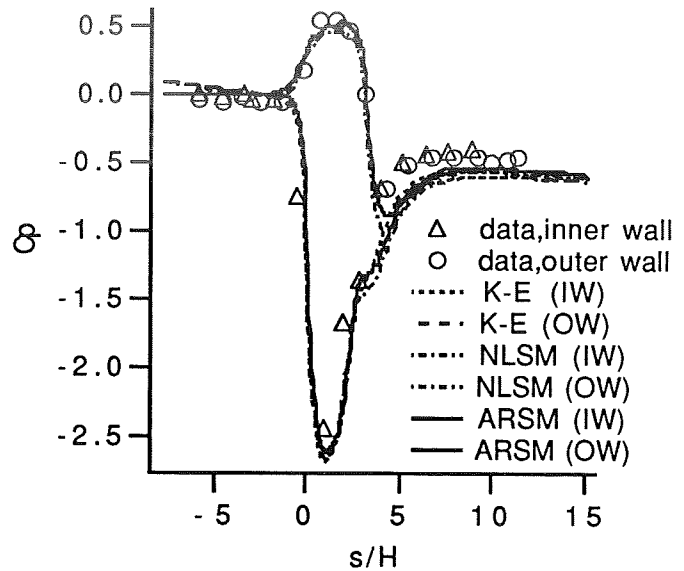


Fig. 2 Static pressure coefficient (C_p) on turn-around duct inner and outer walls; S =streamwise distance, H =duct height, $C_p=(P-P_{ref})/(1/2\rho U_m^2)$, P_{ref} =static pressure at inlet, U_m =bulk velocity

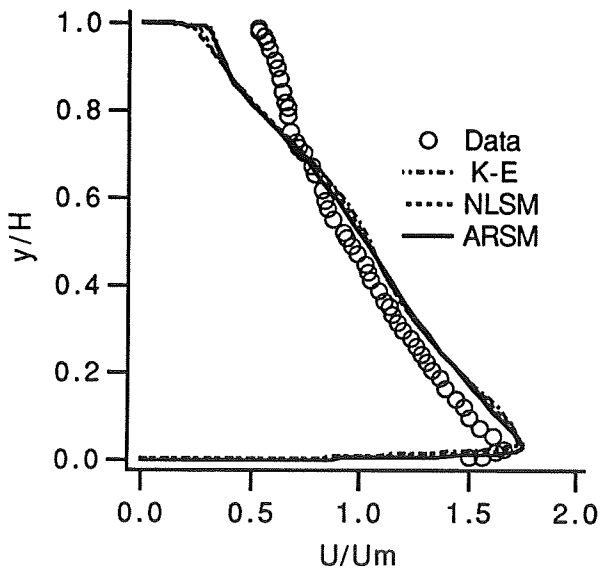


Fig. 3(a) Longitudinal velocity (U) in turn-around duct, $\theta=90$ deg.; U_m =bulk velocity, θ =angle into bend, y =normal distance to the inner wall.

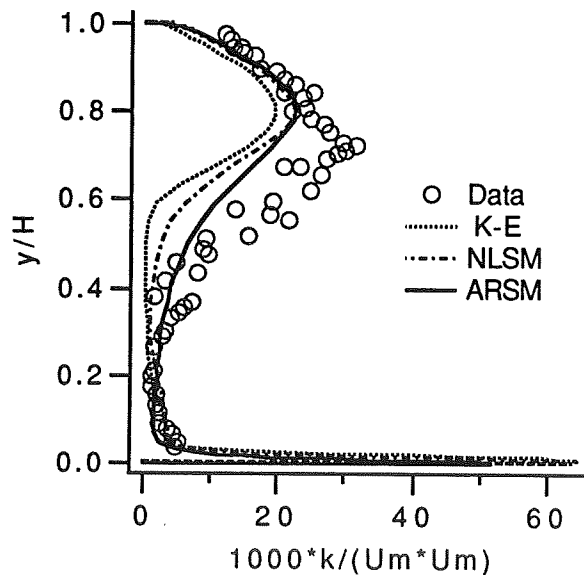


Fig. 3(b) Turbulent kinetic energy (k) profile

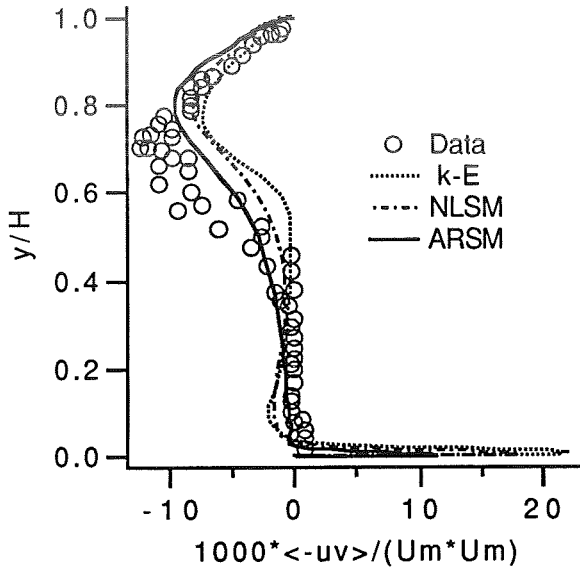


Fig. 3(c) Turbulent shear stress ($\langle -uv \rangle$) profile

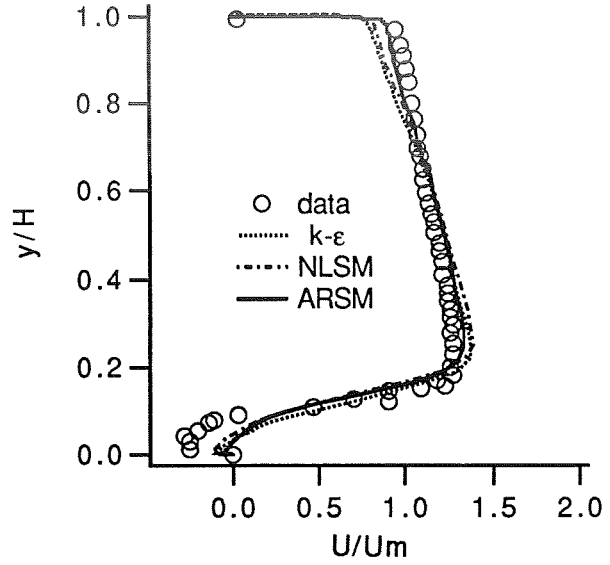


Fig. 4(a) Longitudinal velocity in turn-around duct, $\theta = 180$ deg

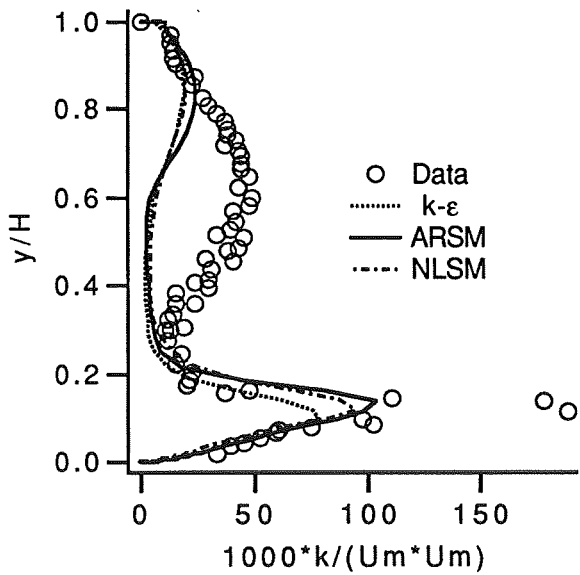


Fig. 4(b) Turbulent kinetic energy profile

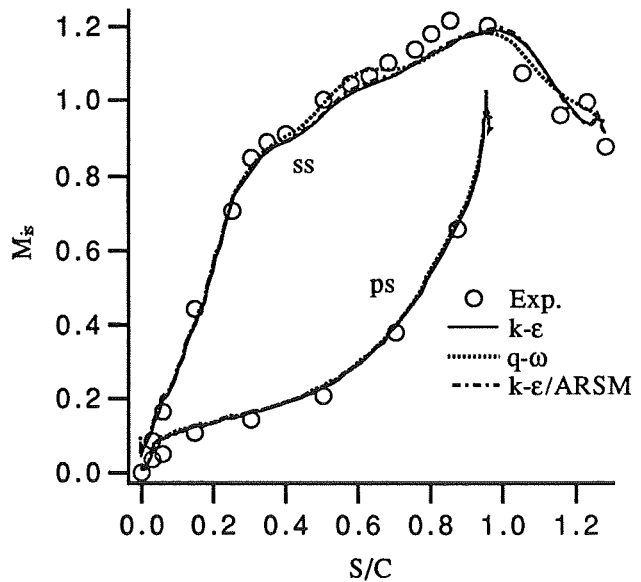


Fig. 5 Blade isentropic Mach no. distribution for case Mur049 ($M_{is,2} = 1.02$, $Re_{is,2} = 1.0 \times 10^6$ and $Tu_\infty = 1\%$); S = coordinate along blade surface, C = chord length, ss = suction surface, ps = pressure surface.

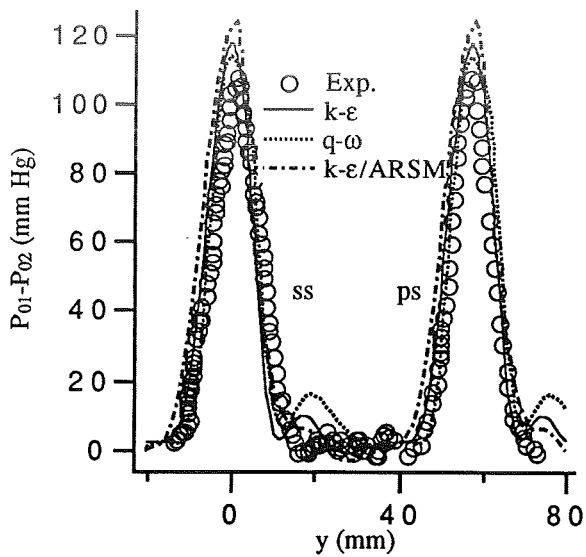


Fig. 6 Computed and measured wakes at $x/C_{ax} = 1.433$ for the above case; $P_{01}-P_{02}$ =total pressure loss, x =coordinate along axial chord, y =pitchwise coordinate, C_{ax} =axial chord length

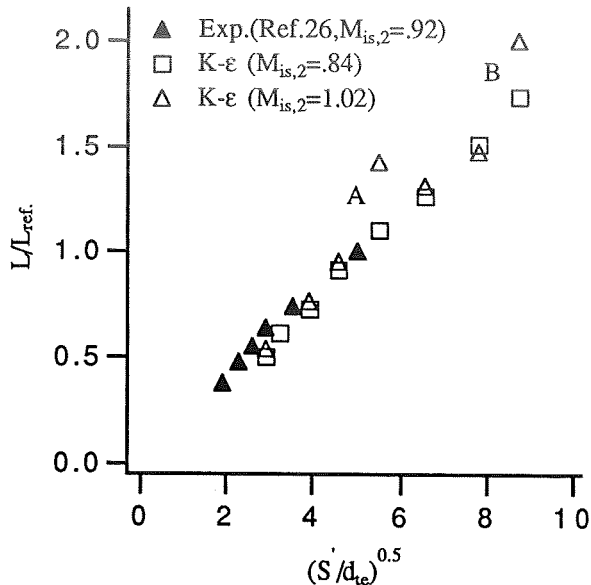


Fig. 7 Wake width growth downstream of the blade. L =semi-wake width, S'/d_{te} =non-dimensional distance in exit flow direction

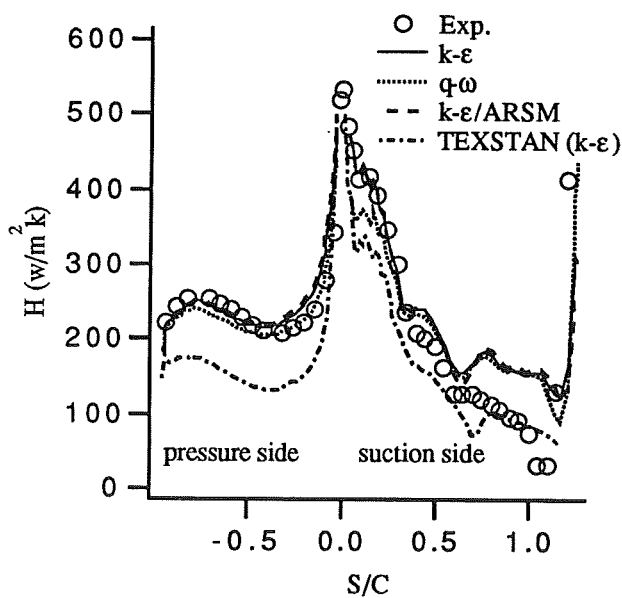


Fig. 8 Heat transfer prediction for case Mur222 ($M_{is,2} = 1.14$, $Re_{is,2} = 0.55 \times 10^6$ and $Tu_{\infty} = 6\%$); H =heat transfer coefficient.

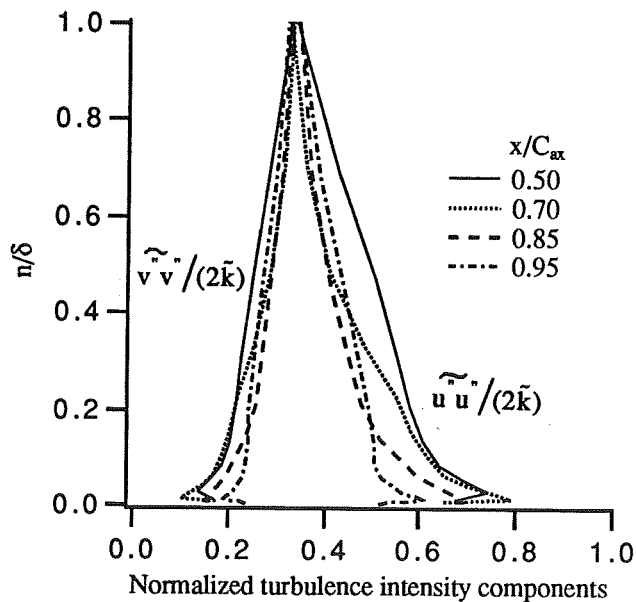


Fig. 9 The normalized turbulence intensity component profiles (Computed by $k-\epsilon/ARSM$) at different axial chordwise locations on the suction surface (n is the normal distance to the wall and δ is the boundary layer thickness)

Fifth Annual Symposium on Space Propulsion
September 8-9, 1993

Margaret P. Proctor
NASA Lewis Research Center
21000 Brookpark Road
Cleveland, Ohio 44135
(216) 977-7526

ABSTRACT

Brush seals are compliant, contacting seals and have significantly lower leakage than labyrinth seals in gas turbine applications. Their characteristics of long life and low leakage make them candidates for use in rocket engine turbopumps. Two-inch diameter brush seals with a nominal 0.005 inch radial interference were tested in liquid nitrogen at shaft speeds up to 35,000 rpm and pressure drops up to 175 psid per seal. A labyrinth seal was also tested to provide a baseline. Performance, staging effects, and wear results are presented.

INTRODUCTION

Brush seals are compliant, contacting seals. They are comprised of a pack of small diameter (0.0028 inch) wire bristles set at an angle (typically 40 degrees) to the radial direction, which is sandwiched between a front and back washer. The back washer serves as a mechanical support to prevent the bristles from blowing out downstream. Typically brush seals are designed to have an interference fit with the shaft. Because the bristles are angled, they act as cantilevered beams during shaft perturbations. Bristles under load from the shaft bend away from the shaft. Unloaded bristles relax and remain in contact with the shaft.

Brush seals have shown a significant improvement in leakage performance over labyrinth seals and have been successfully operated for thousands of hours in gas turbine applications. (Ref.1) These characteristics of low leakage and long life make brush seals candidates for use in rocket engine turbopumps, particularly for space-based engines and reusable launch engines. The low leakage requirement is most critical in meeting the wide-operating range requirement of space engines in which seal leakage can significantly reduce engine performance at low thrust levels.

Testing of brush seals in liquid nitrogen was conducted at the NASA Lewis Research Center at shaft speeds up to 35,000 rpm and pressure drops up to 175 psid per seal. A labyrinth seal was also tested to provide a baseline for comparison. Performance, staging effects, and wear results are presented.

PERFORMANCE

Two-inch diameter brush seals with a nominal 0.005 inch radial interference were tested in liquid nitrogen. A 12-tooth, 0.00513 inch radial clearance labyrinth seal was tested in liquid nitrogen as a baseline. Measured and predicted labyrinth seal performance were in good agreement. As expected, there was no speed dependence in the labyrinth seal. Leakage of a single brush seal was two to three times less than the labyrinth seal. Shaft rotation is necessary to properly seat the seal and achieve the lowest leakage. As expected, the fluid temperature rise across the seal increases with increased shaft speed due to frictional heating between the brush and rotor. An increased pressure drop across the seal, which caused a higher leakage rate, resulted in decreased fluid temperature rise across the seal because more flow was available to carry the heat away. A blowout test at a shaft speed of zero rpm was conducted to determine the maximum pressure a single brush seal could withstand. A pressure gradient of 550 psid was applied to a single seal with no blowout occurring. At this condition the instrumentation became saturated. The power loss due to a single brush with a pressure load of 175 psid at 35,000 rpm was 3.75 Btu/s based on the mass leakage flow through the seal and the fluid enthalpy change between the seal inlet and exit.

STAGING EFFECTS

Staging effects were studied. Two brushes separated by two brush widths leaked about half as much as a single brush. However, two brushes tightly packed leaked about 75% as much as a single brush. As expected, the fluid temperature rise with two or three seals is greater than that with just one brush seal. The maximum temperature rise, measured at a shaft speed of 35,000 rpm and pressure drop across the seal of 25 psid was 95 R for three brushes and 56 R for one brush. In the configuration of three brushes evenly spaced, the leakage performance of the first two seals was nearly equal, but approximately half that of the last brush at zero rpm. However, at 35,000 rpm the leakage performance of each of the seals was nearly equal.

WEAR

The rotor was made of Inconel 718 and the bristles were made of Haynes-25. Shaft rotordynamics were very good; nominal rotor orbits were less than 0.2 mils in diameter. A maximum orbit of 1.0 mil diameter did occur for a brief time during testing. The maximum shaft speed was 35,000 rpm and the maximum surface velocity was 305 ft/s. Four and one-half hours of shaft rotation time was accumulated. This is 36 times the 450 second mission life of an RL-10 rocket engine. After testing, profilometer traces were taken across the axial length of the rotor at four locations: 0, 90, 180, and 270 degrees. The maximum groove depth measured was 0.0010 inch and the nominal groove depth was 0.00075 inch. Some bristle wear did occur; approximately 1-3 mils. Bristle wear is difficult to quantify due to uncertainty in bristle bore diameter measurements. An optical comparator was used to make these measurements and it was found that the bore diameter can vary by 7.5 mils. A few bristles (approximately 10) appeared to have melted. This may have occurred at some early test conditions of shaft speed, but no pressure gradient across the seal. These test conditions were discontinued.

REFERENCES

1. Ferguson, J.G.: Brushes as High Performance Gas Turbine Seals. ASME Paper 88-GT-182, June 1988.
2. Morrison, G.L., et.al.: Labyrinth Seals for Incompressible Flow, Final Report for NASA Contract NAS8-34536, Texas A & M University, November 30, 1983.

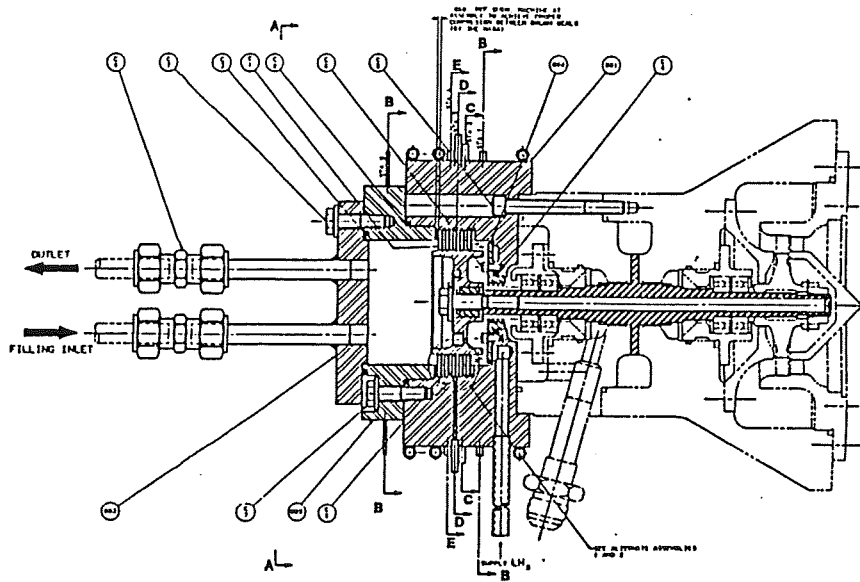


Figure 1.
Cross section of cryogenic brush seal tester.

NOMINAL GEOMETRY

ROTOR:	Outside Diameter	2.0000 inch
	Surface Roughness	32
	Material	Inconel 718
	Coating	none
BRUSHES:	Manufacturer	Technetics
	Outside Diameter	2.8190 in.
	Frontplate I.D.	2.4000 in.
	Bristle I.D.	1.9900 in.
	Backplate I.D.	2.0220 in.
	Axial thickness	0.142 in.
	Backplate thickness	0.056 in.
	Bristle angle	40 degrees
	Bristle diameter	0.0028 in.
	Packing density	3000 bristle/inch-circumference
	Plate material	Hastelloy-X
	Bristle material	Haynes-25
CALCULATED PARAMETERS:		
	Radial interference	0.0050 in.
	Radial clearance between backplate and rotor	0.011 in.
	Radial distance between backplate & bristle id's	0.016 in.
	Radial distance between frontplate & bristle id's	0.205 in.

Table I.

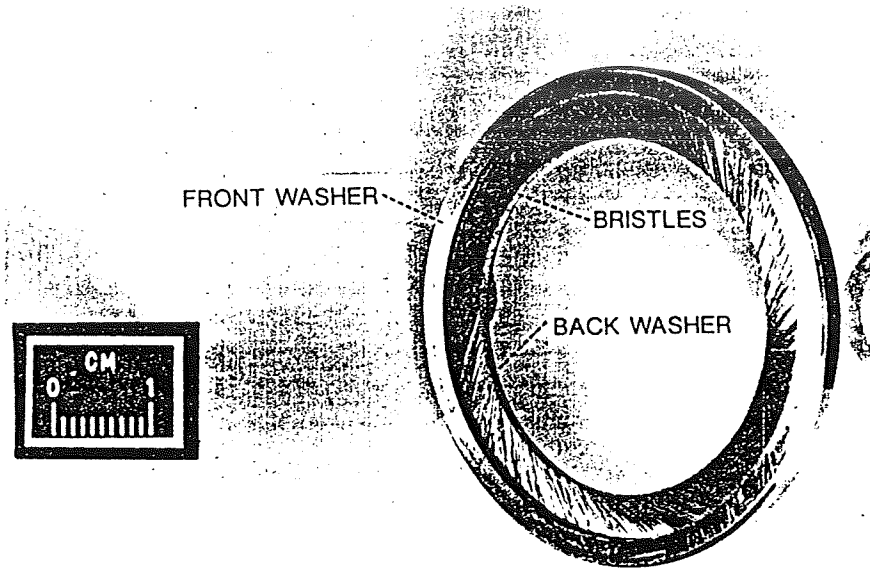


Figure 2.
A typical brush seal.

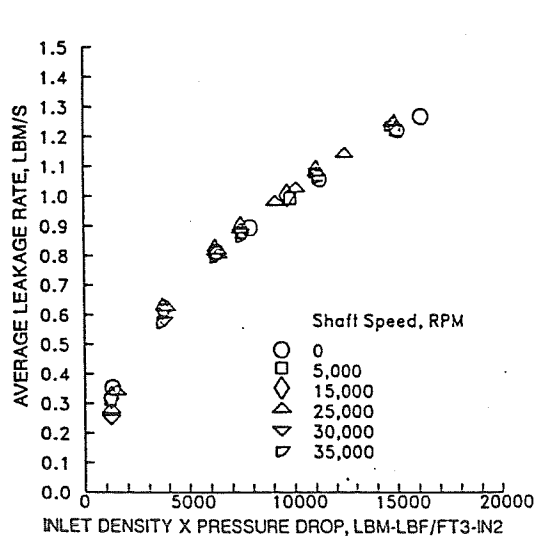


Figure 3.
Leakage rate of a 12-tooth labyrinth seal with 0.00513 inch radial clearance in liquid nitrogen as a function of seal inlet density x pressure drop across the seal.

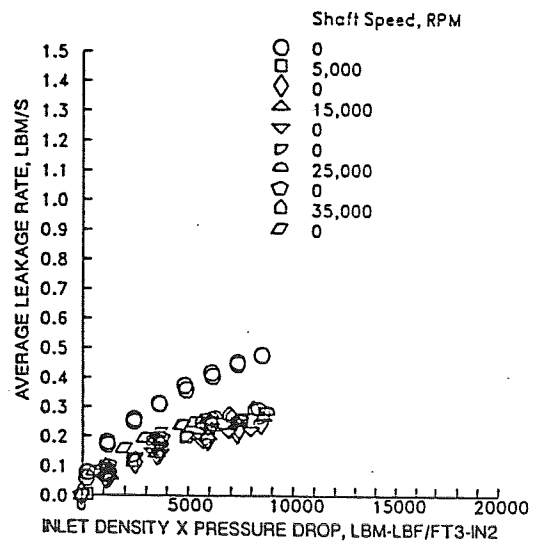


Figure 4.
Leakage rate of a single brush seal in liquid nitrogen of 0.004375 inch radial interference as a function of seal inlet density x pressure drop across the seal.

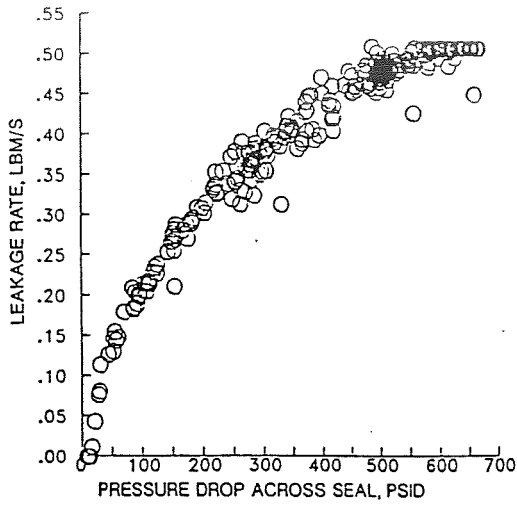


Figure 5.
Blowout test of a single brush seal in LN2 at zero rpm.

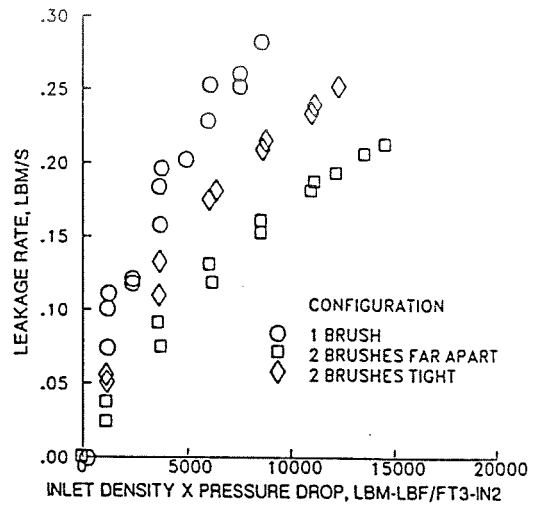


Figure 6.
Comparison of LN2 leakage performance for a single brush, two brushes separated by two brush widths, and two brushes tightly packed at 5,000 rpm.

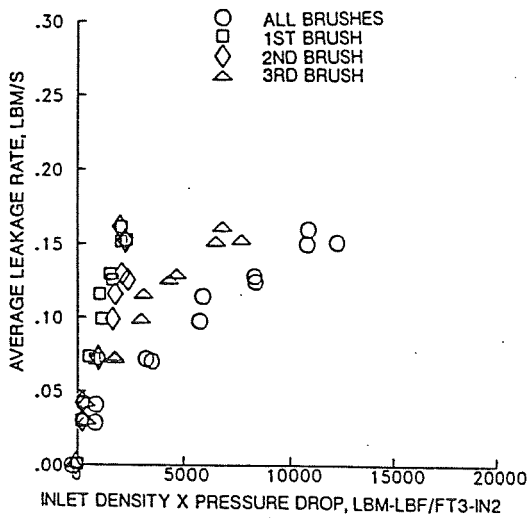


Figure 7.
Comparison of LN2 leakage performance for each seal in the 3 brushes evenly spaced configuration at zero rpm.

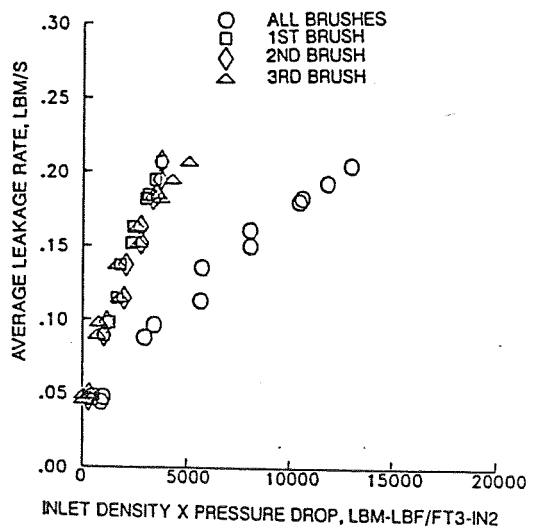


Figure 8.
Comparison of LN2 leakage performance for each seal in the 3 brushes evenly spaced configuration at 35,000 rpm.

RELIABILITY ENHANCEMENT OF NAVIER-STOKES CODES THROUGH CONVERGENCE ENHANCEMENT

K.-Y. Choi and G. S. Dulikravich

Department of Aerospace Engineering, The Pennsylvania State University
University Park, PA 16802

SUMMARY

Reduction of total computing time required by an iterative algorithm for solving Navier-Stokes equations is an important aspect of making the existing and future analysis codes more cost effective. Several attempts have been made to accelerate the convergence of an explicit Runge-Kutta time-stepping algorithm. These acceleration methods are based on local time stepping¹, implicit residual smoothing¹, enthalpy damping¹ and multigrid techniques². Also, an extrapolation procedure based on the power method and the Minimal Residual Method (MRM) were applied² to the Jameson's multigrid algorithm. The MRM uses same values of optimal weights for the corrections to every equation in a system and has not been shown to accelerate the scheme without multigriding. Our Distributed Minimal Residual (DMR) method³⁻⁴ based on our General Nonlinear Minimal Residual (GNLMR) method⁵ allows each component of the solution vector in a system of equations to have its own convergence speed. The DMR method was found capable of reducing the computation time by 10-75% depending on the test case and grid used. Recently, we have developed and tested a new method termed Sensitivity Based DMR or SBMR method that is easier to implement in different codes and is even more robust and computationally efficient than our DMR method.

TECHNICAL DISCUSSION

This method predicts an optimum amount of correction to the solution vector by combining the information from several previous iteration levels. Each of the corrections obtained from the past iterations is multiplied by a different weighting factor and these weighting factors are determined so that they minimize the overall future residual. Although it is based on general Krylov subspace methods, the DMR method differs from them by the fact that weighting factors are different from one variable to another in the system. Recently, we divided the computational domain into several zones and the DMR method was applied separately in each of these zones. This approach did not show noticeable improvement over the original DMR method. Also it was difficult to decide how to divide the domain systematically into several zones. The DMR concept was also applied to minimize the future residual at each grid point rather than to minimize the residual integrated over the whole domain. This approach was not successful, because the weighting factors obtained for each grid point differ too much from one point to another thus making convergence history erratic and often diverging.

SENSITIVITY BASED MINIMAL RESIDUAL (SBMR) METHOD

The residual at a grid point depends on the solution vector Q at the neighboring points including the point itself. The sensitivity of residual R_m ($m=1,2,3$: number of equations) with respect to Q_k (k =typical neighboring

points) is $\frac{\partial R_m}{\partial Q_k}$. Notice that the sensitivity can be determined from the finite difference equation used in the scheme.

For a two-dimensional incompressible flow solved using Chorin's artificial compressibility method the solution vector is $Q = [p \ u \ v]^T$. Suppose we have calculated the solution vector Q at iteration levels up to $t+n$ where n is the number of regular iteration steps between two iteration levels. Then the change in the solutions between the iteration levels can be written as follows.

$$\Delta p_k = (p_k)^{t+n} - (p_k)^t \quad \Delta u_k = (u_k)^{t+n} - (u_k)^t, \quad \Delta v_k = (v_k)^{t+n} - (v_k)^t, \quad (1)$$

Using the first two terms in a Taylor series expansion in artificial time direction, each residual for a two-dimensional system after n iterations will be

$$R_m^{t+n} = R_m^t + \left[\sum_k \frac{\partial R_m^t}{\partial p_k} \Delta p_k \right] + \left[\sum_k \frac{\partial R_m^t}{\partial u_k} \Delta u_k \right] + \left[\sum_k \frac{\partial R_m^t}{\partial v_k} \Delta v_k \right]; \quad m=1,2,3 \quad (2)$$

Similarly, future residual at $t = (t+n)+1$ can be approximated by

$$R_m^{(t+n)+1} = R_m^t + \left[\sum_k \frac{\partial R_m^t}{\partial p_k} \Delta p_k \right] \alpha_p + \left[\sum_k \frac{\partial R_m^t}{\partial u_k} \Delta u_k \right] \alpha_u + \left[\sum_k \frac{\partial R_m^t}{\partial v_k} \Delta v_k \right] \alpha_v \quad (3)$$

Here, α 's are the factors that multiply Δ 's to estimate the future solution vector so that it satisfy a desired objective.

For now, each α is assumed to have the same value over the whole domain. The future solutions are estimated as

$$(p_k)^{(t+n)+1} = (p_k)^t + \alpha_p \Delta p_k \quad (4)$$

with similar expressions for u and v . The α 's are determined such that the L-2 norm of the overall future residual will be minimized, that is,

$$\sum_D \left[\frac{\partial (R^{(t+n)+1})^2}{\partial \alpha_q} \right] = 2 \sum_D \left[R^{(t+n)+1} \frac{\partial R^{(t+n)+1}}{\partial \alpha_q} \right] = 0 \quad (5)$$

where the subscript q stands for each flow variable p , u and v . For simplicity, let us denote the bracketed terms in equation (3) as a_{mp} , a_{mu} and a_{mv} so that

$$a_{mp} = \sum_k \frac{\partial R_m^t}{\partial p_k} \Delta p_k \quad (6)$$

with similar expressions for a_{mu} and a_{mv} . Therefore,

$$R_m^{(t+n)+1} = R_m^t + a_{mp} \alpha_p + a_{mu} \alpha_u + a_{mv} \alpha_v \quad (7)$$

Substituting (7) into (5) gives the following three equations for optimal global α 's.

$$\sum_D \left[\sum_{m=1}^3 (R'_m + a_{mp} \alpha_p + a_{mu} \alpha_u + a_{mv} \alpha_v) a_{mp} \right] = 0 \quad (8)$$

with similar expressions involving a_{mu} and a_{mv} . In equation (8), R's and a's are known from the past iteration results. Since each α is assumed to have the same value over the computational domain, equation (8) gives a system of simultaneous equations for α_p , α_u and α_v .

$$\left[\sum_D \left(\sum_{m=1}^3 a_{mp} a_{mp} \right) \right] \alpha_p + \left[\sum_D \left(\sum_{m=1}^3 a_{mu} a_{mp} \right) \right] \alpha_u + \left[\sum_D \left(\sum_{m=1}^3 a_{mv} a_{mp} \right) \right] \alpha_v = - \sum_D \left(\sum_{m=1}^3 R'_m a_{mp} \right) \quad (9)$$

with similar expressions arising from u and v components. As the grids are clustered (higher cell aspect ratio), local time steps become smaller in those regions in order to meet the stability criterion. Numerical results (Figures 1-6) obtained at low and high Reynolds numbers on non-clustered and moderately clustered grids for straight and U-shaped two-dimensional channel flow demonstrate that SBMR method can: a) be used in conjunction with any basic iterative algorithm, b) be used with only minor modifications in the existing codes, c) significantly accelerates iteration procedure, d) perform more effectively at lower Reynolds numbers, e) perform well on moderately clustered grids.

The SBMR method applied so far calculates the same α 's for the entire computational domain, which cannot represent optimum α 's for both coarse grid regions and fine grid regions. Therefore, a natural conclusion is to allow α 's to have different values in the clustered regions. The future work on SBMR will concentrate on applying this method by lines such that each grid line normal to the clustering direction has its own α 's. We expect that with this approach, SBMR concept will calculate the optimal local corrections to solution vectors on highly clustered grids.

REFERENCES

1. Jameson, A., Schmidt, W. and Turkel, E., "Numerical Solutions of the Euler Equations by Finite Volume Methods Using Runge-Kutta Time-Stepping Schemes," AIAA Paper 81-1259, June 1981.
2. Hafez, M., Parlette, E. and Salas, M.D., "Convergence Acceleration of Iterative Solutions of Euler Equations for Transonic Flow Computations," AIAA Paper 85-1641, July 1985.
3. Lee, S. and Dulikravich, G.S., "Acceleration of Iterative Algorithms for Euler Equations of Gasdynamics," AIAA Journal, Vol. 28, No. 5, pp. 939-942, May 1990.
4. Lee, S. and Dulikravich, G.S., "Distributed Minimal Residual (DMR) Method for Acceleration of Iterative Algorithms," Computer Methods in Applied Mechanics and Engineering, Vol. 86, pp. 245-262, 1991.
5. Huang, C.Y. and Dulikravich, G.S., "Fast Iterative Algorithms Based on Optimized Explicit Time-Stepping," Computer Methods in Applied Mechanics and Engineering, Vol. 63, pp. 15-36, August 1987.

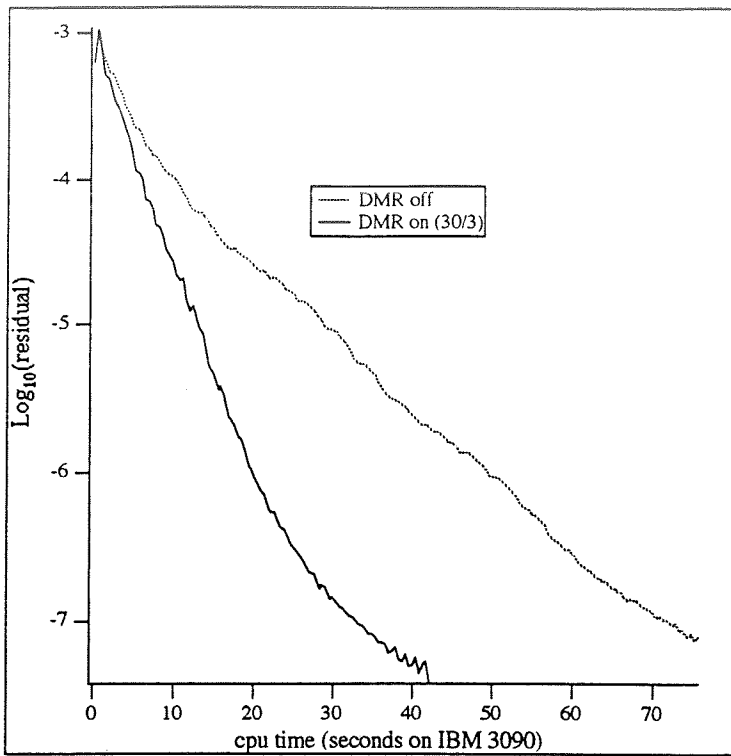


Figure 1. Convergence histories for a cascade flow: $Re=500$, non-clustered 40×30 grid, $CFL=2.8$, $\beta=3.0$. No artificial dissipation was used. Half of NACA 0012 airfoil on top and bottom walls.

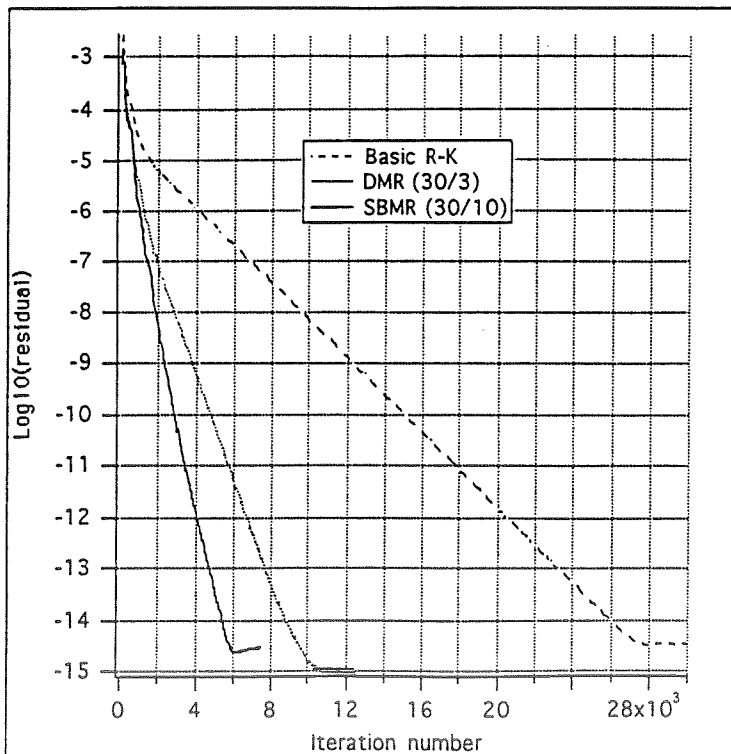


Figure 2. Convergence history for a straight channel flow: $Re=1600$, non-clustered 60×60 grid, x -length=5, y -length=1, $\beta=5$, $\nu=0.4$, $CFL=2.5$, $\omega=0.001$. Initial guess: $u=1.0E-5$, $v=0$, $p=0$. Inlet velocity profile: u =parabolic, $v=0$.

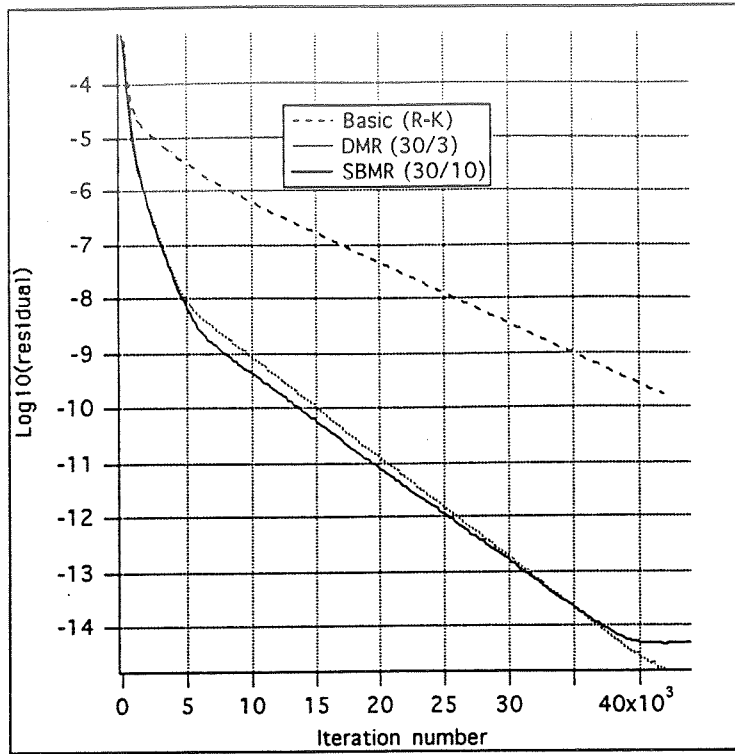


Figure 3. Convergence history for a straight channel flow: $Re=1.6$ million, non-clustered 60×60 grid, x -length=5, y -length=1, $\beta=5$, $CFL=2.8$, $\nu=0.4^{-4}$, $\omega=0.005$. Initial guess: $u=1.0E-5$, $v=0$, $p=0$. Inlet velocity profile: u =parabolic, $v=0$.

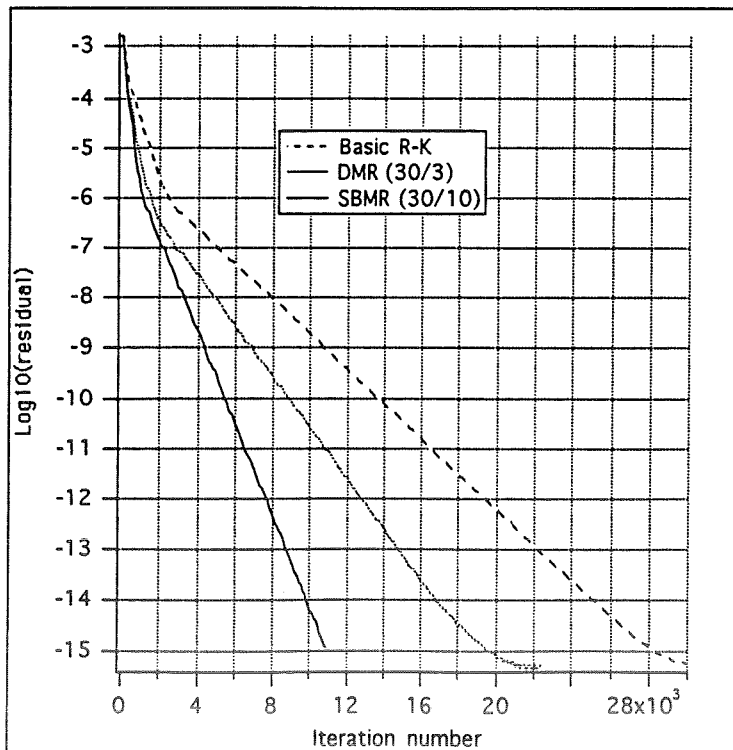


Figure 4. Straight channel flow: $Re=1600$, max AR=100 on 60×60 grid, x -length=5, y -length=1, $\beta=5$, $CFL=2.5$, $\nu=0.4$, $\omega=0.0$. Initial guess: $u=1.0E-5$, $v=0$, $p=0$ everywhere. Inlet velocity profile: u =parabolic, $v=0$.

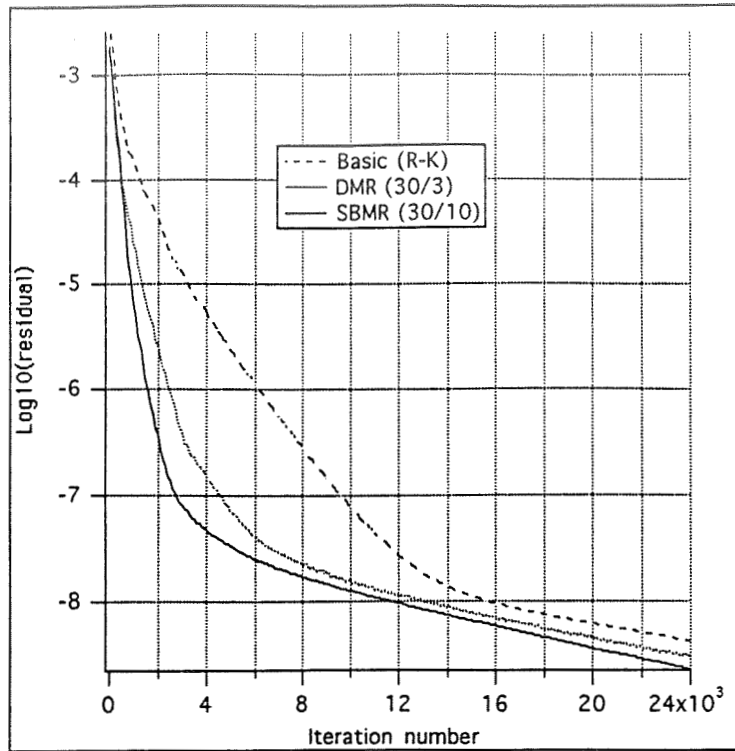


Figure 5. Straight channel flow: $Re=1.6$ million, max AR=100 on 60x60 grid, x-length=5, y-length=1, $\beta=5$, CFL=2.5, $\nu=0.4 \times 10^{-4}$, $\omega=0.005$. Initial guess: $u=1.0E-5$, $v=0$, $p=0$. Inlet velocity profile: u =parabolic, $v=0$.

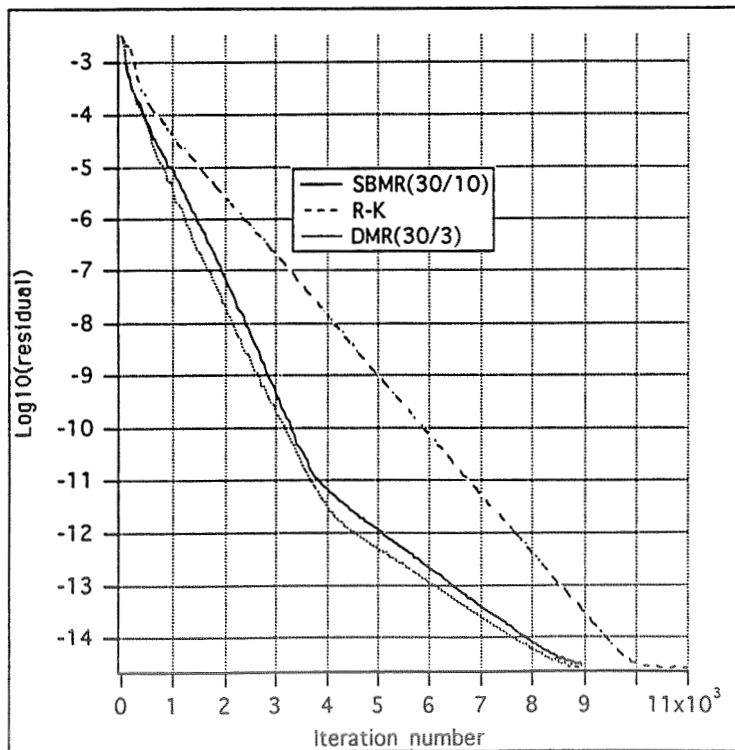


Figure 6. Convergence history for a U-shaped channel flow ($Re=100$, 129x30 grid cells); $\beta=5$, CFL=2.8, $\nu=0.4$, $\omega=0.0$.

OPTIMIZATION OF ENERGY TRANSFER IN MICROWAVE ELECTROTHERMAL THRUSTERS

D. J. Sullivan and M. M. Micci

Propulsion Engineering Research Center

Department of Aerospace Engineering

The Pennsylvania State University

University Park, PA 16802

SUMMARY

Results are presented from preliminary tests conducted to evaluate the performance of a prototype microwave electrothermal thruster. The primary component of the device is a microwave resonant cavity. The device produces stable axial plasmas within a pressurized section of the cavity with the plasma positioned in the inlet region of the nozzle. Plasma stability is enhanced by axial power coupling, an optimal distribution of electric power density within the cavity, and a propellant gas flow which has a large vortical velocity component. The thruster has been operated with a number of propellant gases: helium, nitrogen, ammonia, and hydrogen. Plasmas can be formed in a reliable manner at cavity pressures of 1 kPa and incident power levels ranging from 50 W to 350 W, depending on the gas used, and can be operated at pressures up to 300 kPa at power levels up to 2200 W. Ideal performance results of vacuum I_{sp} and thermal efficiency vs. specific power are presented for each gas. Representative results of this preliminary work are: He - $I_{sp} = 625$ s, $\eta_{thermal} = 90\%$; N_2 - $I_{sp} = 270$ s, $\eta_{thermal} = 41\%$; NH_3 - $I_{sp} = 475$ s, $\eta_{thermal} = 55\%$; H_2 - $I_{sp} = 1040$ s, $\eta_{thermal} = 53\%$.

TECHNICAL DISCUSSION

For the past decade, the development of a microwave powered electrothermal thruster has been pursued by a number of researchers using both experimental and numerical methods [Ref 1-5]. The experimental work conducted at Penn State [Ref. 2-5] has explored the viability of thruster configurations which have incorporated either rectangular or cylindrical waveguides, or cylindrical resonant cavities as their central components. Results of early studies have indicated that a design based upon a cylindrical cavity operating in the TM_{011} resonant mode would be best suited for thruster applications. A microwave powered thruster of this type uses microwaves to form and maintain a plasma within the cavity; cold gas passes through the cavity, is heated by the plasma source, and passes out of the device through a nozzle to produce thrust.

The results of previous experimentation at both Penn State and some recent work which has been initiated at NASA LeRC [Ref. 5], and examination of considerable computational [Ref. 4] and analytical studies [Ref 3] have been used to develop a design for a first-generation microwave resonant cavity thruster prototype which has been designed to produce optimal performance while correcting many of the undesirable operational features of the earlier Penn State devices, in particular, movement of the plasma discharge to off-axis positions at high power operation.; a schematic of the device is shown in Figure 1. The main component of the prototype thruster is a resonant cavity which operates in the TM_{011} mode, this mode is optimal for producing an axial, free-floating plasma. The thruster is designed such that the plasma forms directly upstream of a nozzle inlet which has been fabricated into the stationary short of the cavity. The formation of the plasma discharge near the inlet of the nozzle produces the most efficient transfer of thermal energy to the propellant gas.

The cavity geometry has been chosen such that it concentrates the electric field density pattern within the cavity at the upstream and downstream axial regions, while at the same time producing a relatively low field density in the characteristic annular region located at the midpoint of the cavity. The cavity diameter of 10.16 cm (4.0 in) was chosen to produce this desired electric field density distribution as well as to facilitate fabrication. The cavity is constructed of brass and its interior has been highly polished to remove metal oxides so as to increase the electrical conductivity. At the operating frequency of 2.45 GHz, the ideal resonant length for a cavity of this diameter is 15.87 cm.

The off-axis motion of the plasma which was a significant problem for the original Penn State cavity has been attributed to a poor electric field density distribution and an asymmetrically positioned coupling probe which was introduced into the side of the cavity. This asymmetric introduction of the coupling probe produced a nonaxisymmetric distortion of the electric field density pattern which tended to "push" the plasma away from its position on the central axis. The coupling probe in the prototype is aligned along the cavity axis. This axisymmetric introduction of microwave power does not produce any off-axis field distortions. The smaller radius cavity of the prototype produces a longer resonant length and results in a more favorable electric field density distribution. The lack of field distortions produced by the coupling probe and the better field density distribution of the prototype produce a plasma discharge which is very stable.

The geometry of the prototype design is flexible and the microwave circuit incorporates a three-stub tuning device. A combination of the proper cavity geometry and the settings of the tuner allow the system to be fine tuned producing optimal performance at a specified operating condition. Once these settings are determined, it should be possible to fix that given geometry in a future design and remove the requirements for any moving parts.

The prototype has removed the need for any quartz vessels by making one entire half of the cavity the pressure chamber. This has been accomplished by incorporating a pressure plate at the midplane of the cavity. The plate is 0.32 cm (1/8 in) thick, and it is constructed from a low loss microwave dielectric. The prototype incorporates three gas injection ports which produce a swirling flow that is directed down along the axis, i.e. toward the nozzle, at 15 degrees. The gas flow entering from each port is essentially tangential to the wall of the cavity; the swirling flow pattern enhances the axial stability of the plasma. Optical access of the plasma is made possible by a view port located in the wall of the pressure section of the cavity.

The prototype thruster has been successfully operated using helium, nitrogen, hydrogen, and ammonia propellants. The device is able to form plasmas from all of these propellant gases in a reliable and repeatable manner. The formation process occurs at pressures which are below atmospheric, typically less than 1 kPa, and at power levels ranging from 50 W to 750 W depending upon the propellant gas. For each gas, the plasma discharge can be maintained while the pressure within the cavity is increased to pressures which are above atmospheric; typically between 100 kPa and 350 kPa. The upper limit depends upon the propellant gas, the amount of available power, and the efficiency of the power coupling. Excellent power coupling can be achieved with typically greater than 98% of the incident microwave power being coupled into the plasma discharge at incident power levels of 1000 W.

The initial tests conducted with the prototype utilized helium as the propellant gas. Helium is a monatomic gas and thus is easy to breakdown; typically at 1 kPa the power required for breakdown was less than 50 W. The plasma discharge was very well behaved and it proved very easy to increase both the power and pressure; at the high range of the operational envelope examined, the plasma could be maintained at 2200 W and 340 kPa. The use of helium allowed the performance of the prototype to be compared to that of the original Penn State cavity which was also extensively tested with helium propellant. The performance results (Figure 2a and 2b) are presented in terms of vacuum specific impulse and thermal efficiency vs. specific power. The specific impulse estimates are calculated assuming an ideal isentropic expansion to vacuum. The better performance of the prototype can be primarily attributed to the fact that the plasma discharge is located directly within the nozzle inlet. The plasma produces a significant flow blockage which

results in relatively high pressures for moderate flow rates, and the gas which exits the nozzle is heated to very high temperatures as it passes through the constricted region between the plasma discharge and the nozzle wall. Ideal I_{sp} 's as high as 657 s with thermal efficiencies of 70 % were obtained.

The next series of tests used nitrogen as the propellant. This testing verified that the prototype could produce and maintain plasmas formed from molecular propellants over a large operating range of pressures and powers. The nitrogen plasmas typically formed at pressures of 1 kPa through the application of approximately 100 W of incident power. The plasma discharge was stable and well behaved; a typical operating condition was 350 kPa and 1875 W incident power with 93% power coupling (the three-stub tuner was not used during these tests) resulting in an ideal I_{sp} of 268 s at a specific power of 7.5 MJ/kg with a thermal efficiency of 41%.

The prototype thruster was also operated using ammonia as a working fluid. Ammonia plasmas can be repeatedly and reliably formed at pressures of 1 kPa with the application of approximately 750 W. The higher power required to initiate the breakdown process is a reflection of the greater degrees of freedom of the ammonia molecule. As with the other gases, the plasma is stable and well behaved; a typical operating condition was 147 kPa and 1514 W incident power with 99% power coupling resulting in an I_{sp} of 422 s assuming an ideal equilibrium expansion to vacuum (frozen expansion I_{sp} is 372 s) at a specific power of 21 MJ/kg with a thermal efficiency of 63%.

Hydrogen plasmas have also proven to be easy to produce, typically at 1 kPa and 300 W, are well behaved, and it is possible to operate the plasma at pressures up to 100 kPa. The performance results (Figure 3) do not represent optimal testing conditions. The data shown was taken to verify operation with hydrogen and to explore the pressure range through which the plasma can be maintained; better performance can be achieved by operating the thruster at higher chamber pressures. The performance data takes dissociation into account through the use of a chemical equilibrium code. A typical operating condition was 100 kPa and 1803 W incident power with 97% power coupling resulting in an I_{sp} of 1020 s assuming an ideal equilibrium expansion to vacuum (frozen expansion I_{sp} is 907 s) at a specific power of 95 MJ/kg with a thermal efficiency of 50%.

References

- [1] Balaam, P., Micci, M.M., "The Stabilization and Spectroscopic Study of Microwave Generated Resonant Cavity Plasmas," AIAA-90-2635, AIAA/DGLR/JSASS 21st International Electric Propulsion Conference, Orlando, FL, July 1990.
- [2] Mueller, J., Micci, M.M., "Microwave Electrothermal Thrusters Using Waveguide Heated Plasmas," AIAA-90-2562, AIAA/DGLR/JSASS 21st International Electric Propulsion Conference, Orlando, FL, July 1990.
- [3] Sullivan, D. J., Micci, M.M., "Development of a Microwave Resonant Cavity Electrothermal Thruster Prototype," IEPC-93-036, AIAA/AIDAA/DGLR/JSASS 23rd International Electric Propulsion Conference, Seattle, WA, Sept. 1993.
- [4] Schwer, D.A., Venkateswaran, S., Merkle, C.L., "Analysis of Microwave-Heated Rocket Engines for Space Propulsion," AIAA-93-2105, AIAA/SAE/ASME/ASEE 29th Joint Propulsion Conference, Monterey, CA, June 1993.
- [5] Power, J. L., Sullivan, D. J., "Preliminary Investigation of High Power Microwave Plasmas for Electrothermal Thruster Use," AIAA-93-2106, AIAA/SAE/ASME/ASEE 29th Joint Propulsion Conference, Monterey, CA, June 1993.

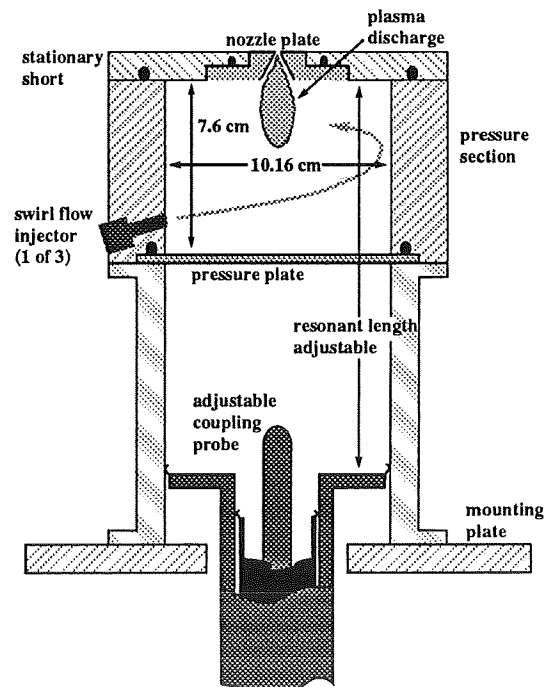


Figure 1: Schematic of the microwave resonant cavity electrothermal thruster prototype. The diameter of the cavity is 10.16 cm and the theoretical resonant length is 15.87 cm. The plasma discharge forms on the axis of the cavity within the inlet of the nozzle.

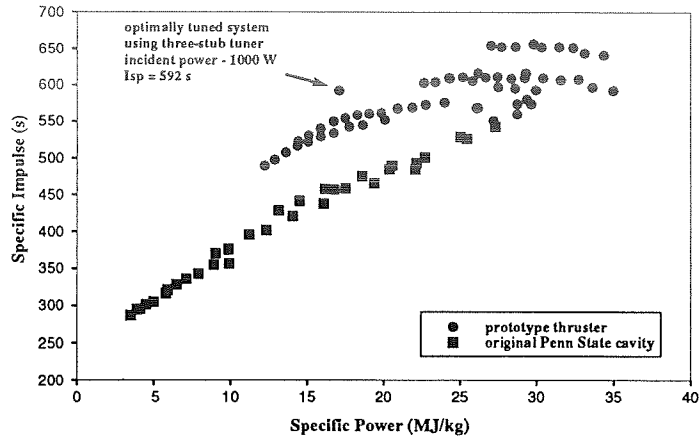


Figure 2a: • Helium Propellant • Performance data comparing the prototype microwave electrothermal thruster with that of the original cavity used at Penn State. The performance of the system when the three-stub tuner is used is noted for an optimally tuned condition at 1000 W.

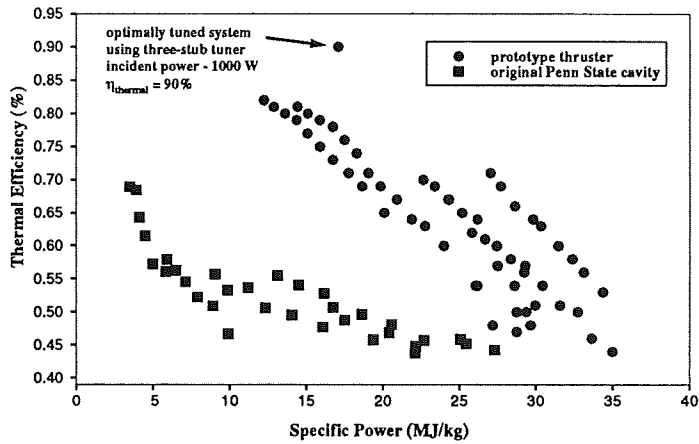


Figure 2b: • Helium Propellant • Thermal efficiency data comparing the performance of the prototype microwave electrothermal thruster with that of the original cavity used at Penn State. The drop off in efficiency results from poor tuning at higher power levels; this can be corrected by including the three-stub tuner into the system.

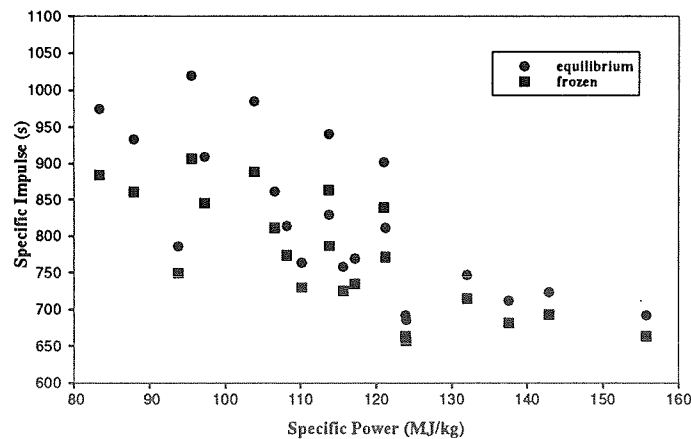


Figure 3: • Hydrogen Propellant • Preliminary performance data. Results account for the dissociation of the H_2 molecule. Isp is presented assuming both equilibrium and frozen flow expansion to vacuum.

CFD MODELING OF MICROWAVE ELECTROTHERMAL THRUSTERS

Douglas A. Schwer, S. Venkateswaran, and Charles L. Merkle
The Pennsylvania State University

Microwave-heated plasmas in convergent nozzles are analyzed using a coupled Maxwell and Navier-Stokes solver to examine relevant issues associated with microwave thermal propulsion. Parametric studies are conducted to understand the effect of power, pressure, and plasma location with respect to the nozzle throat. For nozzles in the 0.5 to 3 N range with helium flow, results show that specific impulses up to 550-650 seconds are possible, with further increases being limited by severe wall-heating. Coupling efficiencies of over 90% are consistently obtained, with overall efficiencies ranging from 40% to 80%. Size scale-up studies—done by scaling the frequency from 2.45 GHz to 0.91 GHz—indicate that plasma migration toward the walls occurs more frequently for the lower frequency. Increasing the cavity aspect ratio and detuning the cavity are found to be effective ways of keeping the plasma on-axis.

Microwave-heated plasmas for space propulsion applications have been considered as an alternative propulsion system since the early 1980's. Like arcjets, microwave thrusters convert electrical energy (in the form of electromagnetic radiation) into thermal energy in a working fluid through a plasma. Unlike arcjets, however, microwave plasmas can be sustained "free-floating" inside an absorption chamber without being attached to any surface, thereby increasing the life of the propulsion system. This has generated considerable interest in determining stable operating regimes and the corresponding thruster performance. Central to this idea is understanding of the strong interaction between the working fluid and the incoming microwave power and the propagation mechanisms of the resultant plasma.

Initial research on microwave plasmas was centered on experimental studies of plasma characteristics at subatmospheric pressures [1,2]. More recent experiments directed toward using the plasma as a means to provide hot gases for propulsive thrust [3-8] have involved higher pressures, typically above one atmosphere. Most of these experiments have dealt with the fundamental characteristics of helium plasmas and the efficiency with which the microwave energy can be coupled to the flowing gas. Stable, free-floating plasmas that are remote from any walls have been routinely observed, but complete propulsive systems have yet to be tested. Companion computational models of the coupling between microwave energy and flowing helium gas have also been developed and validated against experiment [9,10]. In general, the computational trends have supported the experimental findings, showing high coupling efficiencies, proper plasma locations and sizes, and appropriate peak temperatures. These computational efforts have, however, been limited to plasmas in subsonic, unchoked gas flows.

In both the experimental and the computational studies, various coupling methods including resonant cavity plasmas [4,6-9], waveguide-heated plasmas [5,10] and coaxial plasmotrons [3] have been considered. Of these, resonant cavity plasmas appear to offer the best potential coupling method. Cavity plasmas show excellent coupling efficiencies, approaching 100% when some sort of cavity tuning is provided. In addition, they provide good positional stability and long-time operation. In most cases, cavity plasmas are easily positioned on-axis, far away

from the walls. Resonant cavity plasmas are, however, not entirely without difficulties in that plasma migration toward the walls has been observed under certain operating regimes. Resonant cavity plasmas that use asymmetrical input-power coupling tend to induce asymmetrical migration toward the walls at higher powers even though they work well at lower powers [4]. This migration can be curbed by switching to symmetrical power coupling, but wall migration is also observed in some applications with completely symmetric microwave geometries. The reason appears to be associated with movement (or expansion) of the plasma from the on-axis maxima in the axial E-field to the toroidal maxima in the radial E-field. By setting the cavity aspect ratio, the relative intensity of the axial and radial electric field maxima can be controlled, enabling more stable on-axis plasma positioning.

Besides controlling off-axis plasma migration by cavity geometry, experimental results have shown that aerodynamic control methods are also effective. Bluff-body stabilization [1,3] and swirled vortical in-flow [7,8] have both been demonstrated experimentally. The effectiveness of bluff-body stabilization has also been predicted computationally, but swirl stabilization has yet to be modeled.

A prototype microwave thruster and the corresponding numerical simulation are given in Fig. 1. The thruster consists of an absorption chamber followed by a standard propulsive nozzle through which the working fluid (helium) flows. The absorption chamber is surrounded by a microwave cavity in which standing E-M waves are established. As the working fluid flows through the cavity, it is heated by a plasma that is initiated near one of the maxima in the standing wave. Although the presence of the conducting plasma distorts the standing wave very severely from its undisturbed mode shape, the original maxima in the field retain their position sufficiently well that the location of the plasma can be controlled quite effectively by the E-M field, and their axial location can be moved by shifting the cavity position with respect to the flow passage. Once the gas has been heated by the plasma, the fluid is expanded through a standard propulsive nozzle to produce thrust.

Typical solutions for a 2.45 GHz helium plasma in a convergent nozzle are shown in Figs. 2 and 3. The temperature contours in Fig. 2 indicate that the plasma is stabilized near the throat by the lower maximum of the electric field standing wave pattern. The forward half of the plasma tends to be hemispherical while the aft section is pulled downstream into the throat by the strongly accelerating flow causing the overall plasma to be somewhat teardrop in shape. The plasma in Nozzle A (right half), which corresponds to a larger mass flow rate, is more compact than that in Nozzle B (left half). This is because, for the larger flow rate, convective effects dominate over thermal diffusion, while, for the lower mass flow rate, diffusive effects are relatively more significant.

Figure 4 shows the calculated Isp's for three nozzle sizes. For the largest nozzle with the largest mass flow rate (Nozzle A), the plasma derives only a small benefit from microwave heating (approximate increase of 70 seconds of Isp over the cold flow regenerative Isp). The two smaller nozzles (B and C respectively) show significant increases in Isp over the cold flow Isp. In these cases, a larger fraction of the propellant gas flows through the plasma and proportionately higher average temperatures are attained. Nozzle C (with the smallest mass flow rate) has the highest Isp ranging from 600s to 630s. For this case, when power is increased beyond a certain level (about 2.75 kW), the Isp is seen to level off due to increased heat losses to the wall. Isp's of this level are attractive for auxiliary propulsion missions.

References

- [1] Kapitza, P.L., "Free Plasma Filament in a High Frequency Field at High Pressure," *Soviet Physics JETP*, Vol. 30, June 1970, pp. 973-1224.
- [2] Arata, Y., S. Miyake, and A. Kobayashi, "High Power Microwave Discharge in Atmospheric Hydrogen Gas Flow," *Journal of the Physical Society of Japan*, Vol. 44, March 1978, pp. 998-1003.
- [3] Whitehair, S., J. Amussen, and S. Nakanishi, "Microwave Electrothermal Thruster Performance in Helium Gas," *Journal of Propulsion and Power*, Vol. 3, April 1987, pp. 136-144.
- [4] Balaam, P. and M. Micci, "Investigation of Free-Floating Nitrogen and Helium Plasmas Generated in a Microwave Resonant Cavity," AIAA Paper 89-2380, 25th AIAA/ASME/SAE/ASEE Joint Propulsion Conference, Monterey, CA, July 1989.
- [5] Mueller, J. and M.M. Micci, "Microwave Electrothermal Thrusters Using Waveguide Heated Plasmas," AIAA Paper 90-2562, AIAA/DGLR/JSASS 21st International Electric Propulsion Conference, Orlando, FL, July 1990.
- [6] Sullivan, D.J. and M.M. Micci, "The Effect of Molecular Propellants on the Performance of a Resonant Cavity Electrothermal Thruster," AIDAA/AIAA/DGLR/JSASS 22nd Electric Propulsion Conference, Viareggio, Italy, October, 1991.
- [7] Power, J.L. and D.J. Sullivan, "Preliminary Investigation of High Power Microwave Plasmas for Electrothermal Thruster Use," 29th AIAA/SAE/ASME/ASEE Joint Propulsion Conference, Monterey, CA, June 1993.
- [8] Sullivan, D.J. and M.M. Micci, "Development of a Microwave Resonant Cavity Electrothermal Thruster Prototype," 23rd AIAA/DGLR/AIDAA/JSASS International Electric Propulsion Conference, Seattle, WA, September 1993.
- [9] Venkateswaran, S. and C.L. Merkle, "Numerical Investigation of Bluff Body Stabilized Microwave Plasmas," AIAA Paper 91-1503, 22nd AIAA Fluid Dynamics, Plasma Dynamics and Lasers Conference, Honolulu, HI, June 1991.
- [10] Venkateswaran, S., D.A. Schwer and C.L. Merkle, "Numerical Investigation of Waveguide-Heated Microwave Plasmas," accepted to the *Journal of Fluids Engineering*, 1993.

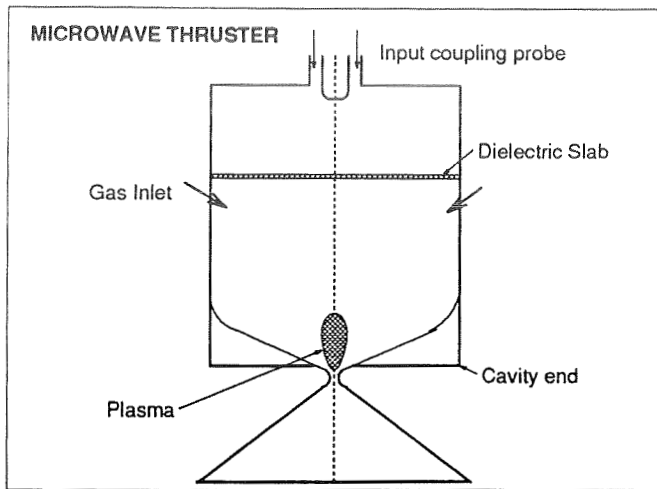


Figure 1: Schematic of a prototype microwave thruster.

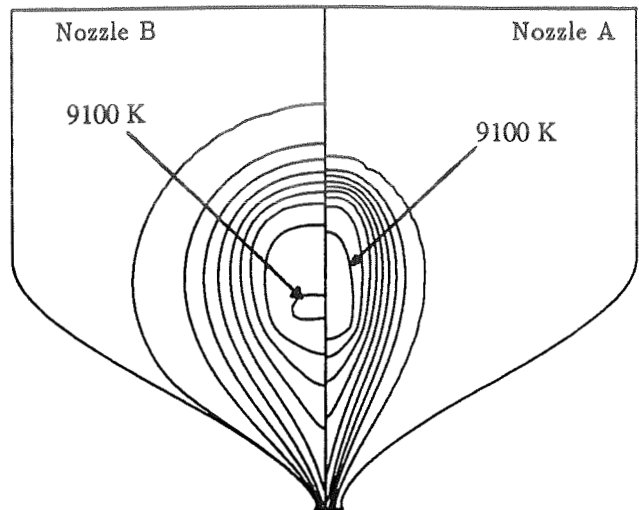


Figure 2: Temperature field for the 1.5 mm nozzle (left side) and the 2.5 mm nozzle (right side). $\Delta T = 1000$ K.

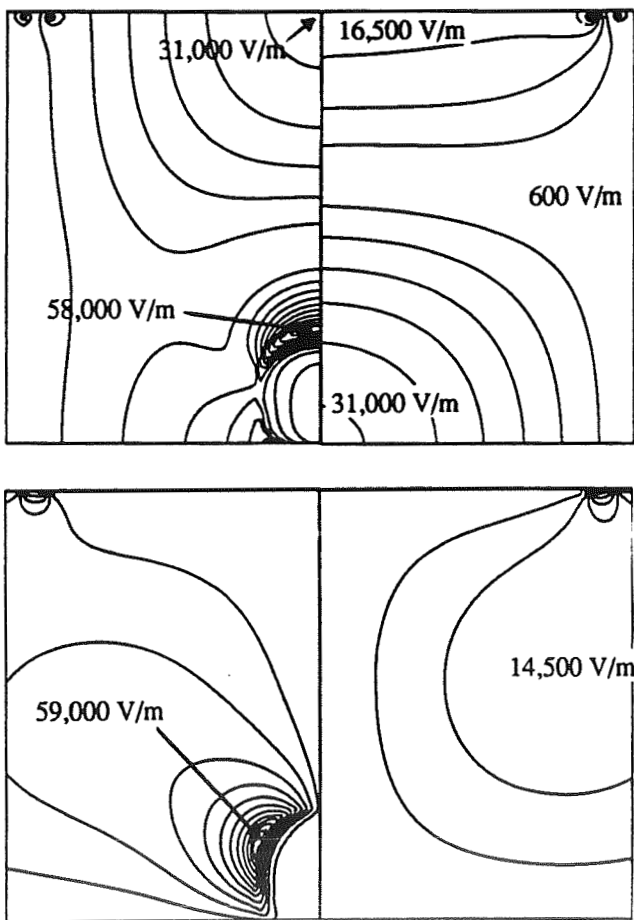


Figure 3: (a) Axial electric field and (b) radial electric field. Left shows electric field distortion due to plasma and right shows undistorted field. $\Delta E = 5000$ V/m.

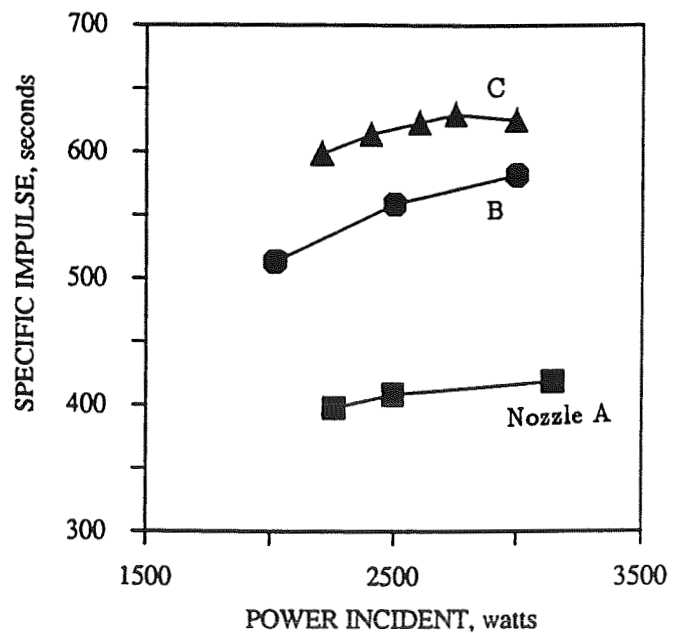


Figure 4: Specific impulse for the three different nozzles at different power levels.

ADVANCED SPACE PROPULSION CONCEPTS

Michael R. LaPointe
Sverdrup Technology, Inc.
LeRC Group, Brook Park, OH 44142

INTRODUCTION

In the early part of the 20th century, Konstantin Tsiolkovsky and Robert Goddard laid the theoretical foundations for chemical propulsion systems which would one day land humans on the moon and send robotic emissaries hurtling beyond the confines of the solar system. Over the past few decades, a variety of missions have been performed with propulsion systems based upon the combustion of chemical fuels. Chemical propulsion has been sufficient during this preliminary epoch of exploration, but a continued reliance on chemical fuels carries the penalty of large, expensive, and often impractical propellant-to-payload mass ratios for several missions of interest. Advancements in spacecraft propulsion are required to sustain an ambitious near-term program of space commercialization, and to support the permanent expansion of mankind into the solar system. Toward this goal, the NASA Lewis Research Center has evaluated a variety of advanced space propulsion technologies. Recent efforts have focused on advanced chemical, plasma, and laser propulsion concepts, which are outlined below.

HIGH ENERGY DENSITY PROPELLANTS

The performance of conventional chemical rockets is constrained by the energy available in chemical combustion to specific impulse values near 500 s. High energy density propellants, which use the recombination energy of free-radicals to supplement the release of chemical bond energy during combustion, have been investigated by a variety of researchers^{1,2}. The Lewis Research Center has focused on the use of atomic hydrogen propellants, which can potentially deliver up to three times the specific impulse of conventional chemical propulsion systems to provide a revolutionary launch vehicle capability³. Fundamental issues to be resolved in the development of atomic hydrogen propellants include the production, storage, and controlled release of free-radical hydrogen in a propellant mixture. To increase the performance over conventional O₂/H₂ launch vehicles, the storage mass density of atomic hydrogen in molecular H₂ must exceed 10-15%³. Current theoretical estimates place an upper bound of approximately 5% on the mass storage density of atomic hydrogen in a solid H₂ matrix, while recent experiments using energetic tritium decay to create free-radical hydrogen have only achieved a few atom percent storage density of H in H₂.⁴ Producing hydrogen atoms in a solid hydrogen matrix at the storage densities required for propulsion may not be feasible using tritium decay schemes, and alternative production methods such as radiofrequency excitation or high energy particle beams may be necessary for the large scale production of atomic hydrogen. Futuristic possibilities include the use of nanotechnology to manipulate and store the hydrogen atoms in an appropriate propellant matrix, or microlasers to selectively locate and split stored hydrogen molecules into atoms. Long term storage possibilities include the use of high field superconducting magnets to stabilize spin-polarized hydrogen atoms within a solid H₂ matrix, delaying the transition to ground state and postponing atom recombination. The magnets and their associated support structure would be an integral part of the launch facility, placed around the propellant tanks to keep the atomic hydrogen from recombining until the vehicle was ready for launch. Because the atomic hydrogen and solid H₂ matrix must remain at cryogenic temperatures, a suitable method for transporting a solid cryogenic H/H₂ matrix from the propellant storage tank to the rocket engine must be designed. Significant breakthroughs in production, storage, and transfer technologies are clearly required before atomic hydrogen becomes a useful rocket propellant, but the potential improvement in launch vehicle performance warrants a continued investigation of this high energy density propellant.

ELECTRODELESS THRUSTER CONCEPTS

The specific impulse values associated with current chemical propulsion systems are limited by the chemical bond energy associated with the combustion of the propellant. An increase in specific impulse can be realized by decoupling the energy source from the propellant, an approach utilized in electric propulsion devices such as the ion engine⁵ and magnetoplasmadynamic (MPD) thruster.⁶ These devices supply electrical energy to ionize and accelerate a gaseous propellant, with maximum specific impulse values approaching 5000 s for the MPD thruster and 10,000

s for the ion engine. Both devices are designed to provide continuous low thrust, and must operate for several thousand hours to provide total impulse values of interest for orbit maneuvering or planetary mission applications. Efforts have focused on mitigating the electrode erosion associated with the accelerating grids in ion thrusters and the arc-sustaining cathodes in MPD thrusters, which significantly limit the useful life of the devices. To achieve the benefits of high specific impulse while avoiding the life-limiting erosion of electrode materials, the Lewis Research Center has been actively involved in the development of electrodeless electric propulsion concepts. Three concepts, the microwave electrothermal thruster, the helicon or whistler wave thruster, and the pulsed inductive thruster, are discussed below.

Microwave Electrothermal Thruster. The LeRC microwave electrothermal thruster (MET) test assembly, depicted schematically in Figure 1, consists of a resonant microwave cavity traversed by a longitudinal propellant discharge tube. A commercially available magnetron converts electric power to 915 MHz cw microwave radiation, which is coupled to the tuned resonant cavity. The resulting electromagnetic fields transfer energy to the propellant electrons, which in turn collisionally transfer their energy to ignite and sustain a free-floating plasma discharge. Propellant flowing around the plasma discharge is heated and expanded through a nozzle to provide thrust. A phase shifter-tuner is used to regulate the amount of microwave power delivered to the resonant cavity, from zero to a maximum deliverable power of 30 kW. Stable plasmas have been created and maintained in an open channel configuration with helium, nitrogen, and hydrogen in both the TM_{011} and TM_{012} resonant modes at discharge pressures from 10 Pa to 69 kPa⁷. Vortical propellant injection is used to form a stable (spike) plasma along the centerline of the discharge tube, enabling maximum power absorption with minimum heating of the discharge tube walls. A maximum applied power level of 11.2 kW has been achieved with 54% coupling efficiency for nitrogen in the spike condition⁷. Microwave coupling efficiencies above 90% have routinely been obtained for the various propellants at absorbed power levels up to 2 kW. Thrust and specific impulse have not been measured, but numerical simulations predict specific impulse values approaching 2000 s may be achieved with hydrogen⁸. A superconducting magnet, capable of producing 5.7 T field strengths, has been used for preliminary investigations of magnetic nozzling effects. In addition to advanced propulsion research, the microwave plasma test facility provides a unique capability for plasma processing and materials applications.

Helicon (Whistler-Wave) Thruster. In collaboration with the Lawrence Livermore National Laboratory (LLNL), LeRC is investigating the use of helicon waves to ignite and sustain a hydrogen plasma discharge in a thruster-relevant geometry. The helicon wave thruster is an electrodeless device, similar in nature to other electron cyclotron resonance heating (ECRH) devices, but operated at a much higher plasma density. Increasing the plasma density allows an increase in the power and thrust density, yielding improved thruster efficiencies and anticipated specific impulse values of several thousand seconds. Typically, an increase in the plasma density would require operating the device at high microwave frequencies for efficient power coupling and the use of strong magnetic fields to mitigate plasma losses, stressing available microwave and magnet technology. Instead, plasma generation and heating in the helicon thruster uses a helicon (whistler) wave, which propagates at frequencies below both the electron cyclotron frequency and the electron plasma frequency. Injecting the microwave power at frequencies below the electron cyclotron frequency allows the use of a magnetic mirror to separate the hot plasma from the thruster backplate, and propagation at frequencies below the electron plasma frequency permits operation at the desired high plasma densities. In the current thruster configuration (Figure 2), a microwave antenna surrounds the plasma region, coupling the whistler waves to the plasma across the magnetic field lines. As the wave propagates into the plasma, energy is efficiently transferred to the plasma electrons to collisionally sustain the plasma discharge. An initial experiment has been designed and fabricated by LLNL, and preliminary tests are currently underway in the microwave plasma test facility at the Lewis Research Center⁹.

Pulsed Inductive Thruster. The pulsed inductive thruster (PIT), developed by TRW with recent funding provided by LeRC, is an electrodeless plasma accelerator which can operate with a variety of gaseous propellants. The PIT, shown schematically in Figure 3, consists of a flat spiral induction coil powered by a set of capacitors. A puff of propellant gas is injected through a fast acting valve, and spreads across the insulated surface of the coil. The capacitor bank is simultaneously discharged to provide a fast rising current pulse within the coil. The current pulse induces a transient magnetic field, which in turn creates a strong azimuthal electric field via Faraday's law. The azimuthal electric field breaks down the propellant gas, and the resulting plasma is pushed away from the surface of the coil via the mutual repulsion between the induced plasma current and the primary coil current. There is

minimal direct contact between the plasma and the insulating surfaces of the coil and propellant injector, mitigating thruster erosion. The current PIT MkVa design consists of a 1 m diameter coil and a 36 microfarad capacitor bank, chargeable to 16 kV¹⁰. Recent experiments with ammonia propellant¹⁰ have produced specific impulse values in the range of 4000 to 8000 s, with thruster efficiencies slightly exceeding 50%. Operation at a lower specific impulse value of approximately 2000 s lowered the thruster efficiency to around 43%. Operation with a simulated hydrazine propellant¹⁰ produced specific impulse values of 4000 s with thruster efficiencies of around 45%. The PIT is capable of operating over a power range from kilowatts to multimewatts, and the performance may be tailored for specific missions of interest. The PIT has demonstrated efficient operation with specific impulse values of interest for orbital transfer and interplanetary missions applications. Pending additional funding, research efforts will focus on quantifying insulator erosion, wear-testing thruster components, and evaluating the effect of radiated EMI on communications and data links.

LASER POWERED PROPULSION

While the electrodeless thruster concepts discussed above seek to decouple the energy source from the propellant, laser powered propulsion concepts seek to decouple the energy source from both the propellant and the spacecraft. Both near-term electric propulsion, and the more far-term advanced electrodeless concepts outlined above, must carry along a power supply which adds mass to the spacecraft and reduces the available payload fraction. Laser powered propulsion concepts seek to keep the power supply on the ground, and beam the required energy to the spacecraft. The efficiency of solar cells are nearly doubled under laser illumination of the proper frequency¹¹, allowing a significant reduction in the size and mass of the photovoltaic arrays required for electric powered propulsion. Alternatively, ground-based laser energy might be absorbed directly to heat a propellant for laser thermal propulsion¹². Near-term applications of ground-based laser beaming include supplemental power for satellites with degraded solar arrays or dead storage batteries, while future applications include laser propelled transfer vehicles and earth-based laser power to sustain a lunar base during the 14-day lunar night¹³. A disadvantage of ground-based laser power is the necessity to propagate through the Earth's atmosphere, where turbulence and temperature induced changes in refractive index can significantly distort and broaden the beam profile. Adaptive optics have been used to sense the distortion of the beam and provide the necessary corrections to propagate a nearly-diffraction limited beam through the atmosphere. LeRC has investigated the use of reportedly nondiffracting beams in conjunction with phase conjugation methods to achieve similar results. Based on theoretical and experimental results, LeRC has shown that nondiffracting wave experiments published in the literature instead conform to standard diffraction theory, and the reports of nondiffracting wave propagation misinterpreted the role of the optical systems used to generate the beams¹⁴. The use of optical phase conjugation methods to propagate a beam through a distorting media was verified at low powers. In addition, an analysis was performed to evaluate the use of current technology for ground-based, low power laser illumination for satellite propulsion applications in low earth orbit (LEO)¹⁵. Preliminary results indicate that the short illumination periods associated with LEO systems make ground-based laser propulsion concepts impractical compared with current chemical and solar electric propulsion systems. High power laser propulsion systems continue to look promising for the variety of applications noted above, but await the development of reliable, high power laser systems to bring the technology to fruition.

CONCLUDING REMARKS

The NASA Lewis Research Center has been actively involved in the evaluation and development of advanced spacecraft propulsion. Recent program elements have included high energy density propellants, electrodeless plasma thruster concepts, and low power laser propulsion technology. A robust advanced technology program is necessary to develop new, cost-effective methods of spacecraft propulsion, and to continue to push the boundaries of human knowledge and technology.

REFERENCES

1. Frisbee, R. H., "Ultra High Performance Propulsion for Planetary Spacecraft: FY'83 Final Report", Jet Propulsion Laboratory, JPL D-1194, December 1983.
2. Cordonnier, M. (ed.), Proceedings of the High Energy Density Matter (HEDM) Conference, U.S. Air Force Phillips Laboratory Document PL-CP-91-3003, October 1991.

3. Palaszewski, B., "Atomic Hydrogen Propellants: Historical Perspectives and Future Possibilities", AIAA 93-0244, January 1993.
4. Fajardo, M., "Metal Atoms in Solid Rare Gases", in Proceeding of the High Energy Density Matter (HEDM) Conference, U.S. Air Force Phillips Laboratory, PL-CP-91-3003, October 1991; also see other papers in same conference proceedings.
5. Rawlin, V., "Advanced Ion Propulsion for Space Exploration", AIAA 91-3567, September 1991.
6. Myers, R., Mantieniks, M., and LaPointe, M., "MPD Thruster Technology", AIAA 91-3568, September 1991.
7. Power, J. and Sullivan, D., "Preliminary Investigation of High Power Microwave Plasmas for Electrothermal Thruster Use", AIAA-93-2106, June 1993.
8. Power, J. and Chapman, R., "Development of a High Power Microwave Thruster, With a Magnetic Nozzle, for Space Applications", NASA TM-102321, August 1989.
9. Hooper, E. B., Stallard, B. W., and Makowski, M. A., "Whistler Wave Driven Plasma Thruster", Proceedings of the 10th Symposium on Space Nuclear Power and Propulsion, M. El-Genk and M. Hoover (eds.), Albuquerque, N.M., January 1993, pp. 1419-1424.
10. Dailey, C. and Lovberg, R., "The PIT MkV Pulsed Inductive Thruster", NASA CR-191155, July 1993.
11. Landis, G. "Photovoltaic Receivers for Laser Beamed Power in Space", NASA CR-189075, December 1991.
12. Black, J., Krier, H., and Glumb, R., "Laser Propulsion 10 kW Thruster Test Program Results", AIAA 92-3218, July 1992.
13. DeYoung, R. (ed.), Second Beamed Space-Power Workshop, NASA Conference Publication 3037, March 1989.
14. LaPointe, M., "Review of Nondiffracting Bessel Beam Experiments", Optics and Laser Technology, Vol. 24 (6), December 1992, pp. 315-322.
15. LaPointe, M. and Oleson, S., "Low Power Ground Based Laser Illumination for Electric Propulsion Applications", IEPC 93-208, 23rd International Electric Propulsion Conf., Seattle, WA, September 1993.

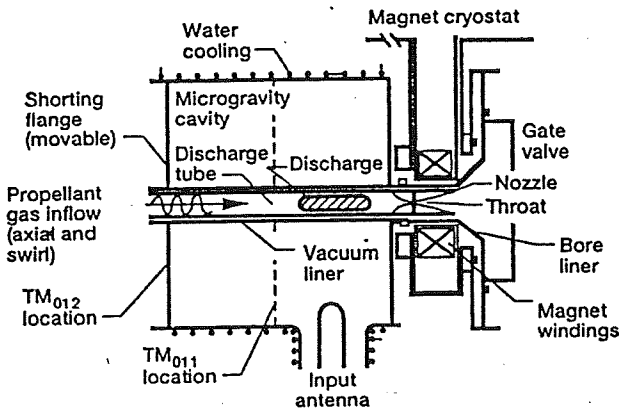


Figure 1. Microwave Electrothermal Thruster.

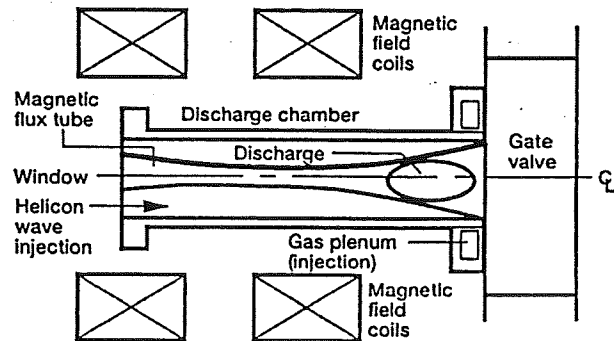


Figure 2. Helicon Wave Thruster.

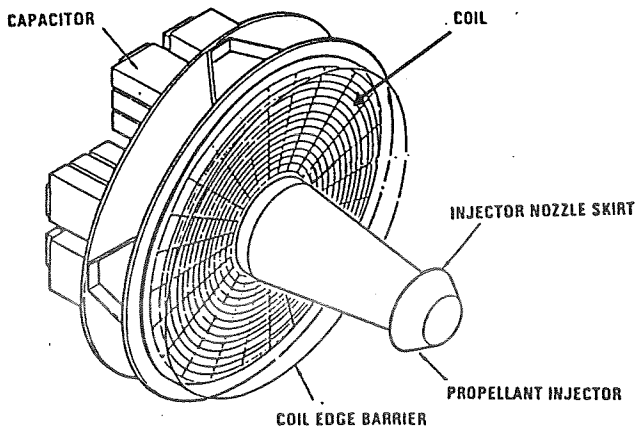


Figure 3. Pulsed Inductive Thruster.

ADVANCED NUCLEAR THERMAL PROPULSION CONCEPTS

Dr. Steven D. Howe
Los Alamos National Laboratory
P.O. Box 1663, MS-E552
Los Alamos, N.M. 87545

In 1989, a Presidential directive created the Space Exploration Initiative (SEI) which had a goal of placing mankind on Mars in the early 21st century. The SEI was effectively terminated in 1992 with the election of a new administration. Although the initiative did not exist long enough to allow substantial technology development, it did provide a venue, for the first time in 20 years, to comprehensively evaluate advanced propulsion concepts which could enable fast, manned transits to Mars. As part of the SEI based investigations, scientists from NASA, DoE National Laboratories, universities, and industry met regularly and proceeded to examine a variety of innovative ideas. Most of the effort was directed toward developing a solid-core, nuclear thermal rocket and examining a high-power nuclear electric propulsion system. In addition, however, an Innovative Concepts committee was formed and charged with evaluating concepts that offered a much higher performance but were less technologically mature. The committee considered several concepts and eventually recommended that further work be performed in the areas of 1) gas core fission rockets, 2) inertial confinement fusion systems, 3) antimatter based rockets, and 4) gas core fission electric systems. Following the committee's recommendations, some computational modeling work has been performed at Los Alamos in certain of these areas and critical issues have been identified.

The gas core fission rocket offers the potential of delivering high thrust with an Isp between 2000 to 5000 s. The underlying principle is that a localized accretion of uranium plasma can be maintained in a rocket chamber by fluid dynamic forces. By utilizing no solid materials in the rocket volume, exhaust gas temperatures can be raised to the several electron volt level to produce high Isp. Some of the obvious problems are:

- 1) efficient containment of the expensive uranium fuel;
- 2) thermal flux loads at the first wall;
- 3) thermal balance of the entire system ;
- 4) nozzle cooling and erosion problems; and
- 5) possible requirement of a magnetic nozzle.

Currently, some calculations of criticality and flow fields are being performed for the counter-flow toroidal rocket concept, shown in Fig. 1. This concept offers potential advantages over the previous, spherical gas

core concept by reducing the Kelvin-Helmholtz mixing at the uranium/hydrogen interface. In addition, the cylindrical geometry may allow magnetic fields to be used to enhance the uranium confinement. Currently, cold flow experiments are being developed to demonstrate the toroid formation process and to determine loss rates of a heavy "fuel" gas.

One of the envisioned problems with the gas core fission reactor, in general, is the low thrust to weight ratio of the engines. This ratio is dependent on the density of uranium which is decreasing with increasing Isp. One concept which may alleviate the critical mass obstacle is to utilize the toroidal geometry and flow characteristics of the fission rocket but to power the system with positron annihilations instead of fission reactions. In addition to the aforementioned issues, this concept would also require evaluation of energy deposition by the annihilation photons, positron storage and production concepts, and positron delivery optics. Preliminary calculations of the photon deposition profiles are currently underway as part of a concept feasibility study.

The concept of using gas or plasma core reactors for propulsion may also be applied to nuclear electric propulsion (NEP) systems. The primary drawback of NEP systems is the large mass associated with the entire power/propulsion assembly. As shown in Fig. 2, a major issue to make the NEP system more competitive with thermal systems is the need for a high efficiency conversion process that has low weight and that produces power compatible with electric thruster requirements. In this context, Los Alamos is hosting a University of Florida student who is planning a series of experiments to demonstrate the feasibility of using a Recoil Enhanced MHD technique to increase fluid conductivity in order to efficiently produce power without moving parts.

In conclusion, the current environment for advanced propulsion research is not strongly supportive. Several advanced concepts exist, however, where small scale experiments and evaluations can demonstrate feasibility. If some of the identified issues can be resolved by university research in the next few years, a higher performance propulsion system might be made available to the country for future manned missions to even farther planets. Now is exactly the time to pursue these proof-of-concept studies in the Laboratory environment.

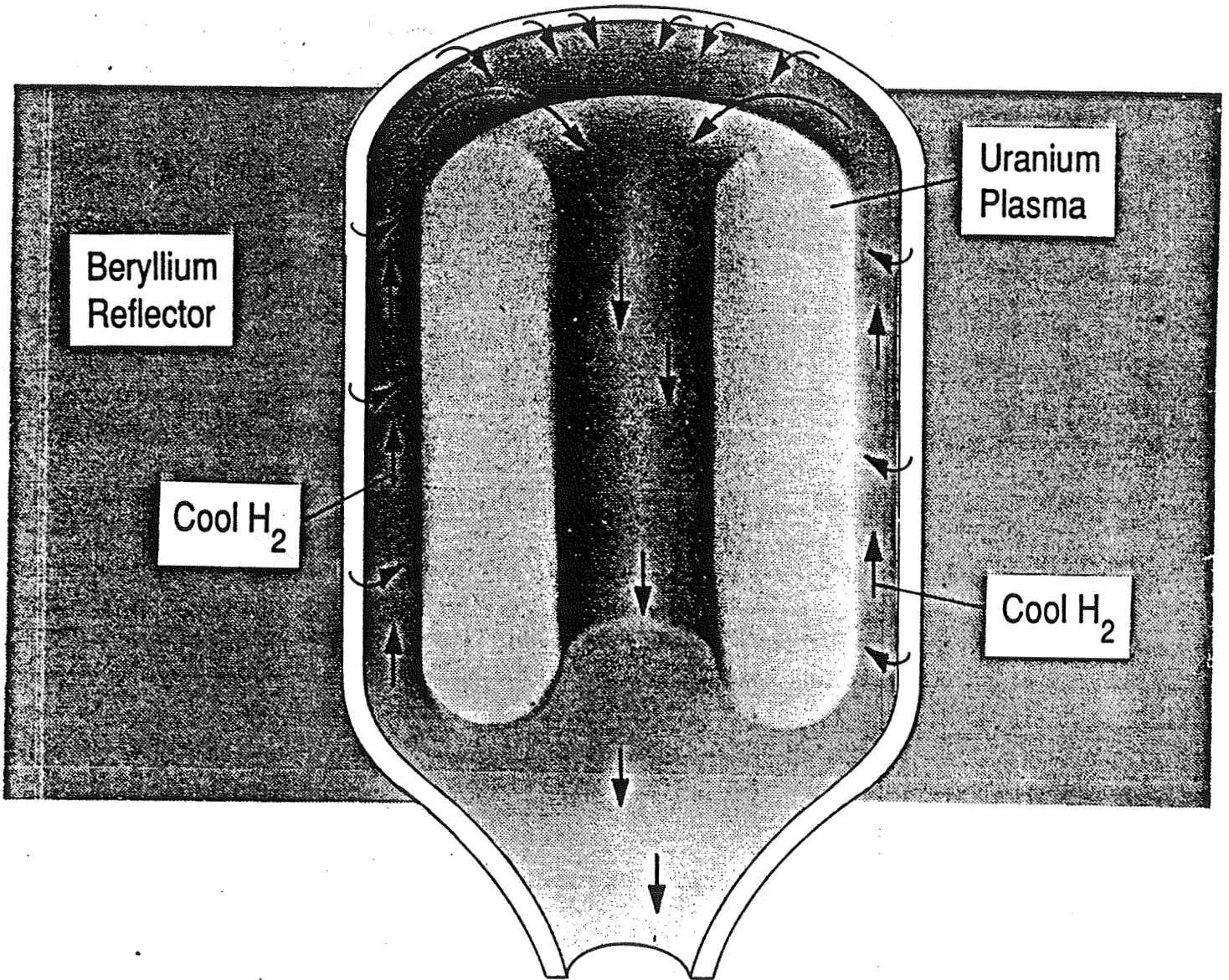
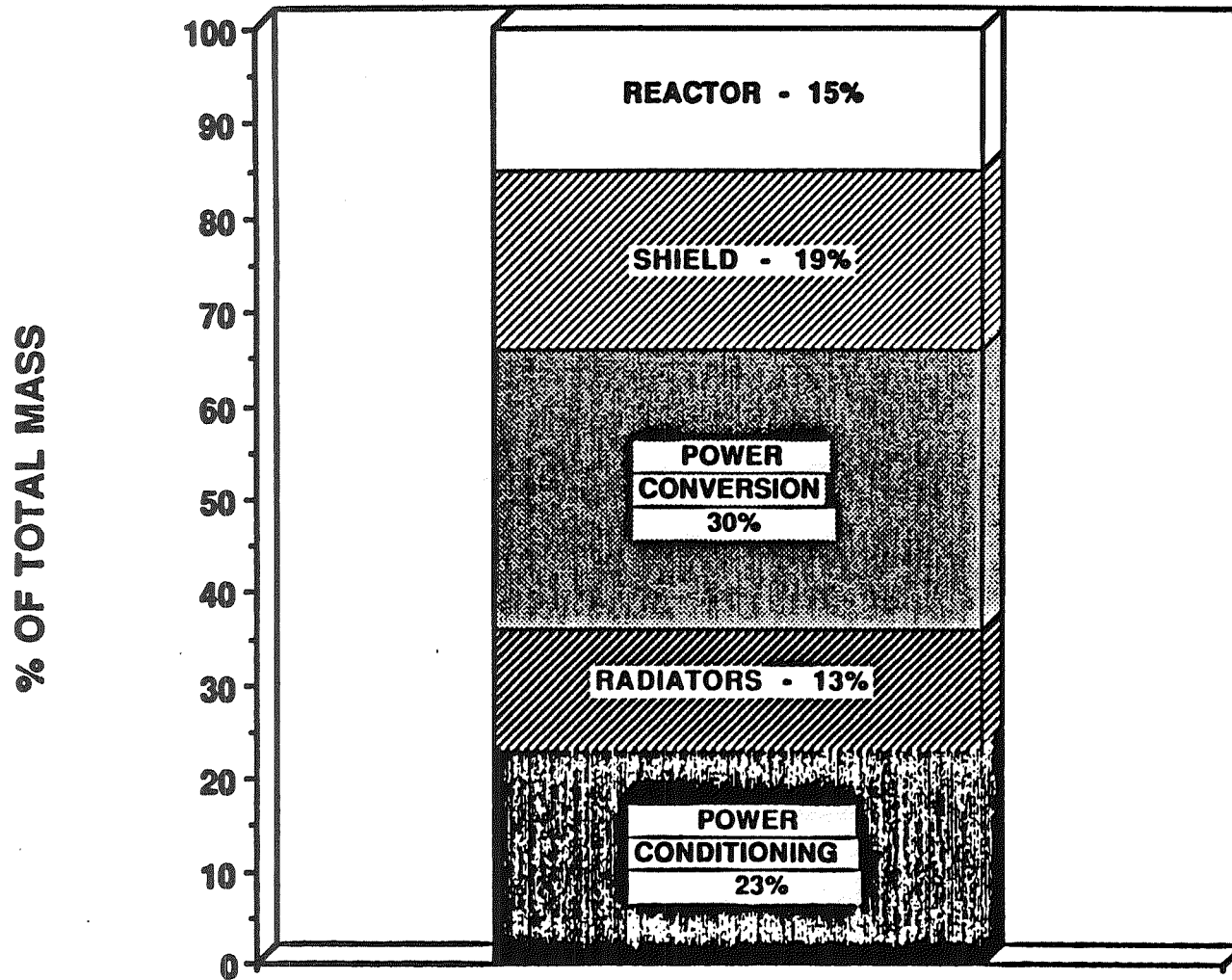


Figure 1. Conceptual Representation of the Counter-Flow Toroidal Gas Core Rocket

Figure 2. NEP SYSTEM MASS BREAKDOWN



Source: SP-100 Derivative Baseline

Courtesy of the NASA Electric Propulsion Workshop

June 1990

AN ANTIPROTON DRIVER FOR ICF PROPULSION*

Pi-Ren Chiang, R. A. Lewis and G. A. Smith
Department of Physics

and

C. Gazze, K. Higman and R. Newton
Department of Nuclear Engineering

and

M. Chiaverini, J. Dailey, M. Surratt, and W. Lance Werthman
Department of Aerospace Engineering

and

S. Chakrabarti
Department of Mechanical Engineering

and

P. Cracraft
Department of Engineering Science
PENN STATE UNIVERSITY

SUMMARY

Inertial confinement fusion (ICF) utilizing an antiprotoncatalyzed target is discussed as a possible source of propulsion for rapid interplanetary manned space missions. The relevant compression, ignition and thrust mechanisms are presented. Progress on an experiment presently in progress at the Phillips Laboratory, Kirtland AFB, NM to demonstrate proof-of-principle is reviewed.

I. INTRODUCTION

Inertial confinement fusion (ICF) could provide thrust and high I_{sp} from plasma created in micro-explosions in uranium-hydrogen pellets. We are studying the practicality of igniting the pellet with antiproton-induced fission. The driver system would include a trap in which antiprotons are stored and an accelerator to deliver antiprotons to the pellet. The antiproton part of the driver would be compact, making it especially attractive for space propulsion applications. A typical manned mission to Mars using this system (called ICAN, for Ion Compressed Antiproton Nuclear system) is graphically illustrated in Figure 1. A modern variant of the pusher plate technology of ORION due to J. Solem (1) for converting motion of hot plasma to thrust is shown in Figure 2.

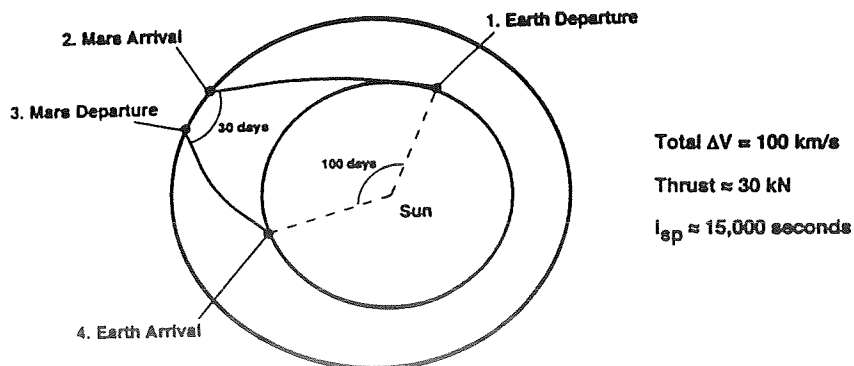


Fig. 1-ICAN Mars Mission for 1 Dec 2011 Launch

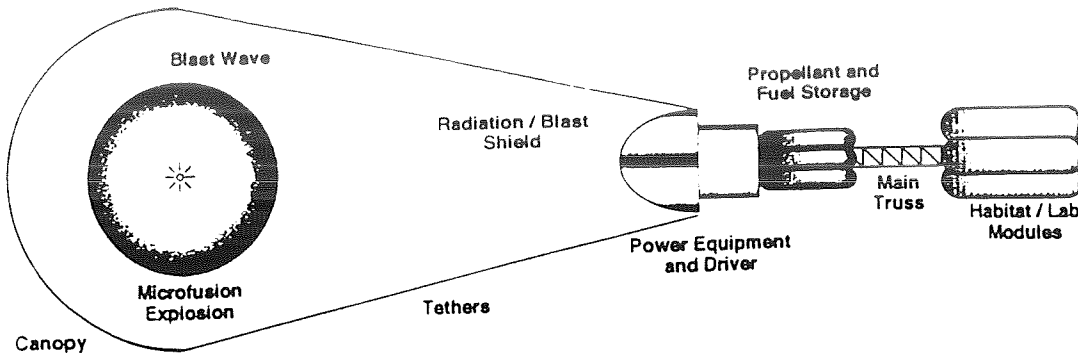


Fig. 2-ICAN spacecraft schematic layout after Solem/Medusa concept (1)

II. ANTIPROTON-CATALYZED MICROFISSION/FUSION

Recently our group has observed large fission and neutron yields from antiproton annihilation at rest in a natural uranium target (2). Calculations indicate that short bursts of stopped antiprotons could induce temperatures of several KeV in a small pellet heated by fission fragments. These conditions may be appropriate for ignition of a hydrogen fusion burn within the microsphere. The driver scheme presently under consideration would utilize antiprotons as a catalyst to the microfission/fusion process. Compression could be provided by a driver such as light ion beams. Targets with yields up to 50 Gjoules have been considered (3).

Figure 3 illustrates the calculated neutron yield per antiproton on a small (27 gram) uranium target versus target density \times radius under conditions corresponding to subcritical gain (see Section III). Neutrons produced directly by antiprotons and charged pions confined by intense magnetic fields produced in the compression contribute equally to the gain.

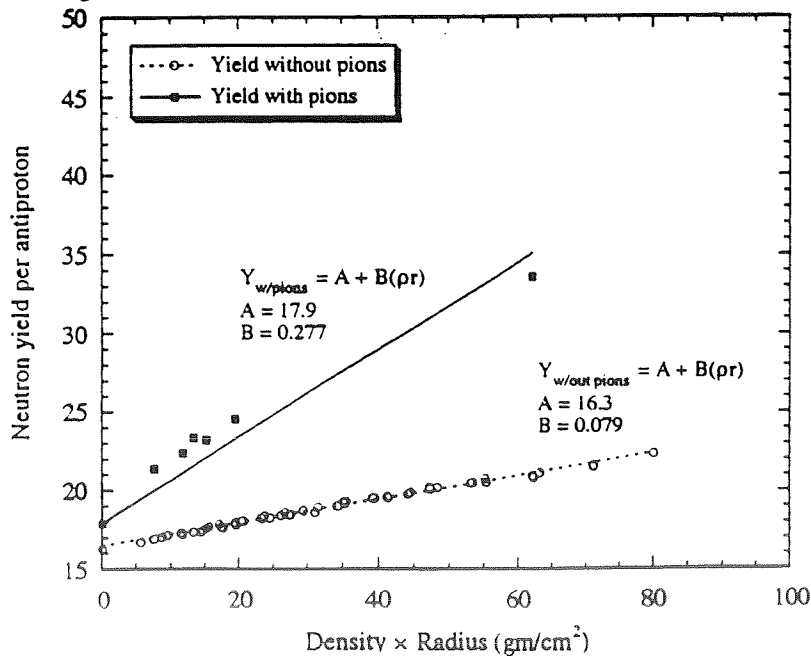


Fig. 3-Subcritical neutron yields for U-238

III. SHIVA STAR EXPERIMENT

We have embarked upon an experimental program using the Shiva Star facility at the Phillips Laboratory, Kirtland AFB. The goal is to demonstrate subcritical neutron multiplication due to antiproton fission in targets compressed to 10-40 Mbar pressure. These proof-of-principle experiments could lead to a program of full target experiments at a later time with direct applications to propulsion needs. Figure 4 shows a schematic layout of the experiment. Antiprotons, stored in a Penning trap, are released at 20 KeV energy, accelerated to 1.2 MeV by a radiofrequency quadrupole (RFQ) accelerator, and then bent and focused onto the compressed target inside an imploding solid liner driven by the SHIVA Star 5.2 MJ capacitor bank.

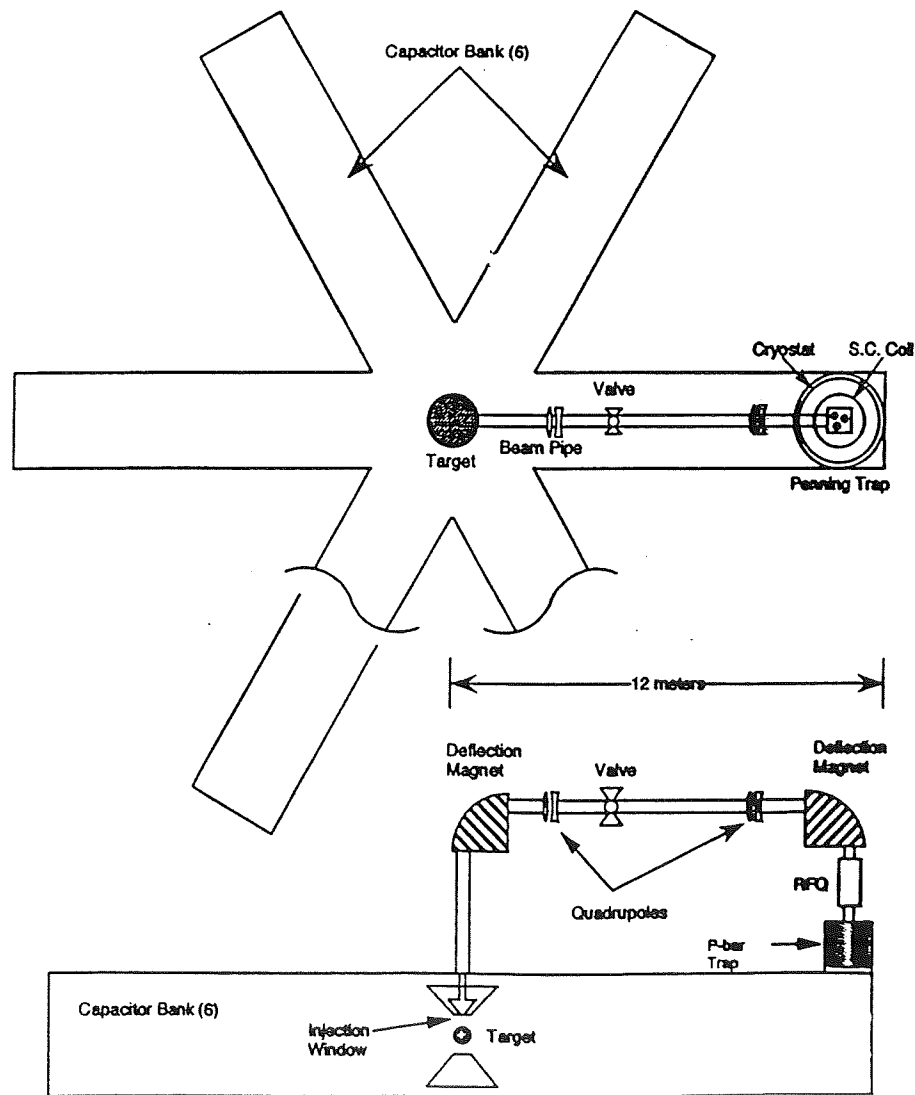


Fig. 4-SHIVA Star antiproton injection system

Figure 5 shows a close-up of the target region, indicating the liner moving in rapidly and compressing a hydrogen working fluid, which in turn compresses the target. A short burst of antiprotons ignites the target as it reaches peak compression.

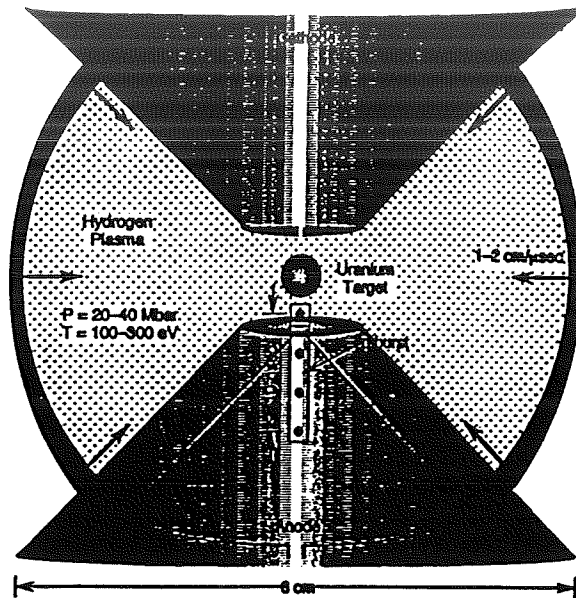


Fig. 5-Solid liner during compression cycle

IV. ANTIPROTON TRAPPING EXPERIMENTS

We are collaborating with the P-15 group at Los Alamos National Laboratory on antiproton trapping experiments at the Low Energy Antiproton Ring (LEAR) at CERN, Geneva, Switzerland. Recently we successfully trapped 700,000 antiprotons from single beam shots from the accelerator. With improved vacuum, using multipulse injection and electron cooling in the catcher trap we hope to trap and confine ten times this number before the end of 1993.

The design of a portable Penning trap and associated transfer optics for moving antiprotons from the catcher trap to the portable trap is complete, and construction of these systems is starting. It is planned to move antiprotons to the Phillips Laboratory in 1995 for the first of a series of subcritical microfission tests.

V. FOOTNOTES AND REFERENCES

* Supported in part by AFOSR, Air Force Palace Knight program, Jet Propulsion Laboratory, National Science Foundation, Penn State center for Space Propulsion Engineering under grant #NAGW-1356 (suppl. 6), and Rocketdyne Corporation.

1. J. Solem, "MEDUSA: Nuclear Explosive Propulsion for Interplanetary Travel", LA-UR-91-1584, Los Alamos National Laboratory, to be published in the Journal of the British Interplanetary Society; "Nuclear Explosive Propulsion for Interplanetary Travel: Extension of the MEDUSA Concept for Higher Specific Impulse", LA-UR-92-765.
2. B. Chen et al., Phys.Rev.C45, 2332 (1992).
3. R. A. Lewis et al., "Antiproton Boosted Microfission", Nuc.Sci.Eng.109, 411 (1991); Fusion Tech. 20, 1046 (1991).

PERFORMANCE ASSESSMENT OF LOW PRESSURE NUCLEAR THERMAL PROPULSION

Harold P. Gerrish Jr. and Glen E. Doughty
Marshall Space Flight Center
Huntsville, Alabama 35812

INTRODUCTION

An increase in Isp for nuclear thermal propulsion systems is desirable for reducing the propellant requirements and cost of future applications, such as the Mars Transfer Vehicle. Several previous design studies have suggested that the Isp could be increased substantially with hydrogen dissociation/recombination. Hydrogen molecules (H_2), at high temperatures and low pressures, will dissociate to monatomic hydrogen (H), see Figure 1. The reverse process (i.e., formation of H_2 from H) is exothermic. The exothermic energy in a nozzle increases the kinetic energy and therefore increases the Isp.

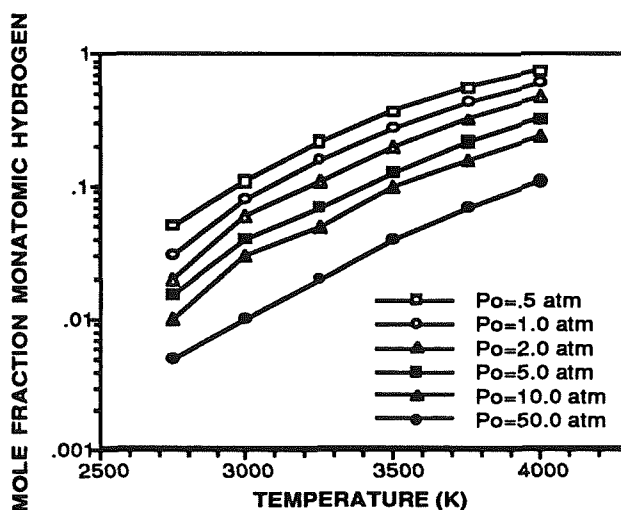


Figure 1. Mole fraction of hydrogen dissociated to monatomic hydrogen¹.

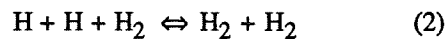
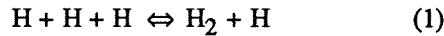
The low pressure nuclear thermal propulsion system (LPNTP) system is expected to maximize the hydrogen dissociation/recombination and Isp by operating at high chamber temperatures and low chamber pressures. The process involves hydrogen flow through a high temperature, low pressure fission reactor, and out a nozzle. The high temperature (~3000 K) of the hydrogen in the reactor is limited by the temperature limits of the reactor material. The minimum chamber pressure is about 1 atm because lower pressures decrease the engines thrust to weight ratio below acceptable limits. This study assumes that hydrogen leaves the reactor and enters the nozzle at the 3000 K equilibrium dissociation level.

Hydrogen dissociation in the reactor does not affect LPNTP performance like dissociation in traditional chemical propulsion systems, because energy from the reactor resupplies energy lost due to hydrogen dissociation. Recombination takes place in the nozzle due primarily to a drop in temperature as the Mach number increases. However, as the Mach number increases beyond the nozzle throat, the static pressure and density of the flow decreases and minimizes the recombination. The ideal LPNTP Isp at 3000 K and 10 psia is 1160 seconds due to the added energy from fast recombination rates. The actual Isp depends on the finite kinetic reaction rates which affect the amount of monatomic hydrogen recombination before the flow exits the nozzle.

A LPNTP system has other technical issues (e.g. flow instability and two-phase flow) besides hydrogen dissociation/recombination which affect the systems practicality. In this study, only the effects of hydrogen dissociation/recombination are examined.

KINETICS MODEL

The two-dimensional kinetics (TDK) nozzle performance computer program² was used to determine the effect of various parameters on hydrogen dissociation/recombination and Isp in a conical nozzle. TDK simulates an inviscid flow from the start of nozzle contraction to the nozzle exit. Boundary layer calculations and heat loss were neglected. The one-dimensional equilibrium (ODE) option of TDK was used to calculate the upper Isp limit due to shifting molar species concentrations in the expansion process. The one-dimensional frozen (ODF) option of TDK was used to calculate the lower Isp limit due to frozen molar species concentrations in the expansion process. The one-dimensional kinetics (ODK) option of TDK accounts for the effects of finite chemical kinetics. Both ODE and ODK calculations provide data in the axial direction only, and the properties for each cross-section are constant. The TDK option calculates changes in the radial direction and uses two third-body reactions for hydrogen (H₂, H):



The reaction rate coefficient equations (k_{H_2} and k_{H}) for each of the above reactions are in the Arrhenius form, which is written as:

$$k = AT^{-N} e^{\frac{-1000B}{RT}} \quad (3)$$

Table 1 shows the forward kinetic k_{H} and k_{H_2} equations obtained from Cohen & Westberg (C&W)³, from the national aerospace plane (NASP) rate constant committee of the NASP high-speed propulsion technology team⁴, and from the default equations used in the TDK. The C&W equations were used in this study.

RESULTS

Pressure Sensitivity

The ODK and TDK Isp curves are close to equilibrium (ODE) at high stagnation chamber pressure (P_0), but approach frozen flow (ODF) at low P_0 , Figure 2. As P_0 decreases from 1000 psia to 100 psia, both ODK Isp and TDK Isp increase. At 100 psia, Figure 2 shows the ODK Isp to be approximately 1007 seconds, and 27 seconds greater than the ODF Isp. From 100 psia down to 10 psia, the ODK Isp and TDK Isp change is minimal. Below 10 psia, the ODK Isp increases like frozen flow due to a lower average molecular weight caused by greater dissociation and less recombination. At 10 psia, the ODK Isp is 1005 seconds, but is only 14 seconds greater than the ODF Isp.

The mole fraction of monatomic hydrogen (X_{H}) entering the nozzle is 17.3% with P_0 at 10 psia and 5.9% with P_0 at 100 psia, see Figure 4. The X_{H} decreases in the nozzle due to monatomic hydrogen recombination. Inside the nozzle, there is 3% recombination at 100 psia and 1.25% recombination at 10 psia. Greater recombination from higher pressures and flow densities is the reason why the difference between ODK Isp and ODF Isp is greater at 100 psia.

Temperature Sensitivity

Plots illustrating Isp versus P_0 at 3200 K are shown in Figure 3. The Isp is almost constant from 10 psia to 100 psia. At 100 psia, the ODK Isp is 1066 seconds and 45 seconds greater than the ODF Isp. Thus, increasing the stagnation chamber temperature (T_0) from 3000 K to 3200 K will increase the ODK Isp by approximately 60 seconds.

Table 1. Kinetic reaction rate coefficient equations.

$H + H + M \rightleftharpoons H_2 + M$

STANDARD TDK²

M=Ar,	$k = 6.4 \cdot 10^{17} T^{-1}$	
M=H,	$k = 25 \cdot k(\text{Ar})$	
M=H ₂ ,	$k = 4 \cdot k(\text{Ar})$	

COHEN AND WESTBERG³

M=H:	$k = 1 \cdot 10^{15}$	LOW
	$k = 3.2 \cdot 10^{15}$	NOMINAL
	$k = 1.0 \cdot 10^{16}$	HIGH
M=H ₂ :	$k = 5 \cdot 10^{16} T^{-0.6}$	LOW
	$k = 1.0 \cdot 10^{17} T^{-0.6}$	NOMINAL
	$k = 2.0 \cdot 10^{17} T^{-0.6}$	HIGH

NASP EQUATIONS⁴

M=H:	$k = 1.5 \cdot 10^{19} T^{-1.0}$
M=H ₂ :	$k = 1.8 \cdot 10^{18} T^{-1.0}$

UNITS=CM³/(MOLE²·SEC)

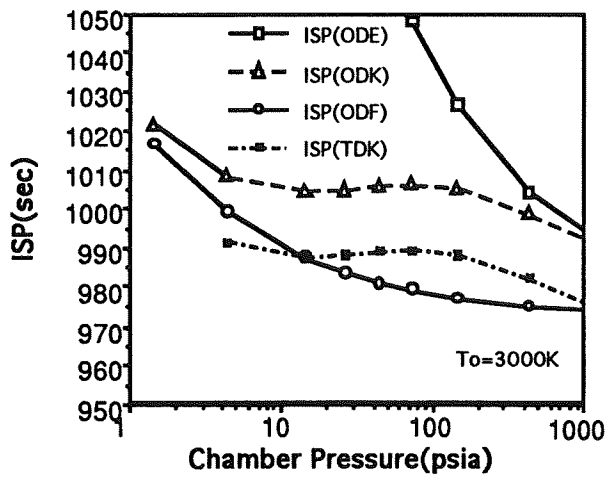


Figure 2. Isp vs. Po.

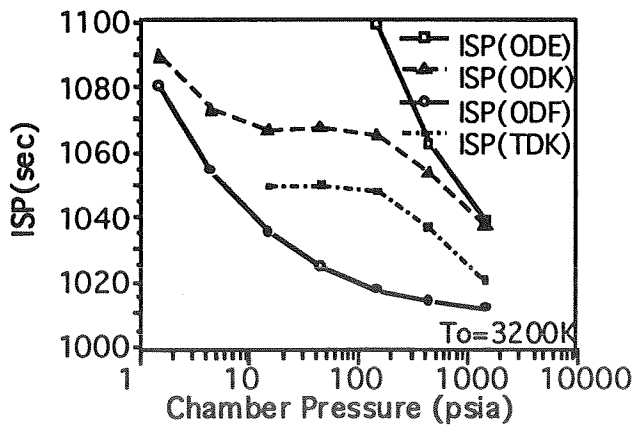


Figure 3. Isp vs. Po at 3200 K.

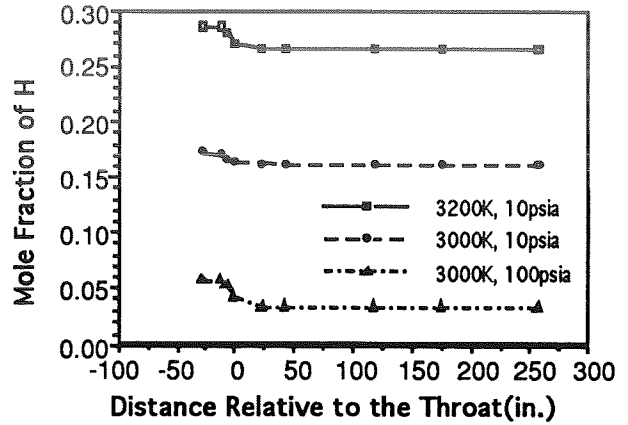


Figure 4. X_H vs. axial nozzle position.

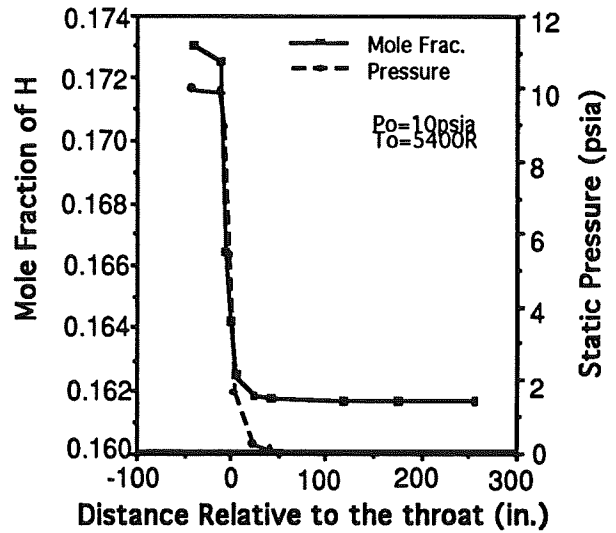


Figure 5. X_H and P vs. X (Po=10 psia).

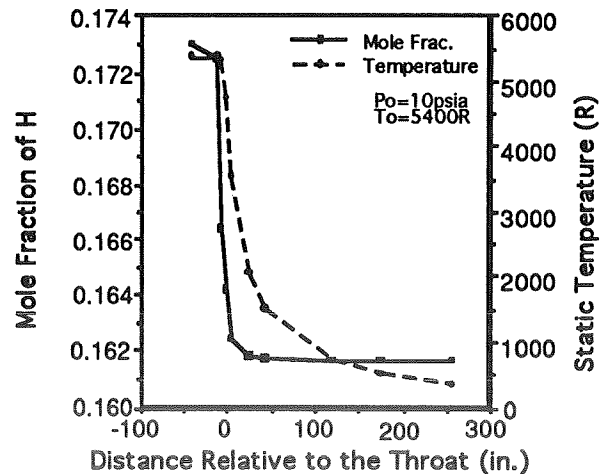


Figure 6. X_H and T vs. X (Po=10 psia).

Increasing T_0 from 3000 K to 3200 K, at 10 psia, increases X_H at the nozzle inlet to 28.6%, see Figure 4. Results show 2% recombination inside the nozzle. In addition, the exiting X_H at 10 psia is higher at 3200 K than at 3000 K which reduces the average molecular weight.

Nozzle Contour Sensitivity

Based on the TDK capabilities, practical changes in the nozzle geometry showed minimal effects on Isp due to dissociation/recombination. The one-dimensional variations of pressure, temperature, and X_H throughout the LPNTP nozzle are displayed in Figures 5 and 6. Both figures show most recombination occurring around the throat. The change in X_H throughout the nozzle is very similar to changes in pressure. At the point where recombination stops, the pressure and flow density is close to zero.

Kinetics Sensitivity

The effects of hydrogen kinetic reaction rate uncertainty was also analyzed. Although differences in reaction rate coefficients should not affect the results of a comparative study such as this, it will be an important aspect in ensuring TDK accuracy and Isp predictions. Previously shown in Table 1 were three different sets of k_H and k_{H_2} equations. Results show a small difference in ODK Isp between the three sets of k_H and k_{H_2} equations. Each set of equations was determined from experimental reaction rates. The uncertainty for each set of k_H and k_{H_2} equations is due to either scatter in experimental data or experiment type. At 10 psia, uncertainty in the C&W k_H and k_{H_2} equations varies the ODK Isp from 999 seconds to 1014 seconds at 3000 K, and 1056 seconds to 1085 seconds at 3200 K.

CONCLUSIONS

TDK Isp is close to equilibrium flow at high P_0 and close to frozen flow at low P_0 . With T_0 at 3000 K, the maximum TDK Isp and maximum difference between ODK Isp and ODF Isp occurs at $P_0 \sim 100$ psia, due to increased monatomic hydrogen recombination. The Isp is ~ 15 seconds higher at a P_0 of 100 psia than at 1000 psia. The optimum P_0 indicates a greater impact on Isp from recombination than from lower average molecular weights. A T_0 of 3200 K increases both the amount of hydrogen dissociation (decrease in the average hydrogen molecular weight) and recombination. These characteristics boost the Isp above the value that would be obtained by only considering temperature effects.

Examination of various nozzle geometries showed a minimum impact on recombination and Isp. The significant changes that did occur were related to a more efficient use of two-dimensional nozzle flow. Most recombination occurs around the nozzle throat due to low static temperatures which foster recombination. Low static pressures and flow densities limit the amount of recombination downstream of the throat.

Finally, the uncertainty of the k_H and k_{H_2} , at high T_0 , has a significant impact on the Isp predictions. There is a large difference between ODE and ODF Isp's at a lower P_0 , and the ODK Isp could be anywhere between depending on the assumed reaction rate. The slow k_H and k_{H_2} used in this study cause the ODK Isp to approach the ODF Isp at low static pressures.

RECOMMENDATIONS

Since the LPNTP Isp predictions were closer to frozen flow Isp than ideal equilibrium Isp at low P_0 , more extensive calculations using a TDK model that accounts for boundary layer effects, and non-adiabatic flow are not recommended at this time.

Faster kinetic reaction rates will increase both the monatomic hydrogen recombination and the Isp. Because there is an uncertainty with the high temperature values of k_H and k_{H_2} , accurate hydrogen dissociation/recombination

bench tests are recommended to determine if the actual reaction rates are different than the published reaction rates used in this study. High temperature sub-scaled nozzle tests with thrust and mass flow sensors are recommended to determine the actual Isp, because actual nozzle flow characteristics (e.g., boundary layer effects) might affect the amount of hydrogen dissociation/recombination.

Based on the results of this study, the chamber pressure recommended is 190 psia for a 3000 K chamber temperature. This chamber pressure is above hydrogen's critical pressure (188 psia) to minimize two-phase flow problems in the feed system (e.g., flow oscillations). Operating at 190 psia has an Isp slightly less than at 100 psia, but produces a higher thrust than at 10 psia and has a higher Isp than at 1000 psia. In addition, the nozzle should have a bell diverging section to shorten the nozzle length and minimize divergence losses. The nozzle's converging/throat section should be designed to maximize the recombination.

Finally, TDK only uses conical converging nozzle sections. Other kinetic computer models which can vary the converging nozzle contour should be investigated to determine the effects on Isp.

REFERENCES

1. Benton, D.: "CREST" computer program, version 4, 1988.
2. Nickerson, G.R., Coats, D.E., Dang, A.L., Dunn, S.S., and Kehtarnavaz, H.: "Two-Dimensional Kinetics (TDK) Nozzle Performance Computer Program." Software and Engineering Associated, Inc., NAS8-36863, March, 1989.
3. Cohen, N., and Westberg, K.: "Chemical Kinetic Data Sheets for High Temperature Chemical Reactions." J Phys Chem. Ref Data, 12, No. 3, 531-590, 1983.
4. Oldenborg, R.: "Hypersonic Combustion Kinetics - Status Report of the Rate Constant Committee, NASP High-Speed Propulsion Technology Team." NASP Tech Memo 1107, May, 1990.

NUCLEAR PROPULSION CONTROL AND HEALTH MONITORING

P.B. Walter and R.M. Edwards
Department of Nuclear Engineering
The Pennsylvania State University
231 Sackett Building
University Park, PA 16802
(814) 865-1341

Summary

An integrated control and health monitoring architecture is being developed for the Pratt & Whitney XNR2000 nuclear rocket. Current work includes further development of the dynamic simulation modeling and the identification and configuration of low level controllers to give desirable performance for the various operating modes and faulted conditions. Artificial intelligence and knowledge processing technologies need to be investigated and applied in the development of an intelligent supervisory controller module for this control architecture.

In recent years, there has been renewed interest in solid core nuclear thermal propulsion systems (nuclear rockets) because of their ability to achieve space mission performance objectives that are well beyond chemical propulsion system capabilities. Because the planned missions for these propulsion systems will require autonomous or nearly autonomous operation, advanced controls and health monitoring systems have been identified as critical technologies for their development.¹ The Pennsylvania State University's Intelligent Distributed Control Research Laboratory is currently defining a control system and required instrumentation for the Pratt & Whitney XNR2000 fast spectrum, CERMET fueled nuclear rocket.² The project includes development of simulation models to evaluate various control algorithms, application of recent advances in intelligent control theory, and evaluation of conventional and unconventional process variable sensors.

To achieve the desired performance objectives of high specific impulse and high thrust to weight ratios, nuclear rockets are designed to operate near the maximum solid core material temperatures. Therefore, the instantaneous temperature distribution in the core is a critical parameter for system safety and reliability, and the control system must have the ability to tightly regulate the core temperatures for all operating conditions. Unfortunately, with current sensor technology, it will be impossible to directly and accurately measure the core temperature distribution at the higher power levels.³ Therefore, a method for system identification/parameter estimation must be included in the control system architecture for verification of the core temperature regulation.

The nuclear rocket control architecture must provide stability, robustness, and good tracking of the desired performance objectives (thrust and specific impulse), while maintaining constraints on system safety and reliability parameters such as instantaneous core temperatures and reactivity margins. In addition, the control architecture must provide for rapid identification of faults and adjustment of the actuator inputs to provide desirable performance without violating the system safety and reliability constraints.

An integrated control and health monitoring architecture that meets the above requirements is currently under development for the Pratt & Whitney nuclear rocket. As shown in Figure 1, the architecture is modular to allow for easier development and upgrades as new algorithms become available, and to permit implementation in a distributed manner. The modules consist of

1. a bank of preprogrammed controllers that have been preconfigured via simulation modeling or ground-based testing to provide desirable performance regulation for various different operation modes and conditions,
2. a signal validation module to provide analytic redundancy of the sensor and control signals to identify if a signal is indicative of a system component failure or of a sensor or signal processing failure,
3. a system identification module to estimate system safety and reliability parameters such as instantaneous and projected core temperature distribution,
4. a health monitoring /diagnostics module to identify the current health and operating conditions of the nuclear rocket (plant), and
5. the intelligent supervisory controller module which evaluates the performance of the system with the information from the system identification and health monitoring modules, and selects a controller from the bank of preprogrammed controllers that will provide the desired performance response without violating the system safety and reliability constraints.

The focus of our current work is to complete a dynamic simulation model of the nuclear rocket and to develop a bank of low level controllers to handle system startup, throttling to full power, shutdown, and several basic system faults such as turbopump or valve failures. A dynamic simulation system for modeling nuclear rockets is being developed using the *Simulink/Matlab* simulation and numerical analysis software. This simulation system consists of a series of modules that model basic physical phenomena such as 1-D compressible flow in a pipe, lumped parameter heat transfer, and point reactor kinetics. These modules can then be connected via the point and click *Simulink* user interface to build the nodes of a one dimensional model. These nodes are then copied, moved, and appropriately connected, again via point and click, to form higher level components of a nuclear rocket such as core regions, transfer pipes, and turbopumps. These components are then connected to build the complete system model. Current model development work consists of building more system components, including valves, tubopumps, and two-phase flow pipes, integrating multiple reactor kinetics modules to more accurately model the temperature reactivity feedbacks, and automating the initialization routines. The

identification and configuration of the low level controllers to give desirable performance for the various operating modes and faulted conditions is being accomplished using modern control development techniques within the *Simulink/Matlab* environment.

There are currently several signal validation, system identification, and health monitoring algorithms available which should be adequate to test the control and health monitoring architecture.^{4,5,6} Therefore, our future efforts will be in the development of the intelligent supervisory controller module. Artificial intelligence and knowledge processing will be key elements of the supervisory controller. There is substantial current work in these areas,^{7,8} but much work remains in the development and application of this technology to nuclear thermal propulsive systems.

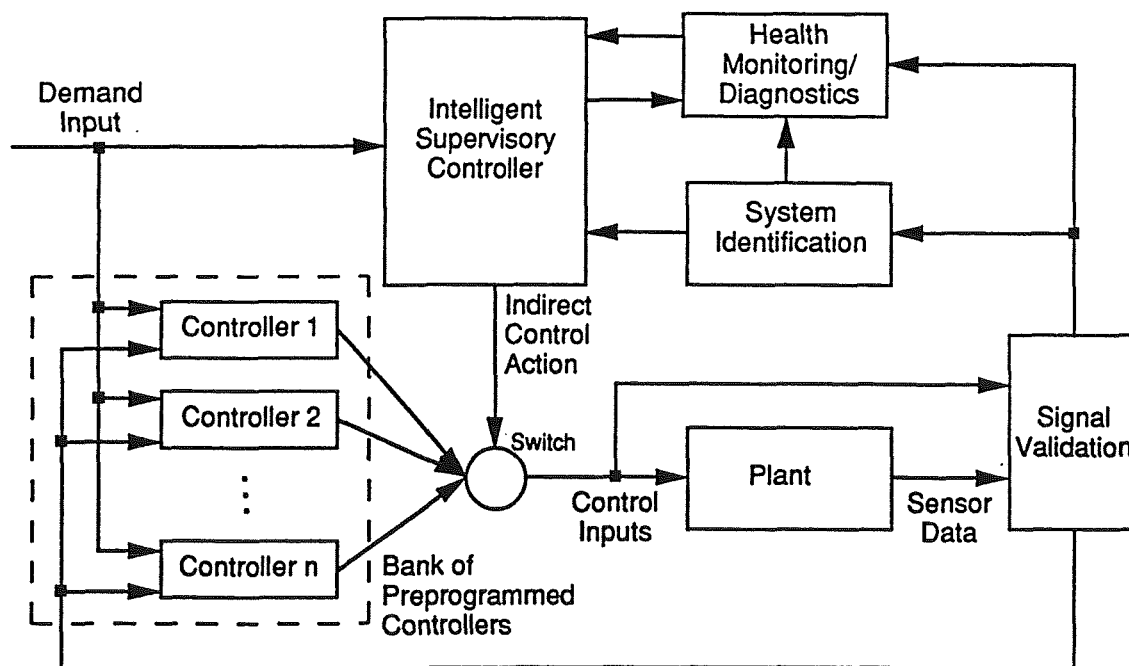


Figure 1: Integrated Control and Health Monitoring Architecture for Nuclear Rockets

Acknowledgments

This work is under contract from Pratt & Whitney. Contract number F433929, "Control and Health Monitoring for Nuclear Propulsion." *Simulink* and *Matlab* are products of The Math Works, Incorporated.

References

1. Clark, J.S., T.J. Wickenheiser, M.P. Doherty, A. Marshall, S.K. Bhattacharyya, and J. Warren, "NASA/DOE/DOD Nuclear propulsion Technology Planning: Summary of FY 1991 Interagency Panel Results," *Proceedings of the ANS Topical Meeting on Nuclear Technologies for Space Exploration*, Jackson, Wyoming, pp. 393-402 (August 16-19, 1992)
2. Peery, S.D., R.C. Parsley, G.J. Feller, and S. Angaie, "A Fast Spectrum Two\Pass Nuclear Thermal Rocket Concept," *Proceedings of the ANS Topical Meeting on Nuclear Technologies for Space Exploration*, Jackson, Wyoming, pp. 393-402 (August 16-19, 1992)
3. Clark, J.S., P. McDaniel, S. Howe, and M. Stanley, "Nuclear Thermal Propulsion Technology: Summary of FY 1991 Interagency Planning," *Presented at the AIAA/NASA/OAI Conference on Advanced SEI Technologies*, Cleveland, Ohio, AIAA 91-3631 (September 4-6, 1991)
4. Gross, K.C., and K. Humenik, "Sequential Probability Ratio Tests for Reactor Signal validation and Sensor surveillance Applications," *Nuclear Science and Engineering*, 105:383-390 (August 1990)
5. Parlos, A.G., A.F. Atiya, K.T. Chong, and W.K. Tsai, "Nonlinear Identification of Process Dynamics using Neural Networks," *Nuclear Technology*, vol. 97, pp.79-96 (January, 1992)
6. Edwards, R.M., D.W. Ruhl, E.H. Klevans, and G.E. Robinson, "Development and Testing of a Diagnostic System for Intelligent Distributed Control at EBR-II," *Proceedings of the 1990 International Fast Reactor Safety Meeting*, Snowbird, Utah, Vol III, pp 299-308 (August 1990)
7. Antsaklis, P.J., and K.M. Passino, "An Introduction to Intelligent and Autonomous Control," Kluwer Academic Publishers, Norwell Massachusetts (1993)
8. Garcia, H.E., "A Reconfigurable Hybrid Supervisory Control System," Doctor of Philosophy Dissertation in Electrical Engineering, The Pennsylvania State University, (December 1993)

The Pennsylvania State University, in compliance with federal and state laws, is committed to the policy that all persons shall have equal access to programs, admission, and employment without regard to race, religion, sex, national origin, handicap, age or status as a disabled or Vietnam-era veteran. Direct all affirmative action inquiries to the Affirmative Action Office, 201 Willard Building, University Park, PA 16802; (814) 863-0471.
U. Ed. ENG 91-79